A High Precision Measurement of the Proton Charge Radius at JLab

by

Weizhi Xiong

Department of Physics
Duke University

Date: _____

Approved:

_____

Haiyan Gao, Advisor

_____

Phillip S. Barbeau

_____

Shailesh Chandrasekharan

_____

Stephen W. Teitsworth

_____

Christopher Walter

Dissertation submitted in partial fulfillment of the
requirements for the degree of Doctor of Philosophy
in the Department of Physics
in the Graduate School of
Duke University

2020

ABSTRACT

A High Precision Measurement of the Proton Charge Radius at JLab

by

Weizhi Xiong

Department of Physics
Duke University

Date: _____

Approved:

_____

Haiyan Gao, Advisor

_____

Phillip S. Barbeau

_____

Shailesh Chandrasekharan

_____

Stephen W. Teitsworth

_____

Christopher Walter

An abstract of a dissertation submitted in partial fulfillment of the requirements for the degree of Doctor of Philosophy in the Department of Physics in the Graduate School of Duke University

2020

Abstract

The elastic electron-proton ($e-p$) scattering and the spectroscopy of hydrogen atoms are the two traditional methods to determine the proton charge radius (r_p). In 2010, a new method using muonic hydrogen (μH)[1] spectroscopy reported a r_p result that was nearly ten times more precise but significantly smaller than the values from the compilation of all previous r_p measurements. This discrepancy is often referred to as the "proton charge radius puzzle". In order to investigate the puzzle, the PRad experiment (E12-11-106[2]) was first proposed in 2011 and performed in 2016 in Hall B at the Thomas Jefferson National Accelerator Facility, with both 1.1 and 2.2 GeV electron beams. The experiment measured the $e-p$ elastic scattering cross sections in an unprecedented low values of momentum transfer squared region ($Q^2 = 2.1 \times 10^{-4} - 0.06$ (GeV/c)^2), with a sub-percent precision. The PRad experiment utilized a calorimetric method that was magnetic-spectrometer-free. Its detector setup included a large acceptance and high resolution calorimeter (HyCal), and two large-area, high-spatial-resolution Gas Electron Multiplier (GEM) detectors. To have a better control over the systematic uncertainties, the absolute $e-p$ elastic scattering cross section was normalized to that of the well-known Møller scattering process, which was measured simultaneously during the experiment. For each beam energy, all data with different Q^2 were collected simultaneously with the same detector setup, therefore sharing the same integrated luminosity. The windowless H_2 gas-flow target utilized in the experiment largely removed a typical background source, the target cell windows. The proton charge radius was determined as $r_p = 0.831 \pm 0.007_{\text{stat.}} \pm 0.012_{\text{syst.}}$ fm, which is smaller than the average r_p from previous $e-p$ elastic scattering experiments, but in agreement with the μH spectroscopic results within the experimental uncertainties.

[1] A muonic hydrogen has its orbiting electron replaced by a muon.

[2] Spokespersons: A. Gasparian (contact), H. Gao, M. Khandaker, D. Dutta

Acknowledgements

First of all, I would like to sincerely thank my advisor, Prof. Haiyan Gao, for giving me the opportunity to work on this project, and for her generous support not only for me but also for the entire PRad experiment. She not only guided me through various difficulties of this project but also provided me the help I needed for my personal life during my graduate school, even though she was very busy all the time. I believe the best way I can appreciate all these is by working as hard as I can.

I would also like to thank all the members in the PRad collaboration, especially senior physicists: Dr. Gasparian, Dr. Khandaker, Dr. Dutta, Dr. Liyanage, Dr. Pasyuk and Dr. Higinbotham for continuously giving me valuable suggestions throughout the years. I would like to thank all the graduate students who worked on this experiment, including Chao Peng, Xinzhan Bai, Li Ye, and Yang Zhang. I enjoyed all the time we spent together in order to solve various problems, to build and test our detectors, to run the experiment and to overcome various difficulties in the analysis. I would like to express my great appreciation for all the postdoc of this experiment, including Xuefei Yan, Chao Gu, Mehdi Meziane, Vladimir Khachatryan, Maxime Levillain and Zhihong Ye, for their important contributions to various aspects of this experiment, and for their valuable guidance and suggestions for the analysis. I would like to thank especially Xuefei Yan and Chao Gu, who had worked very closely with me through out the years, and had a lot of fruitful discussions about the analysis. Xuefei Yan has developed a machine learning algorithm for rejecting the cosmic background for the PRad experiment, and studied the robust fitters for the PRad result. Chao Gu is one of the most important contributors for the PRad simulation software package and spent a lot of efforts on the event generators and radiative corrections.

Lastly I would like to thank Chao Peng, who has been one of the most important

contributors since the early development and preparation stage of the PRad experiment, and has developed the data analysis software framework for the experiment. I appreciate all the help and suggestions he gave me during my years in the graduate school.

Contents

List of Figures

List of Tables

List of Abbreviations

ADC	Analog-to-Digital Convertor
BPM	Beam Position Monitor
CEBAF	Continuous Electron Beam Accelerator Facility
CODA	CEBAF Online Data Acquisition
DAQ	Data Acquisition System
EPICS	Experimental Physics and Industrial Control System
FEC	Front-End Concentrator cards
GEM	Gas Electron Multiplier
HyCal	Hybrid Calorimeter
PMT	Photon Multiplier Tube
QCD	Quantum Chromodynamics
QED	Quantum Electrodynamics
RMS	Root-Mean-Square
SRS	Scalable Readout System
TDC	Time-to- Digital Convertor
TPC	Time Projection Chamber
TPE	Two Photon Exchange
TI	Trigger Interface

Chapter 1

Introduction

Nucleons (protons and neutrons) are primary building blocks of the visible universe, and they make up over 99.9% of visible matter. It is important to understand the basic properties of a proton, such as its root-mean-square (RMS) charge radius[1] r_p. It is related to the spacial distribution of the proton's charge, which is carried by the quarks. A precise knowledge of r_p is certainly important to our understanding about how Quantum Chromodynamics (QCD) - the theory of the strong interaction - works in the non-perturbative region. This quantity is also an important input to the bound state Quantum Electrodynamics (QED) calculations of atomic hydrogen energy levels. For instance, for a muonic hydrogen (μH) atom, the proton charge radius affects the Lamb shift between $2S_{1/2}$ and $2P_{1/2}$ energy levels by as much as 2% [1]. It also impacts the determination of the Rydberg constant (R_∞), which is one of the most precisely measured quantities in physics. A high precision measurement of the Rydberg constant comes from the exact same type of experiments where the proton charge radius can be determined, so that they are highly correlated.

There are two well-established methods to measure the proton charge radius. The more traditional method is the electron-proton ($e-p$) elastic scattering experiment [2], in which one measures the elastic $e-p$ scattering cross section and then extracts the proton electric form factor G_E^p. The proton charge radius can be determined from the slope of G_E^p as the four-momentum transfer squared Q^2 goes to

[1]It is often referred to as the proton charge radius in this dissertation

zero [2]:

$$\langle r_p^2 \rangle \equiv -6 \frac{dG_E^p(Q^2)}{dQ^2}\bigg|_{Q^2=0} \tag{1.1}$$

The second method is hydrogen spectroscopy [3], in which one measures the transition frequency between two energy levels of a hydrogen atom. These energy levels are affected by the proton charge distribution, and one can determine the proton charge radius from the measured transition frequency, combined with the state-of-the-art bound state QED calculations. The hydrogen Lamb shift has been the transition often adopted for this purpose. The physics background and various techniques used in these two types of methods will be discussed in the next chapter.

Results of r_p obtained with these two methods generally agreed with each other prior to 2010. Based on CODATA-2010 [4], the r_p results are 0.8758(77) fm and 0.895(18) fm, obtained from the compilations of previous hydrogen spectroscopy and $e-p$ elastic scattering experiments, respectively. This agreement was further reinforced in the same year by the result from the high precision $e-p$ elastic scattering experiment at Mainz Microtron (MAMI) [5]. It measured about 1400 cross section data points, covering Q^2 from 0.004 to 1 $(\mathrm{GeV/c})^2$. The extracted r_p from the Mainz experiment is 0.8791(79) fm. Combining these results, CODATA-2010 gave the recommended value for r_p as

$$r_p = 0.8775 \pm 0.0051 \text{ fm}. \tag{1.2}$$

However, also in 2010, a new r_p result was reported based on a novel method using the muonic hydrogen (μH) spectroscopy [1]. A μH atom has its orbiting electron replaced by a muon, which is about 200 times heavier than an electron. As a result, the muon orbits much closer to the proton and is more sensitive to the proton charge

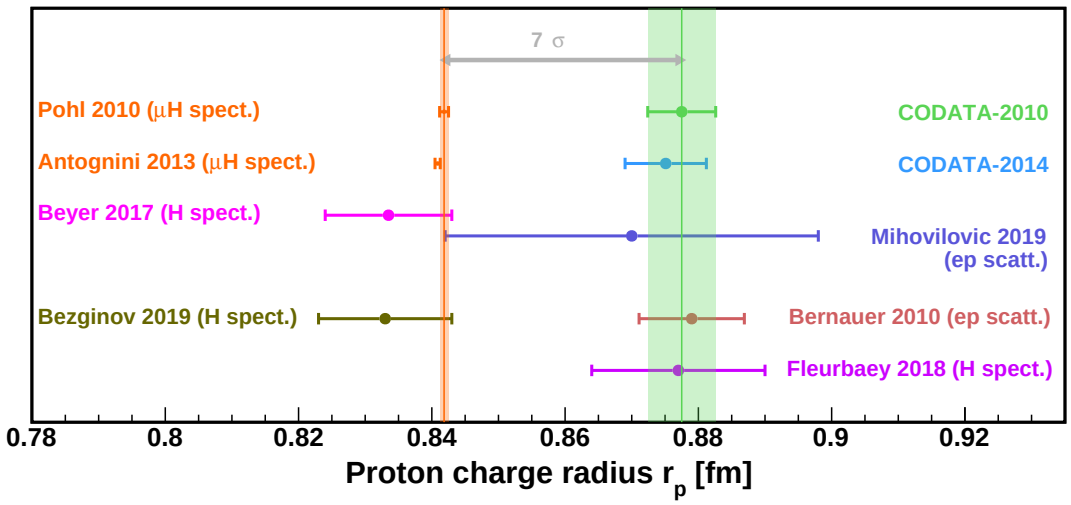

Figure 1.1: Proton charge radius results from recent experiments [1, 5, 6, 18, 19, 20, 22] and world data compilations [4, 7].

radius. The reported result from this experiment is

$$r_p = 0.84184 \pm 0.00067 \text{ fm}, \tag{1.3}$$

with an unprecedented precision of better than 0.1%. However, this value is 7σ smaller than the CODATA -2010 recommended value (see Fig. 1.1), and it was confirmed by a second μH result reported in 2013 [6], which gave

$$r_p = 0.84087 \pm 0.00039 \text{ fm}. \tag{1.4}$$

This discrepancy between the electronic and muonic measurements was unexpected, as the $\mu - p$ and $e - p$ interactions were expected to be the same as described by the Standard Model. The discrepancy is often referred to as the "proton charge radius puzzle", and has triggered intensive experimental and theoretical efforts to resolve this puzzle.

The bound state QED calculations for muonic hydrogen have been scrutinized and refined after the puzzle, yet no convincing evidence could be found to explain the discrepancy [8]. New physics related to lepton[2] universality violation has been proposed [9], which suggests that new particles that couple stronger to the muon and proton can possibly resolve the puzzle. Constraints from other physics such as the muon $(g-2)_\mu$, Kaon decay and the hyper-fine structure measurement in the muonic hydrogen [9], put unusual requirements on the properties of these new particles, though not denying their existence. The definition of the proton charge radius (Eq. 1.1) has been examined rigorously in both the spectroscopic and scattering theories [10]. The same G_E^p slope at $Q^2 = 0$, measured by the elastic scattering experiments, is shown to be responsible for the finite proton size effect in the hydrogen spectroscopy. However, as pointed out also in Ref. [10], the r_p defined in Eq. 1.1 is not strictly related to the second moment of the proton charge density distribution.

Meanwhile, for $e-p$ scattering, the proper Q^2 range of the form factor data and the proper functional forms used in the fit were intensively studied and discussed recently [11, 12]. Numerous re-analyses of the existing $e-p$ scattering data were carried out in order to provide more inputs to the puzzle [13, 14]. However, no conclusive argument can be made at this point. In particular, studies [15, 16] have shown that when using a reduced Q^2 range and lower order fit functions, one can obtain r_p results that are in agreement with the muonic spectroscopic measurements, while others [17] emphasize the need of including data points with higher values of Q^2 and using higher order fit functions for a reliable radius extraction.

From the experimental side, multiple new hydrogen spectroscopic results were published since 2010. These include the 2S-4P transition frequency measurement [18], which published $r_p = 0.8335(95)$ fm in 2017; the 1S-3S transition frequency measure-

[2]Leptons include electrons, muons and taus, and their anti-particles.

ment [19], which gave $r_p = 0.877(13)$ fm in 2018; and the most recent 2S-2P Lamb shift measurement [20], which determined $r_p = 0.833(10)$ fm in 2019. The 2017 and 2019 measurements are very close to each other and both agree with the μH measurements, while the 2018 measurement is in agreement with the CODATA-2010 value. For lepton-proton scattering experiments, the initial state radiation (ISR) experiment at MAMI measured the proton electric form factor in a very low Q^2 region (0.001 to 0.016 (GeV/c)^2) [21]. Their latest extracted r_p is 0.870(28) fm [22], which was published in 2019. The results from these experiments are summarized in Fig. 1.1. For future experiments, The MUSE collaboration [23] aims to extract r_p using 4 different leptons, e^+, e^-, μ^+ and μ^-, and the Q^2 range is from 0.002 to 0.07 (GeV/c)^2. This experiment is the first $\mu - p$ elastic scattering experiment in history and provides unique opportunities for testing the electron-muon universality and the determination of the Two-Photon Exchange (TPE) effect in the lepton-proton scattering. This experiment is currently taking data, and is expected to have results in the next few years. The ProRad experiment [24] at Institut de Physique Nucléaire d'Orsay plans to measure the proton electric form factor in a very low Q^2 region from 10^{-6} to 10^{-4} (GeV/c)^2, using a laminar liquid hydrogen jet target. This experiment is foreseen to take data in the second half of 2020. The ULQ2 collaboration [25] at Tohoku University plans to measure both the proton electric and magnetic form factors in the Q^2 range from 3×10^{-4} to 8×10^{-3} (GeV/c)^2. It will use a 20 to 60 MeV electron beam and high resolution spectrometers to cover the electron scattering angles from 30° to 150°. Another $\mu - p$ elastic scattering experiment is proposed at COMPASS [26]. They plan to use a high pressure Time Projection Chamber (TPC), filled with hydrogen gas, for both an active target and recoil proton detector. The Q^2 coverage is expected to be from 10^{-4} to 1 (GeV/c)^2. The same TPC detector will be used at MAMI to extract the proton charge radius using the $e - p$ elastic scattering [27]. In

addition, a number of new experiments are planed at MAMI, including a new ISR experiment [21], with a point-like jet target and an improved spectrometer entrance flange to further reduce the systematic uncertainties.

At this point, we wish to discuss the PRad experiment (E12-11-106) [28] at the Thomas Jefferson National Accelerator Facility (Jefferson Lab or JLab), which is an elastic $e-p$ scattering experiment. Compared to the previous $e-p$ elastic scattering experiments, it used a magnetic-spectrometer-free and calorimeter based technique, which enabled a number of improvements. First of all, data points at different Q^2 were recorded with the same detector setting during the experiment, with all the elements in the experimental setup fixed in space. This eliminated the need of having a large number of normalization parameters, which are typical for spectrometer-based experiments and may introduce additional systematic uncertainties to the result. Second, the PRad experimental setup covered a minimum scattering angle of 0.7°, which corresponds to a minimum Q^2 close to 2×10^{-4} $(\mathrm{GeV/c})^2$. This is the lowest value ever measured for all the $e-p$ elastic scattering experiments. Together with the maximum angular coverage of 7.0°, the PRad setup covered two orders of magnitude in the low Q^2 region (2×10^{-4} to 6×10^{-2} $(\mathrm{GeV/c})^2$), which provided a large enough leverage that was necessary for a precise r_p extraction. The combination of the low Q^2 and the extreme forward angular coverage also minimized the proton magnetic form factor G_M^p contribution to the cross section, which reduced the systematic uncertainty in the G_E^p extraction. Third, the absolute $e-p$ elastic scattering cross section was normalized to that of the Møller scattering process ($e-e$ scattering), which is a well known QED process and was simultaneously measured during the experiment with the same experimental setup. By taking the $e-p$ to $e-e$ ratio, the luminosity is cancelled out, and this ratio can also enable a cancellation of the energy-independent part of the acceptance and detector efficiency, which is important for the control

of systematic uncertainties. Lastly, the experiment used a windowless, cryogenic-cooled, hydrogen gas-flow target. It removed most of the backgrounds generated from the target cell windows, which was one of the dominant background sources for the previous $e - p$ scattering experiments.

This dissertation presents the analysis and results of the PRad experiment. Chapter 2 provides a general introduction to the physics background and various experimental methods for the r_p measurements. The PRad experimental setup will be introduced in Chapter 3. Details of the analysis, and the $e - p$ elastic scattering cross section results and their systematic uncertainties will be presented in Chapter 4, followed by the r_p extraction in Chapter 5. Lastly, a discussion about possible future improvements on the PRad results will be given in Chapter 6, followed by the conclusion of the PRad project in Chapter 7.

Chapter 2

Physics Background

2.1 Unpolarized electron-proton scattering

The derivation described in this section follows Ref. [29]. At Born level (one photon exchange), an incident electron (with 4-momentum $\ell = (E_l, \vec{\ell})$) can scatter elastically off a proton ($p = (E_p, \vec{p})$) by exchanging a virtual photon. The process is described by the Feynman diagram in Fig 2.1. The 4-momenta of the scattered electron and proton are denoted as $\ell' = (E_{\ell'}, \vec{\ell'})$ and $p' = (E_{p'}, \vec{p'})$, respectively. For a fixed target experiment with an incident electron beam, typically, the target proton is considered at rest in the lab frame. The z-axis can be chosen to be aligned with the momentum direction of the incident electron, and the $x - z$ plane is defined by the momenta of the incident and scattered electrons (the lepton scattering plane) (see Fig. 2.2). In such a coordinate system, the kinematic variables can be expressed as

$$\begin{aligned}
\ell &= (E_\ell, 0, 0, |\vec{\ell}|), \\
p &= (M, 0, 0, 0), \\
\ell' &= (E_{\ell'}, |\vec{\ell'}|\sin\theta, 0, |\vec{\ell'}|\cos\theta), \\
p' &= \ell + p - \ell',
\end{aligned} \tag{2.1}$$

where M is the mass of the proton, θ is the scattering (polar) angle of the scattered electron. The 4-momentum of the virtual photon is denoted as $q = (\nu, \vec{q})$, and the

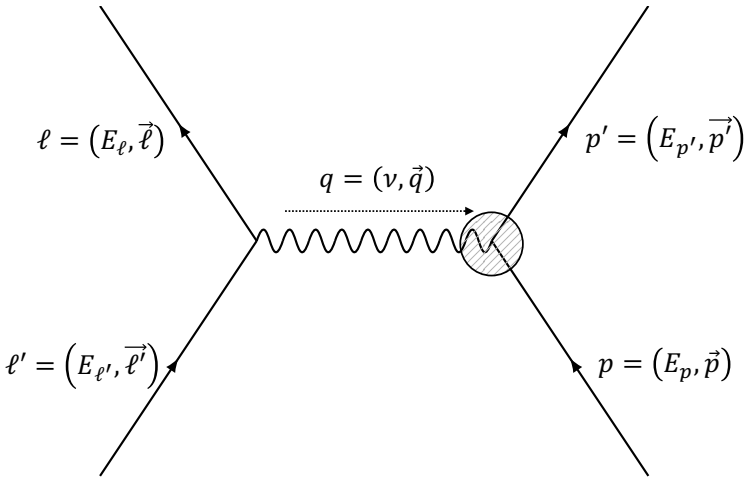

Figure 2.1: The Born level (one photon exchange) Feynman diagram for the $e - p$ elastic scattering.

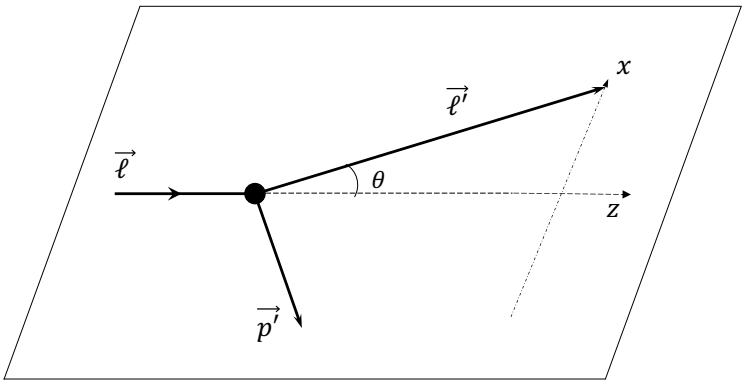

Figure 2.2: Diagram for the $e - p$ elastic scattering. The two lepton momentum vectors define the lepton scattering plane.

minus of this quantity squared defines the 4-momentum transfer squared Q^2,

$$\begin{aligned} Q^2 = -q^2 = -(\ell - \ell')^2 = 2(E_\ell E_{\ell'} - \vec{\ell}\cdot\vec{\ell}') - 2m^2 \\ \approx 4E_\ell E_{\ell'} \sin^2\frac{\theta}{2} = 2\mathrm{E}_\ell \mathrm{E}_{\ell'}(1-\cos\theta), \end{aligned} \tag{2.2}$$

where the approximation is true if the electron mass (m) squared is negligible. In the case of elastic scattering, the Q^2 can also be expressed as

$$Q^2 = 2M\nu = 2M(E_\ell - E_{\ell'}), \tag{2.3}$$

in the lab frame.

For the $e-p$ elastic scattering, the differential cross section in the lab frame can be expressed as

$$d\sigma = \frac{1}{F}\frac{\overline{|\mathcal{M}|^2}}{4\pi^2}\frac{d^3\vec{\ell}'}{2E_{\ell'}}\frac{d^3\vec{p'}}{2E_{p'}}\delta^{(4)}(\ell + p - \ell' - p'), \tag{2.4}$$

where $F = 4\sqrt{(\ell\cdot p)^2 - m^2M^2} \approx 4E_\ell M$ is the incident flux factor (the approximation is true if the electron mass squared is neglected). $\mathcal{M}$ is the invariant amplitude that contains the physics about the electron-proton interaction. It can be expressed as

$$\mathcal{M} = j_\mu \frac{1}{q^2} J^\mu, \tag{2.5}$$

where j^μ (J^μ) is the 4-vector transition current density for the electron (proton), and the Einstein summation convention is applied. The electron transition current density can be completely described by Quantum Electrodynamics as

$$j^\mu = -e\,\overline{u}(\ell')\,\gamma^\mu\,u(\ell)\,e^{i(\ell'-\ell)\cdot x}, \tag{2.6}$$

where e is the charge of the electron. γ^μ consists of four 4×4 Dirac γ-matrices. They

satisfy the anti-commutation relation:

$$\{\gamma^\mu, \gamma^\nu\} = \gamma^\mu\gamma^\nu + \gamma^\nu\gamma^\mu = 2g^{\mu\nu}, \tag{2.7}$$

where $g^{\mu\nu}$ is the metric tensor with $g^{00} = 1$, $g^{11} = g^{22} = g^{33} = -1$, and all the other components are 0. In the Dirac-Pauli representation, these matrices can be expressed as

$$\gamma^0 = \begin{pmatrix} I & 0 \\ 0 & -I \end{pmatrix}, \vec{\gamma} = \begin{pmatrix} 0 & \vec{\sigma} \\ -\vec{\sigma} & 0 \end{pmatrix}, \tag{2.8}$$

where $\vec{\sigma}$ are the Pauli matrices:

$$\sigma_1 = \begin{pmatrix} 0 & 1 \\ 1 & 0 \end{pmatrix}, \sigma_2 = \begin{pmatrix} 0 & -i \\ i & 0 \end{pmatrix}, \sigma_3 = \begin{pmatrix} 1 & 0 \\ 0 & -1 \end{pmatrix}, \tag{2.9}$$

$u(\ell)\, e^{-i\ell\cdot x}$ is the positive-energy solution to the Dirac equation $(i\gamma^\mu\partial_\mu - m)\psi = 0$ for a free particle; $\overline{u}(\ell) \equiv u(\ell)^\dagger\gamma^0$ by definition, and $u(\ell)$ is a 4-component Dirac spinor:

$$u^{(s)} = \sqrt{E+m} \begin{pmatrix} \chi^{(s)} \\ \frac{\vec{\sigma}\cdot\vec{p}}{E+m}\chi^{(s)} \end{pmatrix}, \chi^{(1)} = \begin{pmatrix} 1 \\ 0 \end{pmatrix}, \chi^{(2)} = \begin{pmatrix} 0 \\ 1 \end{pmatrix}. \tag{2.10}$$

On the other hand, if the proton is also a structureless particle, its transition current density can be constructed exactly as in Eq. 2.6, with a positive sign standing for the positive charge of the proton. However, as we know, the proton is an extended object, and the most general form of its transition current density, under

the requirement of Lorentz invariance and parity conservation, can be written as

$$J^{\mu} = e\,\overline{u}(p')\left[F_1(q^2)\gamma^{\mu} + \frac{\kappa}{2M}F_2(q^2)i\sigma^{\mu\nu}q_{\nu}\right]u(p)\,e^{i(p'-p)\cdot x}, \tag{2.11}$$

where $F_1(q^2)$ and $F_2(q^2)$ are the Dirac and Pauli form factors, respectively. They are related to the internal structure of the proton. κ is the proton anomalous magnetic moment and $\sigma^{\mu\nu}$ is the antisymmetric tensor:

$$\sigma^{\mu\nu} = \frac{i}{2}\left[\gamma^{\mu},\gamma^{\nu}\right] = \frac{i}{2}\left(\gamma^{\mu}\gamma^{\nu} - \gamma^{\nu}\gamma^{\mu}\right). \tag{2.12}$$

Combining with Eq. 2.4 and Eq. 2.5, one can derive the differential cross section for the $e-p$ elastic scattering in the lab frame:

$$\begin{aligned}\frac{d\sigma}{d\Omega} = &\left(\frac{d\sigma}{d\Omega}\right)_{\text{Mott}} \times \\ &\left[((F_1(q^2))^2 - \frac{\kappa^2 q^2}{4M^2}(F_2(q^2))^2) - \frac{q^2}{2M^2}(F_1(q^2) + \kappa F_2(q^2))^2 \tan^2\frac{\theta}{2}\right],\end{aligned} \tag{2.13}$$

where $(d\sigma/d\Omega)_{\text{Mott}}$ is the Mott cross section that describes the scattering off the structure-less and spin-less proton:

$$\left(\frac{d\sigma}{d\Omega}\right)_{\text{Mott}} = \frac{\alpha^2\cos^2\frac{\theta}{2}}{4E_{\ell}^2\sin^4\frac{\theta}{2}}\frac{E_{\ell'}}{E_{\ell}}. \tag{2.14}$$

It is common to use the Sachs form factors [30], which are linear combinations of $F_1(q^2)$ and $F_2(q^2)$:

$$\begin{aligned}G_E^p(Q^2) &\equiv F_1(q^2) + \frac{\kappa q^2}{4M^2}F_2(q^2), \\ G_M^p(Q^2) &\equiv F_1(q^2) + \kappa F_2(q^2),\end{aligned} \tag{2.15}$$

such that no interference term of the form factors will appear in the cross section, and Eq. 2.13 can be re-written in a much simpler form:

$$\frac{d\sigma}{d\Omega} = \left(\frac{d\sigma}{d\Omega}\right)_{\text{Mott}} \frac{1}{1+\tau}\left[(G_E^p(Q^2))^2 + \frac{\tau}{\epsilon}(G_M^p(Q^2))^2\right], \tag{2.16}$$

with $\tau = Q^2/(4M^2)$ and $\epsilon = [1 + 2(1+\tau)\tan^2(\theta/2)]^{-1}$. Eq. 2.16 is often referred to as the Rosenbluth formula [30].

It is worth noticing that in the $Q^2 \to 0$ limit, the wavelength of the virtual photon becomes significantly larger than the size of the proton. Effectively it will "see" the proton as a point target with charge e and magnetic moment $(1+\kappa)e/2M$. This requires that $F_1(0) = 1$ and $F_2(0) = 1$, and the Sachs form factors become

$$\begin{aligned} G_E^p(0) &= 1, \\ G_M^p(0) &= 1 + \kappa = \mu_p. \end{aligned} \tag{2.17}$$

In the case that the electron mass is not neglected, as shown in Ref. [31], the Rosenbluth formula is still applicable, provided that one uses the following two expressions for ϵ and the Mott cross section:

$$\epsilon = \left[1 - 2(1+\tau)\frac{2m^2 - Q^2}{4E_\ell E_{\ell'} - Q^2}\right]^{-1}, \tag{2.18}$$

$$\left(\frac{d\sigma}{d\Omega}\right)_{\text{Mott}} = \frac{\alpha^2}{4E_\ell^2}\frac{1 - Q^2/(4E_\ell E_{\ell'})}{Q^4/(4E_\ell E_{\ell'})}\frac{E_\ell|\vec{\ell'}|}{E_{\ell'}|\vec{\ell}|}\frac{M(E_{\ell'}^2 - m^2)}{ME_\ell E_{\ell'} + m^2(E_{\ell'} - E_\ell - M)}. \tag{2.19}$$

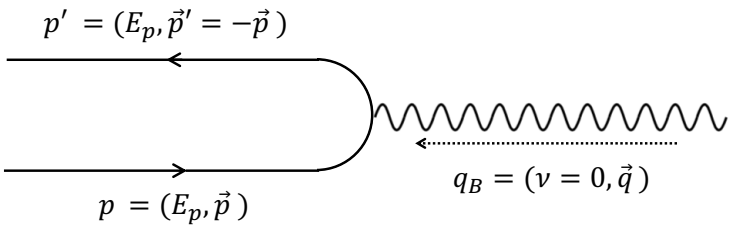

Figure 2.3: The $e - p$ elastic scattering in the Breit frame.

2.2 Proton Form Factors

In the classical literature [29], the proton electric and magnetic form factors are interpreted as the Fourier transforms of the proton charge and magnetic moment distributions in the non-relativistic limit:

$$G^p_{E,M}(Q^2) = \int \rho^p_{E,M}(\vec{x})\, e^{i\vec{q}\cdot\vec{x}} d^3x. \tag{2.20}$$

This can be achieved in the Breit frame (or the brick wall frame), as shown in Fig. 2.3. In this frame, the proton bounces back as if it is hitting a brick wall, after absorbing the virtual photon. The proton has the same energy and momentum magnitude after the scattering but the direction is flipped. With the z-axis pointing in the direction of the incident proton, it is straightforward to write down the following formulae for the kinematic variables in this frame:

$$\begin{aligned} &E_p = E_{p'}, \\ &\nu = 0, \\ &\vec{p} = -\vec{p'} = \frac{1}{2}\vec{q}, \\ &Q^2 = |\vec{q}|^2. \end{aligned} \tag{2.21}$$

Assuming the density distributions are spherically symmetric and if one takes the Taylor expansion at the $Q^2 \to 0$ limit, then:

$$\begin{aligned} G^p_{E,M}(Q^2) &= \int \left(1 + i\vec{q}\cdot\vec{x} - \frac{(\vec{q}\cdot\vec{x})^2}{2} + \dots\right) \rho^p_{E,M}(\vec{x}) d^3x \\ &= 1 - \frac{1}{6}\langle {r^p_{E,M}}^2 \rangle Q^2 + \dots \end{aligned} \tag{2.22}$$

The mean square charge and magnetic radii can then be identified as[1]:

$$\langle {r^p_E}^2 \rangle \equiv -6 \frac{dG^p_E(Q^2)}{dQ^2}\bigg|_{Q^2=0}, \tag{2.23}$$

$$\langle {r^p_M}^2 \rangle \equiv -\frac{6}{\mu_p} \frac{dG^p_M(Q^2)}{dQ^2}\bigg|_{Q^2=0}. \tag{2.24}$$

These two quantities are in general close to each other, but do not have to be the same. The charge radius is related to the charge density distribution, while the magnetic radius is related to the current density distribution. It would be interesting to see what lattice QCD calculations [32] will predict for the relationship between the two in the future.

This Fourier transform interpretation of the form factors (Eq. 2.22) was first proved by Sachs in 1962 [33]. Note that after using the Gordon decomposition

$$\overline{u}(p')\gamma^\mu u(p) = \overline{u}(p') \left[\frac{(p+p')^\mu}{2M} + i\sigma^{\mu\nu}\frac{(p'-p)_\nu}{2M}\right] u(p), \tag{2.25}$$

to replace the tensor term in Eq. 2.11, it is easy to show that the proton 4-vector

[1] As the work of this dissertation focuses only on the proton charge radius, we will use $r_p \equiv r^p_E$ for simplicity.

transition current can be written as

$$J^{\mu} = e\,\overline{u}(p')\left[\gamma^{\mu}(F_1 + \kappa F_2) - \frac{(p+p')^{\mu}}{2M}\kappa F_2\right] u(p)\, e^{i(p'-p)\cdot x}. \tag{2.26}$$

Using Eq. 2.8 and Eq. 2.10, it is straightforward to show that in the Breit frame, the proton transition current becomes:

$$J_{\mu} = 2Me\chi'^{\dagger}\left(G_E^p(Q^2),\, i\frac{\vec{\sigma}\times\vec{q}}{2M}G_M^p(Q^2)\right)\chi, \tag{2.27}$$

where the time-like component $G_E^p(Q^2)$ is clearly related to the charge density of the proton while $G_M^p(Q^2)$ is related to the space-like components and thus related to the magnetization density of the proton. To obtain the Fourier transform interpretation as in Eq. 2.20, one can compute the moments of density distributions and take the non-relativistic ($Q^2 \to 0$) limit, as shown in Appendix II of [33].

In the modern physics context, it is more appropriate to define a two-dimensional charge density distribution in the transverse space [10]. In fact, a three-dimensional charge density distribution cannot be defined properly because the longitudinal component is clearly frame-dependent due to Lorentz contraction. A transverse charge density distribution can be defined in the infinite-momentum frame [10]:

$$\rho(b) \equiv \sum_q e_q \int dx\, q(x,\vec{b}) = \int \frac{d^2q}{(2\pi)^2} F_1(Q^2 = \vec{q}^{\,2}) e^{-i\vec{q}\cdot\vec{b}}, \tag{2.28}$$

where b is the transverse distance from the $z-$axis (along the longitudinal direction), F_1 is the Dirac form factor as appeared in Eq. 2.13, and the summation is performed over all quark flavors. In this case, the mean square charge radius can be determined as:

$$\langle b^2 \rangle = \int d^2b\, b^2\, \rho(b) = -4F_1'(0). \tag{2.29}$$

In other words, the quantity defined in Eq. 2.23 is not strictly related to the second moment of the three-dimensional proton charge density distribution. In Chapter 1, we mentioned that the proton charge radius can also be measured using hydrogen spectroscopy. Thus, it is important to examine whether these two different experimental methods are measuring the same quantity. This consistency is presented in Ref. [10], which shows that the quantity defined in Eq. 2.23 is indeed responsible for the shift in the transition frequency of atomic energy levels due to the proton finite size effect:

$$\begin{aligned}\Delta E &= -4\pi\alpha G'^{p}_{E}(0)|\psi_{n0}(0)|^2\delta_{l0} \\ &= 4\pi\alpha\frac{r_p^2}{6}|\psi_{n0}(0)|^2\delta_{l0}. \end{aligned} \tag{2.30}$$

where $|\psi_{n0}(0)|$ is the electron wave function at the origin in coordinate space and the term is non-vanishing only for a S-state ($l = 0$). However, it is worth noticing that in the spectroscopic case, the measurement is done at $Q^2 = 0$ while for the scattering experiments, the quantity is accessed through an extrapolation from low Q^2 form factor measurements down to $Q^2 = 0$.

2.3 Proton Form Factors from $e - p$ Scattering Experiments

The cross section for the $e - p$ elastic scattering is shown in Eq. 2.16, which contains the contributions from both the electric and magnetic form factors. In order to separate them, in principle, one would need to have at least two independent measurements at the same Q^2. Some techniques for the unpolarized $e - p$ elastic scattering will be introduced in Sub-section 2.3.1, including the most commonly applied Rosenbluth separation method [34], which requires multiple measurements of

the unpolarized cross section at the same Q^2. Another method is to use the polarized $e-p$ elastic scattering, which is sensitive directly to the form factor ratio G_E^p/G_M^p. In this case, the two form factors can be de-coupled by combining the ratio measurement with the unpolarized cross section measurement. The polarized $e-p$ elastic scattering will be discussed in Sub-section 2.3.2 and Sub-section 2.3.3.

2.3.1 Unpolarized Measurements

The most commonly applied technique to extract G_E^p and G_M^p from the unpolarized $e-p$ elastic scattering cross section is the Rosenbluth separation method [34]. First of all, one needs to re-write the cross section (Eq. 2.16) into a reduced form

$$\left(\frac{d\sigma}{d\Omega}\right)_{\text{reduced}} = (1+\tau)\frac{\epsilon}{\tau}\frac{\left(\frac{d\sigma}{d\Omega}\right)_{ep}}{\left(\frac{d\sigma}{d\Omega}\right)_{\text{Mott}}} = (G_M^p(Q^2))^2 + \frac{\epsilon}{\tau}(G_E^p(Q^2))^2, \tag{2.31}$$

where $(d\sigma/d\Omega)_{ep}$ is the Rosenbluth formula (Eq. 2.16). And then, one can obtain $(G_M^p)^2$ and $(G_E^p)^2/\tau$ from the intersection and slope of a linear fit to the reduced cross sections at the same Q^2 but with different values of ϵ. This can be achieved by using different beam energies and scattering angles. An example is presented in Fig. 2.4 where the data points are normalized by the standard dipole form factor:

$$G_D = \frac{1}{(1+\frac{Q^2}{0.71(\text{GeV/c})^2})^2}. \tag{2.32}$$

Alternatively, one can parameterize G_E^p and G_M^p with different functions, and then fit the unpolarized cross section directly to extract the two form factors. Such a technique was used in the Mainz 2010 analysis [5] and a global analysis work [35].

Lastly, in a very low Q^2 region and especially when the scattering angles θ are small, the cross section is completely dominated by the electric form factor. This

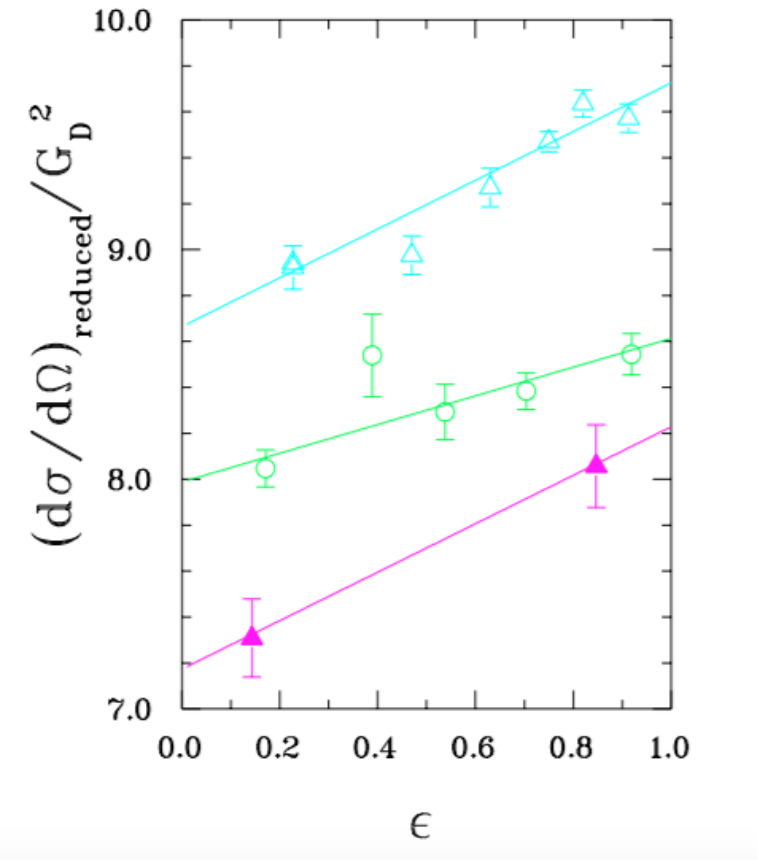

Figure 2.4: An example demonstrating the Rosenbluth separation technique. Data points are shown for the Q^2 values of 2.5 (open triangles), 5.0 (open circles) and 7.0 (filled triangles) $(\mathrm{GeV/c})^2$. The straight lines are linear fits to the corresponding data points. The figure is obtained from Ref. [34].

is due to the kinematic factor τ/ϵ in front of the magnetic form factor. One can extract G_E^p alone assuming G_M^p follows certain models or parameterizations, with an associated systematic uncertainty taken into account. This approach was adopted in the analysis of Simon [36], in which a simple scaling relation

$$G_E^p = \frac{G_M^p}{\mu_p} \tag{2.33}$$

was assumed. The Q^2 coverage of this experiment was from 0.005 to 0.055 $(\mathrm{GeV/c})^2$. For the PRad experiment, the maximum Q^2 is comparable to that of Ref. [36], but the value for the minimum Q^2 is one order of magnitude lower. At the same time, the scattering angular range (0.7° to 7.0°) is very small so that ϵ is nearly 1 (0.99243 to 0.99993), which is its maximum. One would expect a smaller systematic uncertainty for the PRad experiment, if a similar approach is applied.

Previous unpolarized $e-p$ elastic scattering experiments were typically done with the magnetic spectrometer method, in which the spectrometer needed to be shifted to different angles in order to cover the desired angular or Q^2 range. A classical example of this type of experiment is the Mainz 2010 measurement [5], which took place at the Mainz Microtron. In this experiment, over 1400 cross section data points were measured, covering Q^2 from 0.004 to 1 $(\mathrm{GeV/c})^2$, with statistical uncertainties better than 0.2% per point. The experiment used a liquid hydrogen target system, and three spectrometers, with one of the spectrometers in a fixed position in order to determine the relative luminosity. The extracted G_E^p and G_M^p parameterizations, obtained by fitting the cross section data points, are shown in Fig. 2.5, and compared to the results obtained from a number of previous experiments. The extracted proton charge radius from this experiment is $0.879(5)_{\mathrm{stat.}}(4)_{\mathrm{syst.}}(2)_{\mathrm{model.}}(4)_{\mathrm{group}}$ fm, and the proton magnetic radius is $0.777(13)_{\mathrm{stat.}}(9)_{\mathrm{syst.}}(5)_{\mathrm{model.}}(2)_{\mathrm{group}}$ fm.

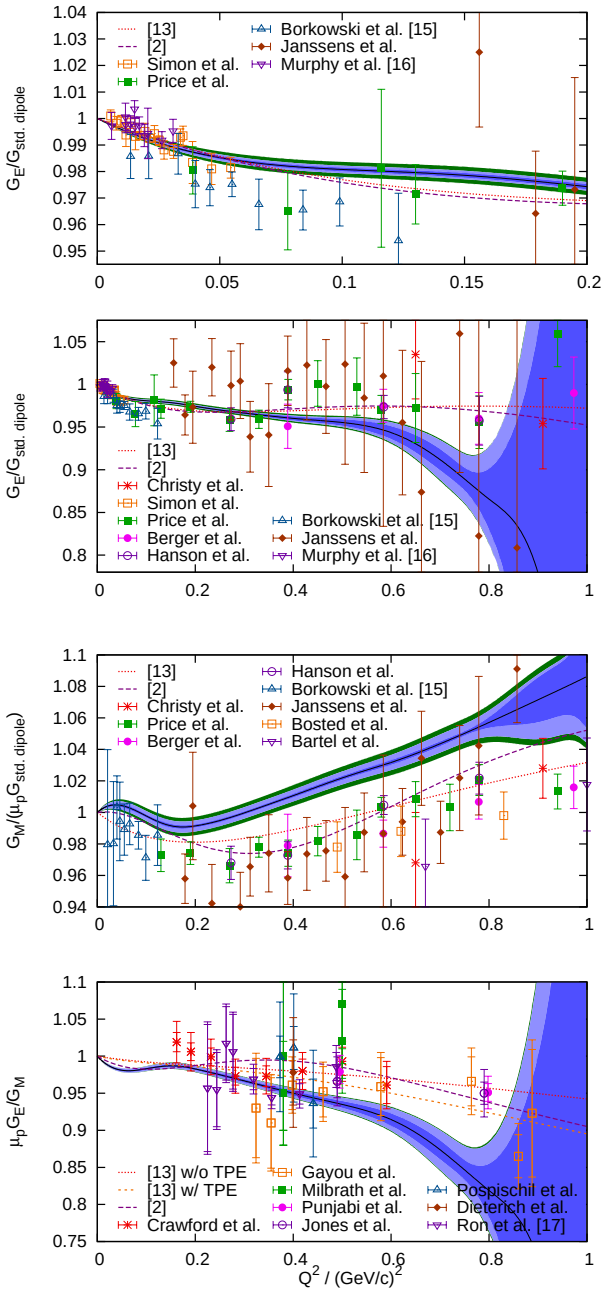

Figure 2.5: The extracted proton G_E^p and G_M^p parameterizations from the Mainz experiment [5]. The figures are obtained from Ref. [5].

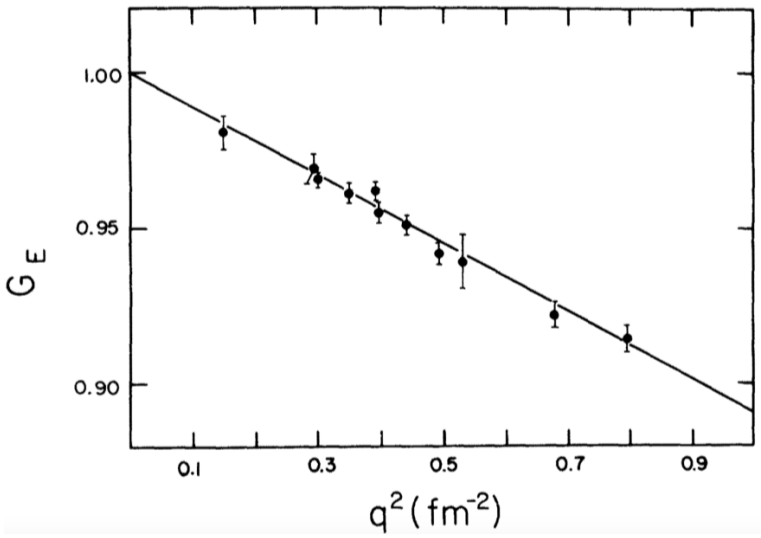

Figure 2.6: The proton electric form factor results from the Saskatoon experiment, obtained by measuring the recoil proton from the elastic $e - p$ scattering. The solid line is a least-squares fit to the data points. The figure is taken from Ref. [37].

Most of the unpolarized $e - p$ cross section measurements, including the Mainz 2010 and the PRad experiments, were done by detecting the scattered electrons. Equivalently, one can measure the cross section by detecting the recoil proton. In this case, one would integrate over the electron variables in Eq. 2.4 instead of the proton variables. One of the major advantages of this approach is that the radiative effects are significantly smaller for the protons than for the electrons. An experiment of this kind was performed in Saskatoon, Canada, and the results [37] were published in 1974. The proton electric form factor results, covering Q^2 from 5.8×10^{-3} to 3.1×10^{-2} $(\mathrm{GeV/c})^2$, are shown in Fig. 2.6. The scaling relation Eq. 2.33 was assumed in the extraction. The proton charge radius determined from this experiment is 0.81(3) fm.

2.3.2 Polarization Transfer Measurements

Most of -and especially early- proton from factor measurements, were obtained by measuring the unpolarized $e-p$ elastic scattering cross sections and by using the Rosenbluth separation method. This method works very well in the kinematic region where both electric and magnetic form factors contribute to the cross section significantly. However, due to the kinematic factor τ/ϵ appearing in front of G_M^p (see Eq. 2.16), the electric form factor will dominate the cross section if Q^2 and θ are small, while the magnetic form factor becomes dominant at high Q^2 and large scattering angles. Thus, the electric form factor data obtained in this way typically have large uncertainties in the high Q^2 region while the magnetic form factor uncertainties are larger in the low Q^2 region. In addition, the Rosenbluth method may be more sensitive to systematic uncertainties that are beam-energy-dependent. These difficulties may be overcome by using the polarized $e-p$ elastic scattering, which allows one to measure directly the form factor ratio G_E^p/G_M^p at a given Q^2 point, in addition to the cross section measurement. One of the techniques is the polarization transfer measurement. In this case, one uses a longitudinally polarized electron beam and an unpolarized proton target, and then measures the polarization transferred to the recoil proton. The form factor ratio can be expressed as [38]

$$\frac{G_E^p}{G_M^p} = -\frac{P_t}{P_l}\frac{E_\ell + E_{\ell'}}{2M}\tan\frac{\theta}{2}, \tag{2.34}$$

where P_t and P_l are the transverse and longitudinal components of the proton polarization in the lepton scattering plane (defined by the incident and scattered leptons). One of the very recent measurements using this technique is the Jefferson Lab E08-007 experiment [38], performed in the experimental Hall A. The experiment was performed using a 1.2 GeV polarized electron beam and a cryogenic hydrogen target.

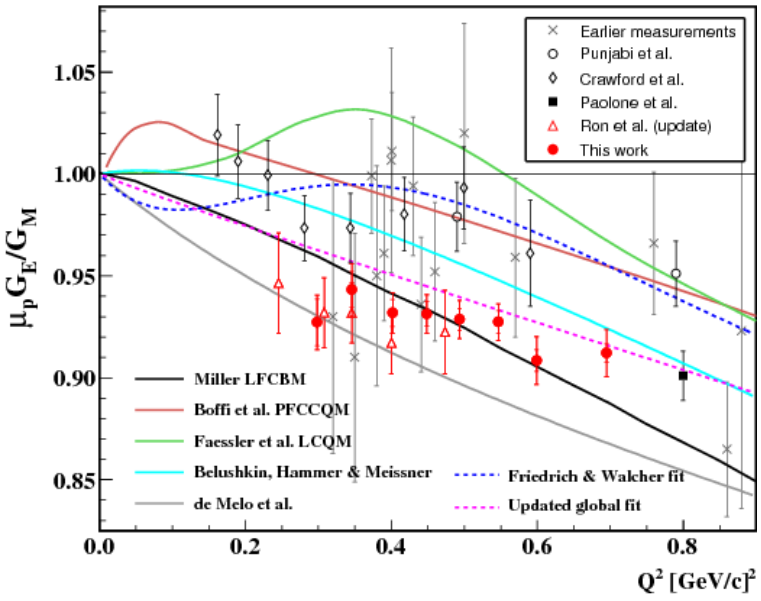

Figure 2.7: Proton form factor ratio measurements in the low Q^2 region, obtained using the polarized $e-p$ elastic scatterings. The figure is taken from Ref. [38].

The scattered electrons were measured by the BigBite spectrometer, and the recoil protons were measured by the High Resolution Spectrometer (HRS) where a focal plane polarimeter was installed to measure the polarization of the recoil protons. The form factor ratios extracted from this experiment, covering Q^2 from 0.3 to 0.7 (GeV/c)^2, are shown in Fig. 2.7.

These types of measurements have had a profound impact on our understanding of the nucleon form factors. The Q^2 dependency of G_E^p and G_M^p was expected to be the same in the high Q^2 region, which was also supported by the form factor data obtained using the Rosenbluth separation method, as shown in the top plot of Fig. 2.8. The polarization transfer measurements, on the other hand, suggest that G_E^p decreases faster than G_M^p in this region. This discrepancy triggered intensive theoretical and experimental efforts, and it has been found that the discrepancy could be largely explained by the Two-Photon Exchange (TPE) effect [39, 40], which was missing in

the earlier analyses using the Rosenbluth separation method. The TPE corrected form factor ratios from the Rosenbluth separation method are shown in the bottom plot of Fig. 2.8, and are compared to the polarization transfer measurements.

Individual form factors can be obtained by combining the ratio measurements with unpolarized cross section measurements. And the proton charge and magnetic radii can be constrained by the low Q^2 ratio measurements. A number of global analyses of this type are presented in Ref. [13, 35, 38].

2.3.3 Double Polarization Measurements

The proton form factor ratio G_E^p/G_M^p can also be extracted from a double polarization experiment, with a longitudinally polarized electron beam and a polarized proton target. In this case, the differential cross section for the $e-p$ elastic scattering can be expressed as [41]

$$\frac{d\sigma}{d\Omega} = \Sigma + h\Delta, \tag{2.35}$$

where Σ is the unpolarized differential cross section as shown in Eq. 2.16. h is the helicity of the incident electron (+1 for positive helicity and -1 for negative helicity), and Δ is the spin-dependent differential cross section:

$$\begin{aligned}\Delta = -\left(\frac{d\sigma}{d\Omega}\right)_{\text{Mott}} f_{\text{recoil}}^{-1}[&2\tau v_{T'}\cos\theta^*(G_M^p)^2 \\ &- 2\sqrt{2\tau(1+\tau)}\, v_{TL'}\sin\theta^*\cos\phi^* G_M^p G_E^p],\end{aligned} \tag{2.36}$$

where $f_{\text{recoil}} = 1+2\epsilon\sin^2(\theta/2)/\text{M}$, $v_{T'} = \sqrt{1/(1+\tau)+\tan(\theta/2)}\tan(\theta/2)$ and $v_{TL'} = -(1/\sqrt{2})/(1+\tau)\tan(\theta/2)$. The angles θ^* and ϕ^* are the polar and azimuthal angles of the proton polarization in the frame with the $x-z$ plane defined by the incoming and outgoing electrons, and with the z-axis along the direction of the virtual photon,

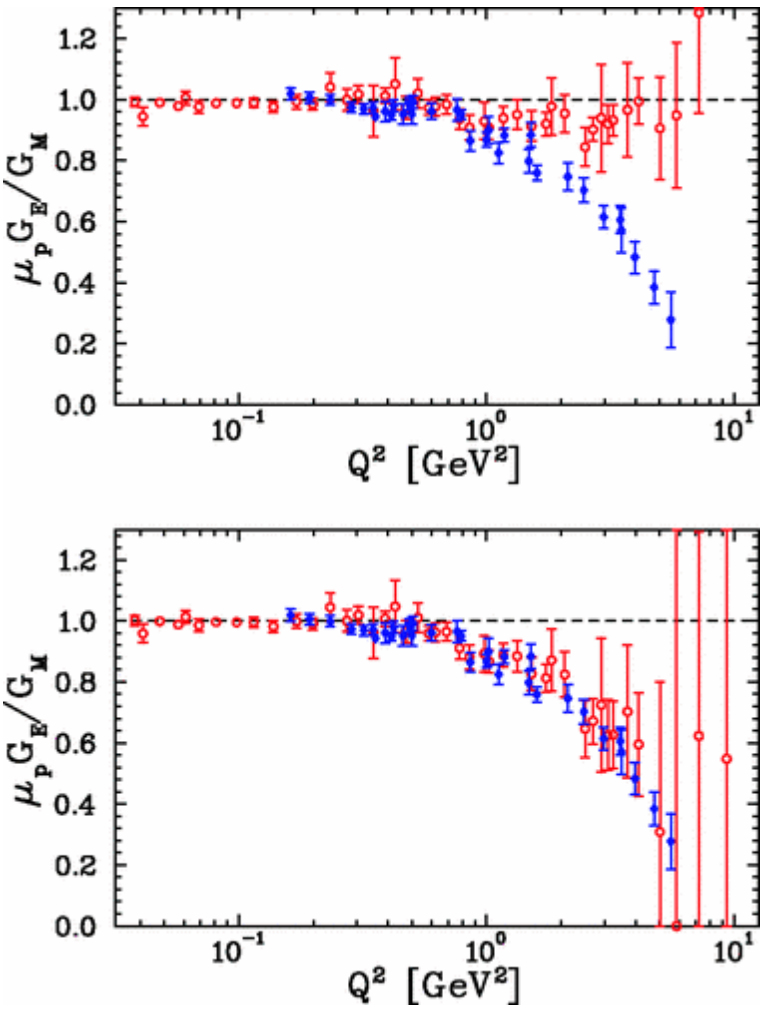

Figure 2.8: Proton form factor ratios obtained using the Rosenbluth separation method (red open circles), and polarization transfer measurements (blue solid diamonds). The Rosenbluth results are shown without (with) the TPE correction in the top (bottom) plot. The figure is taken from Ref. [35]

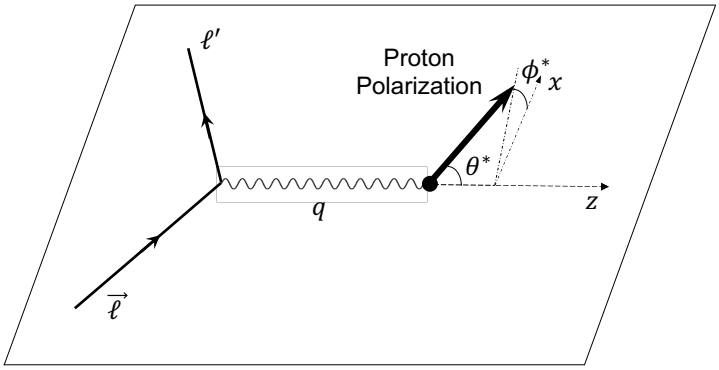

Figure 2.9: Born level diagram for the double polarization $e-p$ elastic scattering. The z-axis is along the direction of the virtual photon and the $x-z$ plane is defined by the incoming and outgoing electrons.

as shown in Fig. 2.9. One can then construct the spin-dependent asymmetry

$$\begin{aligned} A &= \frac{\sigma^+ - \sigma^-}{\sigma^+ + \sigma^-} = \frac{\Delta}{\Sigma} \\ &= -\frac{2\tau v_{T'} \cos\theta^* \, (G_M^p)^2 - 2\sqrt{2\tau(1+\tau)} v_{TL'} \sin\theta^* \cos\phi^* G_M^p G_E^p}{(\tau (G_M^p)^2 + \epsilon (G_E^p)^2)/[\epsilon(1+\tau)]}, \end{aligned} \tag{2.37}$$

and extract the form factor ratio G_E^p/G_M^p by measuring cross sections with positive (σ^+) and negative (σ^-) helicities.

In reality, the measured experimental spin-dependent asymmetry will be diluted by the polarization of the electron beam P_b and the polarization of the target P_t so that

$$A_{\text{exp}} = P_b P_t A. \tag{2.38}$$

One can measure two experimental spin-dependent asymmetries A_l and A_r, at the same Q^2 but with different proton spin orientations (θ_1^*, ϕ_1^*) and (θ_2^*, ϕ_2^*). This can be achieved conveniently by using a detector that has two symmetric components around the incident electron beam. It will allow one to measure simultaneously the

two asymmetries with the same target proton spin orientation in the lab frame. And then, one can extract the form factor ratio and the product of the two polarizations simultaneously. Or one can take the super ratio between the two experimental asymmetries in order to cancel out the polarizations [2], so that

$$R = \frac{A_l}{A_r} = \frac{2\tau v_{T'} \cos\theta_1^* \, (G_M^p)^2 - 2\sqrt{2\tau(1+\tau)} v_{TL'} \sin\theta_1^* \cos\phi_1^* G_M^p G_E^p}{2\tau v_{T'} \cos\theta_2^* \, (G_M^p)^2 - 2\sqrt{2\tau(1+\tau)} v_{TL'} \sin\theta_2^* \cos\phi_2^* G_M^p G_E^p}. \tag{2.39}$$

The proton electric and magnetic factors can be de-coupled by combining the form factor ratio measurements with unpolarized $e - p$ elastic scattering cross section measurements, similar to the polarization transfer experiments.

This double polarization technique was pioneered by the Bates Large Acceptance Spectrometer Toroid (BLAST) experiment at MIT-Bates [42], which measured the form factor ratio from 0.15 to 0.65 $(\mathrm{GeV}/c)^2$. The experiment utilized the BLAST detector [43] (Fig. 2.10), which was equipped with an eight-sector, toroidal, magnetic field. The two horizontal sectors had detector components installed, which were symmetric around the beam and simultaneously measured the two experimental spin-dependent asymmetries, A_l and A_r. The experiment also used a windowless target tube that could be fed with polarized protons produced from either an Atomic Beam Source or a Laser Driven Source. The extracted proton form factor ratios from this experiment are shown in Fig. 2.10. The individual form factor can be extracted by combining the ratio measurements with unpolarized $e-p$ cross section measurements. Fig 2.11 shows the improvement on G_E^p and G_M^p due to the BLAST form factor ratio measurements, when combining with world unpolarized $e - p$ cross section measurements [44, 45, 46, 47, 48, 49, 50, 51, 52]. This technique will be used in an experiment at the Mainz Energy-Recovering Superconducting Accelerator (MESA), which will measure the ratio down to $Q^2 = 0.005(\mathrm{GeV/c})^2$ [53].

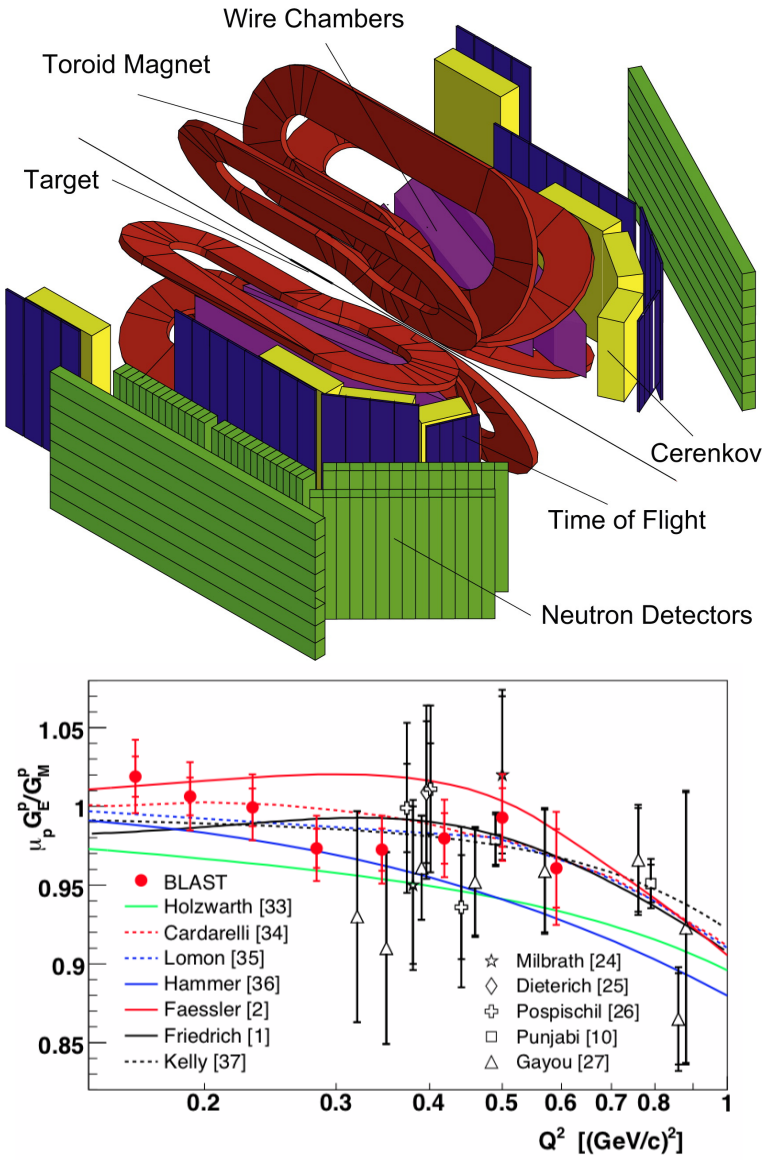

Figure 2.10: Top plot: Main detector components for the BLAST detector. The figure is taken from Ref. [43]. Bottom plot: Proton form factor ratio G_E^p/G_M^p extracted from the BLAST experiment at MIT. The figure is taken from Ref.[42].

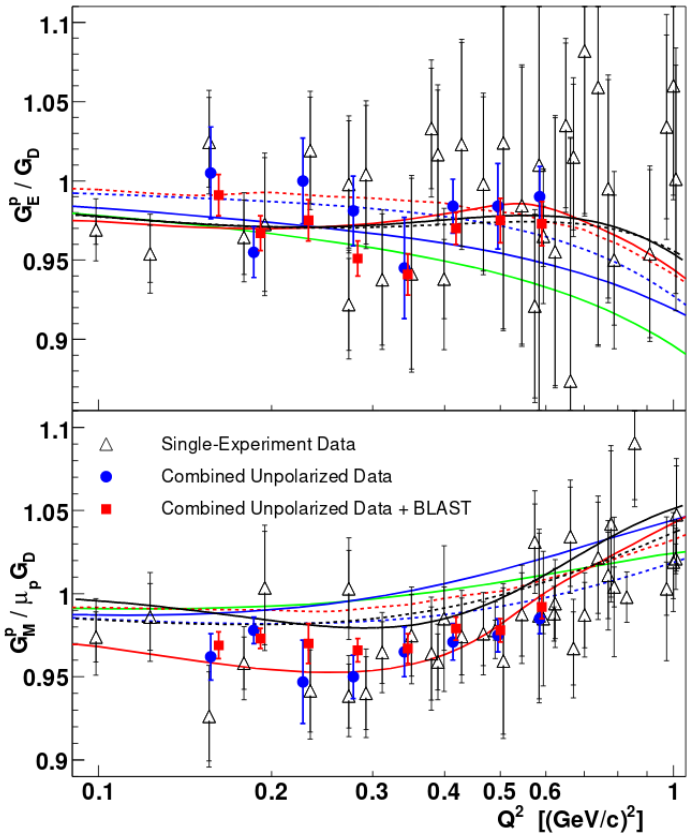

Figure 2.11: Compilation of the G_E^p/G_D (top plot) and $G_M^p/(\mu_p G_D)$ at BLAST kinematics with (red square) and without (blue dot) BLAST form factor ratio measurements. The figures are taken from Ref. [42].

2.4 Hydrogen Sepctroscopy

The proton charge radius can also be extracted from hydrogen spectroscopic experiments, in which the transition frequency between two different hydrogen energy levels is measured and the proton charge radius is extracted based on high precision bound-state QED calculations. In the non-relativistic limit and considering the proton to be infinitely heavy, the time-independent Schrödinger equation is

$$\left[-\frac{\vec{p}^{\,2}}{2m} + V\right]\psi(\vec{r}) = E\psi(\vec{r}), \tag{2.40}$$

where $V = -Z\alpha/r$ is the Coulomb potential of a point-like nucleus with charge Z ($Z = 1$ for a hydrogen atom), m is the mass of the electron and α is the fine structure constant. The energy levels can be obtained by solving the Schrödinger equation

$$E_n = -m\frac{(Z\alpha)^2}{2n^2} = -2\pi R_\infty \frac{Z^2}{n^2}, \tag{2.41}$$

where n is the principal quantum number, and $R_\infty = \alpha^2 m/(4\pi)$ is the Rydberg constant. This is the well-known Bohr energy levels. Although the wave functions obtained with this model depend also on the orbital angular momentum $l = 0, 1, \ldots, n-1$ and the projection of the orbital angular momentum $m_z = 0, \pm 1, \ldots, \pm l$, all energy levels with the same principal quantum number share the same energy. The finite nuclear mass correction can be easily achieved by replacing the electron mass with the reduced mass of the system: $m_r = mM/(m + M)$, where M is the mass of the nucleus.

Considering the relativistic energy dependency and the electron spin, a better description for the hydrogen energy levels can be obtained from the Dirac equation.

In the case of an infinitely heavy proton, the energy levels can be expressed as [3, 54],

$$E_{nj} = mf(n,j), \tag{2.42}$$

where $j = 1/2, 3/2, \ldots n - 1/2$, is the total angular momentum and

$$f(n,j) = \left[1 + \frac{(Z\alpha)^2}{\left(\sqrt{\left(j+\frac{1}{2}\right)^2 - (Z\alpha)^2} + n - j - \frac{1}{2}\right)^2}\right]^{-\frac{1}{2}}. \tag{2.43}$$

Notice that in this case, the degeneracy is lifted by the total angular momentum. However, the energy levels with the same n and j but different $l = j \pm 1/2$ remain degenerate, such as the $2S_{1/2}$ and $2P_{1/2}$ states. For the Dirac energy levels, the finite nuclear mass correction can not be achieved by simply replacing the electron mass with the reduced mass of the system. Instead, a leading relativistic correction with an exact mass dependency can be obtained, up to the $(Z\alpha)^4$ order, with an effective Hamiltonian [3],

$$H = H_0 + V_{Br}, \tag{2.44}$$

where H_0 is the non-relativistic Hamiltonian

$$H_0 = \frac{\vec{p}^{\,2}}{2m} + \frac{\vec{p}^{\,2}}{2M} - \frac{Z\alpha}{r}, \tag{2.45}$$

and V_{Br} is the Breit potential

$$\begin{aligned} V_{Br} =& \frac{\pi Z\alpha}{2}\left(\frac{1}{m^2} + \frac{1}{M^2}\right)\delta^3(\vec{r}) - \frac{Z\alpha}{2mMr}\left(\vec{p}^{\,2} + \frac{\vec{r}(\vec{r}\cdot\vec{p})\cdot\vec{p}}{r^2}\right) \\ &+ \frac{Z\alpha}{r^3}\left(\frac{1}{4m^2} + \frac{1}{2mM}\right)[\,\vec{r}\times\vec{p}\,]\cdot\vec{\sigma}. \end{aligned} \tag{2.46}$$

The result for the energy level is presented in Ref. [3, 55]:

$$\begin{aligned} E_{njl} =& (m+M) + m_r[f(n,j)-1] - \frac{m_r^2}{2(m+M)}[f(n,j)-1]^2 \\ &+ \frac{(Z\alpha)^4 m_r^3}{2n^3M^2}\left(\frac{1}{j+\frac{1}{2}} - \frac{1}{l+\frac{1}{2}}\right)(1-\delta_{l0}), \end{aligned} \tag{2.47}$$

where the first two terms are the rest masses, the third term takes into account the reduced mass effect of the system, and the last two terms are recoil corrections. Notice that the degeneracy in the Dirac energy levels, with the same n and j but different $l = j \pm 1/2$, is lifted by the last term in the expression.

The transition frequency between $2S_{1/2}$ and $2P_{1/2}$ states of a hydrogen atom was measured by Willis Lamb and Robert Retherford in 1947 [56]. The $2S_{1/2}$ state was found to be higher than the $2P_{1/2}$ state by 1 GHz. This difference is certainly not predicted by the Dirac energy level (Eq. 2.42) and it is still too large for the l-dependent term in Eq. 2.47, which contributes about 2 kHz to the transition frequency. This discrepancy was first explained by Bethe in the same year [57]. The main contribution to this shift is the electron self-energy radiative correction, by emitting and then absorbing a virtual photon. This effect will smear out the position of the electron over a certain range and its charge distribution is spread out instead of being a point charge. This effect shifts the $2S_{1/2}$ energy level more than the $2P_{1/2}$ as the electron is much closer to the proton in the former case. Generally speaking, the Lamb shift includes all the contributions to the energy level, beyond the first three terms in Eq. 2.47 and without considering the hyperfine splitting. There are four major items considered in the Lamb shift [54]. Listing with a decreasing order on the contribution, they include radiative corrections (such as the self-energy and vacuum polarization), recoil corrections (due to the finite nuclear mass), radiative-recoil corrections (mixed terms between radiative and recoil corrections) and the finite nuclear size correction.

For a hydrogen atom and in the non-relativistic case, the leading order contribution due to the proton finite size effect is given by Eq. 2.30. This proton finite size effect originates from the slope of the proton electric form factor at $Q^2 = 0$. For a muonic hydrogen atom, the proton size contributes to roughly 2% of the Lamb shift [1] between the $2S_{1/2}$ and $2P_{1/2}$ energy levels, while for an ordinary hydrogen atom, the contribution is only about 0.014% [54].

The basic strategy of a hydrogen spectroscopic measurement for the proton charge radius involves measuring the transition frequency between two different energy levels. The proton charge radius is extracted with all the other terms calculated within the framework of QED. Generally speaking, there will be two unknowns for a transition frequency. One is the proton charge radius, and the other one is the Rydberg constant R_∞. There are two types of spectroscopic measurements [9]. One is the small splitting measurement, which measures the transition frequency between two states that have the same principal quantum number n. In addition, the proton finite size effect is only significant if the S-state is involved, for example, the 2S-2P transition. In this case, the main contributions to the transition frequency are cancelled as the two states share the same principal quantum number, and the Rydberg constant is known precisely enough from external measurements. Recent experiments of this type include the two muonic hydrogen Lamb shift measurements ($2S_{1/2}^{F=1}$ - $2P_{3/2}^{F=2}$ and $2S_{1/2}^{F=0}$ - $2P_{3/2}^{F=1}$) [1, 6], and the 2019 ordinary hydrogen Lamb shift measurement [20] ($2S_{1/2}^{F=0}$ - $2P_{1/2}^{F=1}$). The other type of spectroscopic measurements is the large splitting measurement, which measures the transition frequency between two states with different principal quantum numbers. In this case, the contribution due to the proton finite size effect is much smaller relatively and the Rydberg constant is not known precisely enough. The solution is to measure two transition frequencies at the same time and then solve for both r_p and R_∞ with two equations. In fact, the high pre-

cision Rydberg constant is determined from these types of measurements, and thus it is highly correlated with the proton charge radius. Typically, the 1S-2S transition is measured as one of the equations, as the transition frequency can be determined very precisely. And again the other transition will have an S-state involved in order to include the proton finite size effect. The 2017 [18] and 2018 [19] hydrogen spectroscopy results were both obtained from experiments of this type. They measured the transition frequencies between the 2S-4P and 1S-3S states, respectively.

The most precise measurements of the proton charge radius were obtained with the muonic hydrogen Lamb shift measurements [1, 6], performed at the Paul Scherrer Institute. Since the muon is about 200 times heavier than the electron, they orbit about 200 times closer to the proton and are more sensitive to the proton finite size effect. First of all, these experiments had a low energy muon beam injected into the target hydrogen gas in order to form muonic hydrogen. 99% of the muonic hydrogen atoms would de-excit almost immediately to the ground state, with only 1% of them de-exciting to the meta-stable 2S state (life time about 1 μs), and these were the events of interest (see **A** in Fig. 2.12). A laser with tunable frequency was then used to drive the muons from the 2S state towards the 2P state. Once the muons reached the 2P state, they would de-excit immediately to the ground state, emitting a 1.9 keV K_α X-ray (see **B** in Fig. 2.12), which was measured in coincidence with the incident laser pulse and the electron from the muon decay ($\mu^- \rightarrow e^- \nu_\mu \overline{\nu}_e$). The measured frequency for $2S_{1/2}^{F=1}$ - $2P_{3/2}^{F=2}$ transition is shown in Fig 2.13 from the 2010 Lamb shift experiment [1].

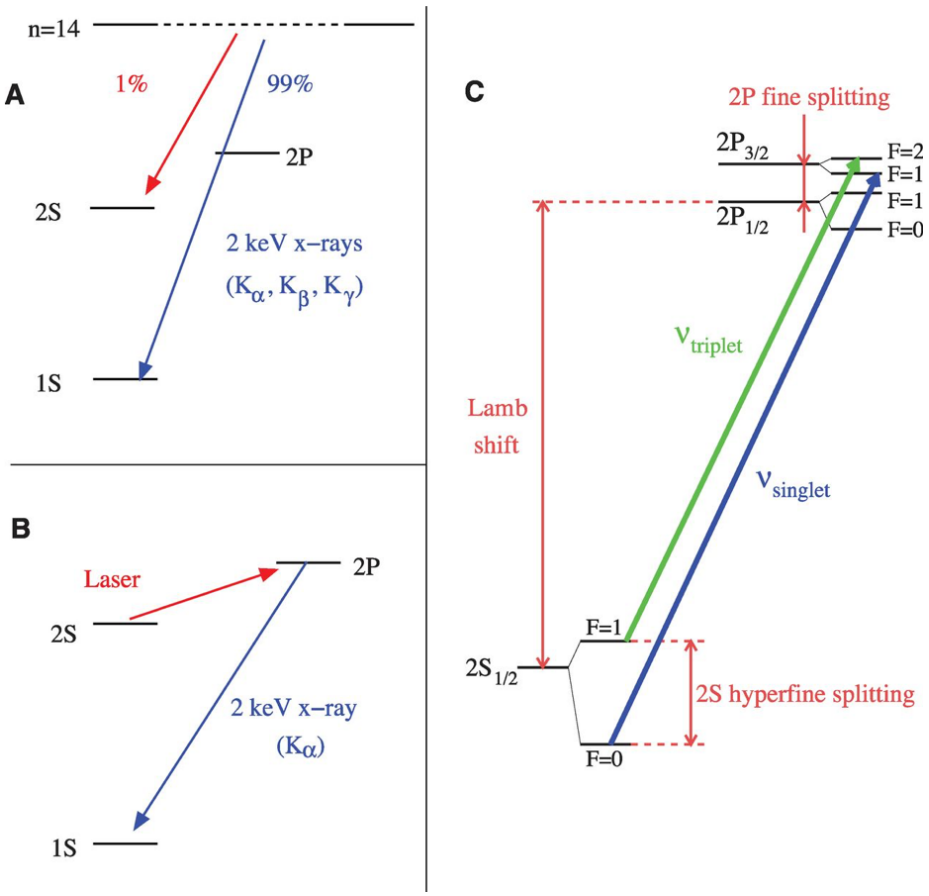

Figure 2.12: **A**: The muonic hydrogen de-excitation after being captured by a proton. **B**: Laser driven 2S-2P transition and the subsequent de-excitation of the muon into the ground state. **C**: 2S and 2P energy levels, with the green and blue arrows indicating the two transitions measured by the muonic Lamb shift experiments [1, 6]. This figure is taken from Ref. [6].

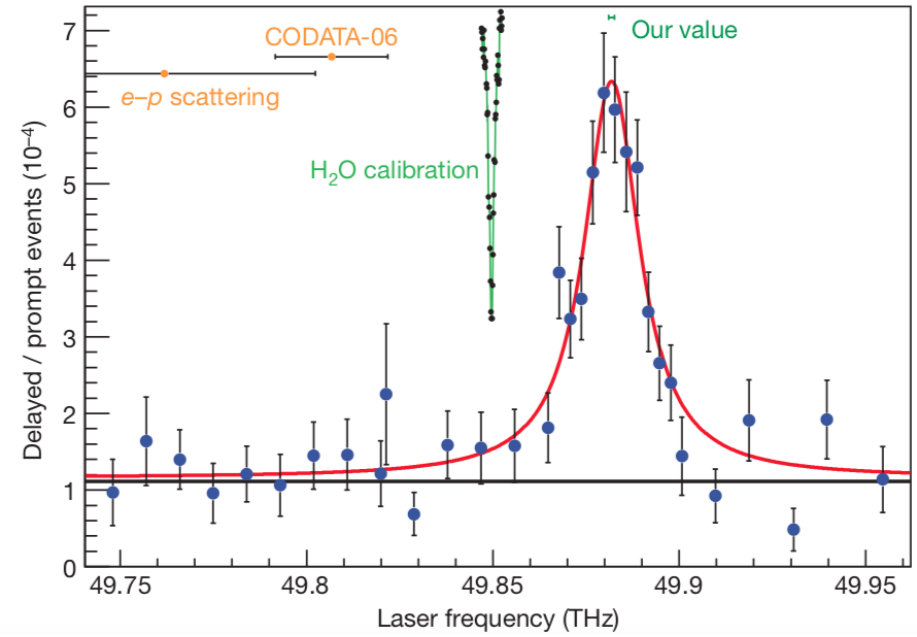

Figure 2.13: The measured frequency for $2S^{F=1}_{1/2}$ - $2P^{F=2}_{3/2}$ transition of a muonic hydrogen atom. The figure is taken from Ref. [1].

Chapter 3

The Experiment

3.1 Overview

The PRad experiment (E12-11-106) [28] was performed in 2016 in Hall B at Jefferson Lab, with both 1.1 and 2.2 GeV unpolarized electron beams on a windowless H_2 gas-flow target. The experiment measured the elastic $e-p$ scattering cross section and the proton electric form factor G_E^p in the Q^2 range $2.1 \times 10^{-4} - 0.06$ $(\mathrm{GeV/c})^2$. The luminosity was monitored by simultaneously measuring the Møller scattering process ($e-e$ scattering), which is a well known QED process. The absolute $e-p$ elastic scattering cross section was normalized to that of the Møller scattering in order to cancel out the luminosity. The PRad experimental apparatus is shown in Fig. 3.1. This experiment used a hybrid electromagnetic calorimeter (HyCal) to detect both the energies and scattering angles of the electrons from both elastic $e-p$ and $e-e$ scatterings. Their scattering angle measurements were further improved by two Gas Electron Multiplier (GEM) detectors that were placed side by side in front of the HyCal. These detectors provided a scattering angular coverage from 0.7° to 7.0° and a full azimuthal angular coverage. To have a better control over the systematic uncertainties, a 4 cm long, windowless, cryo-cooled H_2 gas-flow target was used in order to remove the majority of the backgrounds generated from the target cell windows. This target cell was placed inside a target chamber, which was equipped with multiple turbo pumps in order to maintain a low pressure along the beam-line. A 5 m long, two-stage vacuum chamber was connected to the target chamber in

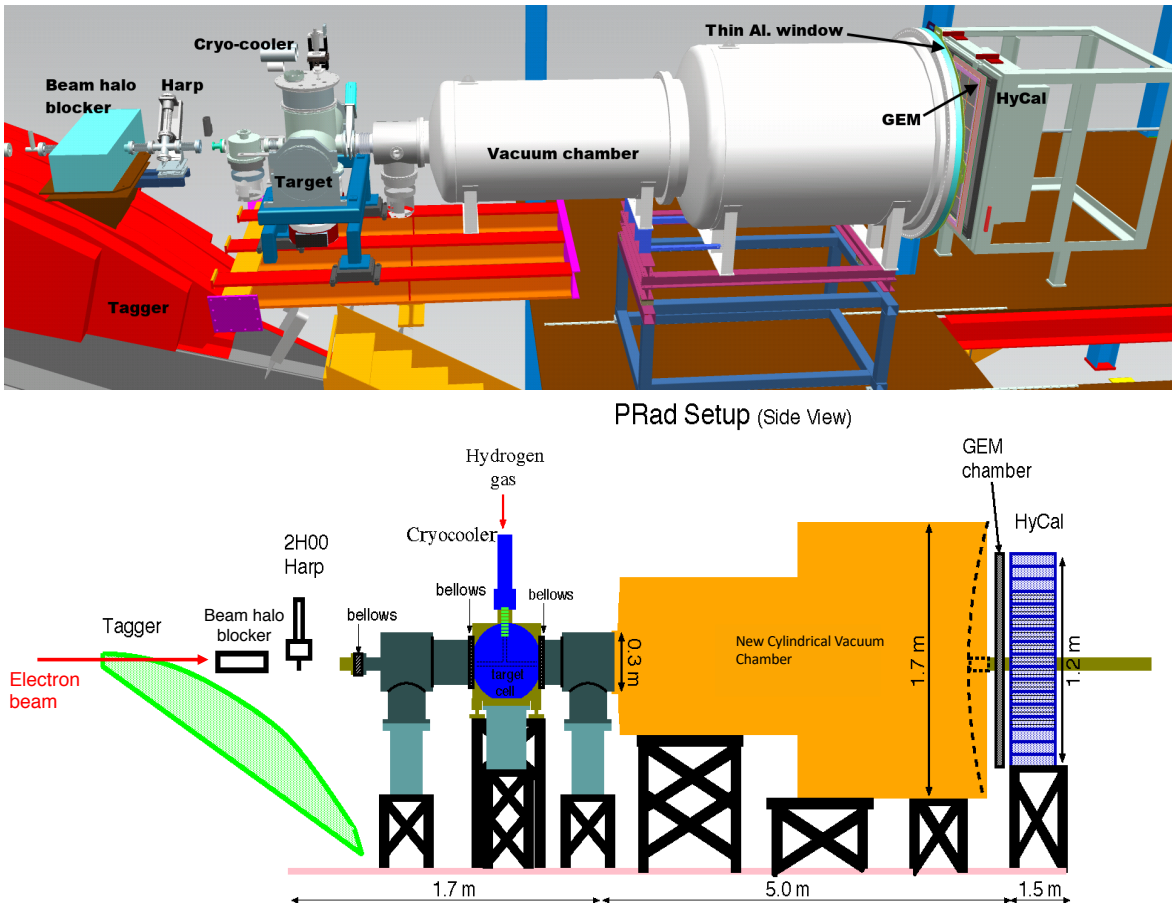

Figure 3.1: Top plot: 3D Schematic layout of the PRad experimental setup in Jeferson Lab, Hall B. Bottom plot: 2D side view of the PRad experimental setup with scales indicated.

order to protect the scattered electrons from other background sources. This vacuum chamber was closed at the downstream end by a 1.6 mm thick aluminum vacuum window. Before the production runs, the Hall B bremsstrahlung photon tagger was used to produce high intensity photon beam, in order to calibrate the HyCal. In this chapter, each important component of the experimental setup will be introduced.

Data set	Beam energy (MeV)	Uncertainty (MeV)
1.1 GeV	1101.0	0.5
2.2 GeV	2143.0	1.5

Table 3.1: Central values and uncertainties of the beam energies for the 1.1 and 2.2 GeV data sets.

3.2 The electron beam

The electron beam of the experiment was provided by the Continuous Electron Beam Accelerator Facility (CEBAF) at Jefferson Lab. There are in total 4 experimental halls in this facility and the PRad experiment was performed in Hall B. This experiment was one of the first experiments to run after the accelerator upgraded from 6 GeV to 12 GeV beam energy [58]. CEBAF is a recirculating linear accelerator, as shown in Fig. 3.2. It consists of two linear sections that are connected by two recirculating arcs. Each linear section contains multiple cyromodules that can provide in total about 1.1 GeV energy to the beam energy. The recirculating arcs contain separated beam lines that are equipped with different dipole and quadrupole magnets. They can recirculate the electron beam back to the linear section for a maximum of 5 times. This will provide a maximum 11 GeV electron beam to Hall A, B and C. The electron beam can be accelerated one more time in the north linear section, delivering a maximum 12 GeV electron beam to Hall D. The electron beam consists of small bunches that are separated by either 2 ns or 4 ns. The bunch length is typically less than 100 microns in distance [59].

Two different beam energies were used in this experiment. Table 3.1 shows the central values and the associated uncertainties from the offline analysis[1]. The energy

[1]The nominal beam energy for the second pass beam from the JLab linear accelerator should be around 2.2 GeV. The actual beam energy 2143 MeV determined later on was slightly less than the requested value of this experiment, but we will still use the 2.2 GeV as a label for the data set taken with the second pass beam, with the understanding that the actual beam energy was slightly lower.

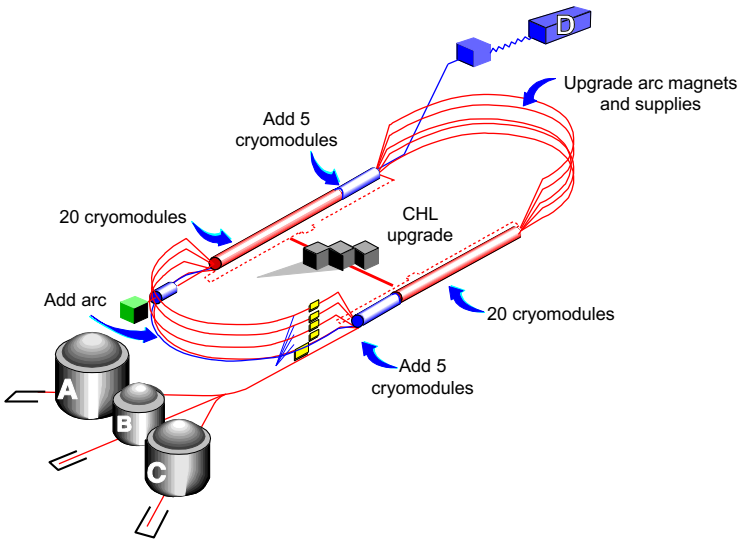

Figure 3.2: An overview of CEBAF at Jefferson Lab.

spread of the electron beam was at the level of 3×10^{-5}, which was significantly smaller than the uncertainty in the central value. The beam position and beam current were monitored continuously during the experiment by Hall B beam position monitors (BPM). In order to study the associated systematic uncertainties, various beam currents were used during the data taking. For the 1.1 GeV data set, the majority of runs were taken with 15 nA while others were taken with 10 nA. For the 2.2 GeV data set, the designated beam current was 55 nA, with several reference runs at 15 nA, 25 nA and 40 nA. The beam profile was also measured multiple times in a data taking period, by various harps in Hall B. An example of the harp scan is shown in Fig. 3.3. The typical profile could be reasonably well described by Gaussian distributions, with their widths at the level of 20 μm.

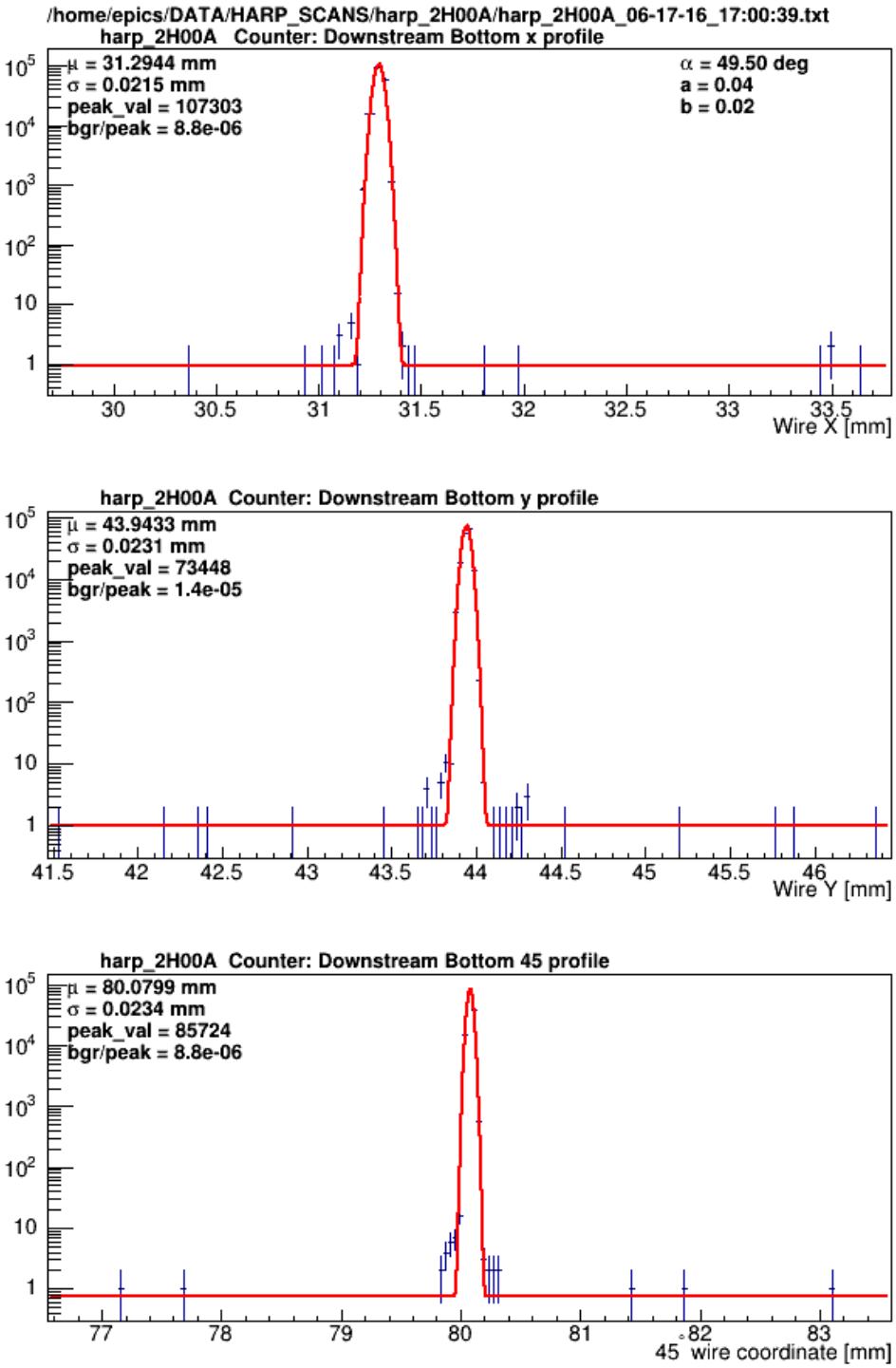

Figure 3.3: Example of the beam profile measured by harps during the PRad experiment.

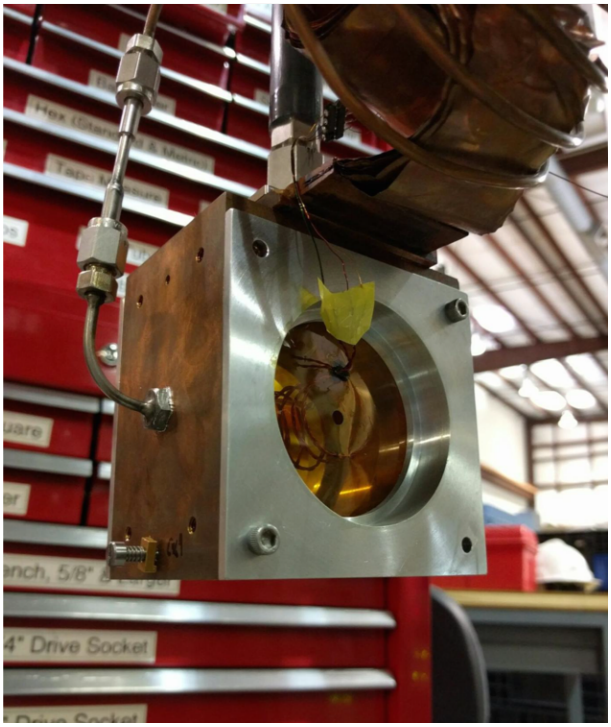

Figure 3.4: The target cell used in the PRad experiment. The cell is a cylinder with 4 cm length and 5 cm in diameter.

3.3 Target system

The target used in the experiment was a windowless H_2 gas-flow target, in order to remove backgrounds generated from the direct interaction between the electron beam and target cell windows. The total length of the target was 4 cm (Fig. 3.4). The body of the cell was made of high conductivity copper C101 and the windows were made of kapton foils with 7.5 μm thickness. Two small orifices with diameters of 4 mm were opened at both ends to allow the electron beam to pass through, effectively achieving the windowless target cell.

The target cell was suspended inside the PRad target chamber (Fig. 3.5) using a carbon fiber tube, and its position was tunable with a 5-axis motion controller. The electron beam delivered by CEBAF typically is very sharp and narrow (see

Fig. 3.3) but may be accompanied by a long tail that is much wider but lower in its intensity (beam halo). Thus, the lateral position of the target cell was fine-tuned at the beginning of each data taking period to align the target cell with the electron beam so that the main beam could pass the orifices, and to minimize the background generated from the beam halo hitting the kapton foils. For full target runs, the H_2 target gas was cooled to approximately 20 K with a Cryomech pulse tube refrigerator PT810, prior to be filled inside the cell at a rate of 600 sccm. This was the first time that a gas-flow target was used on an external beam-line at CEBAF. Due to the fact that the gas was flowing out of the cell from both orifices, and the importance to maintain a low background pressure inside the target chamber and the beam-line vacuum, we needed to pump away the gas flowing into the target chamber from the target cell. Thus, the target chamber was connected to three Pfeiffer 3200 turbo pumps and fore pumps to remove leaking H_2 gas from the orifices. The chamber was also connected to an upstream and a downstream chamber. Each of them was connected to a Pfeiffer 1500 turbo pump and a fore pump in order to maintain low pressure along the beam-line. With the understanding that the H_2 gas inside the target chamber could be a background source that contaminates the measurement, empty target runs were taken every few hours. The purpose was to subtract this background H_2 gas contribution, together with contributions from other beam-line objects like the beam halo blocker (see Fig. 3.1) and target cell windows. For these empty target runs, the H_2 gas was filled in at the same flow rate directly into the target chamber through a second inlet, in order to mimic the residual gas distribution far away from the target cell. All the other conditions remained the same as for the full target runs, for which the second inlet was valved off during the data taking. More related details will be presented in Section 4.5.1.

Various pressure gauges were used during the experiment to continuously measure

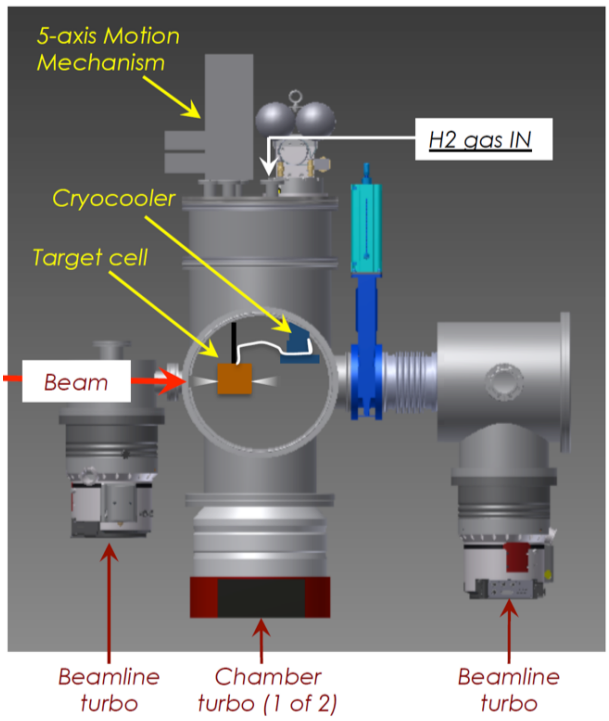

Figure 3.5: 3D view of the PRad target system.

the pressure at different locations of the target system. For full target runs when H_2 target gas was filled inside the cell, the cell pressure was measured to be about 480 mTorr, which achieved approximately an areal density of 2×10^{18} H atoms/cm^2. The pressure of the target chamber was measured to be about 2.5 mTorr while the pressure for the rest of the beamline was kept below 0.1 mTorr. For empty target runs, the measured target chamber pressure was about 2.9 mTorr.

A 5 m long, two-stage vacuum chamber was connected to the target downstream chamber in order to protect the scattered electrons from other background sources. This vacuum chamber was closed at the downstream end by a 1.6 mm thick aluminum vacuum window, immediately in front of the GEM detectors.

3.4 Gas Electron Multiplier

The GEM detector [60] is a novel gaseous tracking device that is able to measure the position of a charged particle, with a position resolution around 100 μm. The working principle of the detector is illustrated in Fig. 3.6. As an ionizing charged particle enters the chamber, its electric field strips primary ionized electrons from the gas (mixture of 70% argon and 30% CO_2 for PRad GEMs) in the drift layer. These primary ionized electrons are accelerated toward the triple-GEM foils a few mili-meters underneath. These GEM foils consist of a 50 μm kapton foil in the middle with both sides coated by thin copper layers with a few microns of thickness. High density of holes (140 μm in pitch and 70 μm in diameter) are pierced through these GEM foils in order to create a strong electric field inside these holes when a high voltage is applied to the two copper layers, as shown in Fig 3.7. Once the primary ionized electrons pass through these holes, they are able to strip even more electrons, resulting in a so-called avalanche process, which is able to amplify the initial signal. These avalanche electrons will eventually reach the readout strips that are attached to the readout plane near the bottom of the chamber, and lead to detectable signals by depositing their charges. The PRad GEMs utilized two sets of readout strips, with a 90° stereo-angle and a 400 μm pitch, corresponding to the $(X - Y)$ Cartesian coordinate.

PRad used two rectangular GEM detectors, which were the largest GEM detectors worldwide at the time they were assembled. The dimensions are about 55 cm in width and 123 cm in length (see Fig. 3.8). The group at University of Virginia designed and constructed them in 2015 and Duke graduate student Yang Zhang participated in the assembling and testing of these detectors. The two GEM detectors were placed side by side with a 4.4 cm $\times$ 123 cm overlapping area in front of the calorimeter, in

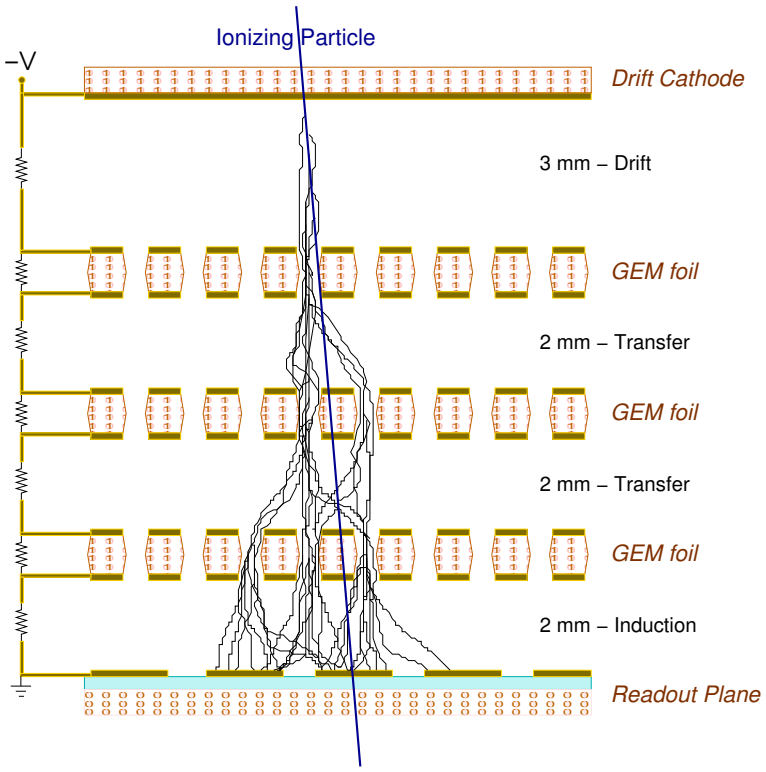

Figure 3.6: Working principle of GEM. The figure is taken from [61]

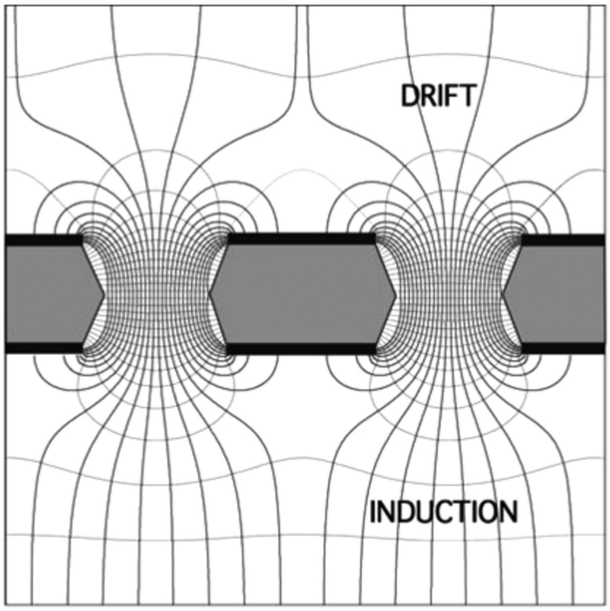

Figure 3.7: The electric field produced by a GEM foil. The figure is taken from [60]

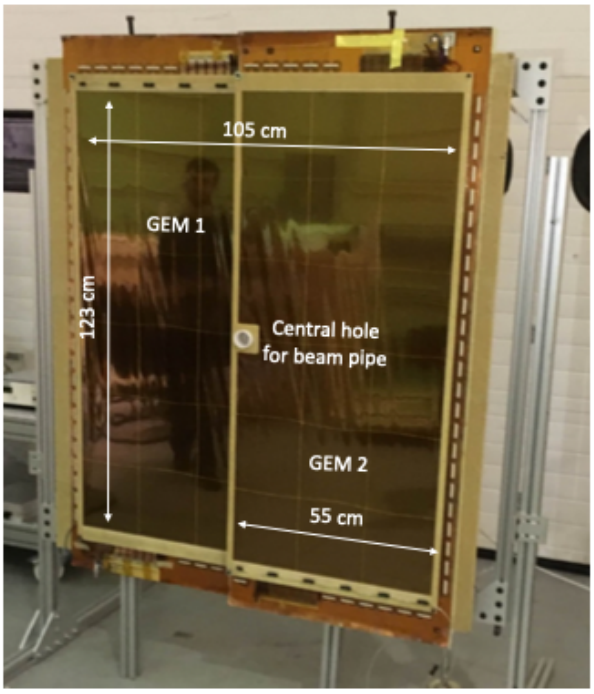

Figure 3.8: PRad GEM detectors in the Experimental Equipment Lab at JLab.

order to fully cover its detection region. Each GEM detector had a 4.4 cm $\times$ 4.4 cm hole located at the center of one of the edges to allow the beam pipe to go through.

To prevent GEM foils from direct contact with each other, multiple dielectric spacers were placed in between them. These spacers are about 3 mm in thickness and their locations are indicated in Fig. 3.9 as the black solid lines. They can cause about 3% loss of detection efficiency for PRad GEMs. Each GEM foil was sub-divided into 60 high voltage sectors, separated by 100 μm gaps. These gaps may also cause inefficiencies for the GEMs but the effect is significantly smaller compared to that from the spacers. This effect is shown in Fig. 3.10, where the hit positions of $e - p$ elastic scattering events on GEMs are shown along one of the readout strip directions. The large spikes (as indicated in the plot) are due to the GEM spacers, the much smaller spikes are due to the gaps between the high voltage sectors. The

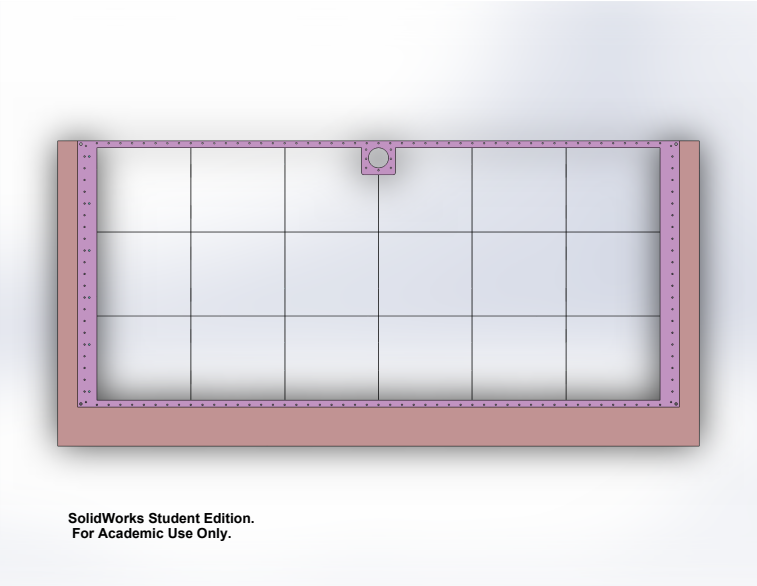

Figure 3.9: Design for the PRad GEM detector. Black solid lines indicate the location of the spacers. The plot is made by Xinzhan Bai of University of Virginia.

GEM efficiency losses due to these spacers and gaps between high voltage sectors were measured using the data and modeled in the simulation.

The position resolutions of these GEM detectors are typically at the level of 100 μm. For PRad GEMs, the resolution is about 72 μm, which is at least 20 times better than the position resolution of HyCal. A detected particle by the calorimeter will eventually have its reconstructed position replaced by that from the GEM detectors. Thus, they are able to significantly improve the scattering angle and Q^2 resolution of the PRad setup.

3.5 Hybrid Calorimeter

The calorimeter used in this experiment is a hybrid electromagnetic calorimeter [62], constructed by the PrimEx collaboration [63] and Jefferson Lab, and used during the PrimEx-I and PrimEx-II experiments [64, 65]. It consists of 1152 $PbWO_4$ modules

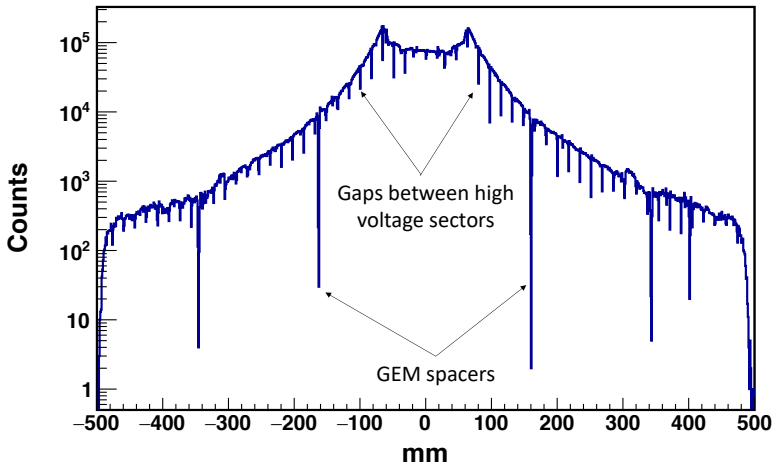

Figure 3.10: The hit positions of $e-p$ elastic scattering events on GEMs are shown along one of the strip directions. The plot is made by Xinzhan Bai of University of Virginia.

within the central region, arranged in an array of 34 by 34 modules, and surrounded by 4 sectors of 6 by 24 Pb-glass modules (576 Pb-glass modules in total), as shown in Fig. 3.11. The dimensions of a $PbWO_4$ (Pb-glass) module (Fig. 3.12) are 2.076 $\times$ 2.076 $\times$ 18 cm^3 (3.815 $\times$ 3.815 $\times$ 45 cm^3), providing a total radiation length X_0 of 20 (17). The lateral dimensions of a module includes the wrapping material as well. For each $PbWO_4$ module, it was wrapped in a 100 μm VM2000 reflective material to improve its light collection and then in a 36 μm Tedlar for the light isolation. The Pb-glass modules were wrapped by 25 μm aluminized mylar foils. The total lateral dimensions of HyCal are about 116 $\times$ 116 cm^2. The edges of the $PbWO_4$ detector region corresponded to a scattering angle of about 3.4°, and its corners corresponded to a scattering angle of about 4.8°. For the Pb-glass detector region, the edges and corners corresponded to scattering angles of about 5.7° and 7.9°, respectively[2]. A hole with the size of 2 by 2 $PbWO_4$ module was opened at the center of the

[2]For the analysis, a cut was applied to remove particles that were hitting the edges and corners in the Pb-glass region, so the actual angular coverage would be slightly smaller.

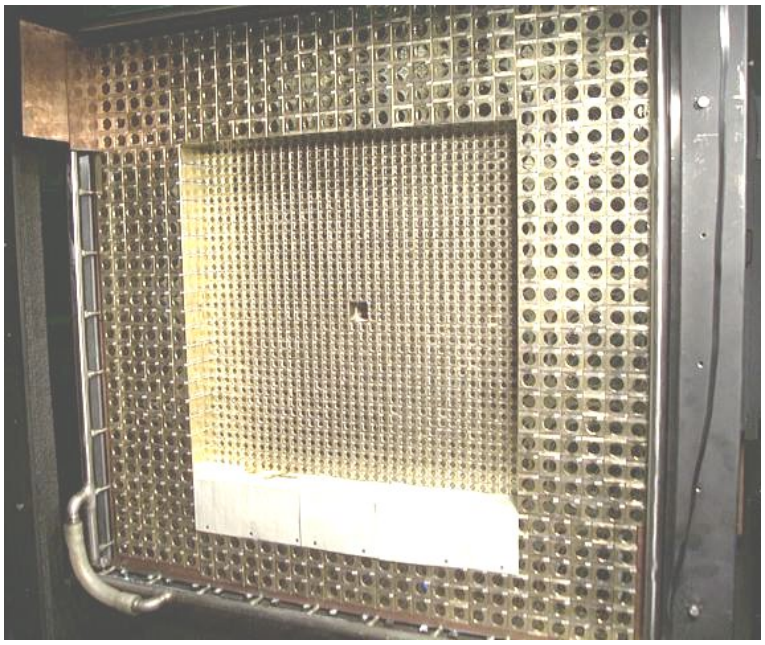

Figure 3.11: Front view of the HyCal electromagnetic calorimeter. The photo is taken from [63].

detector to allow the beam pipe to go through. A square shaped tungstate absorber was located immediately in front of the calorimeter to cover the inner-most layer of $PbWO_4$ modules (12 modules in total). This absorber would partially block events with scattering angles from 0.2° to 0.6°, in order to protect these $PbWO_4$ modules from the ultra-high event rates.

This detector is excellent in detecting and measuring the energy of electrons and photons. As these particles enter HyCal modules, they will initiate electromagnetic showers that are cascades of secondary particles including electrons, positrons and photons, with less and less energy as the showers develop. Even though both $PbWO_4$ and Pb-glass are electromagnetic calorimeters, their working principles are slightly different. $PbWO_4$ is a scintillating type of calorimeter, for which charged particles in the shower produce fluorescence light through the ionization process, while Pb-glass is a Cherenkov type of calorimeter, for which the light is produced by the

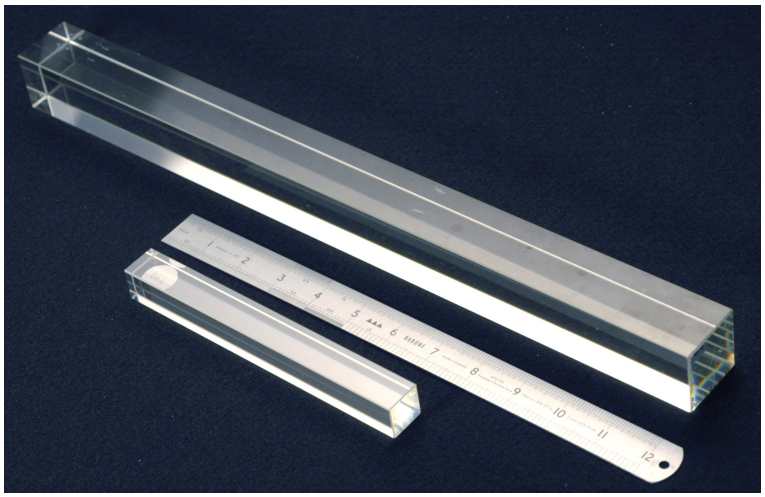

Figure 3.12: $PbWO_4$ (small) and Pb-glass (large) modules of HyCal calorimeter. The photo is taken from [63].

Cherenkov process of the charged particles in the shower [66]. In both cases, the produced photons are collected by a photon multiplier tube (PMT) attached to the back of each module, and the size of the signal is approximately proportional to the energy of the initial incident electron and photon. The proportionality constants (calibration constants) can be obtained, if one calibrates the detected signal from the PMTs to the energy of the incident particle, which needs to be determined by some additional sources. These constants may depend on various variables, such as the light attenuation property of the module, the high voltage applied to the PMT and so on.

Since calibration constants are usually determined at some specific times (calibration runs for instance) while their dependent variables may not be constant during the entire experiment, it is necessary to have a particular system to monitor the possible shifts for these constants. For this purpose, a light monitoring system (LMS) [67] was adopted, based on a pulsed nitrogen laser. The light produced was delivered to all HyCal modules by optical fibers that were attached to their front ends, as shown

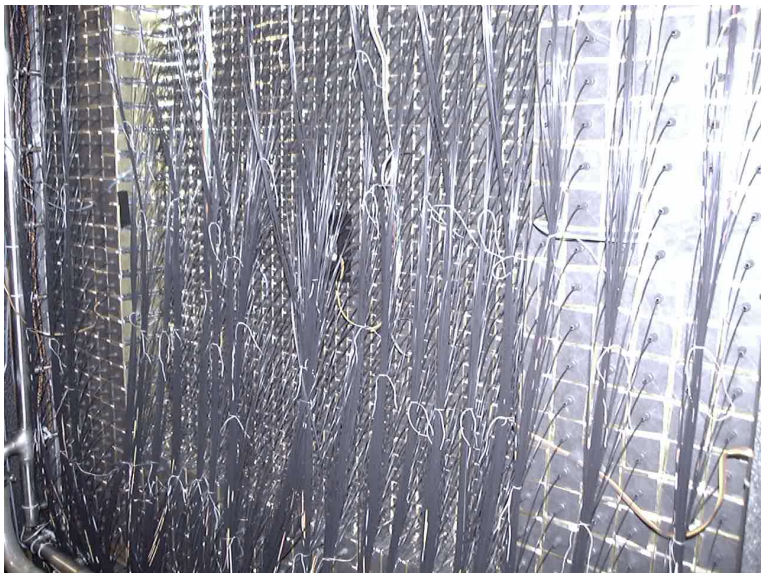

Figure 3.13: Front view of HyCal. Each module has a LMS optical fiber attached to its front end (1728 modules in total). The photo is taken from [63]

in Fig. 3.13. In addition, the light produced by the same source was delivered to three additional PMTs (reference PMTs), which also had ^{241}Am radioactive sources and scintillators attached. The main decay channel of ^{241}Am is α-decay, by emitting an α particle and a photon that are almost at constant energies. This setup allows one to calculate a gain correction factor, which can change as a function of time (t)

$$g(t) = \frac{A_i^{\rm LMS} \times A_{\rm ref}^{\alpha}}{A_{\rm ref}^{\rm LMS}}, \tag{3.1}$$

where $A_i^{\rm LMS}$ is the signal amplitude of the i-th HyCal module due to the LMS light source, $A_{\rm ref}^{\alpha}$ is the signal amplitude of a reference PMT due to the ^{241}Am radioactive source and $A_{\rm ref}^{\rm LMS}$ is the signal amplitude of the same reference PMT due to the LMS light source. To correct for a calibration constant, one can multiply it by the factor $g(t_f)/g(t_0)$, where $g(t_f)$ is the current gain correction factor and $g(t_0)$ is the gain correction factor when the calibration constant was obtained.

For the PRad experiment, HyCal served as the main detector for two major purposes. First, the measured energy of the scattered electron was used for the event selection, which means to select $e-p$ and $e-e$ elastic scattering events and to reject backgrounds. Second, the total energy deposition in HyCal was used for triggering the data acquisition system (DAQ) during the production runs (the full target runs and the empty target runs). Because the performance of Pb-glass modules was expected to be better at a slightly higher energy than that of this experiment, the total energy deposition in Pb-glass modules was solely utilized as an additional trigger with a lower threshold.

3.6 Hall B Photon Tagger

The bremsstrahlung photon tagger [68] in Hall B at Jefferson Lab was used to calibrate the HyCal (calibration runs) prior to the data taking of the production runs. First of all, the electron beam was incident onto a thin wire radiator, and a portion of the electrons would radiate photons through the bremsstrahlung process. As shown in Fig. 3.14, the electrons would be banded by a dipole magnet placed immediately downstream of the radiator while the radiated photon would move along the initial electron beam direction and eventually injected into the HyCal. After the bremsstrahlung radiation, the electrons with different energies will have different curvatures inside the magnetic field. Their energies and timing information are measured by 384 partially overlapping E-counters and 61 T-counters, respectively. The energy of the radiated photon can be determined from the difference between the electron beam energy and the energy determined by the E-counters,

$$E_\gamma = E_b - E_e. \tag{3.2}$$

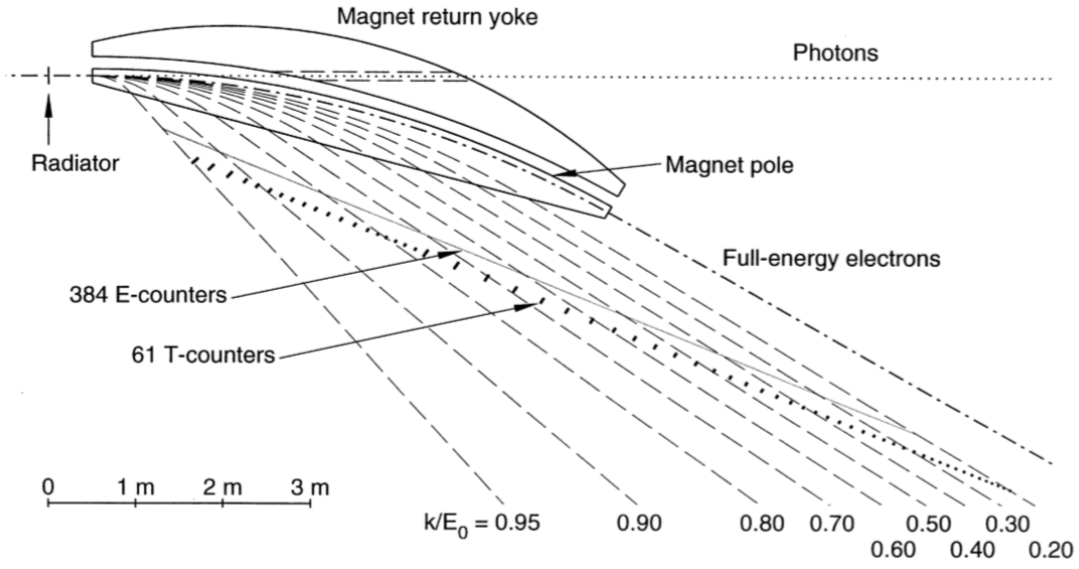

Figure 3.14: The bremsstrahlung photon tagger in Hall B at Jefferson Lab. The Figure is taken from Ref. [68]

This photon tagger is capable of measuring the energy of the radiated photon from 20% to 95% of the electron beam energy (E_b), up to $E_b = 6.1$ GeV, and with an energy resolution of $10^{-3}E_b$ [68]. The timing resolution of this tagger is about 110 ps [68].

3.7 Triggers and Data Acquisition

This experiment used the CEBAF Online Data Acquisition (CODA) system, which recorded the data from front-end electronics and wrote into binary data files (evio). The electronics for HyCal were mostly inherited from the PrimEx experiments [63, 64, 65]. The complete PRad DAQ system for production runs is illustrated by Fig. 3.15. The signals from the PMTs of HyCal modules were divided into anode and dynode signals. The anode signals from all 1728 HyCal modules were recorded using 30 ADC1881M modules contained in 3 FastBus crates. The integrated charge within a 280 ns time window from the PMT of each HyCal module was converted into digital

signals and written into the data stream. These 1728 modules were grouped into 52 Time-to-Digital Convertor (TDC) groups, with about 36 modules in each group. The dynode signals from all modules within a TDC group were first summed linearly by using 52 homemade modules (UVA120A) from University of Virginia. A copy of the produced signals would be sent to the JLab discriminators located in a VME crate. They were recorded by the CAEN v1990 TDC modules in the data stream as the timing information for the TDC groups. Signals from the other copy were summed using 5 NIM modules into a total sum signal, which was then converted into ECL signal (see Fig. 3.16) and sent to the Trigger Interface (TI) master located in the same VME crate. The TI master would then distribute the signal to the TI slaves, which were synchronized to the TI master. The TI slaves would then send signals to all the controlled crates for recording the triggered events. In addition to the triggers from the HyCal, the TI master also received triggers from a pulser of the LMS system of HyCal, and triggers from the ^{241}Am sources attached on the reference PMTs. These triggers were used to monitor the gain of the HyCal at the beginning of each run of the data taking.

The total sum signal was also used to trigger the readout system for the GEM detectors, which was a APV25 [69] based Scalable Readout System (SRS) [70]. 72 APVs, each with 128 channels, were used to record the data from in total 9216 channels from the two GEM detectors. These APV25s are analogue pipe-line readout chips, which measure the signal amplitudes from the GEM readout strips every 25 ns and store the information in a 192-cell analogue pipeline. They were connected, through HDMI connectors, to ADC boards, which were then connected to the Front-End Concentrator cards (FEC) located in the SRS crate. These FECs are FPGA based cards and are capable of managing the outputs from the ADC boards and receiving the triggers. As multiple FECs were used in the PRad experiment, they

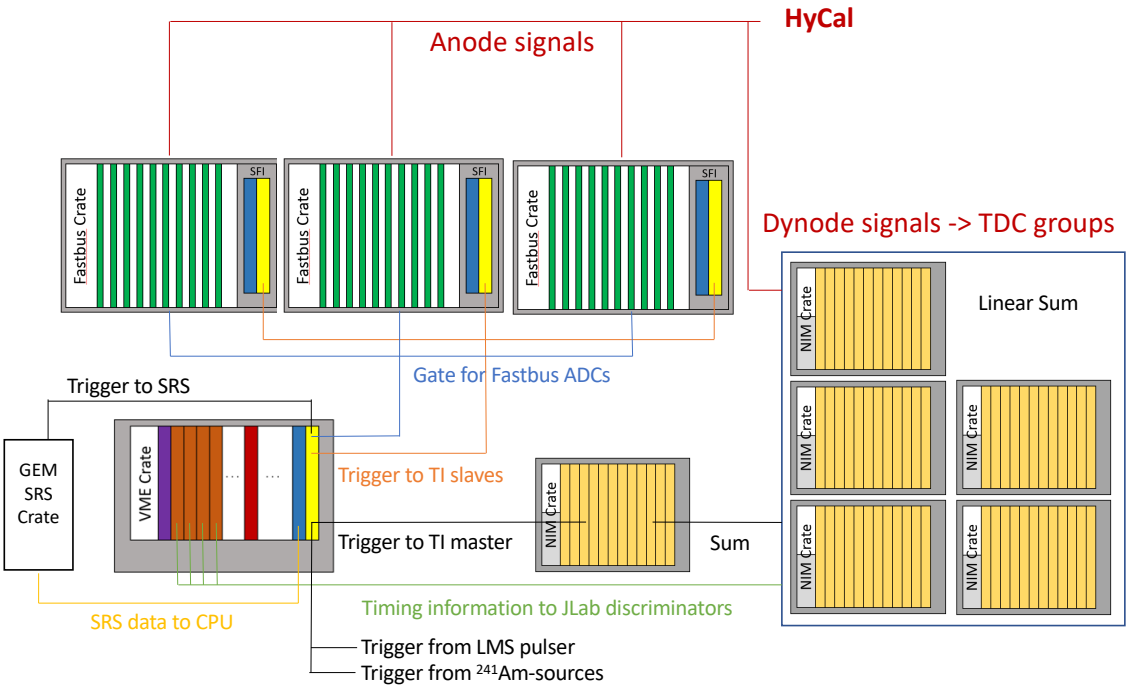

Figure 3.15: The configuration of the PRad DAQ system for the production runs. This plot is made by Chao Peng of Duke University.

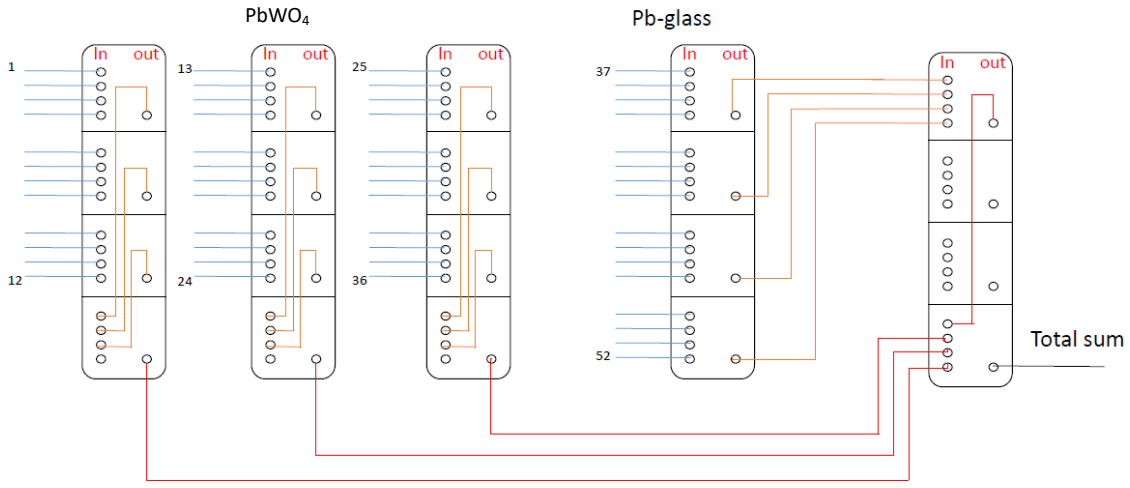

Figure 3.16: Summing all 52 signals from the UVA120A modules, using NIM modules. The final total sum signal is converted into ECL signal in order to be accepted by the TI master. This plot is made by Chao Peng of Duke University.

were connected to a higher level board called Scalable Readout Unit (SRU), which was connected to the DAQ computer using fibers. The HyCal total sum trigger would be sent to this DAQ computer, which would forward this signal to a NIM module to convert it from ECL signal to a NIM signal. This NIM signal would be eventually sent to the SRU, which would distribute it to the hosted FECs. The output data consisted of three consecutive samples from each strip in GEMs, measured by the APV25s, and were transferred to the data stream using a 10 Gb Ethernet.

For the calibration runs, the DAQ configuration was very similar to that of the production runs, with the exception that the trigger was produced by the Hall B photon tagger instead of HyCal, and there was an additional data stream to data files, including the photon energy and timing measured by the tagger. A separated VME crate (tagger crate) was integrated into the DAQ system, which had an additional TI master that received the trigger from the tagger and controlled all the TI slaves shown in Fig. 3.15.

In addition to the data from GEMs and HyCal, the output data also included information from the Experimental Physics and Industrial Control System (EPICS) and the scaler events. The EPICS events were taken every few seconds, which included pressure measurements at various locations along the beam-line, beam positions measured by various Beam Position Monitors (BPM), the target related gas flow rate, pressure, temperature, and so on. The scaler events, which were taken every 20 to 50 seconds, contained the information to calculate the dead time of the DAQ system and the total beam charge. Once the DAQ system received a trigger, it would start recording the current event, which would take about 20 μs. The system would be in a "busy mode" and would not be able to response to additional triggers during this period. This would lead to a "dead time" (t_{dead}) of the system. To measure this, a pulser with a constant frequency of 2.0 MHz was used and t_{dead} could be calculated

as

$$t_{\text{dead}} = \frac{N_{\text{gated}}}{N_{\text{total}}}, \tag{3.3}$$

where N_{total} is the total counts from the pulser and N_{gated} is the total counts while the DAQ system is in "busy mode". The live time (t_{live}) of the system can be obtained as

$$t_{\text{live}} = 1 - t_{\text{dead}}. \tag{3.4}$$

Apparently, the live time of the DAQ system depends on the event rate. The typical live time for a full target run is about 80% to 90% and the live time for an empty target run is about 95%. Another piece of important information recorded in the scaler events is the total charge deposition in the Hall B Faraday cup [71], which measures the beam charge (q_b) to a precision of 0.1%. This information allows one to calculate the live charge,

$$q_{\text{live}} = t_{\text{live}} \cdot q_b, \tag{3.5}$$

which needs to be used for subtracting backgrounds measured from empty target runs.

There were 6 different triggers used in this experiment. Their descriptions are listed in Table 3.2. The first two types of triggers were used for recording the physics events from the production runs. As mentioned in the previous section, the purpose of T1 trigger was to enhance the performance of Pb-glass detectors. For each run of data taking, the first 10,000 events were triggered by T3 and the next 10,000 events were triggered by T4. They were for the purpose of monitoring the calibration constants. The last two triggers were used only during the calibration runs, which were taken before the production runs. During these runs, the HyCal was calibrated

Trigger name	Description
T1	Total energy deposition in Pb-glass part of HyCal
T2	Total energy deposition in HyCal
T3	LMS light source
T4	^{241}Am radioactive source
T5	Hall B tagger counter
T6	Scintillator

Table 3.2: PRad trigger type description.

by high intensity photon beams that were tagged by the Hall B photon tagger, which also provided triggers for these runs. During this period, two scintillators were placed on the beam line and right in front of the GEM detectors. These scintillators could convert a small portion of the photons into electron-positron pairs, so that one could calibrate the efficiency of the GEM detectors, which are only sensitive to charged particles.

Chapter 4

Data Analysis

4.1 Overview

In general, the experimental differential cross section for the $e-p$ elastic scattering, in a particular scattering-angle bin or Q^2 bin can be obtained as

$$\langle\frac{d\sigma}{d\Omega}\rangle^{\mathrm{e,r}}_{ep}(\theta_i) = \frac{N^{\mathrm{e,r}}_{ep}(\theta_i)}{L\cdot f^{\mathrm{e}}_{ep}(\theta_i)\cdot\varepsilon^{\mathrm{e}}_{ep}(\theta_i)}, \tag{4.1}$$

where $N^{\mathrm{e,r}}_{e-p}(\theta_i)$ is the total count for the $e-p$ elastic scattering events in the i-th scattering-angle bin. The superscript "e" indicates that the events are from the experiment and the superscript "r" indicates that they contain the radiative effects. L is the integrated luminosity $L = N^{\mathrm{e}^-}_{\mathrm{beam}}\cdot N^{\mathrm{H}}_{\mathrm{tar}}$, which is the product of the total incident electron number and the number of H atoms/cm^2 (areal density). $f^{\mathrm{e}}_{ep}(\theta_i)$ stands for the geometric acceptance for the $e-p$ elastic scattering events in this angular bin and $\varepsilon^{\mathrm{e}}_{ep}(\theta_i)$ represents the detector efficiency for the same angular bin.

On the other hand, a similar expression for the differential cross section of $e-e$ scattering, in an angular bin j, could be written as

$$\langle\frac{d\sigma}{d\Omega}\rangle^{\mathrm{e,r}}_{ee}(\theta_j) = \frac{N^{\mathrm{e,r}}_{ee}(\theta_j)}{L\cdot f^{\mathrm{e}}_{ee}(\theta_j)\cdot\varepsilon^{\mathrm{e}}_{ee}(\theta_j)}. \tag{4.2}$$

Since both $e-p$ and $e-e$ events were taken simultaneously during the experiment, with the same electron beam and the same target areal density, the integrated luminosity L can be cancelled out if one takes the ratio between the two differential cross

sections,

$$\langle\frac{d\sigma}{d\Omega}\rangle^{\mathrm{e,r}}_{ep}(\theta_i) = \frac{N^{\mathrm{e,r}}_{ep}(\theta_i)}{N^{\mathrm{e,r}}_{ee}(\theta_j)} \cdot \frac{f^{\mathrm{e}}_{ee}(\theta_j)\cdot\varepsilon^{\mathrm{e}}_{ee}(\theta_j)}{f^{\mathrm{e}}_{ep}(\theta_i)\cdot\varepsilon^{\mathrm{e}}_{ep}(\theta_i)} \cdot \langle\frac{d\sigma}{d\Omega}\rangle^{\mathrm{e,r}}_{ee}(\theta_j). \tag{4.3}$$

In addition, the energy-independent part of the geometric acceptance and detector efficiency can be cancelled out if one takes this ratio using the counts from the same angular bin such that $i = j$ (the bin-by-bin method). Alternatively, one can fix j for the Møller and apply it as a common normalization factor for all the bins for $e - p$ (the integrated Møller method). There will be no cancellation for any acceptance and efficiency in the latter case. Typically, the detector efficiencies are measured with reference detectors and the geometric acceptance effect can be obtained using a realistic simulation for the experiment. However, one also needs to note that the experimental differential cross section cannot be used directly for the form factor extraction, as it contains the radiative effects. Furthermore, the cross sections mentioned above are averaged values over angular bins. They are not necessarily equal to the cross section values at the bin centers. So in order to obtain the Born level differential cross section at a particular θ value, one needs to apply a radiative correction and a bin center correction [72],

$$\big(\frac{d\sigma}{d\Omega}\big)^{\mathrm{e,b}}_{ep}(\theta_i) = \frac{R_{bcc}}{R_{rc}} \cdot \langle\frac{d\sigma}{d\Omega}\rangle^{\mathrm{e,r}}_{ep}(\theta_i), \tag{4.4}$$

where R_{rc} is the radiative correction factor and R_{bcc} is the bin center correction factor.

If one has a realistic simulation that includes all the important internal and external radiative effects, one can obtain the radiative correction factor for a particular angular bin as

$$R_{rc} = \frac{\langle\frac{d\sigma}{d\Omega}\rangle^{\mathrm{s,r}}_{ep}(\theta_i)}{\langle\frac{d\sigma}{d\Omega}\rangle^{\mathrm{s,b}}_{ep}(\theta_i)}. \tag{4.5}$$

The superscript "s" indicates that the values are obtained from the simulation and

the superscript "b" indicates that the events are at Born level.

The bin center correction also relies on a realistic simulation. In particular, it requires that the cross section model used in the simulation describes the actual cross section well enough. This can be achieved by tuning the cross section model in the simulation iteratively such that the simulation result converges to the data. The bin center correction factor for a particular angular bin can be obtained as

$$R_{bcc} = \frac{(\frac{d\sigma}{d\Omega})^{\mathrm{s,b}}_{ep}(\theta_i)}{\langle\frac{d\sigma}{d\Omega}\rangle^{\mathrm{s,b}}_{ep}(\theta_i)}. \tag{4.6}$$

Combining with Eq. 4.3, one obtains:

$$(\frac{d\sigma}{d\Omega})^{\mathrm{e,b}}_{ep}(\theta_i) = \frac{N^{\mathrm{e,r}}_{ep}(\theta_i)}{N^{\mathrm{e,r}}_{ee}(\theta_j)} \cdot \frac{f^{\mathrm{e}}_{ee}(\theta_j)\cdot\varepsilon^{\mathrm{e}}_{ee}(\theta_j)}{f^{\mathrm{e}}_{ep}(\theta_i)\cdot\varepsilon^{\mathrm{e}}_{ep}(\theta_i)} \cdot \frac{\langle\frac{d\sigma}{d\Omega}\rangle^{\mathrm{e,r}}_{ee}(\theta_j)}{\langle\frac{d\sigma}{d\Omega}\rangle^{\mathrm{s,r}}_{ep}(\theta_i)} \cdot (\frac{d\sigma}{d\Omega})^{\mathrm{s,b}}_{ep}(\theta_i). \tag{4.7}$$

Since the $e-e$ elastic scattering is a pure QED process, and its radiated cross section can be calculated exactly (at least at the next-to-leading order), one can assume that

$$\langle\frac{d\sigma}{d\Omega}\rangle^{\mathrm{e,r}}_{ee}(\theta_i) = \langle\frac{d\sigma}{d\Omega}\rangle^{\mathrm{s,r}}_{ee}(\theta_i), \tag{4.8}$$

so that one can replace the averaged $e-e$ cross section from the experiment by that from the simulation. And the ratio,

$$\frac{\langle\frac{d\sigma}{d\Omega}\rangle^{\mathrm{s,r}}_{ee}(\theta_j)}{\langle\frac{d\sigma}{d\Omega}\rangle^{\mathrm{s,r}}_{ep}(\theta_i)} = \frac{N^{\mathrm{s,r}}_{ee}(\theta_j)}{N^{\mathrm{s,r}}_{ep}(\theta_i)} \cdot \frac{f^{\mathrm{s}}_{ep}(\theta_i)\cdot\varepsilon^{\mathrm{s}}_{ep}(\theta_i)}{f^{\mathrm{s}}_{ee}(\theta_j)\cdot\varepsilon^{\mathrm{s}}_{ee}(\theta_j)}, \tag{4.9}$$

can be obtained from the $e-p$ and $e-e$ counts by using the simulation that includes the radiative effects for both $e-p$ and $e-e$ elastic scatterings, normalized at the same integrated luminosity.

The acceptance correction is obtained with a simulation that contains accurate

geometric information about the experimental setup and precise models for the actual detector responses. The geometric information of the setup was surveyed prior to the experiment by the JLab survey group, using a high precision laser technique. The detector positions would be further refined by the Møller events taken during the experiment. The detector responses, such as those for the position and energy reconstruction, are included in the simulation and fine-tuned to match those from the actual detectors. With all the realistic acceptance effects incorporated in the simulation, the acceptance factors for the data and the simulation can be cancelled. The imperfection for the acceptance description in the simulation will be taken into account in the associated systematic uncertainties. For the detector efficiencies, they can be extracted from the experimental data and simulation separately. The $e-p$ and $e-e$ counts from the experiment can be corrected by these efficiencies so that

$$\tilde{N}^{\mathrm{e,r}}_{ep}(\theta_i) = \frac{N^{\mathrm{e,r}}_{ep}(\theta_i)}{\varepsilon^{\mathrm{e}}_{ep}}, \tag{4.10}$$

$$\tilde{N}^{\mathrm{e,r}}_{ee}(\theta_i) = \frac{N^{\mathrm{e,r}}_{ee}(\theta_i)}{\varepsilon^{\mathrm{e}}_{ep}}, \tag{4.11}$$

and similar corrections will be performed for those obtained from the simulation. Eventually, the Born level $e-p$ elastic scattering cross section can be extracted using

$$(\frac{d\sigma}{d\Omega})^{\mathrm{e,b}}_{ep}(\theta_i) = \frac{\tilde{N}^{\mathrm{e,r}}_{ep}(\theta_i)/\tilde{N}^{\mathrm{e,r}}_{ee}(\theta_j)}{\tilde{N}^{\mathrm{s,r}}_{ep}(\theta_i)/\tilde{N}^{\mathrm{s,r}}_{ee}(\theta_j)} \cdot (\frac{d\sigma}{d\Omega})^{\mathrm{s,b}}_{ep}(\theta_i). \tag{4.12}$$

A flow chart for the data analysis procedure is shown in Fig. 4.1. In this chapter, details of each item in the flow chart will be discussed except for the radius fitting, which will be discussed in the next chapter. It starts with the event reconstructions, for both the GEMs and HyCal, and then the detector calibrations, including the energy calibration for HyCal and position calibrations for both GEMs and HyCal.

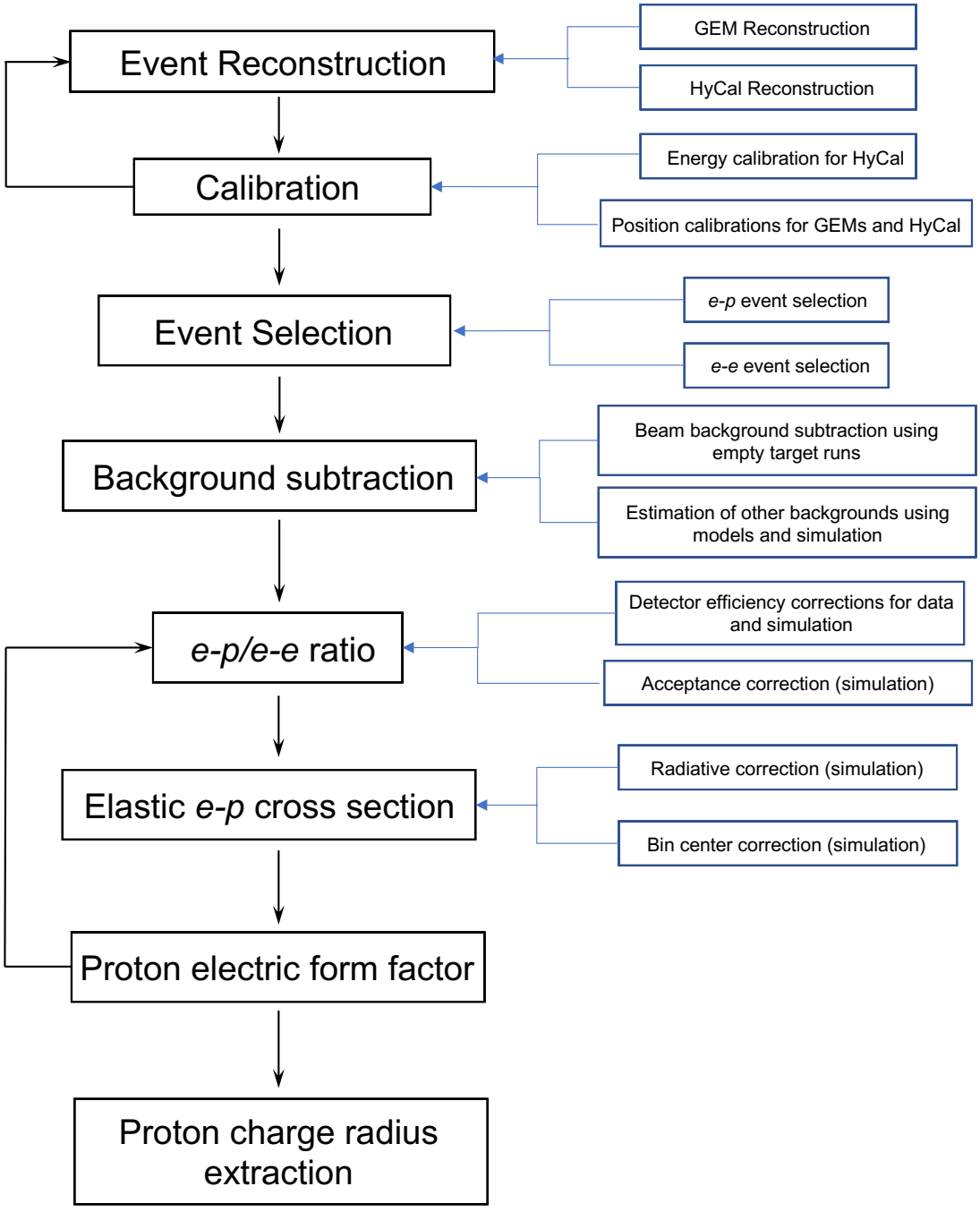

Figure 4.1: The flow chart for the data analysis procedure.

The energy calibration is essential for the $e-p$ and $e-e$ event selections as they are primarily distinguished by the energies of the scattered electrons. The position calibration is important for the scattering angle reconstruction, which will affect the Q^2 determination. The event reconstructions and detector calibrations need to be performed iteratively in order to obtain the energy calibration constants for all the HyCal modules. The event selection will be presented next, with the details about the event selection cuts for both $e-p$ and $e-e$ scatterings. Typically, not all the events satisfying the selection cuts are coming from the reactions of interest. Some of them may come from backgrounds generated from objects near the beam-line or from other reaction channels such as inelastic $e-p$ scatterings. So one will need to perform a background subtraction before forming the $e-p$ to $e-e$ ratio. The cross section and its radiative correction will be presented next. This is another iterative procedure, which involves fine tuning the form factors used in the simulation so that eventually the $e-p$ to $e-e$ ratios in the data and the simulation agree with each other. After the cross section is obtained, the proton electric form factor G_E^p can be extracted by assuming G_M^p with certain models, as the contribution to the cross section is dominated by G_E^p in the PRad kinematic range. This aspect will be discussed in the last part of this chapter.

4.2 Event Reconstruction

The direct information obtained from the experiment is the Analog-to-Digital Convertor (ADC) signals from all the readout channels of the GEMs and HyCal. The event reconstruction involves analyzing these ADC signals, and extract information that contains physical meanings about the scattered electrons, such as the hit positions as they penetrate the GEM detectors and the energy depositions in the HyCal.

The ADC signal from each channel is superimposed on the pedestal noise, which was measured at the beginning of each run, triggered by the radioactive sources attached to the reference PMTs (see Section. 3.5). These triggers are completely uncorrelated with the signals from the $e-p$ and $e-e$ events, so they can be used to measured the pedestal noise. These noises can be reasonably well described by Gaussian distributions for both the GEMs and HyCal. Only when the ADC signal of a channel exceeds 5σ of its pedestal noise, then the channel is considered fired, and the ADC signal will be analyzed to extract physical information.

Usually, when an electron enters the GEMs and HyCal, they will fire multiple consecutive channels in these detectors, for example, 2 to 3 consecutive channels for the GEMs on each set of readout strips, and over 10 consecutive modules for the HyCal. These consecutive fired channels are called clusters. The event reconstruction thus involves with identifying the clusters and reconstruct the kinematic information from them.

The clustering algorithm for GEMs is a simple peak-valley splitting algorithm. That is, it first groups all the consecutive strips that have signals above the threshold into a cluster, and then searches for peak-valley patterns. If two peaks are identified with a valley in between, the cluster is split at the valley with half of the ADC signal on the valley strip distributed into each cluster. The position of a cluster is then reconstructed using the center of gravity method, with the ADC amplitude of a strip as the weight

$$x_{\text{recon}} = \frac{\sum_i^N (A_i x_i)}{\sum_i^N A_i}, \tag{4.13}$$

where x_{recon} is the reconstructed x-coordinate of a hit, index i runs through all the strips of a cluster, x_i is the center position of the strip, and A_i is the ADC signal of the strip. The same algorithm is applied to reconstruct the y-coordinate of a hit as

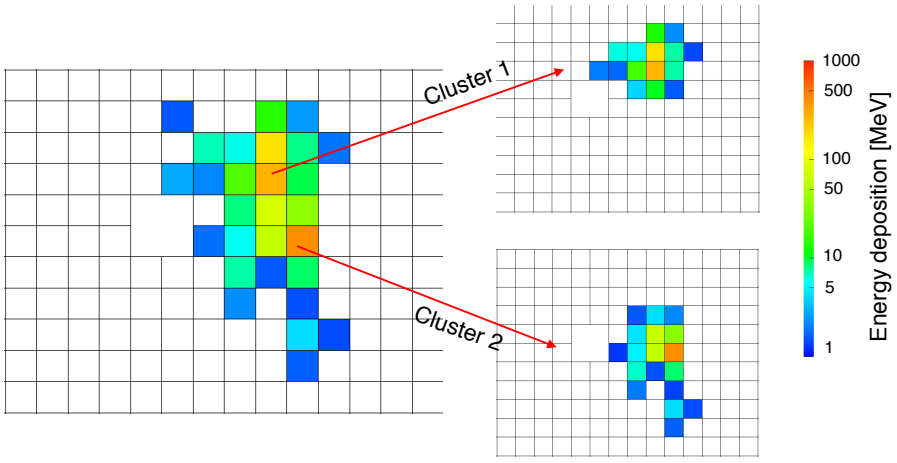

Figure 4.2: Examples of HyCal cluster reconstruction for an event that has two maxima in the same group. The two clusters are separated by finding a best match with the simulated cluster profiles. Reconstructed energy is obtained by taking the total sum of from all the modules that belong to a cluster. The reconstructed position is evaluated using the center of gravity method in these modules.

well.

There are two cluster reconstruction algorithms implemented for the HyCal. The first one is a 5×5 algorithm. It firstly identifies all the modules with local maximum energy deposition (higher ADC values than all of their neighbors), and then groups their surrounding 5×5 modules. This algorithm is excellent in the execution speed, but is expected to perform less accurately in separating the scattered electron and radiated photons. The second method is called the "island" algorithm, which is used in the analysis. Firstly, the algorithm will group all the neighboring modules with the signals above a certain threshold. Then it identifies the local maxima within each group. If two or more local maxima were found in one group, the algorithm will subdivide the group iteratively until a best match is achieved with the simulated cluster profiles (see Fig. 4.2). For a module that is shared by multiple clusters, its energy distribution among the clusters is determined to achieve a maximum accordance

with the simulated cluster profiles. In this case, the likelihood function of a double exponential distribution was used as the estimator. After the clustering is finished, the reconstructed energy can be obtained from the sum of the energy depositions from all the modules in the same cluster. The reconstructed position is obtained from the center of gravity of the cluster with logarithmic weights, which correspond to the exponential decay of the signal strength as a function of the distance from the center

$$x_{\text{recon}} = \frac{\sum_i^N (w_i x_i)}{\sum_i^N w_i}. \tag{4.14}$$

x_{recon} is the reconstructed x-coordinate of a hit, index i runs through all the modules of a cluster, x_i is the center position of a module, and w_i is the weighting factor of a module

$$w_i = \text{Max}[0, \text{a} + \log(\text{E}_\text{i}/\text{E}_{\text{total}})], \tag{4.15}$$

where E_i is the energy deposition in this module, E_{total} is the total energy deposition of a cluster and a is a free parameter, which when set to 3.6, gives the best position resolution for HyCal[1]. This calculation is repeated to reconstruct the y-coordinate of a hit as well.

4.3 Calibration

4.3.1 Energy Calibration

The HyCal was calibrated during the calibration runs using a photon beam, generated by a 1.1 GeV electron beam incident on a thin wire target. The energy of the photon beam was measured by the Hall B photon tagger [68]. There were three major purposes for this calibration. First, the photons with tagged energies could be used

[1]The notation Max[a, b] means it returns the larger value between a and b.

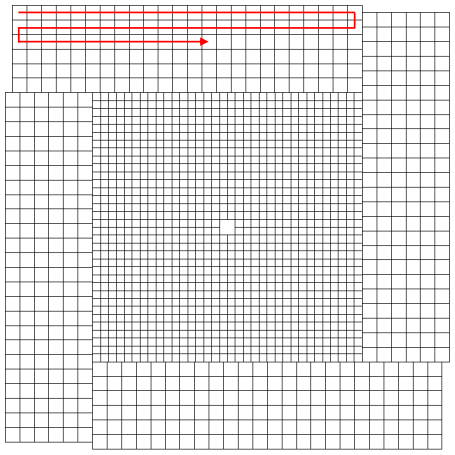

Figure 4.3: The HyCal movement during the calibration runs. The photon beam was fixed in the space, while HyCal was suspended on a transporter to move in a way such that the beam would hit each module one at a time in a snake-like pattern, as indicated by the red arrow.

to obtain the energy calibration constants for the HyCal modules. Second, the photon beam energy ranged from 220 MeV to 1050 MeV (0.2 to 0.95 of the incident electron beam energy, limited by the measurement range of the Hall B photon tagger), which could be used to study the non-linearity properties of the HyCal modules. Third, the events recorded in the calibration runs were triggered by the Hall B photon tagger so that one could study the trigger efficiency of the calorimeter.

During these calibration runs, the HyCal was suspended on a transporter so that the photon beam could be injected on each HyCal module, one at a time, in a snake-like pattern as shown in Fig. 4.3. Once a photon enters the calorimeter, it will generate a shower, which results in detectable signals in several consecutive modules. A calibration constant was assigned to each module to convert the measured ADC values into the deposited energies. A HyCal reconstruction algorithm was applied to identify and group these modules into a cluster, and obtain the reconstructed energy by summing the energy depositions in all the modules of the cluster. The energy

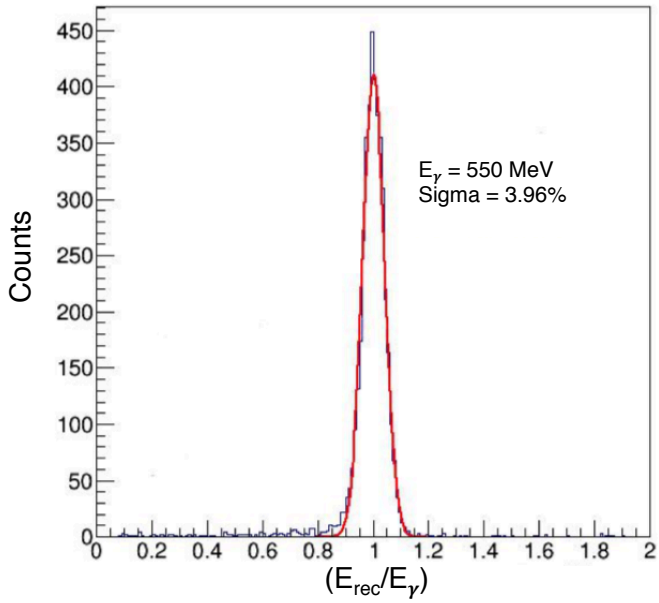

Figure 4.4: The ratio between the reconstructed energy E_{rec} and the beam energy E_γ, for beam energy around 550 MeV. The black histogram comes from the data of the calibration runs, the red curve is a Gaussian fit to the data. The width (sigma) of the Gaussian fit is 3.96%. The figure is made by Li Ye of Mississippi State University.

calibration of the calorimeter was done iteratively, by fine tuning the calibration constant of each module such that eventually, the reconstructed energy converged to the energy of the incident photon. An example for the ratio between the reconstructed energy E_{rec} and the incident photon energy E_γ, for E_γ around 550 MeV, is shown in Fig 4.4.

Typically, due to reasons such as the light attenuation property of a module and the pedestal noise in the electronics, the calibration constants obtained at a particular incident photon energy are not necessarily applicable if the incident photon is at a different energy. The calorimeter is linear if the calibration constants can correctly reconstruct the energy of a photon, regardless of its incident energy, otherwise, the calorimeter is non-linear. The photon beam could be used to study this property conveniently, as it was generated through the bremsstrahlung process and the tagged

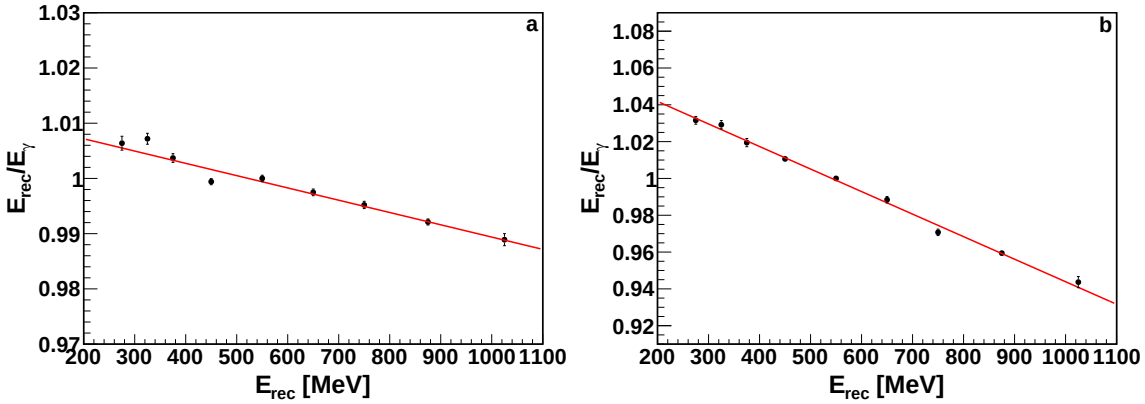

Figure 4.5: The non-linearity behavior of (**a**) a $PbWO_4$ module W213 and (**b**) a Pb-glass module G507. Red lines are linear fits to the data points, for which only statistical uncertainties are shown as the error bars.

photon energy range was from 220 MeV to 1050 MeV. The nonlinear effect can be studied by plotting the ratio $E_{\rm rec}/E_\gamma$ as a function of $E_{\rm rec}$, and then fit the data with a polynomial such as

$$\frac{E_{\rm rec}}{E_\gamma} = 1 + \sum_{i=1}^{i=N} \alpha_i (E_{\rm rec} - E_{\rm cali})^i, \tag{4.16}$$

with α_i as the free parameters, up to some maximum power of N. $E_{\rm cali}$ is the energy where the calibration constants were obtained from, so that around this energy, one has $E_{\rm cali} \approx E_{\rm rec}$. For a perfectly linear calorimeter, one would obtain zero for all values of α_i. For HyCal, usually this ratio was rather linear as a function of $E_{\rm rec} - E_{\rm cali}$, so that only the first term was kept in the fit, and the nonlinear effect was corrected by

$$E_{\rm corr} = \frac{E_{\rm rec}}{1 + \alpha_1 (E_{\rm rec} - E_{\rm cali})}. \tag{4.17}$$

Examples of the nonlinear behavior for two HyCal modules and their fits are shown in Fig. 4.5.

The reconstructed energy was then corrected for the nonlinear effect using the above correction. The resolution for the $PbWO_4$ part of the detector is shown in

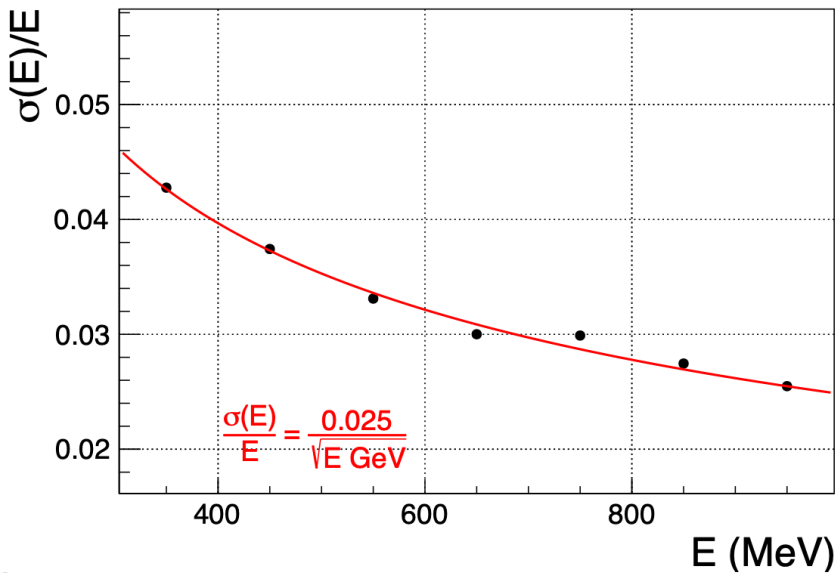

Figure 4.6: The energy resolution of the $PbWO_4$ detector. This figure is made by Maxime Lavilain of North Carolina A&T State University.

Fig. 4.6. The resolution is about 2.5%, which is the nominal value for this detector, based on the PrimEx measurements [63, 64, 65]. The energy resolution of Pb-glass is much worse, at about 6%.

The third purpose of the calibration runs was to obtain the trigger efficiency of the HyCal. During these runs, the events were recorded based on the triggers from the photon tagger. One could then search for a trigger signal from HyCal. The trigger efficiency was determined as the number of events that produced HyCal triggers over the total number of events. A number of cuts were applied to suppress the accidental backgrounds from the photon beam, including the coincidence time between the tagger TDC and HyCal TDC signals, the HyCal energy deposition and so on. The measured HyCal trigger efficiency is shown in Fig 4.7, for some $PbWO_4$ and Pb-glass detectors. Typically, the efficiency reaches a plateau at about 99.9% once the incident photon energy exceeds 400 MeV. A few low efficiency modules were

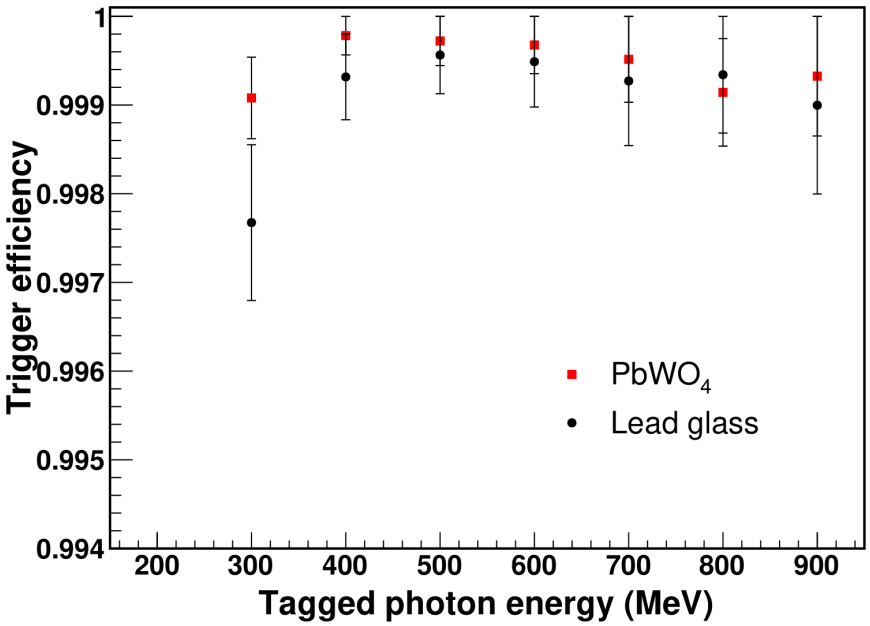

Figure 4.7: The trigger efficiency for $PbWO_4$ and Pb-glass detectors, as a function of the incident photon beam energy.

identified and removed during the analysis.

Even though for the HyCal, signals produced by electrons are highly similar to those produced by photons, there could be some small differences [73]. In addition, certain experimental conditions could be slightly shifted relative to those from the calibration runs. In order to resolve these issues, the scattered electrons from the $e-p$ and $e-e$ events during the production runs (the full target and empty target runs) were also used for various purposes, such as fine tuning the calibration constants, extracting certain fine-corrections for the HyCal reconstruction, and also fine tuning the nonlinearity constants extracted from the photon beam calibration data. In the first case, one would calibrate the calorimeter to the expected energies of the scattered electrons from these reaction channels. For the $e-p$ elastic scattering, the expected

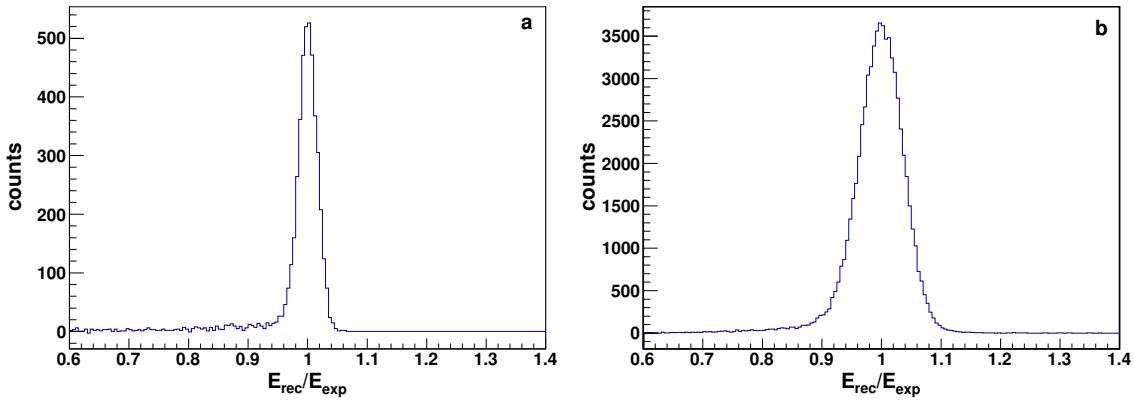

Figure 4.8: The reconstructed energy E_{rec} over the expected energy E_{exp} for (**a**) the $e-p$ elastic scattering and (**b**) the $e-e$ elastic scattering.

energy for a scattered electron (given as equation (2.27) in Ref. [31]) is

$$E_{\rm exp} = \frac{(E_b + M)(ME_b + m^2) + \sqrt{M^2 - m^2\sin^2\theta}|\,\vec{\ell}\,|^2\cos\theta}{(E_b + M)^2 - |\,\vec{\ell}\,|^2\cos^2\theta}, \tag{4.18}$$

where $\vec{\ell}$ is the 3-momentum of the incident electron. This formula does not neglect the mass of an electron. If one replaces the proton mass M with the electron mass m, one obtains the expected energy for a scattered electron from the $e-e$ elastic scattering,

$$E_{\rm exp} = m\frac{E_b + m + (E_b - m)\cos^2\theta}{E_b + m - (E_b - m)\cos^2\theta}. \tag{4.19}$$

The ratio between the reconstructed energy and the expected energy $E_{\rm rec}/E_{\rm exp}$ from both $e-p$ and $e-e$ elastic scatterings are shown in Fig 4.8.

Secondly, certain fine-corrections for the HyCal reconstruction cannot be obtained from the calibration runs as the incident photon beam was very narrow and it could not cover the entire area of HyCal. These corrections are better to be obtained from the production runs, from the $e-p$ and $e-e$ events. An important correction is for the non-uniformity in the reconstructed energy from HyCal. Fig. 4.9 shows the

$E_{\rm rec}/E_{\rm exp}$ ratio for the $e-p$ events in a $PbWO_4$ module W521[2] and a Pb-glass module G238, as a function of the normalized reconstructed position, which is the difference between the reconstructed position and the module center position, normalized by the size of the module:

$$t_x = \frac{x_{\rm rec} - x_c}{S}, \tag{4.20}$$

$$t_y = \frac{y_{\rm rec} - y_c}{S}, \tag{4.21}$$

where the size S of a $PbWO_4$ module is about 20.76 mm, and the size of a Pb-glass module is about 38.15 mm. The reconstructed energy tends to be slightly larger when the electron is hitting the edges and corners. The reason is that for the purpose of mechanical supports, the front end of HyCal modules are covered by bronze flanges with 2 mm thickness and a 13 mm diameter hole in the middle (see Fig. 3.11). These flanges can behave like pre-showers, and change the shower depths of the incident electrons. This effect is a few times larger for the Pb-glass detectors as they are more sensitive to various shower position effects, as shown in (**c**) of Fig. 4.9. A detailed description about how to correct this effect is provided in Ref. [74]. (**b**) and (**d**) of Fig. 4.9 show the results after this correction.

Lastly, providing that the energy of the incident electron from the Møller scattering is large enough (at least 20% of the beam energy) for a particular HyCal module, the $e-p$ and $e-e$ events from the production runs can also be used to fine tune the non-linearity correction of this module, since from the calibration runs the measured non-linearity could be well described by a linear function over the measured range. However, the Møller electrons appearing in the Pb-glass region often have energy below 200 MeV for both 1.1 and 2.2 GeV energy settings. And this linear description is expected to break down if the energy of the incident particle is too low, which is due

[2]Pb-glass channel ID start with the letter "G", $PbWO_4$ channels start with "W"

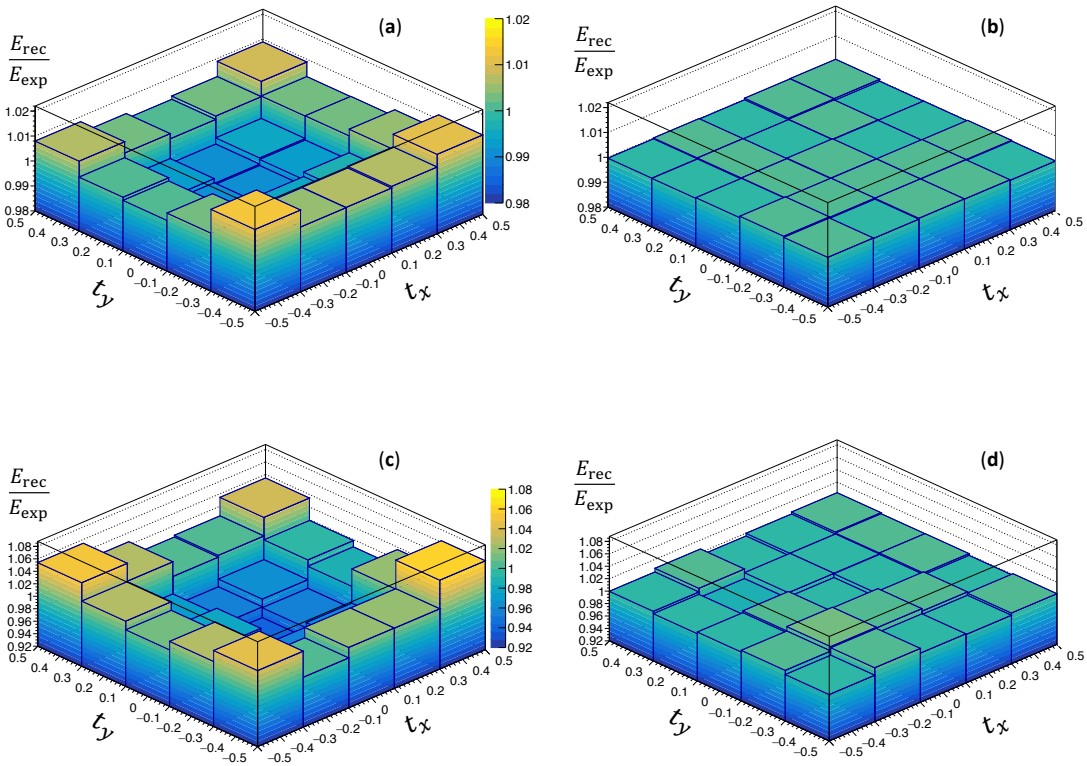

Figure 4.9: The non-uniformity in the HyCal reconstructed energy for $e-p$ events in a $PbWO_4$ module W521, as shown in (**a**), and in a Pb-glass module G238, as shown in (**c**). t_x and t_y are defined in Eq. 4.20 and Eq. 4.21. The z-axis shows the ratio between the reconstructed energy and the expected energy, obtained using equation Eq. 4.18. (**b**) and (**d**) show the ratio after the correction, for W521 and G238 respectively.

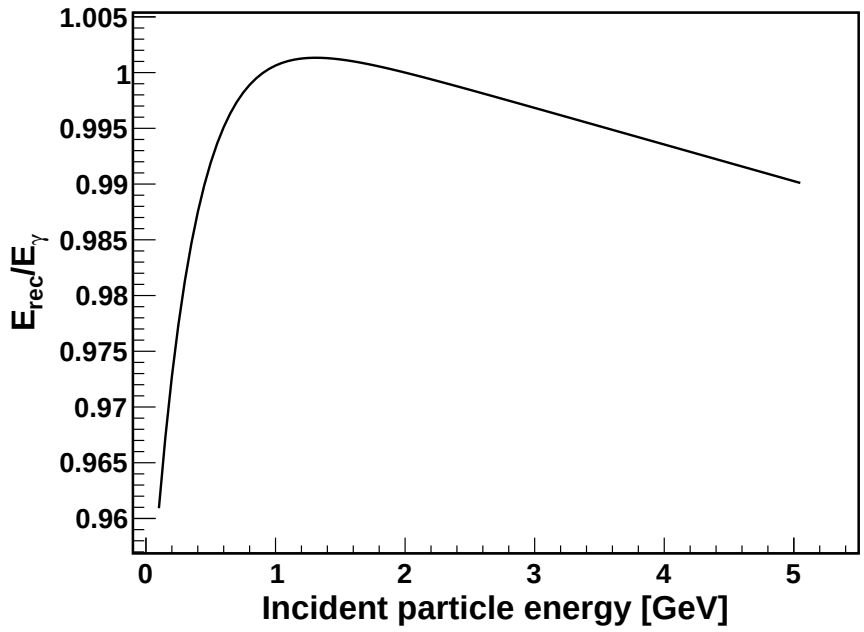

Figure 4.10: The non-linearity correction function of a Pb-glass module from the PrimEx-II experiment. The correction is very linear if the energy of the incident particle is high, but drops rapidly if the energy is low, which is expected due to reasons such as the pedestal cuts and the light attenuation property of the module.

to reasons such as the pedestal cuts and the light attenuation property of a module. This effect is expected to be more significant for the Pb-glass modules. This turning point could not be determined with the PRad photon calibration data due to the limited photon energy range, but was measured by the PrimEx-II experiment [65]. An example of the PrimEx-II non-linearity correction function for a Pb-glass module is shown in Fig 4.10. For this reason, a conservatively estimated systematic uncertainty was assigned for the Pb-glass non-linearity correction, which will be discussed in section 4.10.

As introduced in Section 3.5 and 3.7, the gain of each HyCal module was monitored by the HyCal light monitoring system during the experiment and was measured at the beginning of every run. The gain factors, obtained from Eq. 3.1, fluctuated

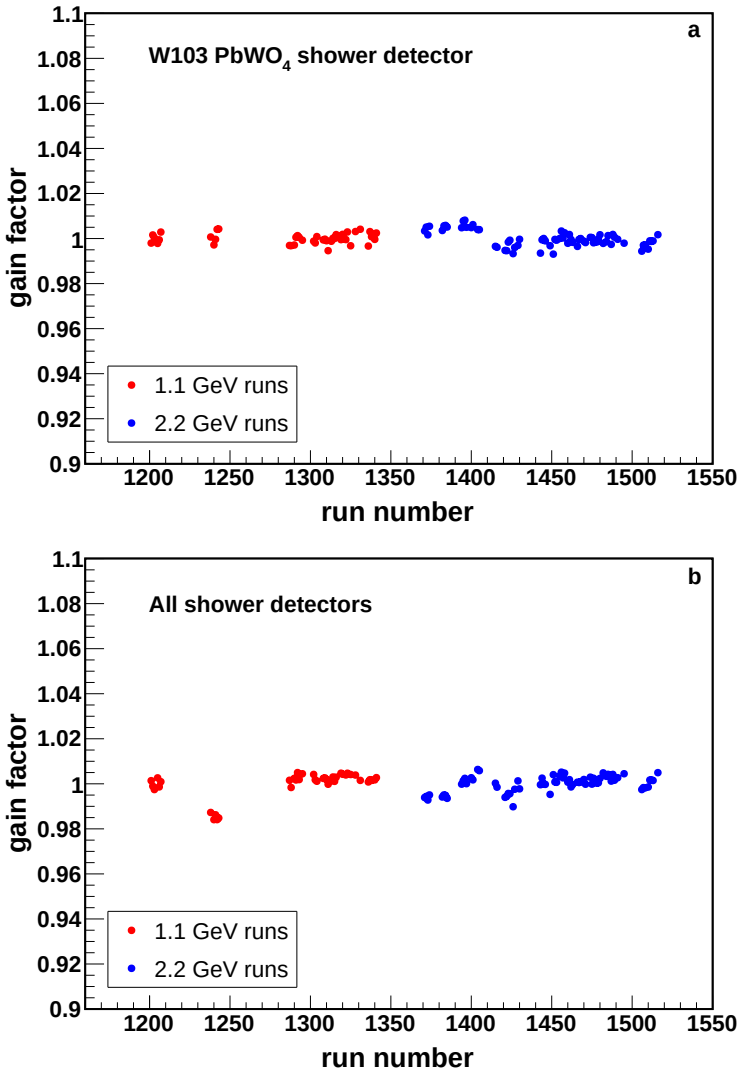

Figure 4.11: The HyCal gain factors for (**a**) the module W103 and (**b**) the average of all HyCal modules are shown as a function of run number.

mostly within 5% during the production runs, as shown in Fig. 4.11 as a function of the run number. These gain factors were used to correct the calibration constants of all HyCal modules for all the runs, and after the correction, the fluctuations in the elastic peaks for both $e-p$ and $e-e$ events were less than 0.5% during the production run period. These fluctuations were much smaller than the energy resolution of the calorimeter, as shown in Fig. 4.12.

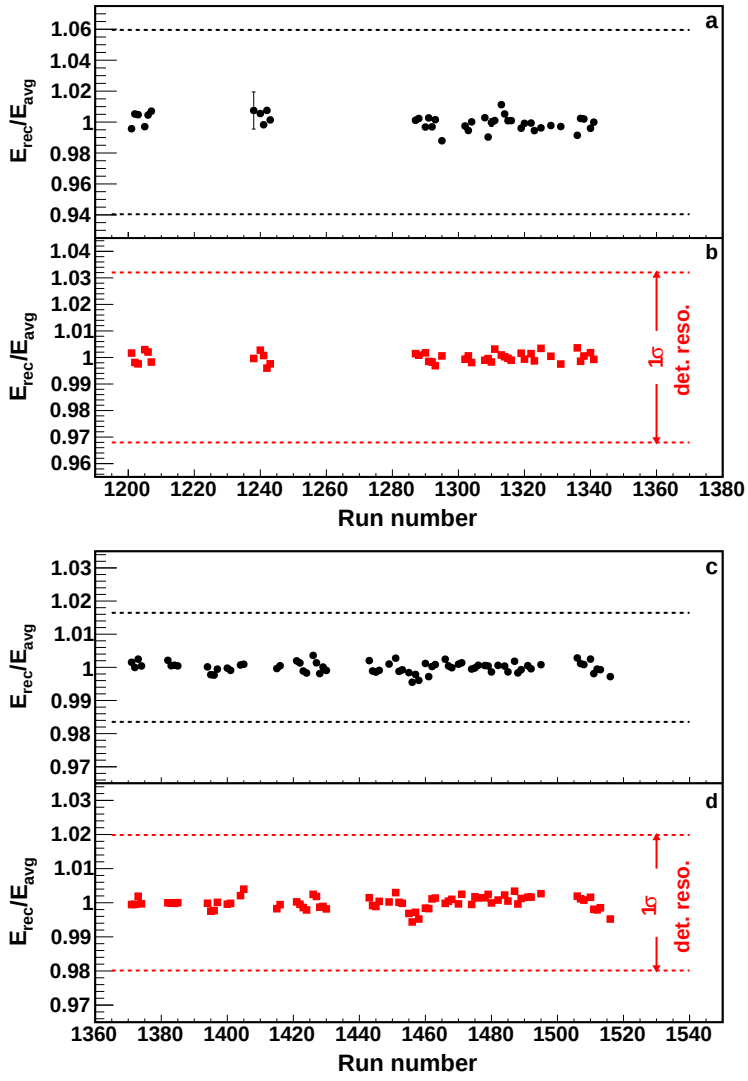

Figure 4.12: The reconstructed elastic peak positions from each run over the averaged peak position from all the runs for, (**a**): 1.1 GeV $e-p$ from 5.0° to 7.0°, (**b**): 1.1 GeV $e-e$ from 1.6° to 1.8°, (**c**): 2.2 GeV $e-p$ from 2.5° to 3.5°, and (**d**): 2.2 GeV $e-e$ from 0.8° to 0.9°. The fluctuation is mostly within 0.5%, and it is significantly smaller than the detector resolution, as marked by the dash lines on each plot.

Detector type	Energy resolution (%)	Position resolution (mm)
$PbWO_4$	$2.4/\sqrt{E(\text{GeV})}$	$2.4/\sqrt{E(\text{GeV})}$
Pb-glass	$6.2/\sqrt{E(\text{GeV})}$	$6.5/\sqrt{E(\text{GeV})}$

Table 4.1: The energy and position resolutions for the $PbWO_4$ and Pb-glass shower detectors of HyCal. E is the energy of the incident electron in unit of GeV.

The energy and position resolutions of the HyCal for the electrons from the production runs are shown in Table 4.1. These values were used during the analysis to determine the size of various event selection cuts.

4.3.2 Position Calibration

It is critically important to know precisely the position of the detectors as they will directly affect the reconstructed scattering angle and Q^2. The position of the detectors and also various important components of the PRad setup (PRad target, vacuum box window...) were surveyed by the Jefferson Lab survey group before the experiment using their laser technique, with a precision better than 1 mm. In addition, the $e-e$ elastic scattering events can also be used to refine this knowledge. For this purpose, both scattered electrons must be detected in coincidence (double-arm Møller events). First of all, the transverse momentum conservation requires that the transverse position of the electron beam must fall in the same plane determined by the two scattered electrons (co-planarity). One should expect to obtain a distribution centered at 0° if one computes the variable

$$\Delta\phi = \phi_{e1} - \phi_{e2} - \pi, \tag{4.22}$$

where ϕ_{e1} and ϕ_{e2} are the reconstructed azimuthal angles of the scattered electrons from the $e-e$ scattering, as indicated in Fig 4.13. The distributions of the co-planarity from the data and simulation are shown in the top plot of Fig. 4.14.

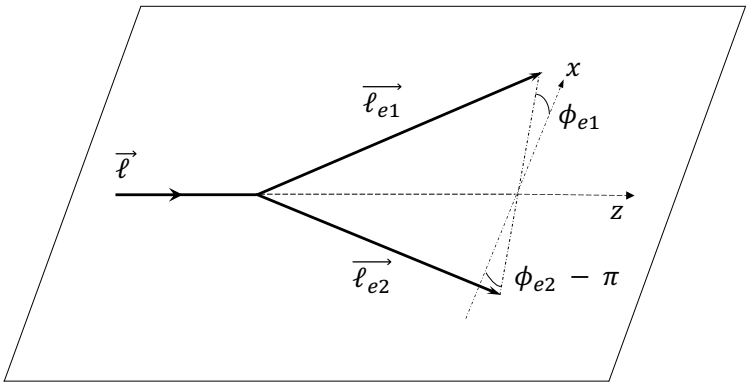

Figure 4.13: A diagram that indicates the azimuthal angles (ϕ_{e1} and ϕ_{e2}) of the scattered electrons from the $e - e$ scattering process.

This information is used to determine the transverse coordinates of the detectors, relative to the beam position. After this correction, the longitudinal distance between the target center and the detectors can be determined from the energy and momentum conservation laws for the $e - e$ elastic scattering, which leads to

$$z = \sqrt{\frac{(m + E_\ell)R_1R_2}{2m}}, \tag{4.23}$$

where m is the electron mass, E_ℓ is the energy of the incident electron, R_1 and R_2 are the transverse distance between the hit positions and the beam-line. One can determine z using both the 1.1 GeV or the 2.2 GeV data. As an example, the difference between the reconstructed vertex z (z_{rec}) and the z distance between the target center and the GEM detectors (z_{target}), using the 2.2 GeV $e - e$ events, is shown in the bottom plot of Fig. 4.14.

The determined z positions for both GEMs and HyCal, using both 1.1 and 2.2 GeV data sets, are shown in Table 4.2. The determined values differ by no more than 1 mm (0.02% of the distance). They are well consistent with each other given the uncertainties in the beam energy, and also agree with the surveyed results at 1 mm

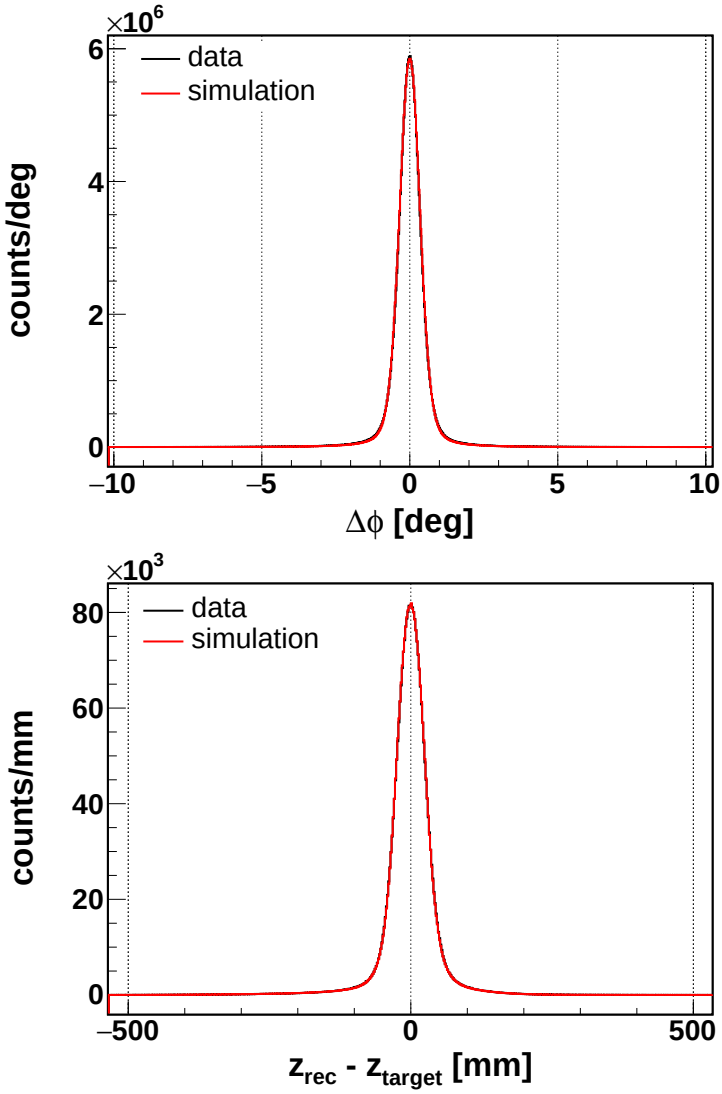

Figure 4.14: Top plot: the co-planarity distributions for the 2.2 GeV data and simulation. Bottom plot: the difference between the reconstructed vertex z and the distance between the target center and the GEM detectors for the 2.2 GeV data and simulation. Only the double arm Møller events with two hits on the GEMs were used for these computations, and the distributions were obtained based on the GEM reconstructed coordinates.

	HyCal z (mm)	GEM-I z (mm)	GEM-II z (mm)
1.1 GeV data	5646.56	5226.44	5186.46
2.2 GeV data	5645.68	5225.87	5186.43
Average	5646.12	5226.16	5186.45

Table 4.2: The longitudinal z distance between target center and detectors. GEM-I refers to the one on beam left (looking downstream).

level. This result can be considered as a validation for the beam energy measurement from our offline analysis, and the results were listed in Table 3.1. The averaged positions from the two beam energy settings were used in the later analysis.

4.4 Event Selection

The event selection cuts will be discussed in this section. For all the electrons detected by HyCal, it is required that a matching hit must be found on the GEM detectors. First of all, all the reconstructed hits from the GEMs and HyCal are projected onto a common transverse plane located at the surface of the $PbWO_4$ modules, assuming the track is produced at the center of the target cell. For each HyCal hit, the matching GEM hits must fall inside a circle that is centered at the HyCal hit position and with its radius determined by the position resolution of HyCal. If multiple GEM hits satisfy this condition, then the closest one to the HyCal hit will be chosen as its matching hit. The detectors were well aligned after the position calibration, so that the difference of the projected coordinates from these detectors form Gaussian peaks that are centered at 0, as shown in Fig 4.15. The size of the matching radius was chosen to be 6 times larger than the position resolution of HyCal in order to minimize the effects due to the non-uniformity in the HyCal coordinate reconstruction.

The second common cut applied for all the events is the dead module removal cut. As mentioned in the previous section, a number of HyCal modules had low trigger

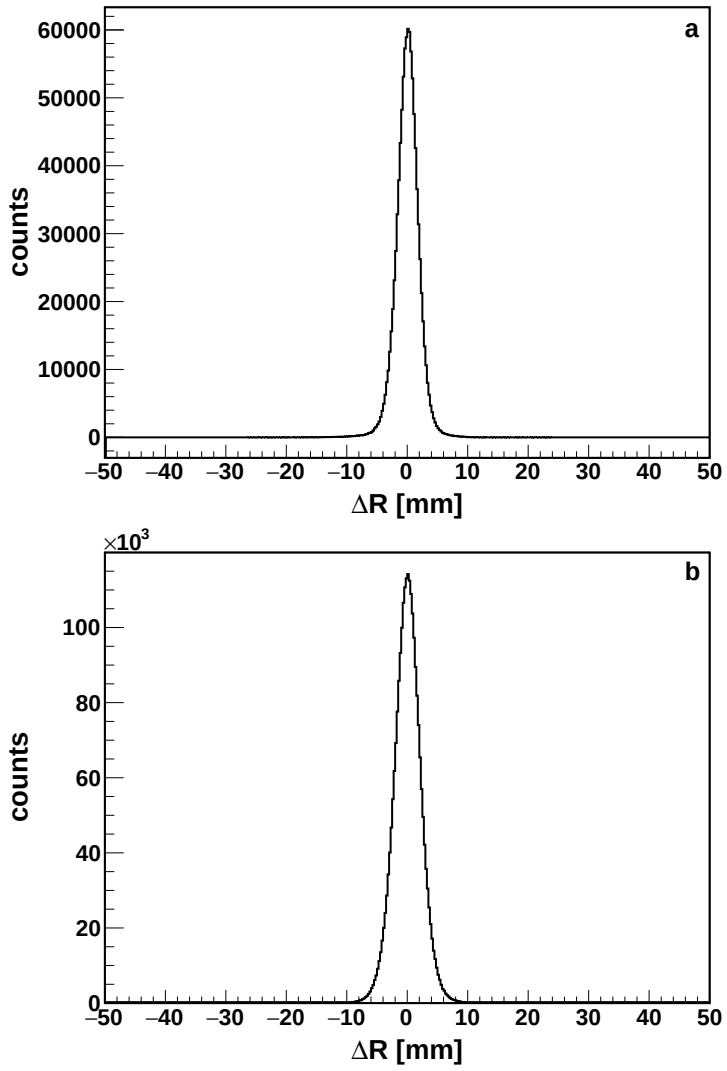

Figure 4.15: ΔR distributions between the HyCal and GEM reconstructed hits, for (**a**) the elastic $e-p$ and (**b**) $e-e$ scattered electrons, after being projected to the same plane located at the surface of $PbWO_4$ modules. Similar distributions can be obtained for both ΔX and ΔY distributions.

efficiencies during the experiment. These included channels G486, G732 and W230. In addition, there were also a few modules, including G775, G900, W835 and W891, that had no ADC readout. To remove possible errors due to the trigger efficiency correction and mis-calibration, a module removal cut was applied, using circles that were centered at the centers of these modules and with radii as 1.5 times the size of the modules[3]. The events with their reconstructed positions falling inside these circles would be removed from the analysis. In addition, the events with their reconstructed positions falling on the inner most and outer most layer of HyCal modules were also removed from the analysis. These events might suffer significantly from the energy leakage issue, as part of their showers could leak out of the calorimeter through the edges.

The scattered electrons from the elastic $e-p$ and $e-e$ scatterings can be well distinguished by their energy deposition in the calorimeter. Fig 4.16 shows the reconstructed energy from HyCal as a function of the reconstructed scattering angle determined by the GEMs. It also shows the angle-dependent kinematic cuts that were applied to select the events near the expected energies for the scattered electrons from these two channels, as given in Eq. 4.18 and Eq. 4.19. These cuts are usually symmetric around the expected energy such that

$$|E_{\rm rec} - E_{\rm exp}| < N\sigma_{\rm det}, \tag{4.24}$$

where $\sigma_{\rm det}$ is the detector energy resolution as shown in Table 4.1, N is usually between 3.0 to 4.5. However, due to the fact that the inelastic $e-p$ scattering events become noticeable in the large Q^2 region and the energy resolutions of Pb-glass detectors are not good enough to reject them from the elastic $e-p$ events, the

[3]Size of a $PbWO_4$ module is about 20.76 mm, and the size of a Pb-glass module is about 38.15 mm

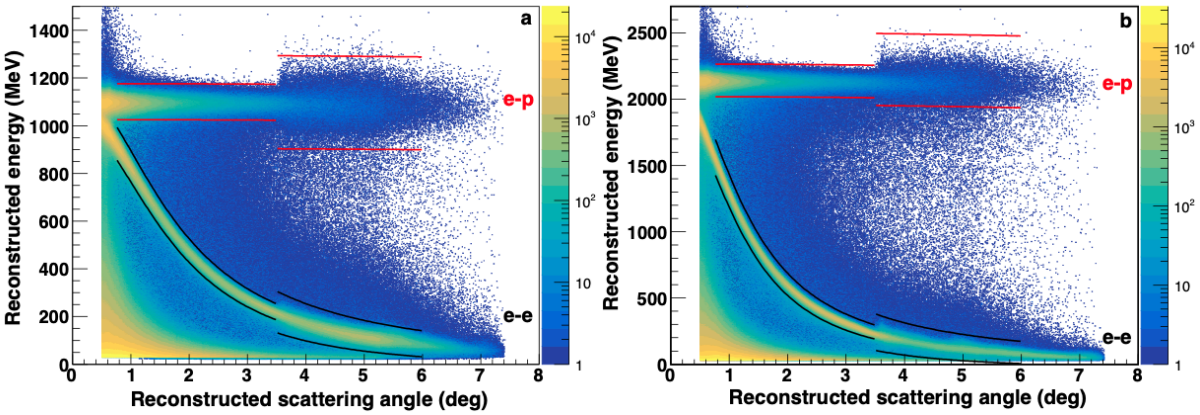

Figure 4.16: The reconstructed energy as a function of the reconstructed scattering angle for (**a**) 1.1 GeV and (**b**) 2.2 GeV data sets. The solid lines show the kinematic cuts for the elastic $e-p$ and $e-e$ event selections.

2.2 GeV $e-p$ kinematic cuts were chosen to be asymmetric for the Pb-glass detectors (from -2 to 4 σ_{det}) for most of their angular coverage. The cut is slightly wider (from -2.5 to 4 σ_{det}) for the last two angular bins (scattering angle $> 5.6°$) due to a worse energy calibration in the area. This will reduce the sensitivity of the results on the systematic uncertainties associated with the energy calibration, various modelings in the simulation for the HyCal response and so on.

The range of the scattering angle for an $e-p$ event is from $0.70°$ to $7.00°$ for the 2.2 GeV data set, limited by the HyCal angular acceptance. For the 1.1 GeV data set, the minimum scattering angle is $0.75°$ because below this angle, the elastic $e-p$ and $e-e$ peaks start to merge and the distance between the two peaks becomes less than 6σ of HyCal energy resolution (3σ kinematic cuts were used for the event selection for the 1.1 GeV data set). For the $e-e$ elastic scattering events, since the detector setup was able to detect both scattered electrons at the same time, it would be better to use the double-arm Møller events as they would have less contaminations from various backgrounds. The angular range for the 2.2 GeV Møller selection is from $0.70°$ to

2.00° and from 0.75° to 4.00° for the 1.1 GeV Møller[4]. The minimum scattering angles are limited by the same reason as for the $e-p$ events, while the maximum scattering angles for Møller are limited by the minimum ones as they are completely correlated.

In addition, for the double-arm Møller event selection, one could apply additional cuts, such as the co-planarity cut, which requires the azimuthal angle difference between the two scattered electrons to be about 180°

$$|\phi_{e1} - \phi_{e2} - \pi| < 10^{\circ}, \tag{4.25}$$

the elasticity cut, which means the total energy of the two scattered electrons must agree with the initial beam energy

$$|E_{\text{total}} - E_b - m| = |E_{e1} + E_{e2} - E_b - m| < N\sigma_{\text{det}}. \tag{4.26}$$

And lastly, one can apply a cut on the reconstructed vertex-z, calculated from Eq. 4.23, in order to ensure that the Møller event is coming from the target region.

In principle, if one requires both $e-e$ scattered electrons to be detected at the same time by the GEM detectors, the GEM efficiency needs to be $\varepsilon_{e-e} = \varepsilon_{e-e}(\theta_1) \times \varepsilon_{e-e}(\theta_2)$, where θ_1 and θ_2 are the scattering angles of the two $e-e$ electrons. In this way, the GEM efficiency for $e-e$ would be inevitably different from the GEM efficiency for $e-p$, which only depends on the scattering angle of one electron. And there will be no cancellation for the GEM efficiency regardless how one forms the $e-p$ to $e-e$ ratio. This difficulty can be overcome by using a combinatory Møller selection method. First of all, one uses only HyCal and apply the above mentioned Møller selection cuts to select the double arm Møller events. And then after matching

[4]Most of the double-arm Møllers are inside the $PbWO_4$ detector region.

Beam energy	Category	Cut
1.1 GeV	Kinematic cut in $PbWO_4$	$-3.0 \cdot \sigma_{\rm det} < E_{\rm rec} - E_{\rm exp} < 3.0 \cdot \sigma_{\rm det}$
	Kinematic cut in Pb-glass	$-3.0 \cdot \sigma_{\rm det} < E_{\rm rec} - E_{\rm exp} < 3.0 \cdot \sigma_{\rm det}$
	Angular cut	$0.75^\circ < \theta_{\rm rec} < 7.00^\circ$
2.2 GeV	Kinematic cut in $PbWO_4$	$-3.5 \cdot \sigma_{\rm det} < E_{\rm rec} - E_{\rm exp} < 3.5 \cdot \sigma_{\rm det}$
	Kinematic cut I in Pb-glass	$-2.0 \cdot \sigma_{\rm det} < E_{\rm rec} - E_{\rm exp} < 4.0 \cdot \sigma_{\rm det}$
	Kinematic cut II in Pb-glass	$-2.5 \cdot \sigma_{\rm det} < E_{\rm rec} - E_{\rm exp} < 4.0 \cdot \sigma_{\rm det}$
	Angular cut	$0.70^\circ < \theta_{\rm rec} < 7.00^\circ$

Table 4.3: Selection cuts for $e-p$ elastic scattering events. $E_{\rm rec}$ is the reconstructed energy by HyCal, $E_{\rm exp}$ is the expected energy at a given angle based on elastic $e-p$ kinematics, $\sigma_{\rm det}$ is the energy resolution of a HyCal module (see Table 4.1) and $\theta_{\rm rec}$ is the reconstructed scattering angle. In the case of 2.2 GeV beam setting, kinematic cut II in Pb-glass is used if the scattering angle is larger than 5.6° in order to reduce the sensitivity of the result on the size of this cut. Otherwise, kinematic cut I is used.

with the GEM detectors, one only uses the electron that has a matching hit on GEMs (two if both are matched), and do not requires that both $e-e$ electrons have matching hits at the same time. In this way, the GEM efficiency correction factor for the Møller counts in an angular bin θ is still $\varepsilon_{e-e}(\theta)$, which is similar to that for the $e-p$ events. This method is still superior in suppressing various backgrounds from the beam-line, and the energy-independent part of the GEM efficiency can still be cancelled if one takes the ratio between $e-p$ and $e-e$ counts from the same angular bin. However, the efficiency and acceptance effects from HyCal will not be cancelled, and one has to make a corresponding correction based on the simulation. In addition, when applying the co-planarity and vertex-z cuts, one has to use the HyCal reconstructed coordinates. These co-planarity and vertex-z distributions from the data and the simulation are shown in Fig. 4.17. The event selection cuts are summarized in Table 4.3 and Tabel 4.4, for the $e-p$ and $e-e$ events, respectively. The GEM matching cuts and the dead module removal cuts are not listed in the tables as they are universal regardless of the reaction channels.

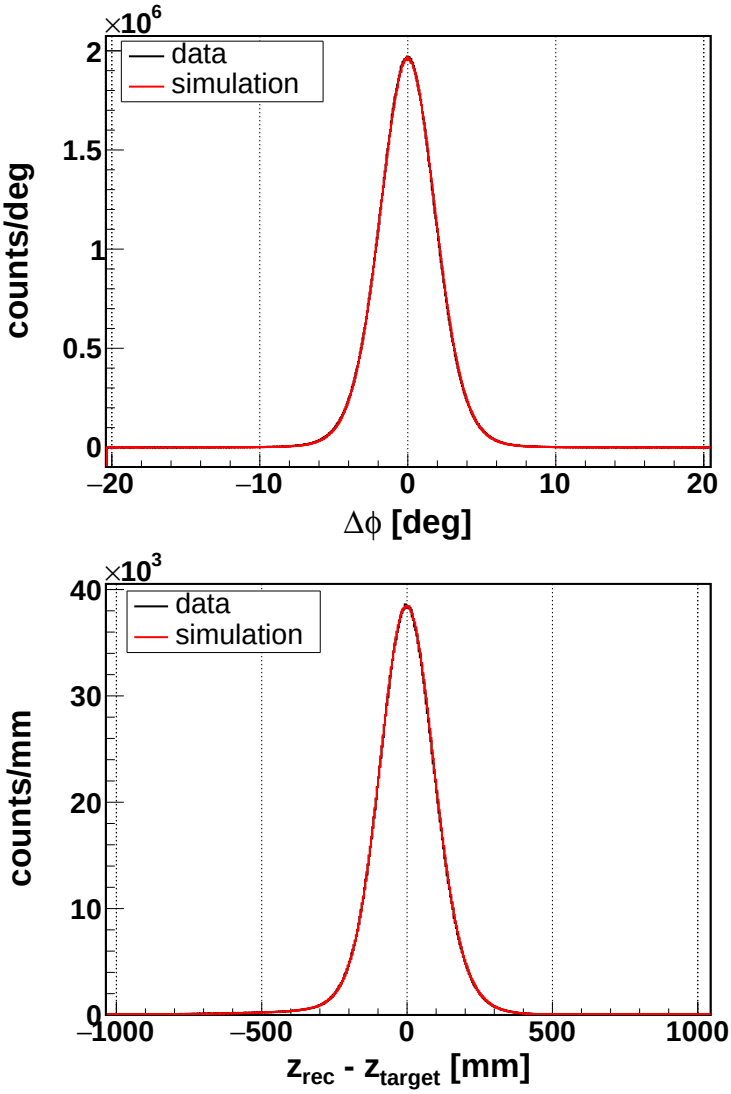

Figure 4.17: Top plot: the co-planarity distributions for the 2.2 GeV data and simulation. Bottom plot: the difference between the reconstructed vertex z and the distance between the target center and the HyCal for the 2.2 GeV data and simulation. The distributions were obtained using the HyCal reconstructed coordinates.

Beam energy	Category	Cut
1.1 GeV	Kinematic cut in $PbWO_4$	$-3.0 \cdot \sigma_{\rm det} < E_{\rm rec} - E_{\rm exp} < 3.0 \cdot \sigma_{\rm det}$
	Kinematic cut in Pb-glass	$-3.0 \cdot \sigma_{\rm det} < E_{\rm rec} - E_{\rm exp} < 3.0 \cdot \sigma_{\rm det}$
	Angular cut	$0.75^\circ < \theta_{\rm rec} < 4.00^\circ$
	Elasticity cut	$\lvert E_{\rm total} - E_b \rvert < 3.0 \cdot \sigma_{\rm det}$
	Co-planarity cut	$\lvert \phi_{e1} - \phi_{e2} - \pi \rvert < 10^\circ$
	vertex-z cut	$\lvert z_{\rm rec} - z_{\rm target} \rvert < 500$ mm
2.2 GeV	Kinematic cut in $PbWO_4$	$-4.5 \cdot \sigma_{\rm det} < E_{\rm rec} - E_{\rm exp} < 4.5 \cdot \sigma_{\rm det}$
	Kinematic cut in Pb-glass	$-4.5 \cdot \sigma_{\rm det} < E_{\rm rec} - E_{\rm exp} < 4.5 \cdot \sigma_{\rm det}$
	Angular cut	$0.70^\circ < \theta_{\rm rec} < 2.00^\circ$
	Elasticity cut	$\lvert E_{\rm total} - E_b \rvert < 4.5 \cdot \sigma_{\rm det}$
	Co-planarity cut	$\lvert \phi_{e1} - \phi_{e2} - \pi \rvert < 10^\circ$
	vertex-z cut	$\lvert z_{\rm rec} - z_{\rm target} \rvert < 500$ mm

Table 4.4: Selection cuts for $e-e$ elastic scattering events. $E_{\rm rec}$ is the reconstructed energy by HyCal, $E_{\rm exp}$ is the expected energy at an given angle based on elastic $e-p$ kinematics, $\sigma_{\rm det}$ is the energy resolution of a HyCal module (see Table 4.1), $\theta_{\rm rec}$ is the reconstructed scattering angle, ϕ_{e1} and ϕ_{e2} are the reconstructed azimuthal angles of the two scattered electrons, $z_{\rm rec}$ is the reconstructed vertex-z and $z_{\rm target}$ is the distance between the target center and the detectors.

4.5 Background Subtraction

Not all the events that satisfy the event selection cuts are coming from the reactions of interest. Some of them may come from the interaction of the electron beam halo with other objects near the beam-line, such as the upstream beam halo blocker and the target cell windows, the electron beam interaction with the background H_2 gas outside the target cell, etc. While such backgrounds can be subtracted using the empty target runs, some other backgrounds cannot be treated this way. These include the backgrounds from the inelastic $e-p$ scattering channels, multiple scatterings of the small angle $e-p$ and $e-e$ events from downstream objects around the beam-line, and also the photon induced hits on the GEMs through processes like pair production and small angle Compton scattering. In the following sub-sections, the details about subtracting these backgrounds will be discussed.

4.5.1 Background from Beam-Line

To subtract the backgrounds in this category, an empty target run was taken every few hours during the production data taking of the experiment. These empty target runs ((b) in Fig 4.18) had all experimental conditions the same as for the full target runs ((a) in Fig. 4.18), except that the H_2 gas was filled through a second inlet, directly into the target chamber instead of the cell, in order to mimic the background gas distribution far away from the target when the data taking was for the full target. They also included contributions from the backgrounds that were generated from objects near the beam-line, such as the upstream beam halo blocker and the target cell window foils. The $e-p$ and $e-e$ counts from these runs were first normalized by the total live charge (Eq. 3.5), and then subtracted from the corresponding counts from the full target runs, before forming the $e-p$ to $e-e$ ratio. (c) and (d) in Fig. 4.18 were used to study the background contribution from some individual sources. For instance, after normalization by the live charges, one can subtract (c) from (b) in order to obtain backgrounds generated from the background H_2 gas, and one can study the backgrounds generated from the target cell windows by subtracting (d) from (c). The backgrounds from (d) were mainly generated by the beam halo hitting the upstream beam halo blocker.

The ratios between the $e-p$ and $e-e$ counts from the background runs ((b), (c) and (d) in Fig. 4.18) and those from the full target runs are shown in Fig. 4.19, for the 2.2 GeV $e-p$ and $e-e$ events. For the 2.2 GeV $e-p$ events, the background rate is high at nearly 10% of the full target rate in the forward angular region ($< 1.1^\circ$) due to the backgrounds generated from the upstream beam halo blocker, otherwise the background ratio is around or below 2%. For $e-e$, the ratio is much lower in general, due to the coincidence measurement of the two scattered electrons. For both cases,

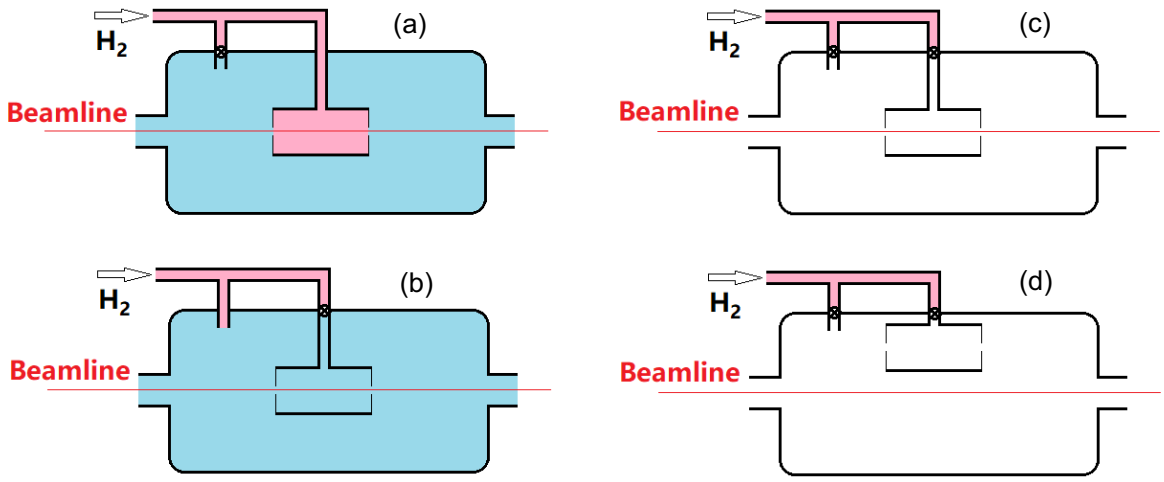

Figure 4.18: Main target configurations during the PRad data taking. In (**a**) full target runs, H_2 gas was filled directly into the target cell, as marked by the pink area. Blue area stands for low pressure background H_2 gas from the orifices of the cell. (**b**) is for the empty target runs, H_2 gas was filled directly into the chamber though a second inlet to mimic background H_2 gas far away from the cell. These runs were used for the beam line background subtraction of the full target runs. No H_2 gas filled to the target system at all for (**c**) and (**d**), as marked by the white area. They were used to study background contributions from individual sources.

the background contribution from the background H_2 gas is below 1% (on average 0.7% for the $e-p$ and 0.6% for the $e-e$). For the 1.1 GeV data, these background contributions are generally higher due to worse beam conditions (larger beam halo for instance). The backgrounds from the empty target runs account for nearly 30% of the $e-p$ events at angles $< 1.1^\circ$ and reduces to less than 10% elsewhere, and about 2% for $e-e$ events as shown in Fig. 4.20. For the 1.1 GeV $e-p$ events, the forward angular background is also dominated by those generated from the beam halo hitting the upstream beam halo blocker. The slight decrease of the background ratio at extreme forward angles is because the elastic $e-p$ rate increases faster than this background as we go to smaller angles. As indicated by the harp scans, it is most likely that the beam halo for the 1.1 GeV data set is larger and more unstable compared to that for the 2.2 GeV. Another possible evidence can be observed from the the double-arm Møller background rates. For the $e-e$ events, the selection cuts can completely reject the background generated from the upstream beam halo blocker, so that the Møller is only sensitive to the backgrounds generated around the target region, such as from the beam halo hitting the target cell and the main beam interacting with the background H_2 gas. One can see this by looking at the rate from type (d) of the background runs, which is negligible. The background generated from the target cell can be studied by type (c) of the background runs[5]. For the 1.1 GeV $e-e$, this is the dominant background while for the 2.2 GeV $e-e$, this background rate is rather small compared to the total rate. On the other hand, the rates from the background H_2 gas between these two energy settings are at a similar level. Thus, the beam halo is most likely larger for the 1.1 GeV setting.

The background subtracted and normalized $e-p$ to $e-e$ ratios as a function

[5]This is only for the $e-e$ events, for the $e-p$ events background run type (c) also include the contribution from the upstream beam halo blocker.

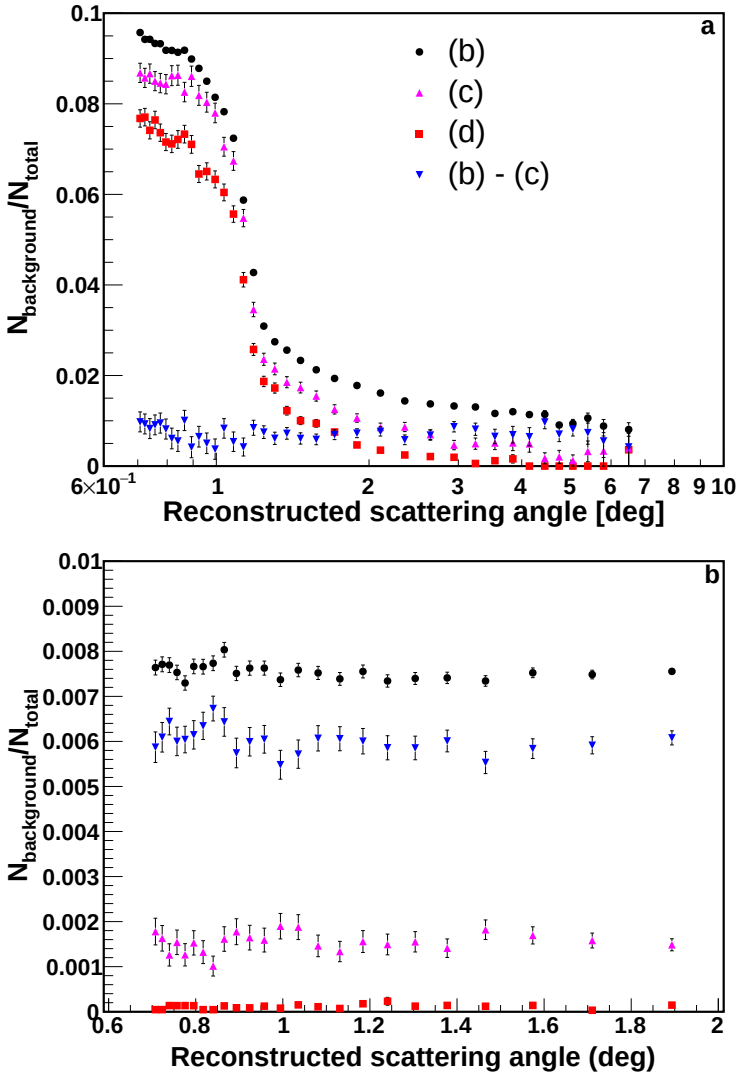

Figure 4.19: The counts from the runs with target configuration (b), (c) (d) in Fig. 4.18 over that from the full target runs. Plot (**a**) shows the ratios for 2.2 GeV $e-p$ events, Plot (**b**) is for 2.2 GeV $e-e$ events.

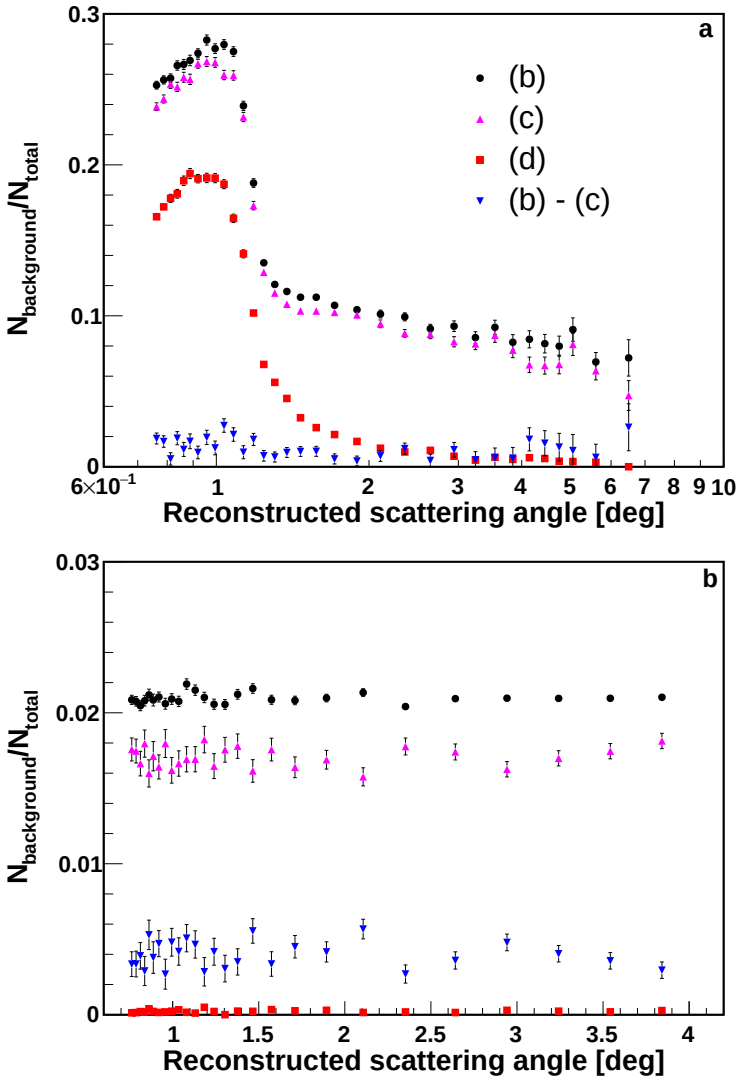

Figure 4.20: The counts from the runs with target configuration (b), (c) (d) in Fig. 4.18 over that from the full target runs. Plot (**a**) shows the ratios for 1.1 GeV $e-p$ events, Plot (**b**) is for 1.1 GeV $e-e$ events.

of the run number (about 1 hour for each run) are shown in Fig. 4.21, covering the scattering angles from 1.3° to 3.5° for the 1.1 GeV data set and from 0.9° to 2.0° for the 2.2 GeV data set. The data points are normalized by the weighted averages from all the data points, so that they are fluctuating around unity. They are reasonably stable over a long period of time. Also different beam currents were used during the data taking for each beam energy setting, in order to study possible rate-dependent systematic uncertainties. The weighted averages from runs with the same beam current are reasonably consistent with each other statistically. For the 1.1 GeV, the weighted average from the 10 nA runs is $1.0021 \pm 0.0012_{\text{stat.}}$, and that from the 15 nA runs is $0.9995 \pm 0.0006_{\text{stat.}}$. For 2.2 GeV, the weighted averages for the 25 nA, 40 nA and 55 nA are $1.0001 \pm 0.0012_{\text{stat.}}$, $1.0001 \pm 0.0003_{\text{stat.}}$ and 0.9993 $\pm$ $0.0011_{\text{stat.}}$ respectively. There is no clear rate-dependent systematic uncertainty observed in the data. The only one that has a clear dependency on the rate is the pile-up effect, but its overall effect on the cross sections is much less than 0.1% even with the highest rate. This effect is included in the PRad simulation, and corrected for the cross section results.

4.5.2 Background from Inelastic $e-p$ channels

The second type of background comes from the inelastic $e-p$ channels, and it cannot be removed by performing the empty target run subtraction. One has to rely on certain models to estimate its contribution. It was found that the Christy 2018 empirical fit to the inelastic $e-p$ cross section [75] was able to produce a decent agreement between the data and simulation, for the position and amplitude of the Δ-resonance peak as shown in Fig. 4.22.

To evaluate the goodness of the agreement, a χ^2 is defined,

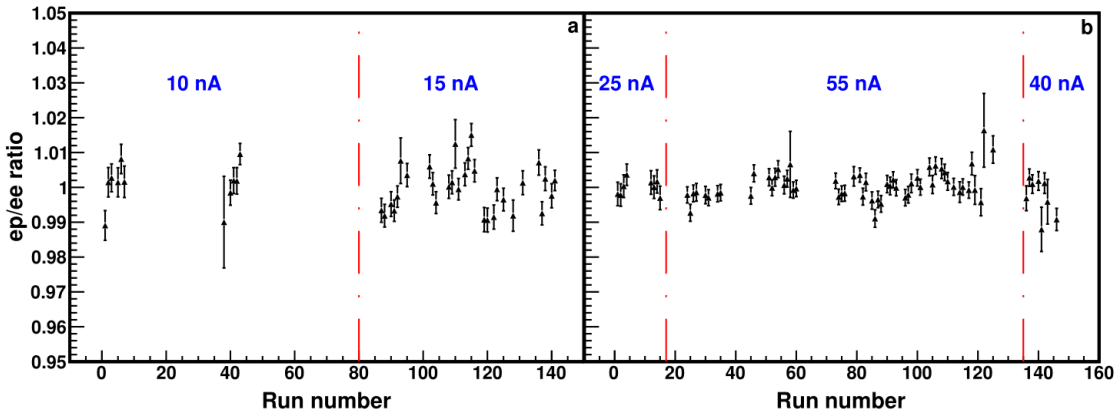

Figure 4.21: The normalized ratios between $e-p$ and $e-e$ counts after the background subtraction using the empty target runs, as a function of the run number. The left plot (**a**) shows the ratios from the 1.1 GeV data set. The right one (**b**) shows the same ratios from the 2.2 GeV data set. The data points are normalized by the weighted averages from all the data points in each data set, so that they are fluctuating around unity.

$$\chi^2 = \sum_{i=1} \frac{(N^i_{\rm data} - N^i_{\rm sim})^2}{(\sigma^i_{\rm data})^2 + (\sigma^i_{\rm sim})^2} \tag{4.27}$$

where the index i runs through all the energy bins in the range from around 1700 MeV to 1850 MeV, in which the Δ-resonance peak could be visible. $N^i_{\rm data}$ ($N^i_{\rm sim}$) is the counts in the i-th bin in the data (simulation), and $\sigma^i_{\rm data}$ and $\sigma^i_{\rm sim}$ are their corresponding statistical uncertainties, evaluated based on the Poisson statistics. The inelastic $e-p$ model is then scaled and stretched, by a scale and a stretch factor respectively, in the simulation. The inelastic $e-p$ cross section is multiplied by the scale factor so that it scales the amplitude of the Δ-resonance peak, and the energy of the scattered electron is multiplied by the stretch factor so that it shifts the position of the peak. One can then obtain many different values of χ^2 and search for the best agreement by requiring the minimum χ^2. The results for some angular bins are shown in Fig. 4.23. Typically, the minimum χ^2 is found very close to the

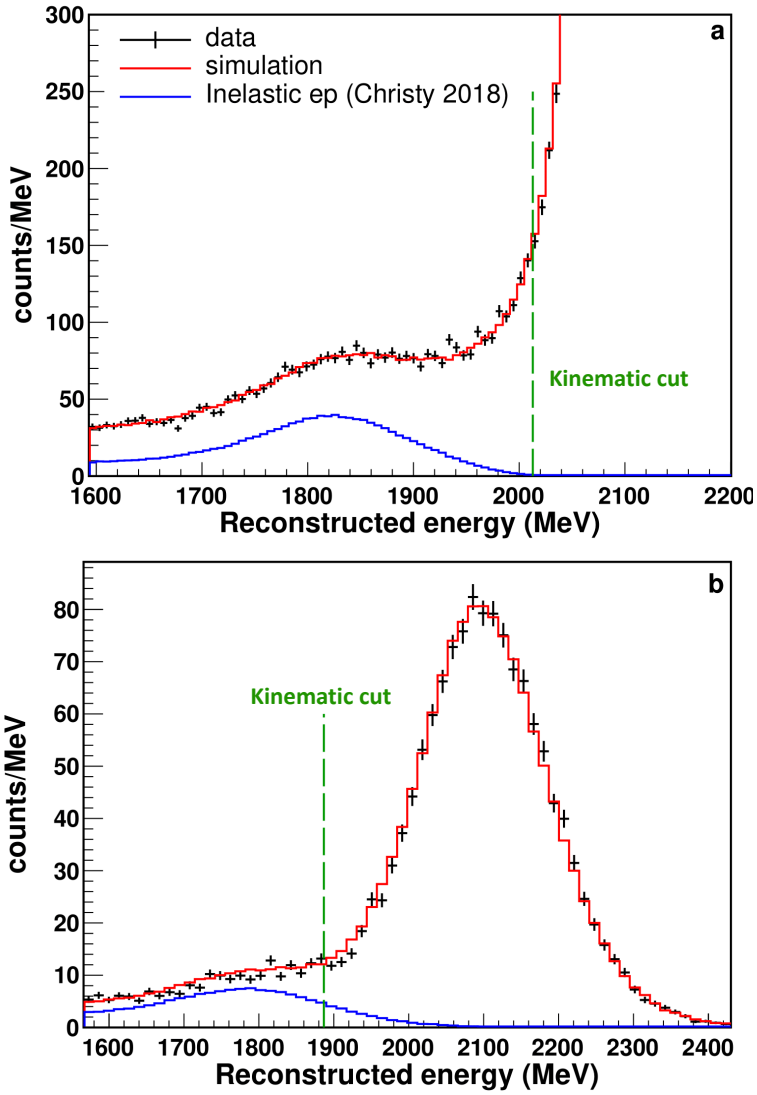

Figure 4.22: The comparison between the reconstructed energy spectrum from the 2.2 GeV data (black) and the simulation (red) for part of the $PbWO_4$ detector region (**a**) and Pb-glass detector region (**b**). (**a**) covers scattering angle from 3.0° to 3.3°, which corresponds to Q^2 around 0.014 $(GeV/c)^2$. (**b**) covers scattering angle from 6.0° to 7.0°, which corresponds to Q^2 around 0.059 $(GeV/c)^2$ (largest Q^2 for PRad). Blue histograms show the inelastic $e-p$ contribution from the simulation, using the Christy 2018 model. Due to a large difference in amplitudes, the elastic $e-p$ peak (amplitude 2800 counts/MeV) is not shown in (**a**), in order to display the Δ-resonance peak.

original Christy 2018 model (scale factor = 1 and stretch factor = 1), particularly for the $PbWO_4$ region where there is a clear separation between the Δ-resonance peak and the elastic $e-p$ peak (see (**a**) in Fig. 4.22). The scale factor is found typically from 0.9 to 1.1 for the minimum χ^2, and from 0.995 to 1.005 for the stretch factor. For Pb-glass region, the agreement can be slightly worse for certain angular bins, for example, the minimum χ^2 for scattering angles from 6.0° to 7.0° (shown in (**b**) of Fig. 4.22) appears when the stretch factor is 1.01 and the scale factor is 0.9. This is most likely due to the nonlinear properties of the Pb-glass modules, which may also shift the position of the Δ-resonance peak. One may disentangle these two effects by studying the spectrum agreement in the polar-angle overlapping region between the $PbWO_4$ detectors and the Pb-glass detectors, and the agreement was found to be better in the $PbWO_4$ detectors. However, this study cannot be applied reliably to the 1.1 GeV data set as the inelastic $e-p$ contribution is much smaller and the Δ-resonance peak is not clearly visible anywhere. It is assumed that for the 1.1 GeV data set, the scale factor and the stretch factor would also be in the range from 0.9 to 1.1, and 0.995 to 1.005, respectively.

With the Christy 2018 model, the inelastic $e-p$ contribution is estimated to be negligible in the $PbWO_4$ region. Due to the good energy resolution, the kinematic cut for $e-p$ event selection is sufficiently good to reject most of the inelastic $e-p$ events, as shown in Fig. 4.22. However, for Pb-glass detectors, the tail from the Δ-resonance peak starts to leak under the $e-p$ elastic peak, due to a worse detector resolution. The contribution is determined as no more than 2% and 0.2%, for the 2.2 GeV and 1.1 GeV data sets, respectively, and the contribution increases with larger Q^2.

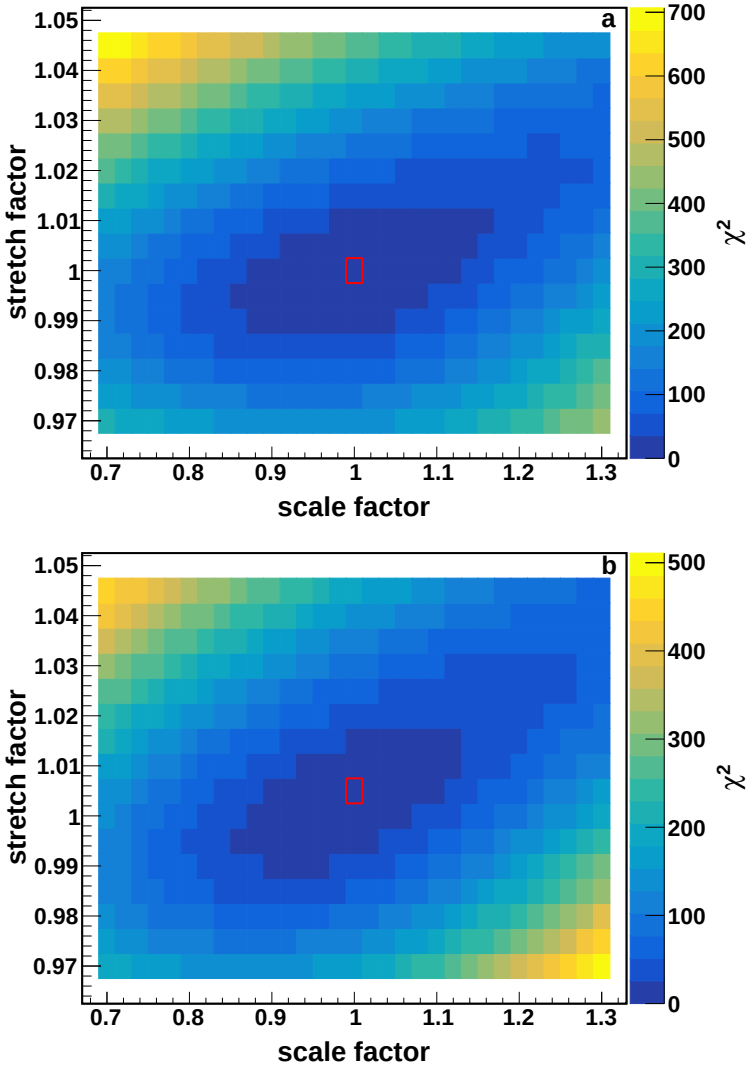

Figure 4.23: χ^2 from Eq. 4.27, as a function of scale factor and stretch factor for the 2.2 GeV beam energy setting. (**a**) is for the scattering angles from 3.0° to 3.3°, corresponding to Q^2 of 0.014 $(GeV/c)^2$, (**b**) is for the scattering angles from 4.0° to 4.3°, corresponding to Q^2 of 0.024 $(GeV/c)^2$. The red boxes mark the cell corresponding to the minimum χ^2. The minimum χ^2/ndf is about 0.67 for (**a**) and 1.11 for (**b**).

4.5.3 Background from photon induced GEM hits

The possible contamination due to the photon induced GEM hits was studied using the simulation. Such a contamination is highly suppressed because of the angular-dependent energy cuts used to select $e-p$ and $e-e$ events and the matching condition between the GEMs and HyCal (the GEM hits projected to the HyCal assuming they are coming from the target, must agree with HyCal hits within 6σ of the detector resolution). If the photons satisfy $e-p$ or $e-e$ kinematic cuts from HyCal, they have about 1.5% - 2% chance to produce matching GEM hits and contaminate the data, otherwise the chance is negligible. This number is dominated by the contributions from the 1.6 mm thick aluminum vacuum window, but also contains the contributions from other sources, such as the GEM frames, the GEM foils and the back-scattering of secondary particles from the HyCal. The number of photons relative to the electrons was estimated by varying the energy cut for the elastic peak ($1\sigma - 4\sigma$, where σ is the detector resolution) and noting the change in the GEM efficiency. The photon to electron ratio was estimated to be at the most 0.4% - 0.5% for most of the energy cuts. This experimental value of the photon to electron ratio agrees with the simulated value for the same energy cuts. The contamination is the product of the photon to electron ratio and the chance that the photon can produce a matching pair of hits in the GEM and HyCal. Thus, the upper bound of this contamination due to the photon induced GEM hits is about 0.01%.

4.5.4 Background from Multiple Scattering of Small Angle Events

The events with very small scattering angles, for instance $< 0.6^\circ$, have a probability to scatter into the angular range for the event selection, through multiple scatterings from objects near the downstream beam pipe or the beam pipe itself. The down-

stream beam pipe started near the exit of the vacuum chamber and went through the centers of the GEMs and HyCal. Other objects that could produce such a background included the vacuum window fringe, GEM frames, and the tungstate absorber that was placed immediately in front of the HyCal. The background generated from these objects could not be subtracted with the empty target run subtraction, since the majority of these very small angle scattering events came from the high density H_2 gas filled inside the target cell during the full target runs. Thus, one has to rely on the simulation to estimate this type of background. First of all, this type of background will primarily come from events with scattering angles between 0.2° and 0.6°. Those with scattering angles smaller than 0.2° will simply go through the central hole of the HyCal without producing anything. This is indicated by the simulation as well. And 0.6° corresponds to the corner of the HyCal tungstate absorber located immediately in front of HyCal. Second, the majority of this type of background can be rejected, once the matching cut between the GEMs and the HyCal is applied. If one assumes the track is coming from the target center, the projected GEM hit on the HyCal will be sufficiently far away from the HyCal reconstructed hit, so that the event cannot pass the matching cut. However, this type of background will affect the GEM efficiency measurement, in which one first selects events using only the HyCal and then looks for whether there is a matching hit on the GEMs. This background is significantly larger for the efficiency measured by the $e-p$ events, since for the $e-e$ events, the coincidence detection of both scattered electrons can largely suppress this background. The ratios between the background counts due to these events and total counts are shown in Fig. 4.24, in the angular range of the event selection. Once the GEM matching is required, this background is suppressed to be below 0.01% in general, which is negligible. However, if using only HyCal, this background can be significant, particularly for the 1.1 GeV $e-p$. This means that the GEM efficiency

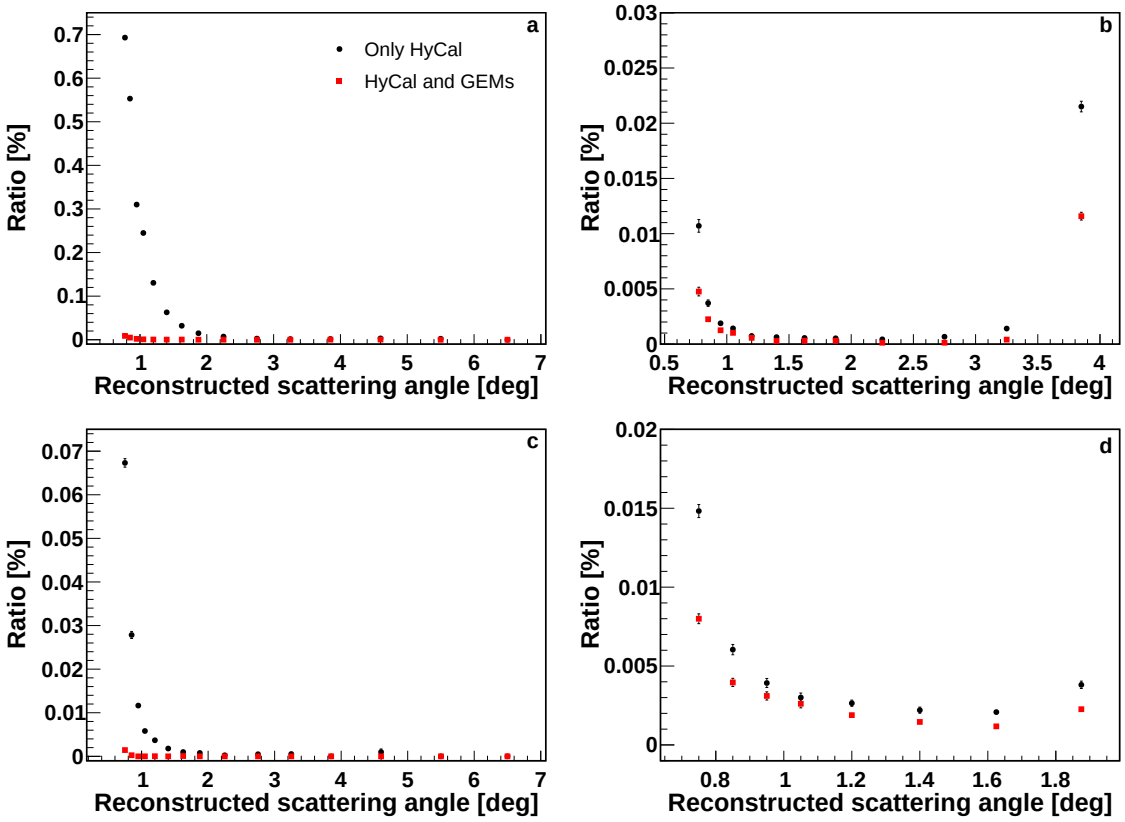

Figure 4.24: The ratio between background counts due to the events with scattering angles from 0.2° to 0.6° and the total counts using the PRad simulation, for (**a**): 1.1 GeV $e-p$, (**b**): 1.1 GeV $e-e$, (**c**): 2.2 GeV $e-p$ and (**d**): 2.2 GeV $e-e$. Black dots are obtained using only the HyCal. Red squares are obtained after requiring there is a matching hit on the GEMs.

measured using the $e-p$ events can be underestimated in the forward angular region. The inefficiency due to this background is corrected using the simulation and since it affects mostly scattering angles less than 1.3°, for which the bin-by-bin method is applied and the GEM efficiency is not needed, the systematic uncertainty for this correction is considered negligible for the results.

4.6 Efficiency of GEM

The GEM efficiency was determined using both the $e-p$ and $e-e$ events from the production runs. During this process, the events of interest were first identified using the HyCal reconstructed information alone and then one would search if there were matching GEM hits. If there were, then the GEMs were counted as efficient. All the event selection cuts for $e-p$ and $e-e$ were applied to this study, with much tighter cuts (1σ of the HyCal energy resolution) on the energy of the scattered electrons in order to reject high energy radiated photons, cosmic events and other backgrounds. A cluster profile cut was also applied, which put requirements on the size and shape of a cluster, in order to further reject the cosmic events. A background subtraction using the empty target runs was also performed for the efficiency calculation. In this case, the efficiency could be calculated as

$$\varepsilon_{\mathrm{GEM}} = \frac{N^{\mathrm{full}}_{\mathrm{GEM}} - C{\cdot}N^{\mathrm{emp}}_{\mathrm{GEM}}}{N^{\mathrm{full}}_{\mathrm{HyCal}} - C{\cdot}N^{\mathrm{emp}}_{\mathrm{HyCal}}}, \tag{4.28}$$

where N is the number of counts, the subscripts "GEM" and "HyCal" indicate which detector they come from, and the superscripts "full" and "emp" indicate that the counts are from the full target runs and the empty target runs, respectively. C is the live charge ratio between the full target and empty target runs. The statistical uncertainties were estimated using the Binomial statistics. Notice that the backgrounds generated from the electron beam should be scaled with the live charge while the cosmic backgrounds should be scaled with the total time (weighted by DAQ live time) of the data taking. Thus, the runs and periods with an unstable beam status were removed from this study so that C is also about the same as the total time ratio between the full target runs and the empty target runs, as shown in Fig. 4.25. The data point for the first sub-period of the 1.1 GeV data set ((**a**) of Fig. 4.25) had a

beam stability issue, which is the reason that its data point is far away from unity, and thus it was excluded in the entire analysis. Otherwise, the live charge ratios agree with the total time ratios mostly within 0.2%. This enables a subtraction of the cosmic backgrounds as well. The background subtracted GEM efficiencies for $e-p$ and $e-e$ events for various scattering angles are shown in Fig. 4.26. The efficiencies are very stable regardless of the size of the energy cut. In the case of the 1.1 GeV beam energy setting, the kinematic cut variation is limited to 3σ as the $e-p$ and $e-e$ events can not be well distinguished at very forward angles if a larger cut is used. Typically, the variation on the efficiency is smaller than 0.2% except for the efficiency in the very forward angular region measured by the 1.1 GeV $e-p$ events. This is expected due to the background generated from the very-small-angle-scattering events (see Section 4.5.4). Otherwise, the slight increase in the efficiency with narrower cuts can be explained by high energy radiative photons. In addition, a machine learning algorithm based on the auto-encoder [76] and the convolutional neural network [77] was developed by Duke Postdoc researcher Xuefei Yan, and trained using the cosmic runs taken during the PRad experiment in order to reject the cosmic backgrounds. The GEM efficiency results obtained after applying this cosmic rejection algorithm is consistent statistically with the efficiency results obtained after the background subtraction using the empty target runs, which demonstrates that the cosmic backgrounds were under control.

The background due to high energy radiative photons generated from the $e-p$ and $e-e$ bremsstrahlung processes was studied using the generators for $e-p$ and $e-e$ elastic scatterings. They included the exact calculations for the next-to-leading order Feynman diagrams and were capable of generating radiative photons up to nearly the energy of the incident electron beam. The effect is expected to be around 0.06% or less in the Pb-glass detector region, and <0.01% in the $PbWO_4$ region if

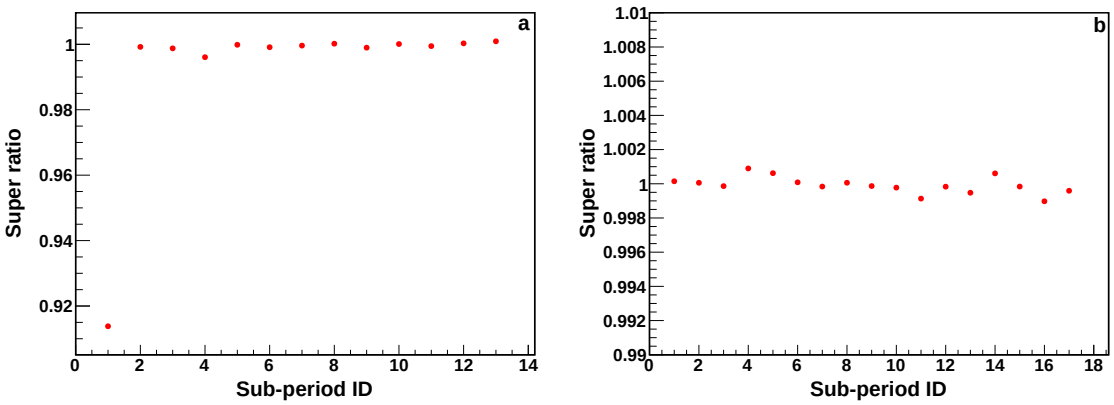

Figure 4.25: Super ratio of the live charge ratio, between the full target and the empty target runs, over the total time (weighted by ADC live time) ratio, between the full target and the empty target runs, as a function of the sub-period for the background subtraction. Left plot (**a**) for the 1.1 GeV data set, right plot (**b**) for the 2.2 GeV data set.

using a kinematic cut with 1σ of detector resolution, and around 0.26% or less in the Pb-glass detector region and around 0.08% in the $PbWO_4$ region if using a kinematic cut with 4σ of detector resolution.

The GEM efficiencies measured using the 1.1 GeV $e-p$ and $e-e$ events, and those from the 2.2 GeV data set are shown in Fig. 4.27. The GEM efficiencies measured by the $e-e$ events have smaller angular coverage than that for the $e-p$ events, as the double-arm Møller event selection was applied in the study, and it would limit the angular acceptance. These GEM efficiencies include the efficiency loss due to the GEM spacers and the gaps between the high voltage sectors. There are a number of reasons for the slight differences between the efficiencies measured using these two types of events. First of all, the matching cuts between the GEMs and HyCal are different for $e-p$ and $e-e$ events. The electrons from the Møller scattering have lower energies and thus are more sensitive to the multiple scattering effect and have worse HyCal position resolution. The matching cut for $e-e$ events is larger than that for the $e-p$ events. Second, for a particular angular bin, the efficiency losses due

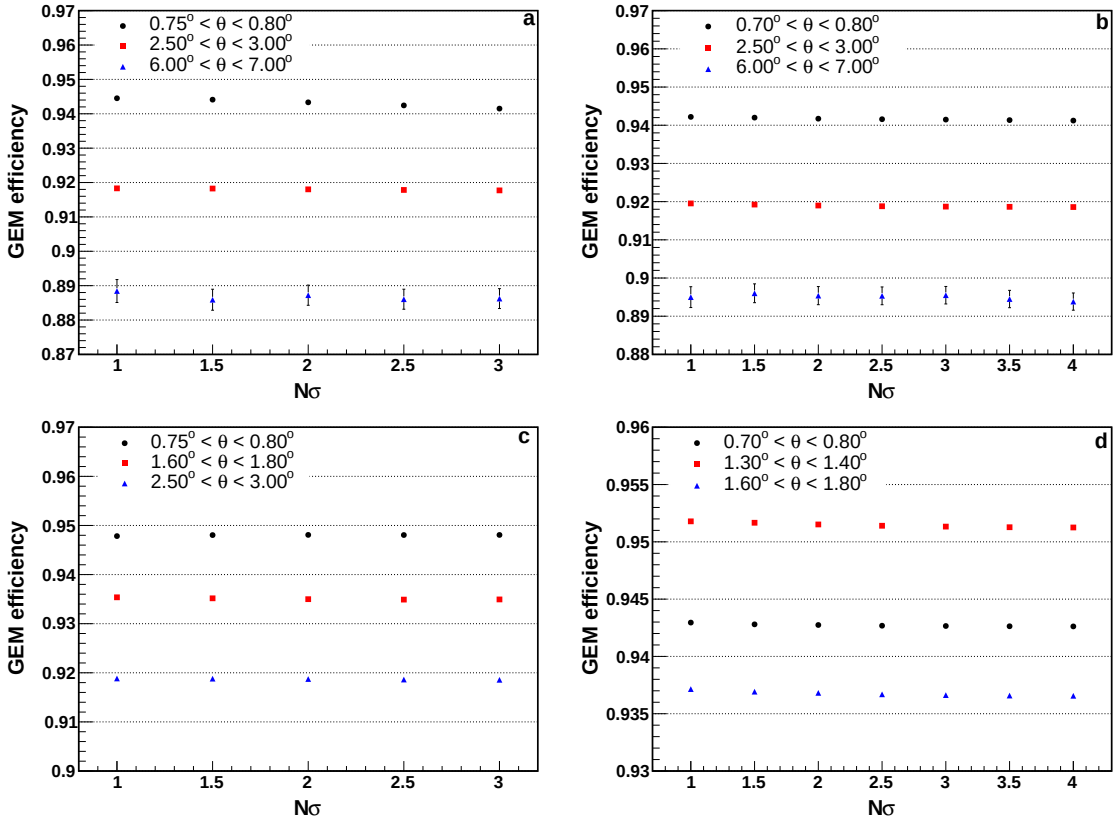

Figure 4.26: GEM efficiencies for 1.1 GeV $e-p$ (**a**), 2.2 GeV $e-p$ (**b**), 1.1 GeV $e-e$ (**c**), 2.2 GeV $e-e$ (**d**) for various scattering angles as indicated in the legends, as a function of the size of the kinematic cuts, which are measured in unit of the energy resolution of HyCal.

to the GEM spacers and the gaps between the high voltage sectors can be slightly different between the $e-p$ and $e-e$ events, as the angular distributions for these two types of events are very different. The $e-p$ events always focus more on the lower edge of an angular bin, while the $e-e$ events tend to go to the upper edge of a bin, particularly if the scattering angle is large. Thus, this effect is more dominant at the large angles, such as those larger than 1.5°, but this is expected and can be reproduced using the simulation. Third, the efficiencies measured by the $e-p$ events are typically smaller than that from the $e-e$ events in the forward angular region ($< 1.3°$), and it is more obvious in the case of the 1.1 GeV efficiencies. This is due to the background from the very-small-angle-scattering events (see Section 4.5.4). This background has a significantly impact on the efficiency measured by the 1.1 GeV $e-p$ events in the very forward angular region, and quickly becomes less than 0.1% when the scattering angle is larger than 1.3°. However, since the GEM efficiency in the forward angular region can be cancelled by using the bin-by-bin method, the effect due to this background is further minimized. This effect will be corrected using the simulation and since the overall effect is expected to be less than 0.1%, the systematic uncertainty for this correction was considered negligible. And lastly, the efficiencies measured by the $e-p$ and $e-e$ events may be affected differently by the HyCal finite resolution effect, which is in fact, one of the major systematic uncertainty sources for the GEM efficiency measurements.

The HyCal position resolution (see Table 4.1) is not good enough to resolve the spacers and the gaps between high voltage sectors, and also it is about the same size as the forward angular bins. It causes a significant bin migration problem, particularly for the very forward angular region[6]. One can study this effect using

[6]The multiple scattering can also cause a similar effect, but it is much smaller than the HyCal resolution effect.

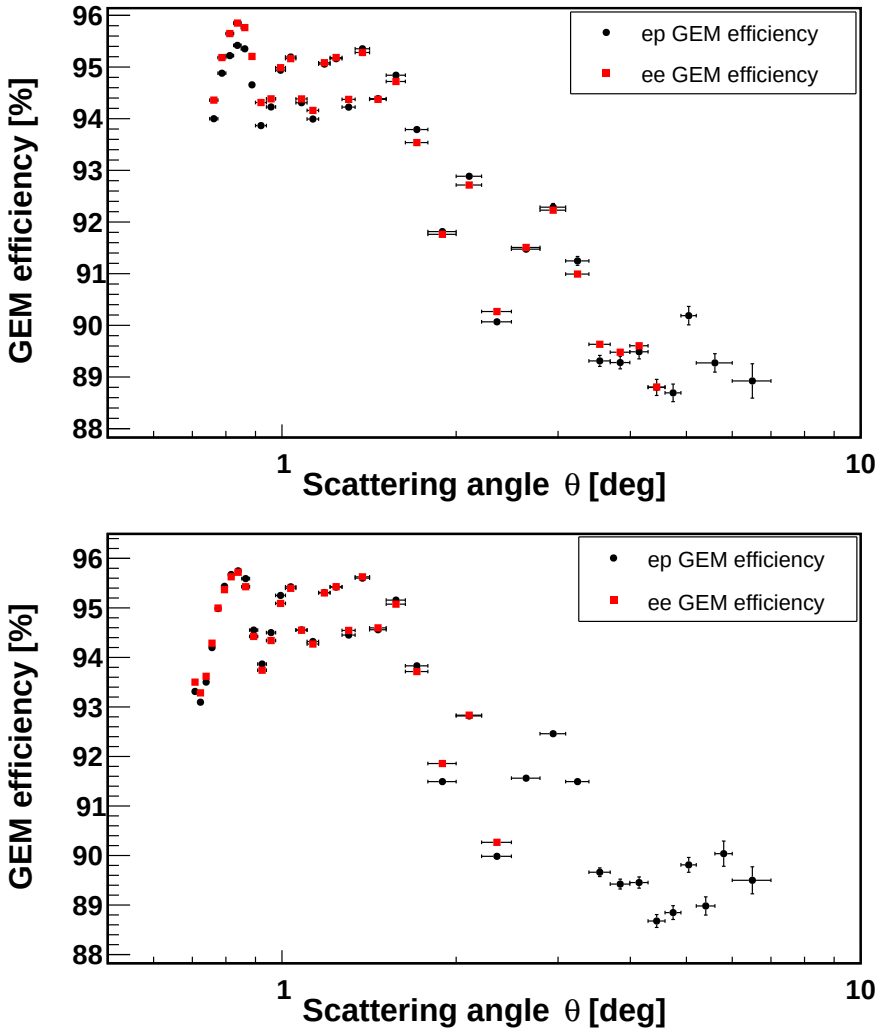

Figure 4.27: GEM efficiencies measured using (top) 1.1 GeV $e-p$ and $e-e$ events, and (bottom) 2.2 GeV $e-p$ and $e-e$ events, as a function of the scattering angle.

the simulation, by comparing results from the simulation that uses perfect GEM detectors and simulation that uses more realistic GEM detectors including all the dead areas. The GEM efficiency obtained from these two cases are shown in Fig. 4.28. The intrinsic efficiency (probability for the ionization, avalanche, and producing a detectable signal on the readout strips) is assumed to be 100% for this study. In the case with no GEM spacers and dead areas, the efficiency is nearly 100%. The small loss for the GEM efficiencies is mainly due to the finite matching radius used in the analysis (6σ of the HyCal position resolution) and can be removed if one uses larger ones. In the other case, the efficiency is highly non-uniform due to the GEM spacers and the gaps between the high voltage sectors, and the inefficiency can be as large as 6%. One can study the GEM efficiency corrected $e-p$ to $e-e$ ratio obtained from these two cases. If the GEM efficiency calculation and correction are accurate, one would expect the two ratios agree with each other. However, due to the systematic uncertainty related to the HyCal finite resolution, there can be certain deviations from unity, and the effect is particularly large in the forward angular region. As shown in (**a**) of Fig. 4.29, the deviation can be significantly larger than 0.2% at the very forward angular region ($< 1.3^{\circ}$) for the 2.2 GeV beam energy setting, with the maximum deviation slightly above 0.5%. This deviation is slightly larger for the 1.1 GeV setting (about 0.7% for the maximum deviation) as the HyCal position resolution is energy-dependent and it is better at a higher energy. To overcome this difficulty, one can apply the bin-by-bin method when forming the $e-p$ to $e-e$ ratio, that is, taking the $e-p$ counts and $e-e$ counts from the same angular bin. In this case, the energy-independent part of the GEM efficiency is cancelled. This is demonstrated in (**b**) of Fig. 4.29, where the forward angle data points ($< 1.6^{\circ}$) are obtained with the bin-by-bin method. The deviation for the bin-by-bin method is no more than 0.05% in this angular range. However, the bin-by-bin method cannot be

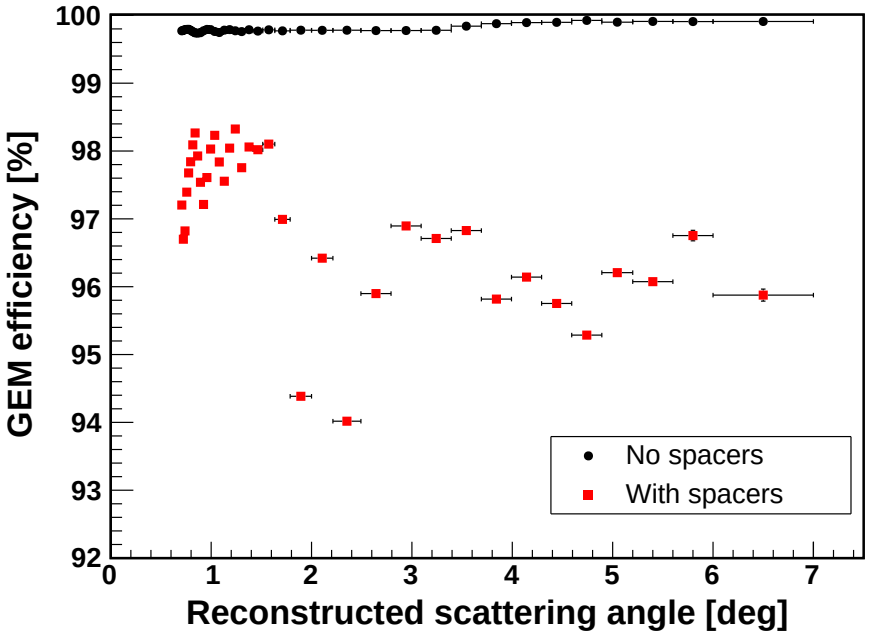

Figure 4.28: The GEM efficiencies obtained from the PRad simulation. The black dotted points are obtained with perfect GEM detectors with no spacers and no dead area. The red squares are obtained with more realistic GEM detectors that include the GEM spacers and the gaps between the high voltage sectors.

applied to the entire angular acceptance of HyCal if one requires the two electrons from the $e-e$ scattering to be detected at the same time. This is because for the $e-e$ scattering, if one electron goes to a large angle, the other one may hit the HyCal tungstate absorber or even pass HyCal through its central hole, so that there is only one electron detected. This limits the angular acceptance of the double-arm Møllers to be less than 4.0° for the 1.1 GeV beam setting and less than 2.0° for the 2.2 GeV beam setting, and the $e-p$ to $e-e$ ratio in larger angular range has to be obtained from the integrated Møller method, which requires a GEM efficiency correction. As shown in Fig. 4.29, the deviations for the $e-p$ to $e-e$ ratio obtained from the integrated Møller method at large angles are mostly within 0.2%, which is still acceptable.

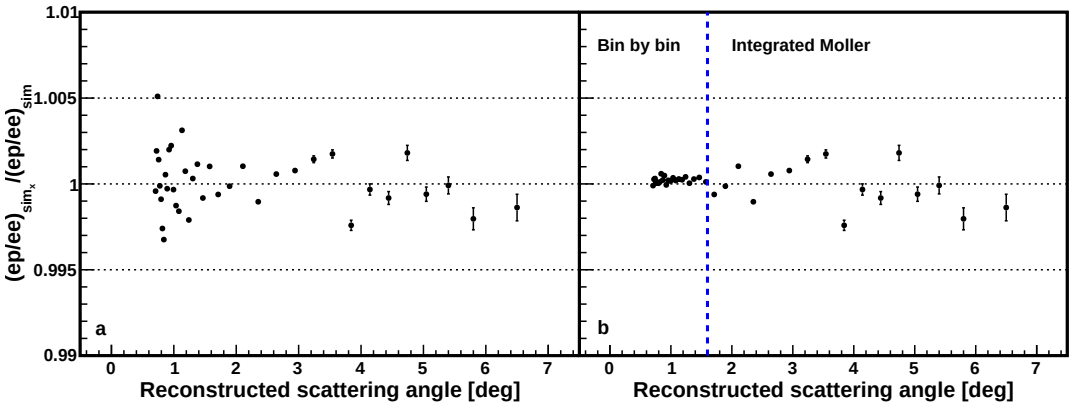

Figure 4.29: The GEM efficiency corrected $e-p$ to $e-e$ ratio from the simulation with more realistic GEM detectors that include all the dead areas, over the same ratio from the simulation with perfect GEM detectors. The results in (**a**) are obtained using the integrated Møller method. For (**b**), the results on the left hand side of the blue dash line are obtained with the bin-by-bin method, while the results on the right hand side remain the same as those shown in (**a**).

The GEM efficiency measured with the 2.2 GeV $e-p$ events, from the regions that are far away from the spacers, is shown in Fig. 4.30. The efficiency is rather uniform when the scattering angle is less than 3°, while it drops by 5% at larger angles. This drop was due to an issue with the front-end electronics. All the channels that were parallel to the $y-$axis, in the range -460 mm $<$ x $<$ -200 mm, were connected to the same Frontend Concentrator Card (FEC) during the experiment. They all suffered from this issue, which led to early saturations for the APV channels, and resulted in smaller ADC signals from the APV25s, compared to other channels. As a result, the GEM efficiency in this region was more sensitive to the pedestal cuts, and the efficiency was lower by nearly 10% compared to the efficiencies in other unaffected regions. This efficiency drop can be reproduced very well by the simulation. To further validate the GEM efficiency correction, the $e-p$ to $e-e$ ratios between the data and the simulation from different quadrants of the detecters are compared, and shown in Fig 4.31. Two different quadrant definitions were used in this study. In the

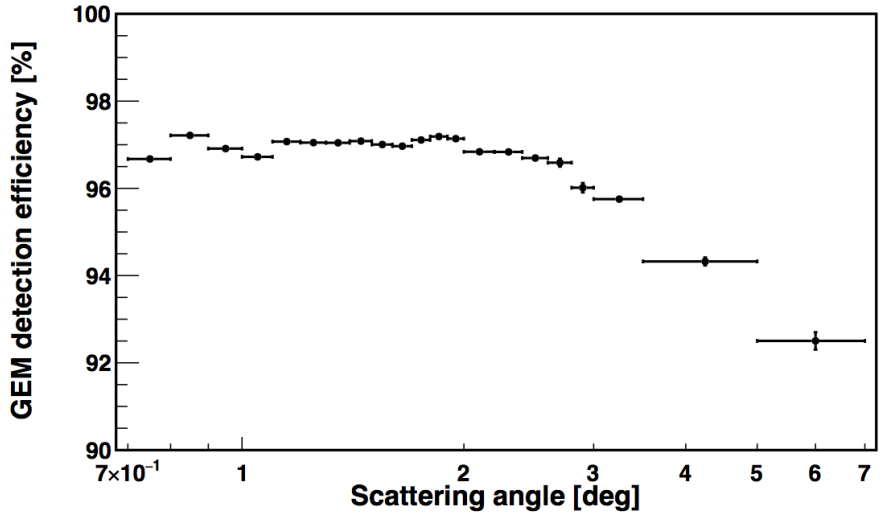

Figure 4.30: The GEM efficiency measured using 2.2 GeV $e-p$ events, from regions that have no GEM spacers. This figure is made by Xinzhan Bai of University of Virginia.

first case, the y-axis is vertical to the ground and the x-axis is to the right if one looks downstream towards the detectors. In the second case, the $x-y$ plane is rotate by 45° clockwise around the z-axis. The ratios, after the GEM efficiency correction, are consistent within their statistical uncertainties for all the angular bins. Lastly, one can study the extracted $e-p$ elastic scattering cross sections in the Q^2 overlapping region between the 1.1 GeV and 2.2 GeV data sets (more details in Section 4.9.3). This efficiency drop is the same for both 1.1 GeV and 2.2 GeV data sets. If this drop is artificial, it will cause the 1.1 GeV data point at the highest Q^2 (about 0.016 (GeV/c)^2) to shift by nearly 5%, while its statistical uncertainty is about 1%. On the other hand, for the 2.2 GeV data set, the data point at the same Q^2 will not be affected by the drop as the corresponding scattering angle is about 3.4°. This will cause a significantly discrepancy between the two data sets, which is not observed as their cross section data points are highly consistent statistically around this Q^2 value. To sum up, we are confident that this decrease of the GEM efficiency at large

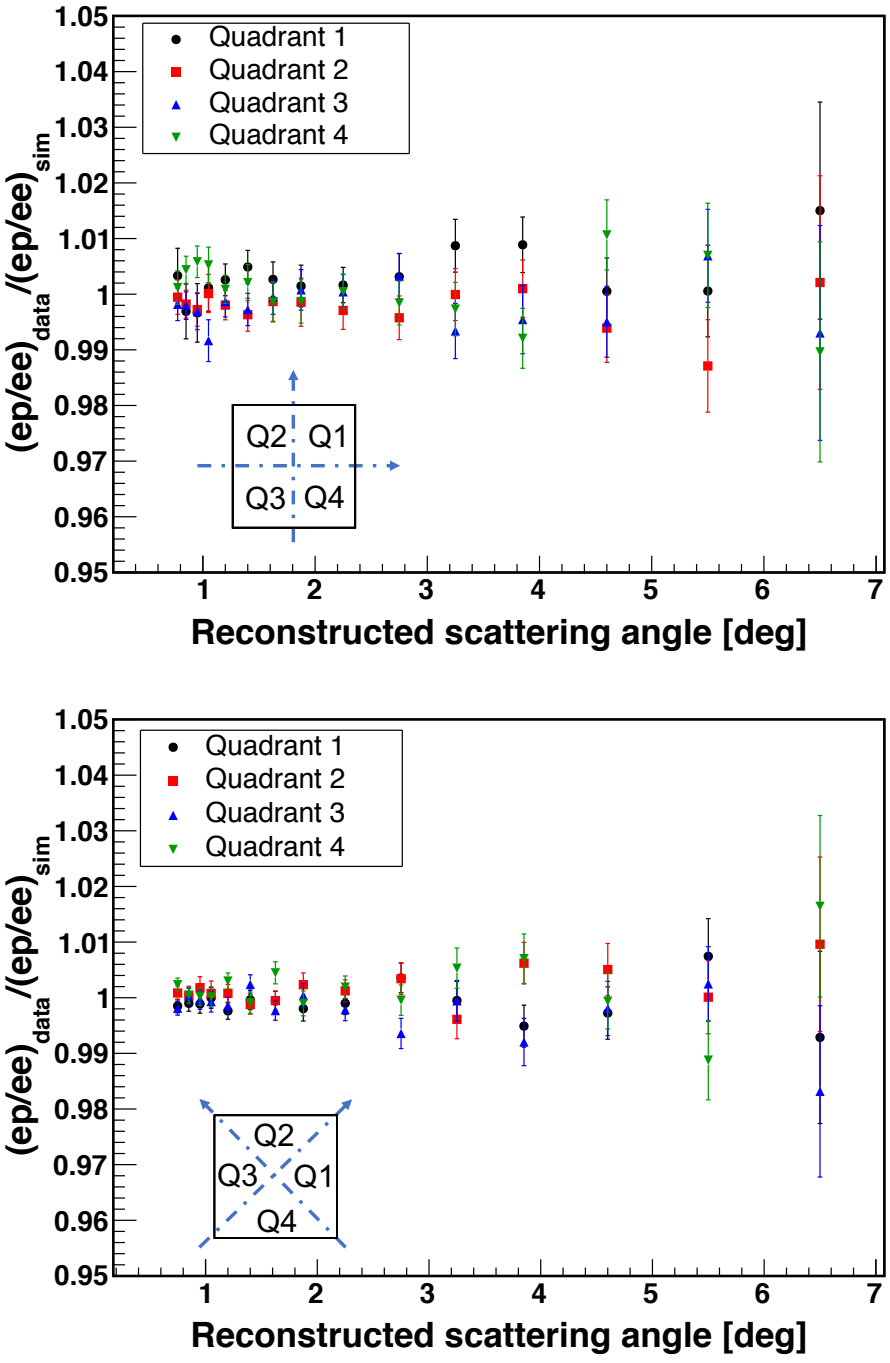

Figure 4.31: The $e-p$ to $e-e$ ratios between the data and the simulation from different quadrants, using the 1.1 GeV data (top) and the 2.2 GeV data (bottom). The areas included in the quadrants are indicated by the diagrams at the lower left corners. The black boxes represent the GEMs and HyCal if one looks downstream into the detectors.

angles was indeed due to the electronic issue and it can be corrected successfully by the GEM efficiency correction.

4.7 Simulation

As mentioned at the beginning of this chapter, the analysis of this experiment requires a comprehensive and realistic Monte Carlo simulation. This is necessary for the studies of the acceptance, radiative effects, bin center correction, various systematic uncertainties and so on. A simulation program was developed based on the Geant4 toolkit [78], which is capable of calculating possible radiative effects such as the energy loss and bremsstrahlung radiation, and multiple scatterings as particles pass through the external materials in the experimental setup. It will also generate possible secondary particles in the process. The program uses the geometric information determined from the position calibration for the GEMs and HyCal, and also the surveyed and blueprint information for other objects in the experimental setup. The simulation also includes an external package for the detector digitization, whose purpose is to turn the Geant4 simulation results into ADC values, like one would obtain directly from the experiment. During this process, one would also include various electronics effects like the pedestal noises and pile-up effects into the ADC values. The pedestal data used in the simulation were obtained from the experiment. They were taken at the beginning of each run and were triggered by the radioactive sources attached to the reference PMTs (see section 3.7), which were uncorrelated to the HyCal total sum trigger used for the physics events. These pedestal events were taken while the electron beam was on so that they could be used to measure the pile-up effects in the corresponding run.

For the internal radiative effects of $e-p$ and $e-e$ scatterings, two separate event

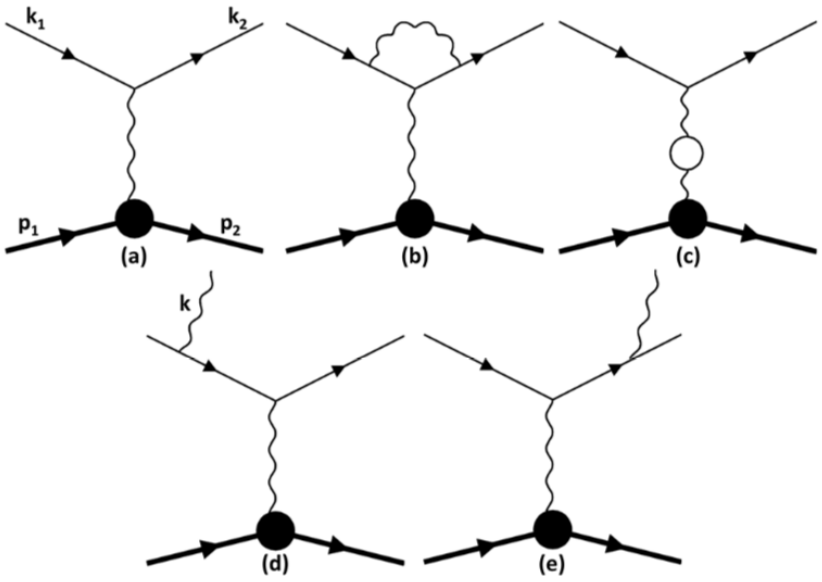

Figure 4.32: Feynman diagrams calculated in the generator for the $e-p$ elastic scattering, including (**a**) the Born level $e-p$ elastic scattering, (**b**) vertex correction, (**c**) vacuum polarization and (**d** and **e**) bremsstrahlung processes. The figure is obtained from [79].

generators [79] were built, which included the next-to-leading order contributions to the Born cross sections as shown in Fig 4.32 for the $e-p$ and Fig 4.33 for the $e-e$ elastic scatterings. The calculations for both $e-p$ and $e-e$ were completed without the usual ultra relativistic approximation (URA), where the mass of the electron is neglected. A second independent elastic $e-p$ event generator [31] was used as a cross check. The radiative corrections to the proton line, which were often neglected, were included in this generator. All the next-to-leading order diagrams included in this generator are shown in Fig. 4.34. However, the radiative corrections to the proton line is highly suppressed due to its heavy mass and it is negligible in the PRad kinematic range. The two $e-p$ generators were found to be in excellent agreement. The $e-p$ event generators also included the contribution from the two-photon exchange processes [80, 81, 82], which were estimated to be less than 0.2% of the $e-p$ elastic

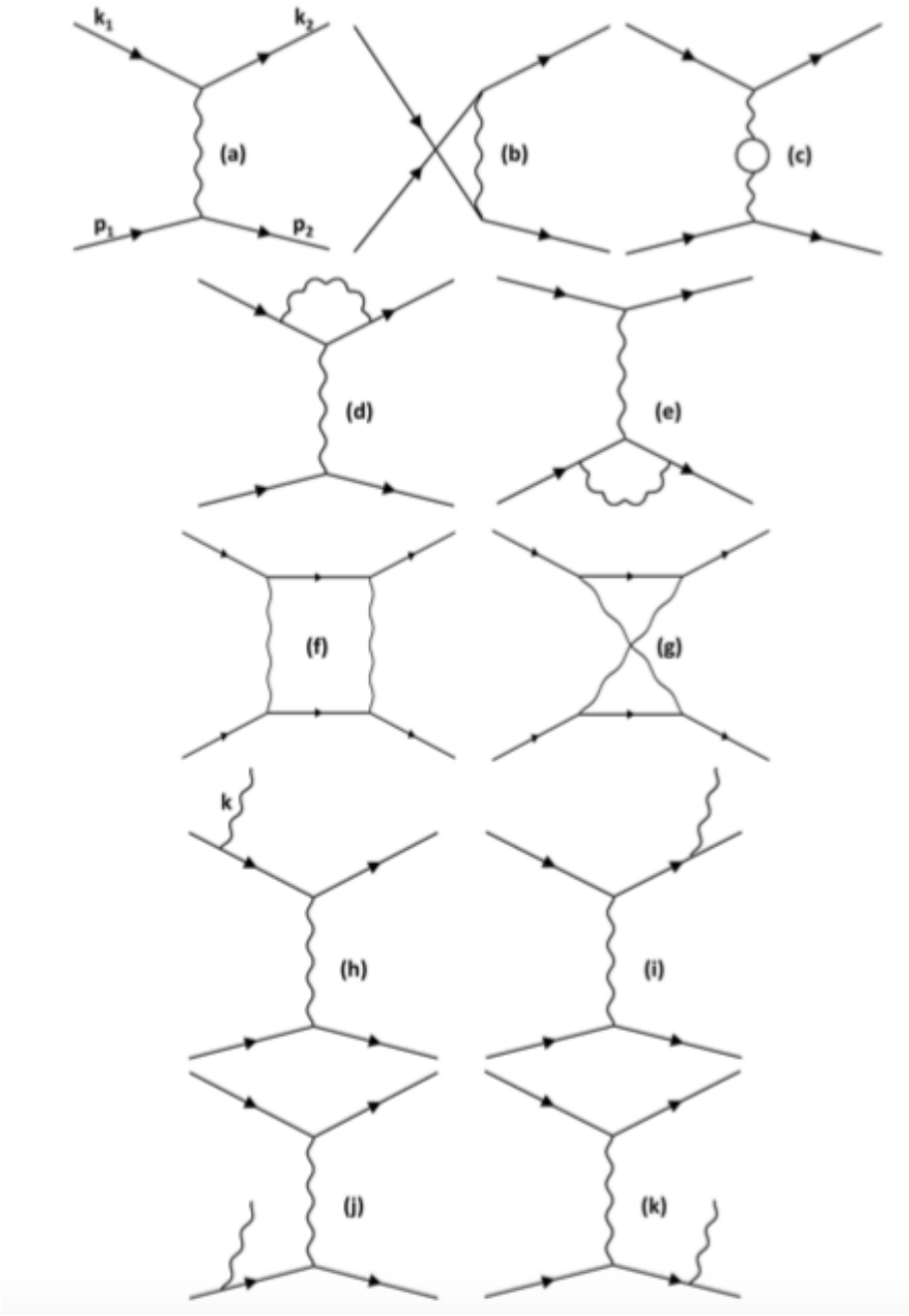

Figure 4.33: Feynman diagrams calculated in the generator for the $e - e$ elastic scattering, including (**a** and **b** for the t and u channels, respectively) the Born level $e-e$ elastic scattering, (**c**) vacuum polarization, (**d** and **e**) vertex correction, (**f** and **g**) two-photon exchange and (**h** to **k**) bremsstrahlung processes. The figure is obtained from [79].

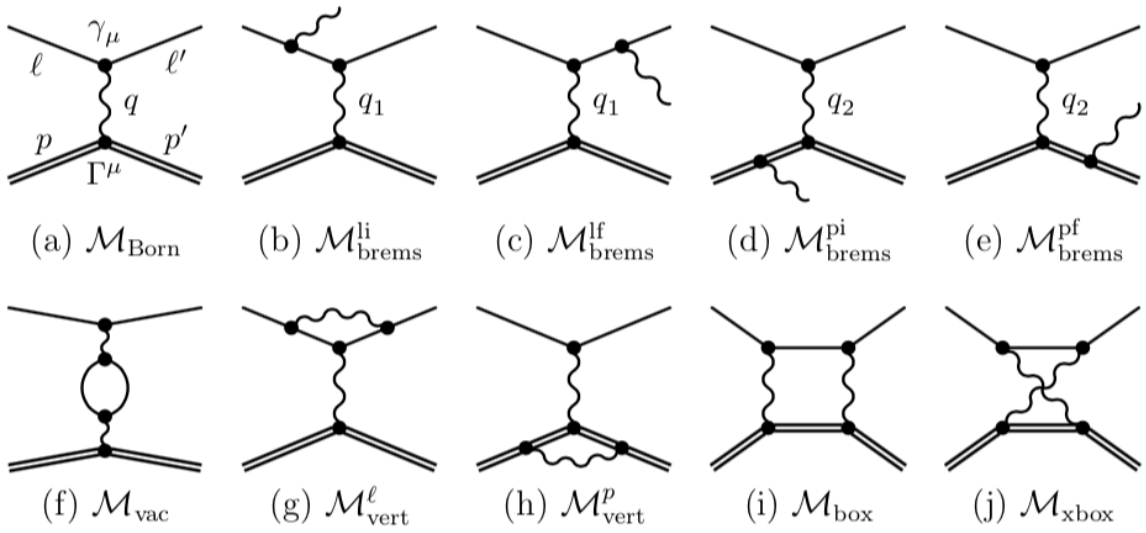

Figure 4.34: All the Feynman diagrams considered in Ref. [31], including (a) Born level $e-p$ elastics scattering, (b and c) bremsstrahlung radiations from the lepton line, (d and e) bremsstrahlung radiations from the proton line, (f) vacuum polarization, (g) the lepton and (h) proton vertex correction, and (i and j) box diagrams. The figure is obtained from Ref. [31].

scattering cross section in the PRad kinematic range. All the generators are able to generate hard radiated photons, beyond the peaking approximation[7] [83]. This is crucial for the calorimeter simulation, as the HyCal will integrate some of the radiated photons into the electron cluster, if they are close enough to each other when they hit the HyCal.

The inelastic $e-p$ scattering events were included in the simulation using an empirical fit [75] to the $e-p$ inelastic scattering world data. The inelastic $e-p$ scattering contributes as a background to the elastic $e-p$ events. And the simulation was able to reproduce the measured energy spectrum reasonably well (see section 4.5.2) once the inelastic $e-p$ scattering events were included.

After normalizing the integrated luminosities for the outputs of these generators, the generated particles are then propagated in the experimental setup using the

[7]In the peaking approximation, the radiated photon will be co-linear with the electron.

Geant4 simulation. Eventually, the results are digitized into the ADC counts in the readouts and reconstructed with the same event reconstruction algorithm as for the data. The simulated energy spectrum is highly similar to that from the data, as shown in Fig. 4.35.

In addition, as introduced in Section 3.3, a number of pressure gauges and temperature sensors were used during the experiment to monitor the gas pressure and temperatures at multiple locations across the entire target system. These measured temperature values, together with the inlet gas flow rate, pumping speeds of the vacuum pumps, and the detailed geometry of the target system were used to simulate the hydrogen density profile in the target using the COMSOL Multiphysics ® simulation package. The average pressure obtained from the simulation agreed with the measured values within 2 mTorr for both the target cell and the target chamber, under the PRad full target running conditions. The simulated gas density profile along the beam-line is shown in Fig. 4.36.

4.8 Angular Resolution and Q^2 Resolution

Using the PRad simulation package, the polar-angle resolution of the experimental setup can be extracted and it is shown in (**a**) of Fig. 4.37, for which the GEM detectors were used for the (two-dimensional) position reconstruction. This resolution is dominated by the multiple scatterings when electrons pass through external materials, in particular, the 1.6 mm thick aluminum vacuum window. The extended target effect also plays a role, but the effect is only significant when the polar angle is large. The polar-angle resolution is about 0.1 and 0.06 mrad at the very forward angle, for the 1.1 and 2.2 GeV energy settings, respectively, and increases to 0.27 and 0.24 mrad at the largest angle.

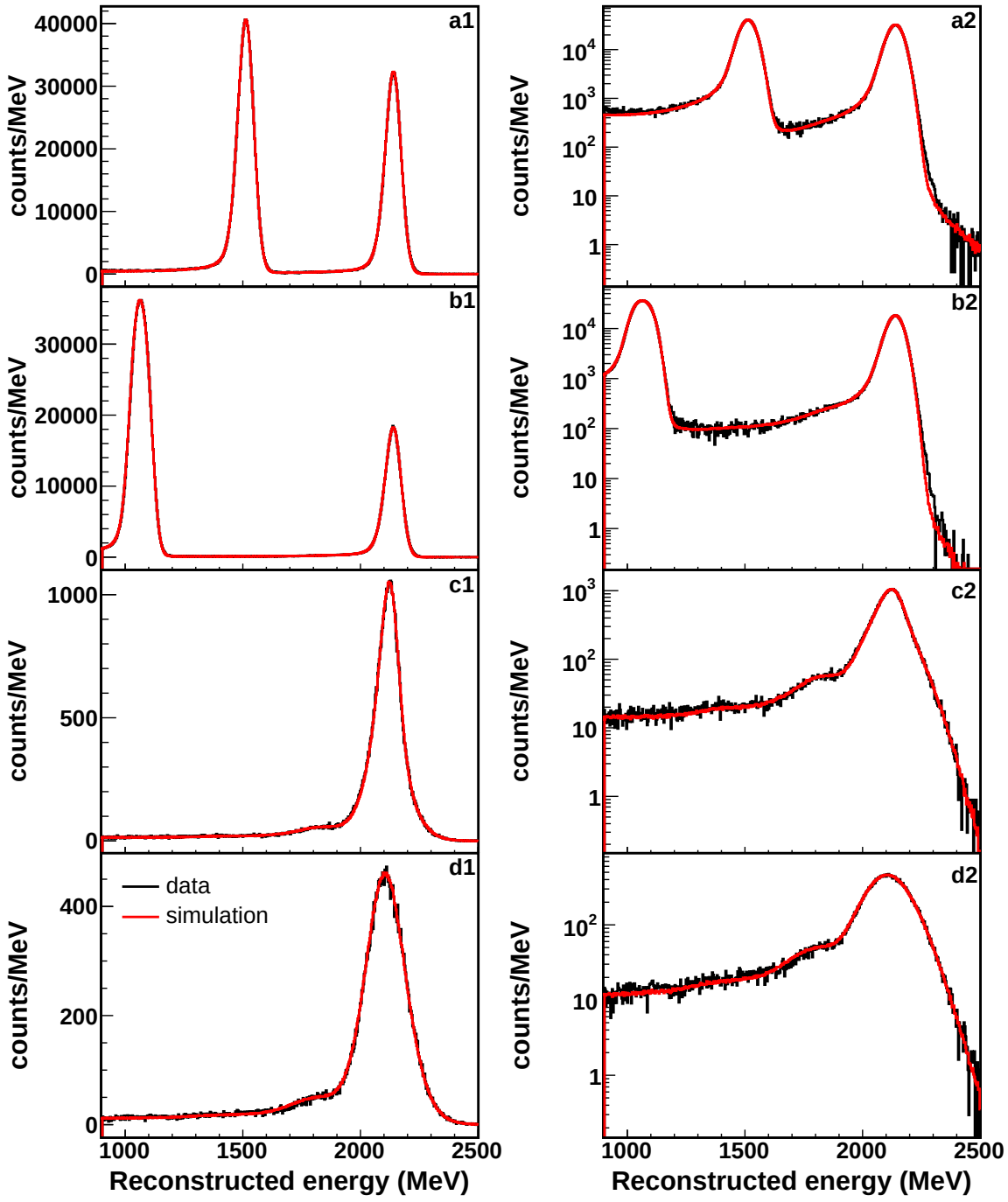

Figure 4.35: The reconstructed energy spectrum from the data and simulations for the 2.2 GeV beam energy setting. The data are shown as the black histograms and the simulations are shown as the red ones (as indicated in the legend in (**d1**)). Each row shows a spectrum with a different scattering angle, (**a1**): 0.78° to 0.82°, (**b1**): 1.20° to 1.30°, (**c1**): 3.80° to 4.20°, (**d1**): 5.00° to 6.00°. Plots in the right column are the same as those on the left, except the y-axes are in log scales.

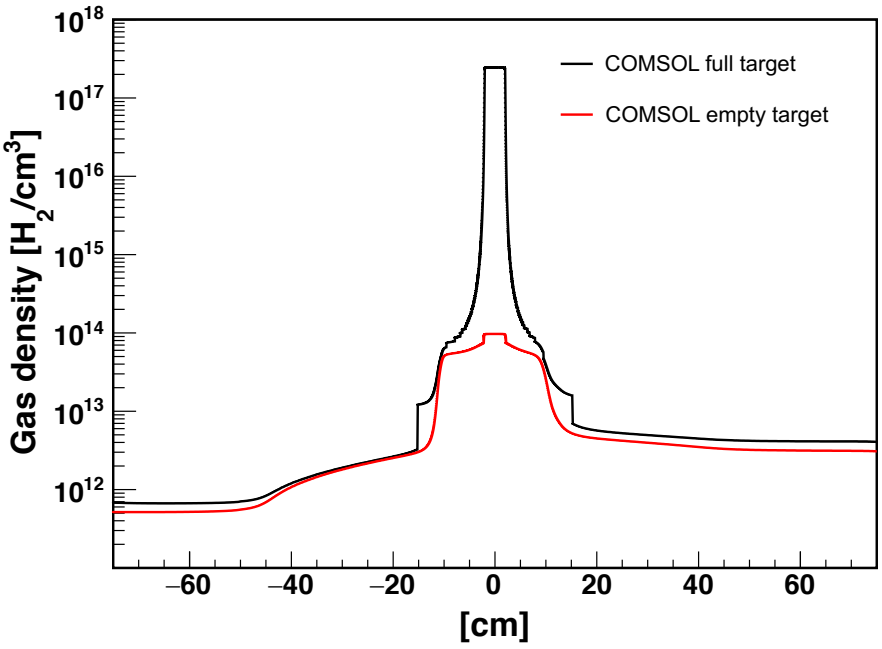

Figure 4.36: The simulated gas density profile along the beam line by COMSOL Multiphysics ® simulation package, for the full target run condition (black curve) and empty target run condition (red curve). The target center is placed at 0 cm in the plot.

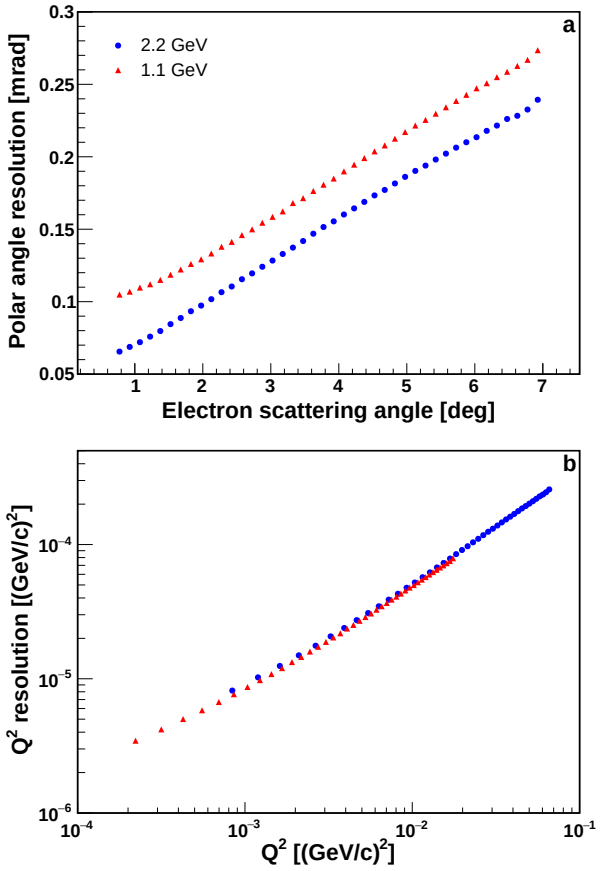

Figure 4.37: The polar-angle (**a**) and Q^2 (**b**) resolutions of the experimental setup, for the 1.1 and 2.2 GeV beam energy settings. They include the multiple scatterings due to detector materials, detector resolutions, and the extended target effect.

To determine Q^2, since the selected events are considered elastic (after subtracting the backgrounds), only the scattering angle is needed as the energy of a scattered electron is constrained by its scattering angle. Thus, only the resolution of the scattering angle and the energy of the incident electron beam will affect the resolution of Q^2. The electron beam energy delivered by CEBAF was measured with an uncertainty of 0.5 MeV and 1.5 MeV for the central values, for the 1.1 and 2.2 GeV beams, respectively. And the energy spread is at the level of 3×10^{-5}. The Q^2 resolution is shown as (**b**) in Fig. 4.37 and it is dominated by the polar-angle resolution.

4.9 Cross Section Extraction

4.9.1 $(e-p)$ /$(e-e)$ Ratio

The $e-p$ elastic scattering cross section is extracted based on Eq. 4.12 for the experiment. It states that after making the efficiency corrections in both the data and simulation, the $e-p$ elastic scattering cross section equals to the $(e-p)/(e-e)$ ratio from the data over the $(e-p)/(e-e)$ ratio from the simulation (super ratio), multiplied by the Born $e-p$ cross section used in the simulation.

Before obtaining the $(e-p)/(e-e)$ ratio from the data, one needs to subtract the $e-p$ and $e-e$ counts measured in the empty target runs from those in the full target runs, after normalization by the total live charges between these two types of runs. Due to possible fluctuations in the background rate, the entire data set was split into smaller sub-periods (10 for the 1.1 GeV data set, and 20 for the 2.2 GeV data set), with most of the sub-periods consisted of about 3 to 4 full target runs, and sandwiched by two empty target runs. For an angular bin at θ_i, the background subtracted $e-p$ and $e-e$ counts are

$$N_{ep}^{\mathrm{e,r}}(\theta_i) = \sum_j \left[(N_{ep}^{\mathrm{e,r}})_{\mathrm{full}}(\theta_i) - C_j \cdot (N_{ep}^{\mathrm{e,r}})_{\mathrm{emp}}(\theta_i) \right], \tag{4.29}$$

$$N_{ee}^{\mathrm{e,r}}(\theta_i) = \sum_j \left[(N_{ee}^{\mathrm{e,r}})_{\mathrm{full}}(\theta_i) - C_j \cdot (N_{ee}^{\mathrm{e,r}})_{\mathrm{emp}}(\theta_i) \right]. \tag{4.30}$$

The subscript "full" indicates that the counts are from the full target runs, and the subscript "emp" indicates that the counts are from empty target runs. C_j is the live charge ratio (see Eq. 3.5) between the full target runs and the empty target runs in the j-th sub-period, and the index j runs through all sub-periods for a beam energy setting. After this subtraction procedure, the $e-p$ to $e-e$ ratio can be obtained after

making the detector efficiency correction to the $e-p$ and $e-e$ counts separately. Other than taking the total sum of all the background subtracted counts from all the sub-periods, one can also obtain an $(e-p)/(e-e)$ ratio from each sub-period and obtain the final ratio by taking a weighted average using their statistical uncertainties. The two results differ by no more than 0.05% for all angular bins, which is negligible. For the inelastic $e-p$ contribution, one has the option to either subtract this in the data or add this in the simulation. The difference in the super ratio between these two approaches was much smaller than 0.05% for all angular bins.

For the simulation, one can obtain the $(e-p)/(e-e)$ ratio by using the $e-p$, $e-e$ and inelastic $e-p$ event generators and then transport the generated particles in the Geant4 simulation. The events from these generators must be normalized to the same integrated luminosity (the integrated luminosity of $e-e$ in this study) as they all share the same luminosity in the data. The exact same event selection cuts were applied to the simulation to obtain the $(e-p)/(e-e)$ ratio.

As mentioned at the beginning of the chapter, there are two methods to form the $e-p$ to $e-e$ ratio. The first method is the bin-by-bin method, for which one will form the ratio using the $e-p$ and $e-e$ counts from the same angular bin. This method has the ability to cancel out the energy-independent part of the GEM efficiency (see section 4.6). However, this method is limited to the angular range of the double-arm Møller acceptance, which is significantly smaller than that for the $e-p$, and it may also introduce angular-dependent systematic uncertainties from the $e-e$. The other method is the integrated Møller method, which uses the $e-e$ counts from a selected angular range and is applied as a common normalization factor for all angular bins of the $e-p$. It is applicable to all the angular bins in principle, but requires the GEM efficiency corrections whose systematic uncertainties could be significant especially in the forward angular region ($< 1.3^\circ$). However, the systematic

uncertainties from the $e-e$ can only affect the normalization of the data points, and will not affect the extracted r_p. Taking various considerations into account, the range for the bin-by-bin method is applied up to 3.0° and 1.6° for the 1.1 and 2.2 GeV data sets, respectively. And the data points in larger angular ranges are obtained from the integrated Møller method. The selected angular ranges for the $e-e$ integration are 1.3° to 3.0° for the 1.1 GeV data and 1.3° to 2.0° for the 2.2 GeV data. The major reason of choosing these ranges is that the GEM efficiency can be determined more precisely. One can also choose some other ranges, for example 0.7° to 1.0° or 1.0° to 1.3°, and the difference on the super ratio is about 0.05% compared to the default range. The $e-p$ to $e-e$ super ratios obtained with both the bin-by-bin and the integrated Møller method are very consistent in the range that they can be reliably compared, as shown in Fig. 4.38.

The azimuthal symmetry of the super ratio between the data $(e-p)/(e-e)$ and the simulated $(e-p)/(e-e)$ was studied by comparing the results obtained from each quadrant of the HyCal calorimeter. The super ratio from each quadrant was found to be consistent with each other within the statistical uncertainties, as shown in Fig. 4.31 in Section 4.6. The purpose of this comparison was not only to validate the GEM efficiency correction, but also to check the combined systematic effects such as, the beam position, tilting angles of both the beam and detectors, HyCal detector responses and geometric acceptances. Note that a number of these systematic effects, such as the beam position and tilting angles of both the beam and detectors, could be averaged out significantly when combing the data from all the quadrants. In addition, as various properties, including the triggers, are different between the two types of shower detectors of the HyCal, the consistency between the $PbWO_4$ and Pb-glass modules was also verified by comparing the super ratio with and without using the Pb-glass modules. The super ratio in the angular range where

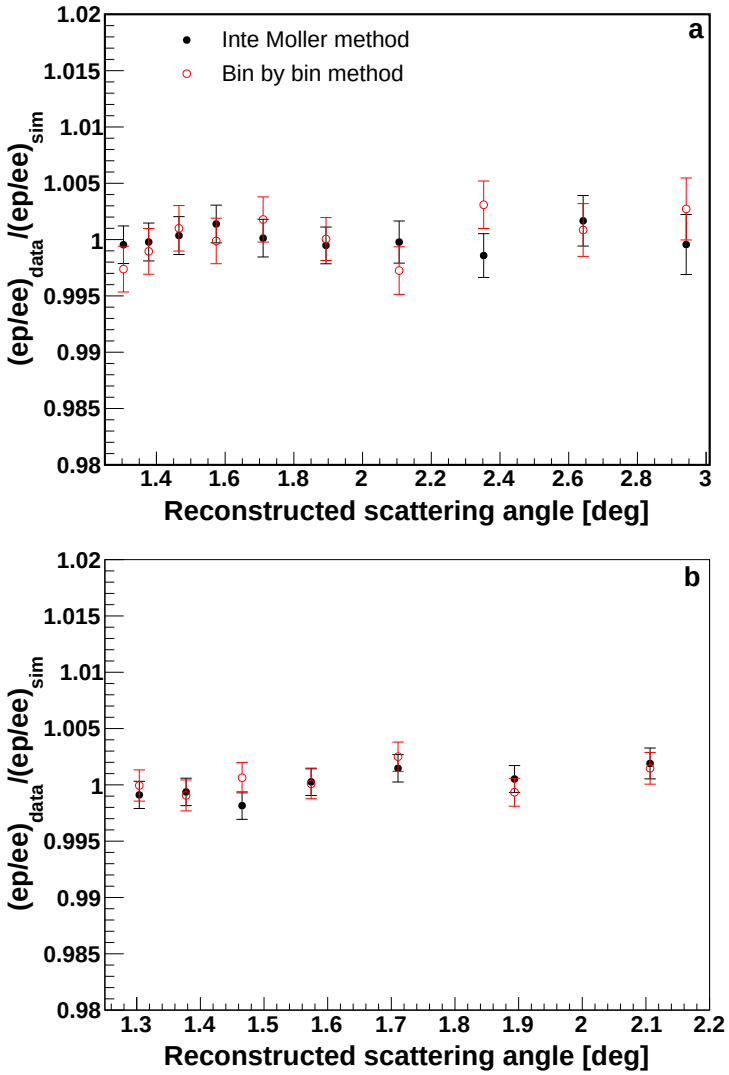

Figure 4.38: The super ratios ($e-p$ to $e-e$ ratios from the data over that from the simulation) obtained using the integrated Møller method (black solid dots) and the bin-by-bin method (red open circle). The 1.1 GeV data are shown in (**a**) and 2.2 GeV data are shown in (**b**).

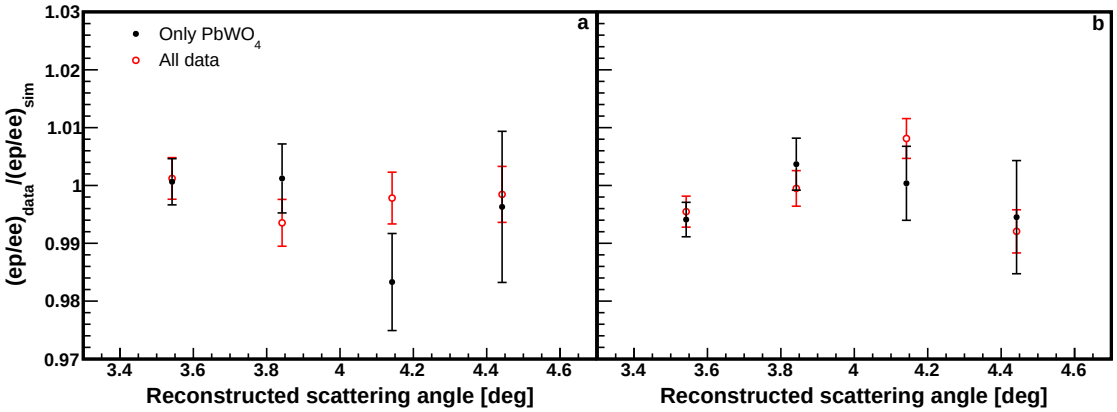

Figure 4.39: The super ratio obtained when using only the $PbWO_4$ modules and when using all modules for the angular region where the two types of modules have overlapping coverage. Plot (**a**) is for the 1.1 GeV and plot (**b**) for the 2.2 GeV electron beam energy settings.

the two types of modules have overlapping coverage is shown in Fig. 4.39.

4.9.2 Radiative Corrections

The radiative corrections for the $e-p$ elastic scattering cross section include the internal radiative corrections calculated by the $e-p$ and $e-e$ event generators [31, 79] and the radiative correction for effects due to particles passing through external materials, which is performed by the Geant4 simulation. There are four important parameters for the generators, including the minimum and maximum scattering angles ($\theta_\ell^{\min}$ and $\theta_\ell^{\max}$), the maximum allowed bremsstrahlung photon energy cut ($E_\gamma^{\max}$) and the soft photon energy cut ($E_\gamma^{\min}$). Based on the Feynman diagrams presented in Section. 4.7, the generators will generate all possible scattered electrons within the angular and energy ranges defined by these four parameters, and also their associated bremsstrahlung photons. In the ideal case if one wants to cover the full phase spaces within the experimental kinematic range, one would generate events in the entire 4π

solid angle and with all possible energies for the radiated photons. However, this is not practical computationally and the ranges for the generators have to be limited by these parameters. They have to be chosen carefully so that the effects due to neglecting events outside the ranges are negligible, and the results from the simulation are not sensitive to the choices for these parameters. The angular range for the generators is chosen to be from 0.5° to 8.5°, slightly larger than the angular acceptance of the experimental setup. Even though events outside this range may still bounce into the acceptance through multiple scatterings, this effect is rather negligible as shown by the simulation. First of all, the events with smaller scattering angles will be rejected by the matching condition between the GEMs and HyCal, as discussed in Section 4.5.4. For the $e-e$ events with larger scattering angles, their energies will be too small to satisfy the event selection cuts. And for the $e-p$ events, even though they may still have enough energy, the cross section is decreasing drastically with larger scattering angles. The purpose of the soft photon cut is to deal with the infrared divergent problem of the radiated photons with very low energies, and it is typically chosen to be much smaller than the energy resolution of the detector. For the analysis, $E_\gamma^{\min} = 1$ MeV is used for both beam energy settings and Fig. 4.40 (**a**) shows that in the case of the 1.1 GeV beam energy setting, the results with $E_\gamma^{\min} =$ 2 MeV, 5 MeV and 10 MeV are consistent statistically with the one obtained with $E_\gamma^{\min} = 1$ MeV. Similar results can be obtained from the 2.2 GeV simulation. For $E_\gamma^{\max}$, the difference in the simulation results becomes negligible once this cut is set to a large enough value, such as larger than 1000 MeV for the 1.1 GeV setting, and 1800 MeV for the 2.2 GeV setting. However, the results are sensitive to this parameter if it is set to be too low, as shown in Fig. 4.40 (**b**) for the 1.1 GeV setting, in which case the results are normalized to the one obtained with $E_\gamma^{\max} = 1100$ MeV. The reason is that the PRad detector setup cannot distinguish the electrons and pho-

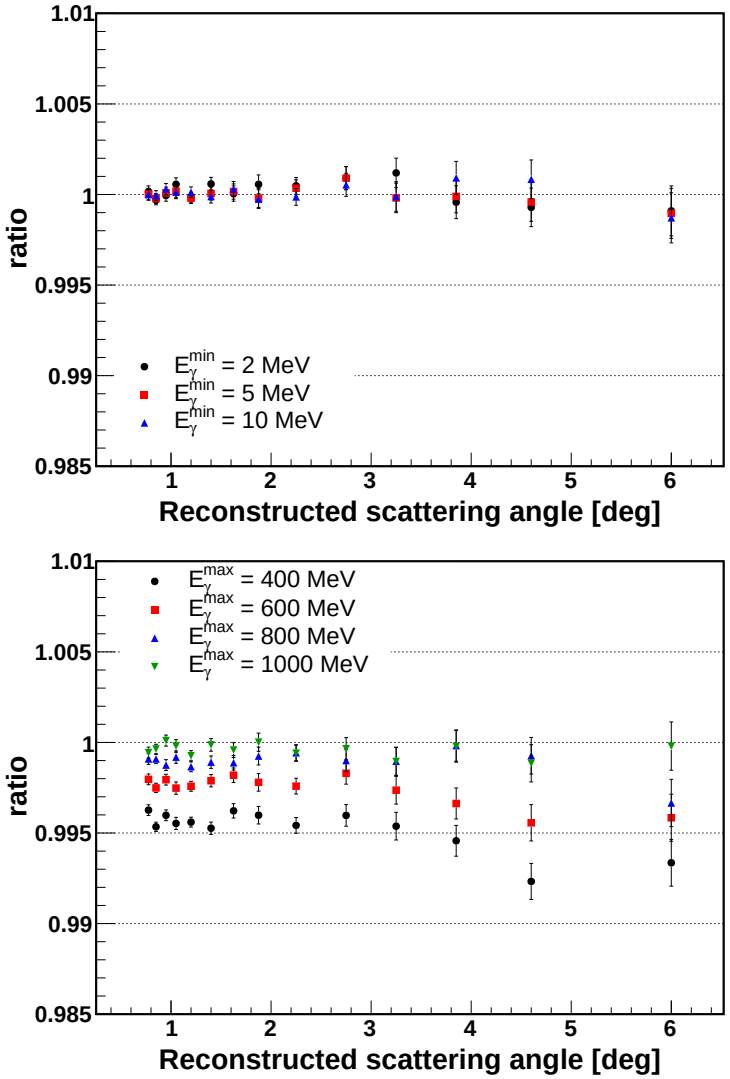

Figure 4.40: The elastic $e - p$ counts from the simulation, obtained with different $E_\gamma^{\min}$ (top) and $E_\gamma^{\max}$ (bottom) cuts, for the 1.1 GeV beam energy setting. The results in both plots are normalized to the case with $E_\gamma^{\min} = 1$ MeV and $E_\gamma^{\max} = 1100$ MeV. For the top plot, $E_\gamma^{\max}$ is fixed at 1100 MeV for all the cases while for the bottom one, $E_\gamma^{\min}$ is fixed at 1 MeV for all the cases.

tons if they are almost co-linear. In this case, they will produce only one cluster on the HyCal and also produce a hit on the GEMs that is able to satisfy the matching condition. This type of events mostly come from the bremsstrahlung radiation of the final state electrons, in which case the probability for the photon emission decreases drastically as the photon energy increases. Thus, once this cut is large enough, the results start to saturate. In addition, this cut mostly affects the normalization of the results, so that the systematic uncertainty on r_p is expected to be negligible once a large cut is applied in the generators.

The radiative correction was applied using an iterative procedure, which would replace the electric form factor used in the $e-p$ event generator by the one extracted from the data so that the $e-p$ to $e-e$ ratios between the data and simulation would converge to unity eventually. This procedure is important also for the bin center correction, which requires a good agreement between the simulation and the data. A flow chart for this procedure is presented in Fig. 4.41. The Kelly form factors [84] were used before the iteration. The super ratios before and after this iterative procedure (4 iterations for the 1.1 GeV and 5 iterations for the 2.2 GeV data sets) are shown in Fig. 4.42. The super ratios converged very fast after a few iterations. The differences for the differential cross section results, before and after the iterative procedure are shown in Fig. 4.43. The cross section results are insensitive to these cross section models used in the simulation, as the data points are consistent statistically before and after the iteration.

4.9.3 Born Level $e-p$ Elastic Scattering Cross Section

The $e-p$ elastic scattering cross sections were obtained by comparing the measured $e-p$ to $e-e$ ratio to the simulated $e-p$ to $e-e$ ratio, as indicated by Eq. 4.12, after the efficiency corrections for both the data and simulation. For angles below 3.0°

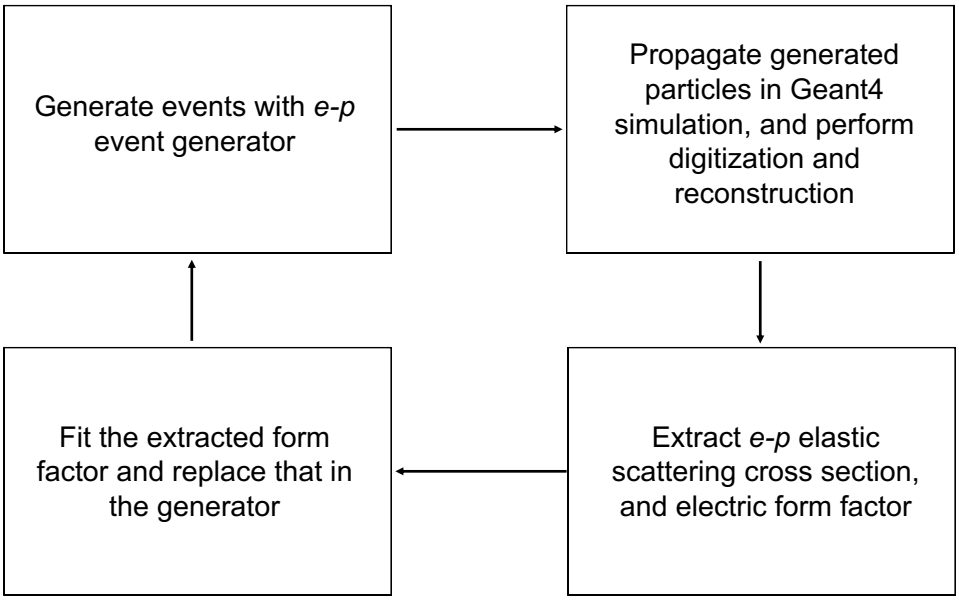

Figure 4.41: The iterative procedure for the radiative correction. This procedure is terminated once the $e-p$ to $e-e$ ratios between the data and simulation converge to unity.

and 1.6° for 1.1 GeV and 2.2 GeV respectively, the bin-by-bin method was applied to cancel the GEM efficiency. For larger angles, the integrated Møller method was applied, and the selected angular range for the Møller counts integration was 1.3° to 3.0° for the 1.1 GeV data set and 1.3° to 2.0° for the 2.2 GeV data set. The extracted differential cross sections for the $e-p$ elastic scattering are shown in Fig. 4.44. There are in total 33 data points from the 1.1 GeV data set, covering Q^2 from 2.1×10^{-4} to 1.6×10^{-2} $(\mathrm{GeV/c})^2$. The Q^2 range for the 2.2 GeV data set is from 7.0×10^{-4} to 5.9×10^{-2} $(\mathrm{GeV/c})^2$, covered by 38 data points. For the 1.1 GeV data set, the statistical uncertainties are about 0.2% in the forward angular region, and increases to nearly 1% for the largest Q^2 bin. The systematic uncertainties are larger (about 0.5%) in the forward angular region due to the systematic uncertainties related to the beam-line background subtraction, and in general between 0.3% to 0.5% at larger angles. For the 2.2 GeV data set, the statistical uncertainties are about 0.15% in the

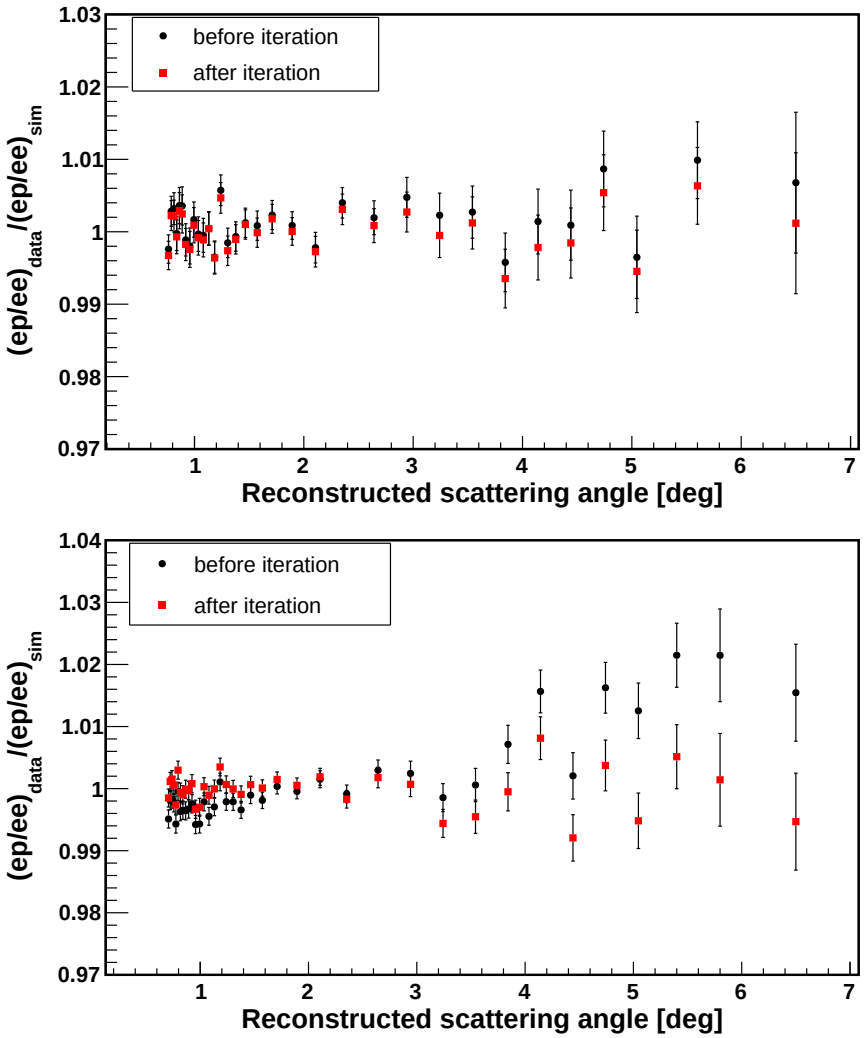

Figure 4.42: The super ratios before and after the iteration process. The top plot is for the 1.1 GeV beam energy setting and the bottom plot for the 2.2 GeV beam energy setting. Before the process, the Kelly form factors [84] were used in the simulation. The error bars contain the statistical uncertainties only.

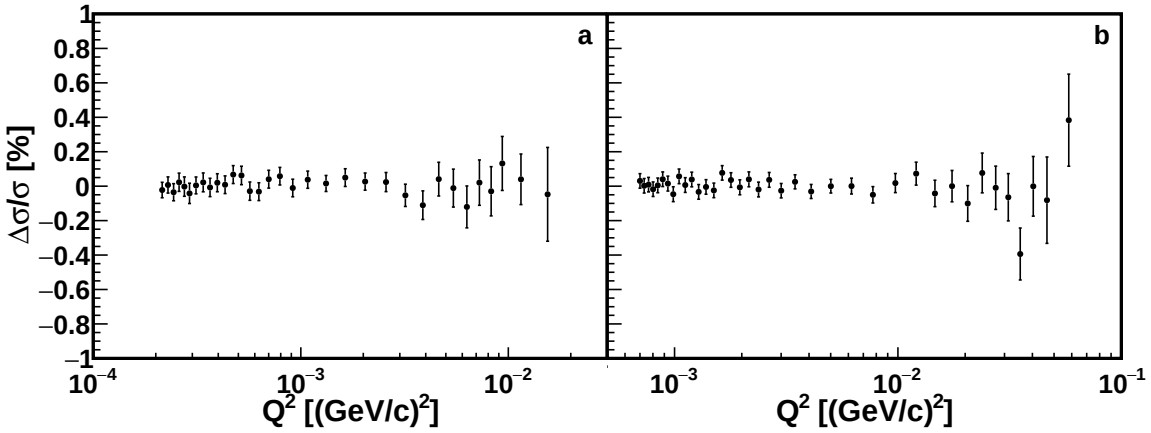

Figure 4.43: The relative difference in the cross sections before and after the iteration process for (**a**) the 1.1 GeV and (**b**) the 2.2 GeV data sets. Before the process, the Kelly form factors [84] were used in the simulation. The error bars contain only the statistical uncertainties from the simulation.

forward angular region, and increases to nearly 0.8% for the largest Q^2 bin. The systematic uncertainties are larger in the high Q^2 region (maximum 1.1%) due to the inelastic $e-p$ contribution and the energy response of the Pb-glass shower detectors, and in general in between 0.25% to 0.32% in the $PbWO_4$ region ($< 3.5°$).

To have a better visualization of the proton electromagnetic form factors, one can divide out the kinematic factors and the Mott cross sections in the Rosenbluth formula (Eq. 2.16), and define a reduced cross section

$$\sigma_{\text{reduced}} = \frac{E(1+\tau)\left(\frac{d\sigma}{d\Omega}\right)_{ep}}{E'\left(\frac{d\sigma}{d\Omega}\right)_{Mott}} = (G_E^p)^2 + \frac{\tau}{\epsilon}(G_M^p)^2. \tag{4.31}$$

Notice that this definition of the reduced cross section differs slightly from the one for the Rosenbluth separation, which is defined in Eq. 2.31. The latter requires a division of another kinematic factor of ϵ/τ. The reduced cross section results are shown in Fig. 4.45 for both the 1.1 GeV and 2.2 GeV data sets.

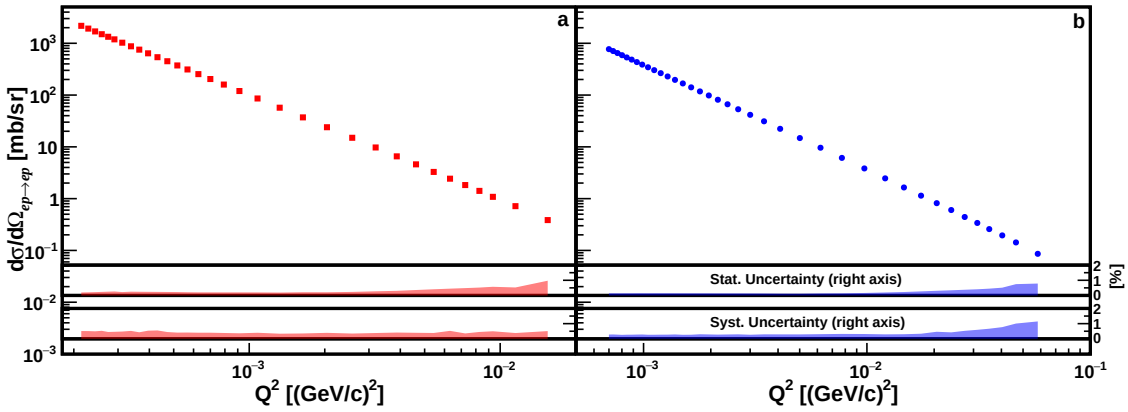

Figure 4.44: The Born level differential cross sections for the $e-p$ elastic scattering from (**a**) the 1.1 GeV and (**b**) the 2.2 GeV data sets. Statistical and systematic uncertainties are shown as separate bands and are scaled to the right axes of each plot.

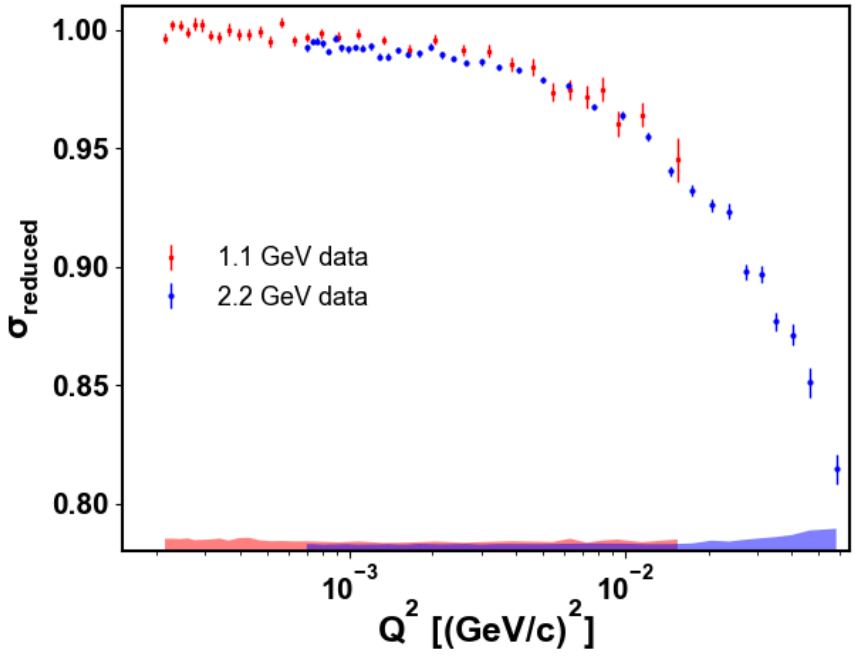

Figure 4.45: The reduced cross section as defined in Eq. 4.31, for the 1.1 GeV and 2.2 GeV data sets. After dividing out the kinematic factors, the reduced cross section is a linear combination of the electromagnetic form factors squared.

4.10 Systematic Uncertainties on Cross Section

The systematic uncertainties of the PRad experiment are grouped into uncorrelated uncertainties and correlated ones. The latter are further divided into normalization uncertainties and Q^2-dependent uncertainties. Only a few systematic uncertainties may be considered uncorrelated, that is, no clear correlations are observed among different angular or Q^2 bins. These include the uncertainties in the detector efficiency measurements, parts of the energy calibration of the HyCal modules, and also parts of the detector responses for the Pb-glass detectors. Unlike the $PbWO_4$ modules, which show clear similarities, the Pb-glass modules have some differences in their responses and no clear correlations are observed among them. So, these systematic uncertainties are assumed to be uncorrelated. Most of the other systematic uncertainties are considered to be correlated, and their angular dependencies are extracted using either the data or the simulation, and are included in the systematic uncertainty studies. A few items, such as the energy cuts in the event selection, and the time-stability of the background subtraction are considered to be mixed, that is, they are partially correlated and partially uncorrelated. Studies for their systematic uncertainties involve using many different sizes for the event selection cuts and using different combinations of empty target runs to do the background subtraction. All the systematic uncertainties that are considered for the cross section results are shown in the following list:

1. Event selection
2. Detector efficiency
3. Beam-line background
4. HyCal response

5. Geometric acceptance

6. Beam energy

7. Energy loss and multiple scattering due to external materials

8. Radiative corrections for $e-p$ and $e-e$

9. Inelastic $e-p$

The total relative systematic uncertainties for the cross sections are shown in Fig. 4.46 for both the 1.1 and 2.2 GeV data sets. The first item is related to various cuts used to select the $e-p$ and $e-e$ elastic scattering events, which will be discussed in the Sub-section 4.10.1. Various systematic uncertainties can arise from the imperfect knowledge about the experimental setup, such as the beam energy, positions and efficiencies of the detectors, the HyCal energy response to incident particles, and fluctuations and possible biases in the beam-line background subtraction. These are related to various conditions while the experiment was taking place and they will be discussed in the Sub-section 4.10.2. Lastly, the cross section results depend inevitably on certain models and calculations, such as the radiative corrections for the $e-p$ and $e-e$ and also the inelastic $e-p$ subtraction. They are discussed in the Sub-section 4.10.3.

4.10.1 Systematic Uncertainties Associated with Cuts

A series of cuts were used in the analysis to select the elastic $e-p$ and $e-e$ events, such as the kinematic cuts for both reaction channels, and the coplanarity and vertex-z cuts for the $e-e$ events. Slightly different cross sections results can be obtained once the sizes of these cuts are changed, and this variation arises from the fact that there are always some slight differences between the data and simulation. For example, for

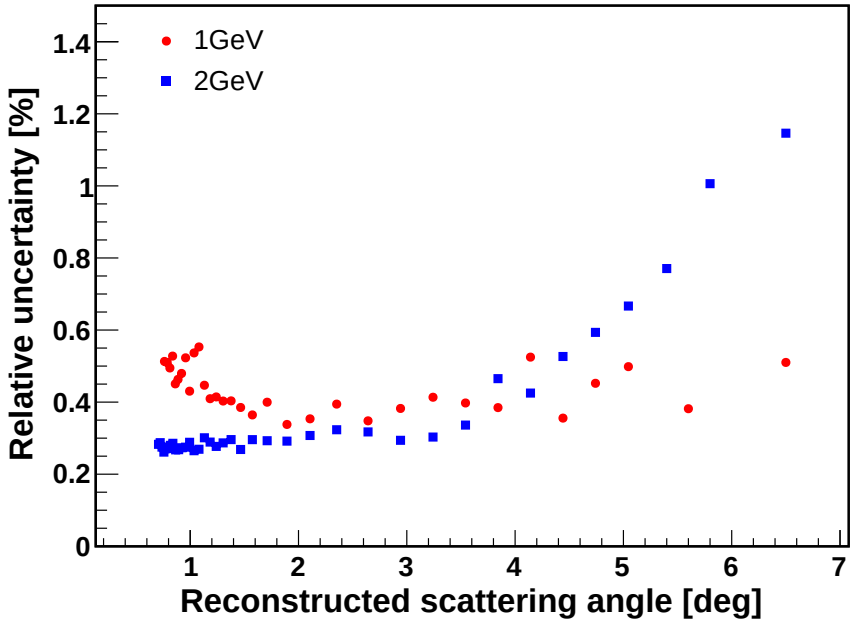

Figure 4.46: Total relative systematic uncertainties for the $e-p$ elastic scattering cross sections for the 1.1 and 2.2 GeV data sets.

the shape of the elastic $e-p$ peak, the central positions and widths obtained from the data and simulation match very well, however, there can be small differences in the tail regions (see Fig. 4.35). These differences may arise from various sources such as the light attenuation in the modules, the non-linearity, the gaps between HyCal modules that are not simulated perfectly, other electronics related effects that were unaccounted for in the detector digitization and so on. These sources are typically very difficult to be isolated and studied separately. In order to quantify their overall effects, the sizes of the event selection cuts are varied around the nominal cuts used to obtain the cross section results (see Table 4.3 and Table 4.4). The root-mean-squares (RMS) of the cross section results as one changes these cuts are used as the uncertainties due to the event selection.

The uncertainties for the event selection are dominated by those cuts related to the HyCal reconstructed energy, such as the kinematic cuts. And the variations

are not uniform across different detector modules of the HyCal, especially given that it consists of two different types of shower detectors. These variations may come from small inter-module differences in properties such as the light attenuation, non-linearity of detector responses, microscopic gaps between detector modules and the energy calibrations. The effect of this systematic uncertainty was studied by varying the kinematic cuts over a wide range, which is ± 20% for the 1.1 GeV default kinematic cuts and at least ± 50% for the 2.2 GeV default kinematic cuts (see Table 4.3 and Table 4.4). The reason of a smaller range for the 1.1 GeV data set is because the $e-p$ and $e-e$ elastic peaks are very close, particularly in the very forward angular region ($< 1.0^\circ$ for instance). Increasing the cut size for the $e-p$ events can include significant amount of $e-e$ events and vice versa.

The super ratios (proportional to the cross section) as a function of the $e-p$ kinematic cut size, are shown in Fig 4.47 and Fig 4.48. The variation of the kinematic cut leads to changes in the extracted cross section of about 0.1%, on average, and is typically within ± 0.15%, except for the last few bins in the large angular region. This is most likely due to the lack of statistics in the fine tuning process of the energy calibrations for the Pb-glass modules and the effect is more significant if the size of the kinematic cut is reduced. In the $PbWO_4$ region ($< 3.4^\circ$), the variation is significantly smaller and it is most likely due to the light attenuation property of the $PbWO_4$ modules and the gaps between them. The variations when changing the energy cuts for the $e-e$ (see Fig 4.49 and Fig 4.50) are typically slightly larger than those for the $e-p$ in the similar detector region. This is because the double-arm Møller selection requires three cuts on the HyCal reconstructed energy for each event (two kinematic cuts for the two scattered electrons and an elasticity cut for the total energy of these two electrons). However, the variation is more uniform

across the HyCal[8], which means varying energy cuts for the $e-e$ mostly just changes the normalization of the data points and the angular dependency of the variation is significantly smaller than that for the $e-p$. The RMSs of the cross section results, due to the change in the size of the energy cuts, are used as the systematic uncertainty.

For the co-planarity and vertex-z cuts, the variations are negligible compared to those from the energy cuts. Only a 0.02% difference was observed when changing the sizes of these cuts by $\pm 20\%$, and the difference is mostly on the normalization of the data points. The cross section results are also shown to be insensitive to the matching cuts between the GEMs and HyCal. The default value for this cut is 6σ of the HyCal position resolution. When using 5σ, 7σ and 8σ cuts, the RMSs of the cross section results are about 0.02% (mostly uncorrelated) of the nominal ones. The sensitivity on the selected angular ranges for the integrated Møller method was also included for the systematic uncertainties of the event selection. These ranges are, by default, 1.3° to 3.0° for the 1.1 GeV data set and 1.3° to 2.0° for the 2.2 GeV data set, as the GEM efficiency could be more precisely determined in these ranges. Typically around 0.05% difference would appear if some other ranges are used, such as 0.7° to 1.0° or 1.0° to 1.3°. This difference is assigned as the corresponding systematic uncertainty.

4.10.2 Systematic uncertainties from Experimental Conditions

Detector efficiency: These systematic uncertainties include two items. The first item includes the statistical uncertainties in the detector efficiency measurements, namely, measurements of the HyCal trigger efficiency and the GEM efficiency. These statistical uncertainties are determined using the Binomial distribution. For the HyCal trigger efficiency, the uncertainties are typically less than 0.03% for each module, so

[8]Partially because the double-arm Møllers are mostly inside the $PbWO_4$ detector region.

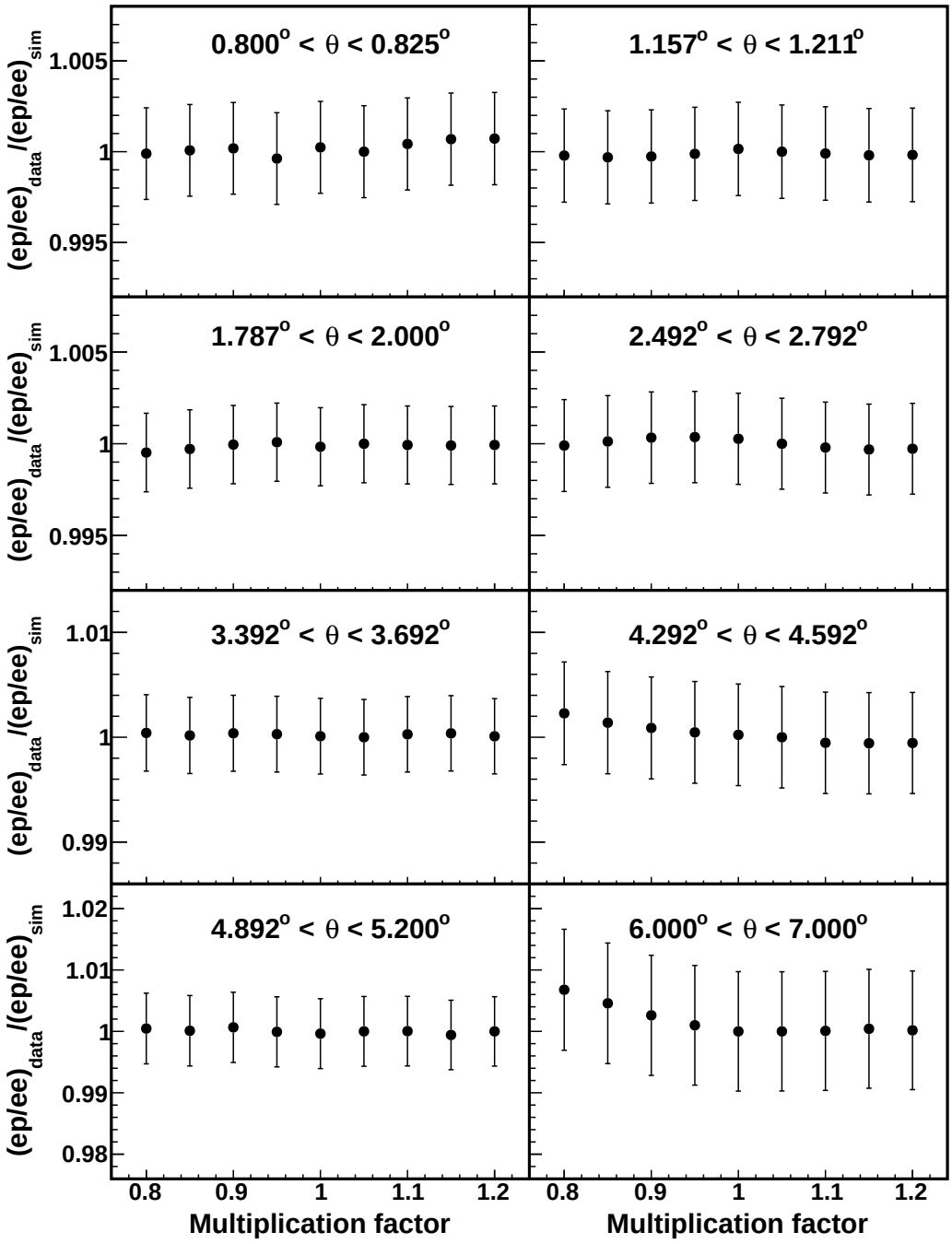

Figure 4.47: The variations of the super ratio results when changing the size of the kinematic cuts for the 1.1 GeV $e-p$ event selection, for different scattering angular bins. The multiplication factor is to be multiplied on top of the default sizes of the kinematic cuts, listed in Table 4.3. A multiplication factor of 0.8 means reducing the sizes by 20%, which leads to -2.40 $\sigma_{\rm det}$ to 2.40 $\sigma_{\rm det}$ for the size of the cut in the $PbWO_4$ region for instance. Data points are shifted so that the super ratio with the default cut size is at unity.

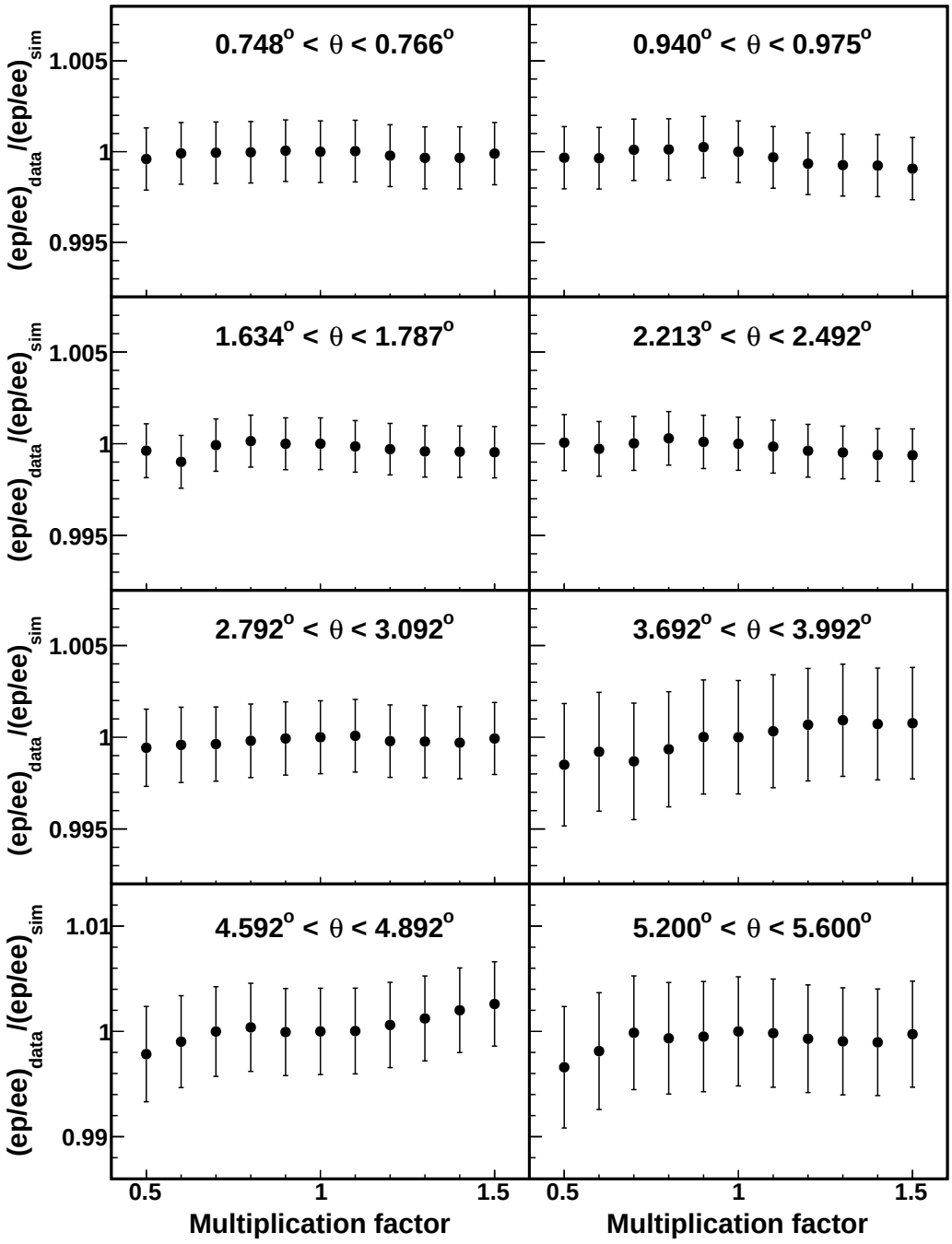

Figure 4.48: The variations of the super ratio results when changing the size of the kinematic cuts for the 2.2 GeV $e-p$ event selection, for different scattering angular bins. The multiplication factor is to be multiplied on top of the default sizes of the kinematic cuts, listed in Table 4.3. A multiplication factor of 0.5 means reducing the sizes by 50%, which leads to -1.75 $\sigma_{\rm det}$ to 1.75 $\sigma_{\rm det}$ for the size of the cut in the $PbWO_4$ region for instance. Data points are shifted so that the super ratio with the default cut size is at unity.

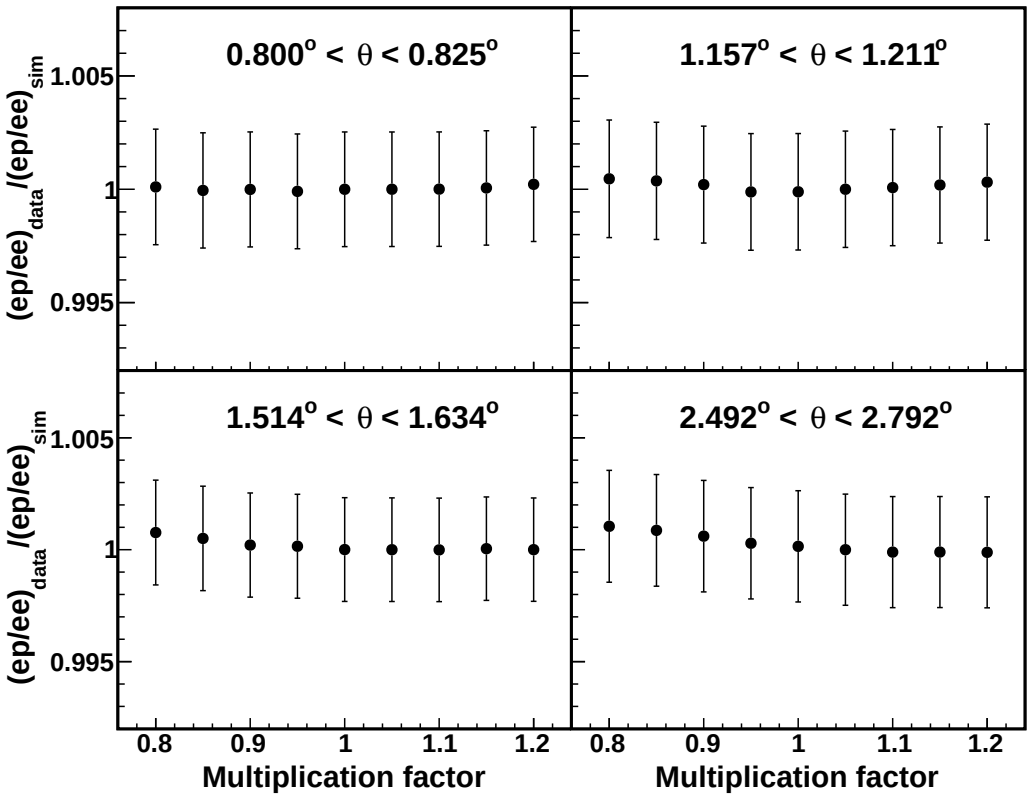

Figure 4.49: The variations of the super ratio results when changing the size of the energy cuts for the 1.1 GeV $e-e$ event selection, for different scattering angular bins. The multiplication factor is to be multiplied on top of the default sizes of the kinematic cuts, listed in Table 4.4. A multiplication factor of 0.8 means reducing the sizes by 20%, which leads to -2.40 $\sigma_{\rm det}$ to 2.40 $\sigma_{\rm det}$ for the size of the cut in the $PbWO_4$ region for instance. Data points are shifted so that the super ratio with the default cut size is at unity.

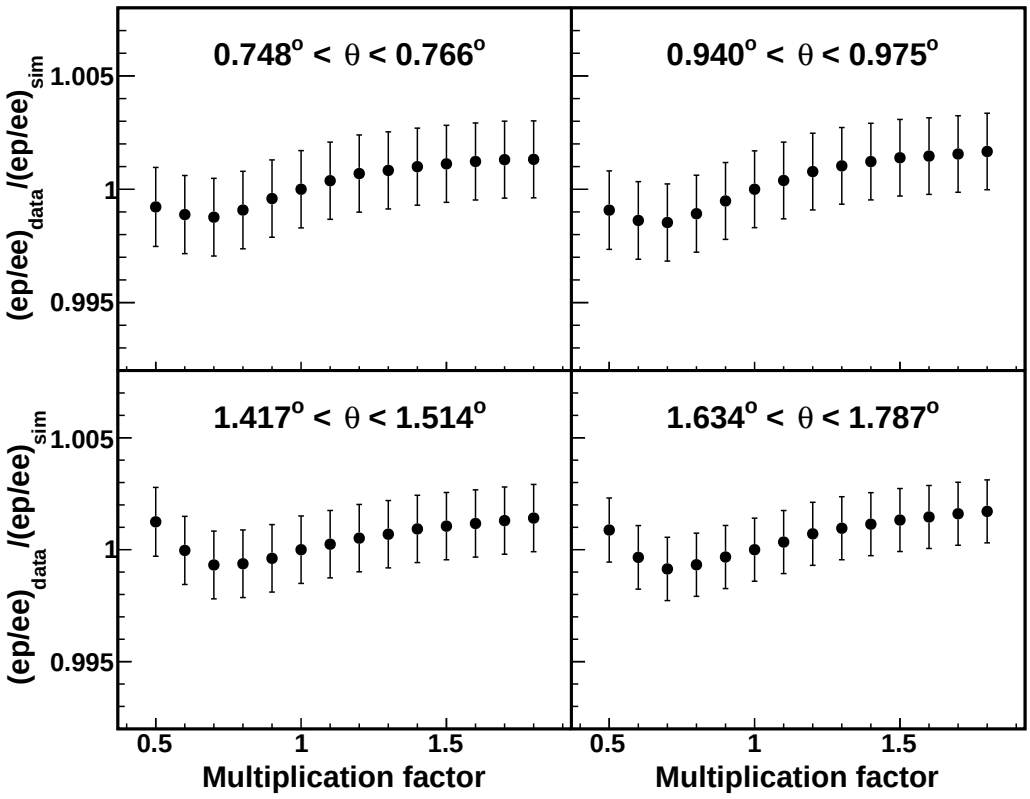

Figure 4.50: The variation of the super ratio results when changing the size of the energy cuts for the 2.2 GeV $e - e$ event selection, for different scattering angular bins. The multiplication factor is to be multiplied on top of the default sizes of the kinematic cuts, listed in Table 4.4. A multiplication factor of 0.5 means reducing the sizes by 50%, which leads to -2.25 $\sigma_{\rm det}$ to 2.25 $\sigma_{\rm det}$ for the size of the cut in the $PbWO_4$ region for instance. Data points are shifted so that the super ratio with the default cut size is at unity.

the effect is negligible. For the statistical uncertainties of the GEM efficiency, only data points obtained using the integrated Møller method can be affected (scattering angles larger than 3.0° for 1.1 GeV and 1.6° for 2.2 GeV data sets), as the GEM efficiency correction is not needed for the bin-by-bin method. For the 2.2 GeV data set, this uncertainty is about 0.05% at 1.6° and increases to 0.3% for the largest angular bin. For the 1.1 GeV data set, it is about 0.1% at 3.0° and increases to 0.4% for the largest angular bin. These statistical uncertainties should be considered uncorrelated among different angular bins. The second item includes the uncertainties in the GEM efficiency measurements due to the finite HyCal position resolution effect (see Section 4.6). The uncertainties from this source are estimated by running multiple simulations with slightly different widths and locations for the GEM spacers, and then compared the GEM efficiency corrected cross section results to those obtained with perfect GEMs (no GEM spacers and other dead areas). These simulations include ± 0.9 mm variations around the nominal width (3.0 mm) and ± 2 mm variations around the measured locations for the GEM spacers. This source can introduce a maximum uncertainty of 0.35% on the 1.1 GeV cross sections and 0.25% on the 2.2 GeV cross sections. The background related systematic uncertainties for the GEM efficiency, such as those due to cosmic events, high energy photons and very-small-angle-scattering events (see Section 4.5.4 and Section 4.6) are considered negligible.

Beam-line background: There are three items included in the systematic uncertainties due to the beam-line background subtraction. The first one is the time variation of the background, which was studied by performing the background subtraction using different combinations of the empty target runs, such as, the empty target run before or after the corresponding production runs, or the average of these two empty target runs. The RMSs of the cross sections were used as the systematic

uncertainties due to the time variation of the background subtraction. These uncertainties are negligible for the 2.2 GeV cross section results ($\sim 0.02\%$) as the beam-line background was highly stable during the experiment, but is one of the dominant uncertainties for the 1.1 GeV data set. It introduces nearly 0.5% uncertainties on the cross sections in the very forward angular region, and reduces to around 0.25% for larger angles. The second item is the uncertainty in the live charge measurement, and the nominal uncertainty is about 0.1%. This leads to a maximum 0.05% and 0.02% uncertainties on the cross sections below 1.1° for the 1.1 and 2.2 GeV data sets, respectively, as the background rates are high in this region. The last item is related to the background hydrogen gas distribution around the target cell. When the hydrogen gas is filled directly into the target cell, it produces two diffusing tails as it exits the window-less cell through the orifices. The empty target runs can only be used to subtract hydrogen gas that is far away from the cell and cannot reproduce these tails, as the gas is filled directly into the chamber. In this case, effects due to these tails can cause systematic uncertainties for the results. One way to quantify this effect is to study the vertex-z distributions in the data and simulation, reconstructed by two hits on the GEMs from the double arm Møller events. Over 10 different gas profiles were used to study the comparisons of the vertex-z distributions between the data and simulation, and also to study the effects on the cross section results. They include gas profiles from the COMSOL simulation and a number of variations based on that, no gas outside the target cell, and profiles based on a simple gas diffusion relation $1/(d_z + c)^2$, where d_z is the $z-$coordinate difference between a point outside the cell and the orifice, and c is a tunable parameter that can control the size of the diffusing tails. To estimate the possible systematic uncertainties, we use the two extreme cases. In the first case (min. tails), the gas profile has no diffusing tails outside the target cell. The vertex-z distribution simulated with this profile always gives

smaller tails compared to the same distribution from the data, as shown in Fig. 4.51 for the 2.2 GeV setting. In the second case (max. tails), we use one of the gas profiles based on the simple gas diffusion model, which always gives larger tails compared to the same distribution from the data. The ratios between the $e-p$ to $e-e$ ratios, obtained with these two gas profiles, are shown in Fig. 4.52 for the 2.2 GeV setting. The effect on the cross section results is correlated. The $e-p$ to $e-e$ ratios obtained in the second case are larger than those in the first case by around 0.2% for the very forward angles, and then converge almost linearly with larger angles. This effect is about the same for the 1.1 GeV setting. The differences in the results obtained with these two gas profiles are used as the 3σ boundaries for the systematic uncertainties due to the diffusing gas tails.

HyCal response: This item is mainly related to the HyCal energy response for an incident particle with different energies (non-linearity). There are a number of factors that can affect the nonlinear behavior of a module, such as the light attenuation, pedestal cuts, back scattering of secondary particles and so on. A typical nonlinear behavior of a HyCal module is shown in Fig. 4.10 over a very broad energy range of an incident particle, based on measurements from the PrimEx-II experiment [65]. The linearity is usually very good when the energy of the incident particle is high, but changes rapidly at the low energy side mainly due to the pedestal cuts. For the PRad experiment, the non-linearity near the elastic $e-p$ peak can be measured using the data from production runs if the energies of the scattered electrons from both $e-p$ and $e-e$ scatterings are high enough, so that they are both on the linear part of the response curve. This is true for most of the $PbWO_4$ modules and some of the Pb-glass modules that are covering smaller scattering angles. However, when the scattering angles are too large, the incident energies of the $e-e$ electrons become so low that they will fall on the rapidly changing part of the response curve, and it can no longer

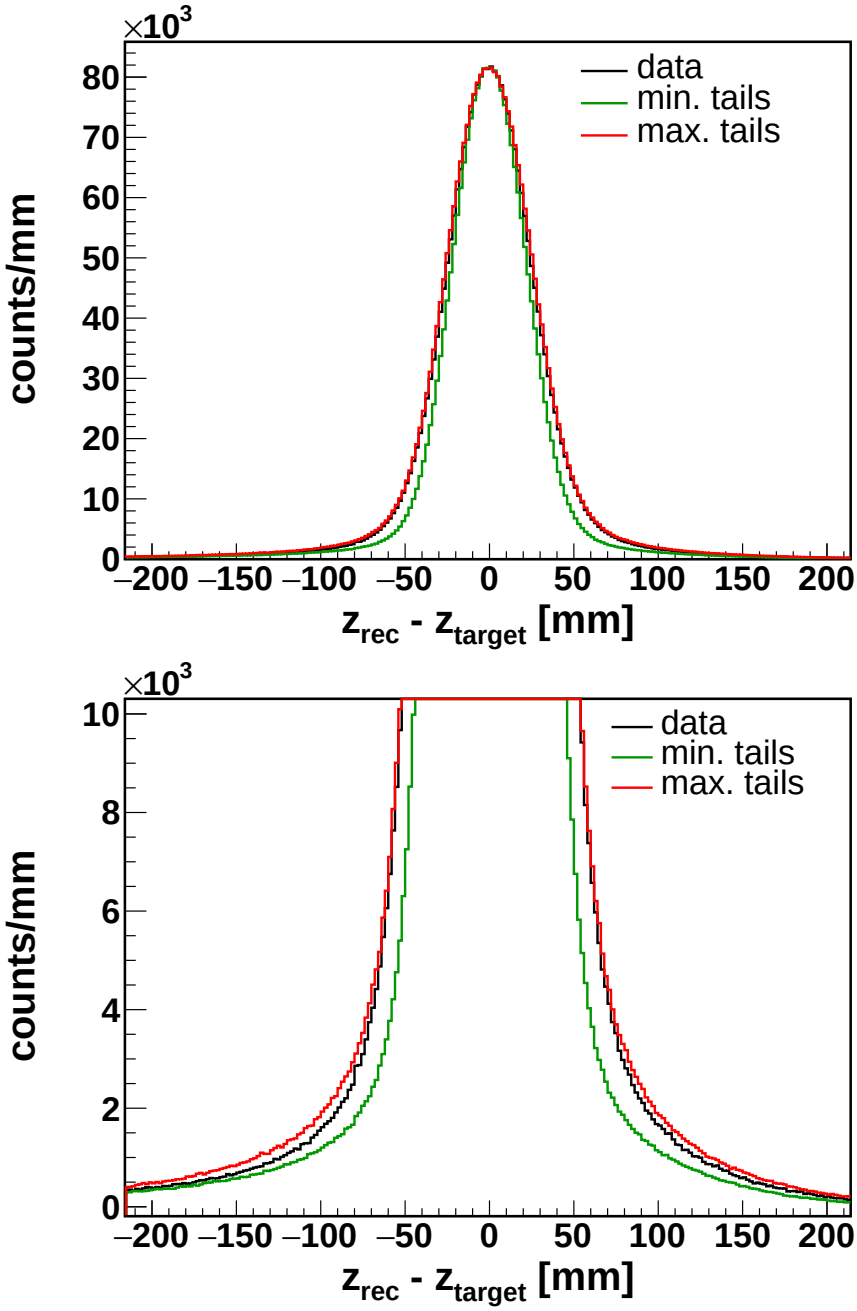

Figure 4.51: The z-vertex distributions from the 2.2 GeV data (black histogram), and simulations using the gas profiles with min. tails (green histogram) and max. tails (red histogram). All distributions are normalized by the integrals in the peak region (from -20 mm to 20 mm, size of the target cell). The bottom plot is a zoom-in of the top plot. The distribution from the data is completely within the two boundaries set by the simulations with min. and max. tails.

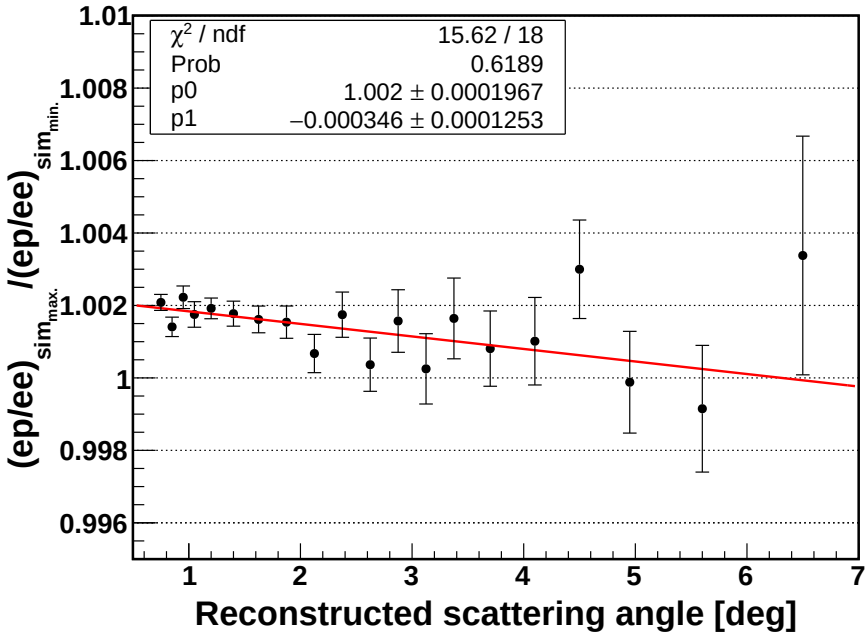

Figure 4.52: The $e-p$ to $e-e$ ratios obtained with the gas profile with max. tails over those with the min. tails, in the case of the 2.2 GeV energy setting. The red solid line is a linear fit to the super ratios.

be used to measure the non-linearity near the $e-p$ peak. Thus, the uncertainty associated with non-linearity corrections primarily affects data points in the large angular region and it is expected to be larger for the 2.2 GeV setting as the HyCal gain was lower and the effect due to the pedestal cuts would be more significant. In addition, for the 2.2 GeV data set, these corrections affect directly the position of the Δ-resonance peak, which is significantly larger than that in the 1.1 GeV data set. To estimate these uncertainties, a few versions of the non-linearity corrections are used for modules in the large angular region, including those from the PrimEx-II experiment and those that can produce the best match for the Δ-resonance peak in the data and simulation. For the 2.2 GeV setting, the uncertainties are mostly correlated and are estimated to be negligible in the $PbWO_4$ region ($< 3.4^\circ$) but increase linearly to about 1% at the largest angular bin. Additional uncorrelated uncertainties are assigned in order to take into account the module-by-module differences in the Pb-glass nonlinear properties. These systematic uncertainties are negligible at 3.4° and grow linearly to 0.4% at the largest angular bin. On the other hand, for the 1.1 GeV data set, the differences between results obtained with different non-linearity corrections are much smaller than the statistical uncertainties of the data points and the effect is expected to be negligible. The other item considered for the HyCal response is the non-uniformity correction for the HyCal energy reconstruction (discussed in section 4.3.1). In principle, to extract this correction, one will need to study the ratio $(E_{\rm rec}/E_{\rm exp})$ as a function of the reconstructed position for each module separately. This is particularly important for the Pb-glass modules as their non-uniformities are very different from each other. This requires a sufficient amount of statistics from the production runs for each module. However, the $e-p$ cross section drops drastically at large scattering angles, and one has to group multiple neighboring modules in order to extract this correction. And one has to assume that the correction is

applicable to all modules within the group, which makes this correction much less reliable compared to that for the $PbWO_4$ modules. The systematic uncertainties are expected to be larger for the 2.2 GeV data set, as the non-uniformity effect is relatively larger than that for the 1.1 GeV data and a tighter energy cut is used in order to reject inelastic $e-p$ events. Given that no clear correlations are observed for this non-uniformity behavior among the Pb-glass modules, uncorrelated systematic uncertainties are assigned for the 2.2 GeV data points in the large angular region. The sizes of these uncertainties are considered negligible at 3.4° and increase linearly to 0.3% at the largest angular bin.

Beam energy: The measured beam energy for the 1.1 GeV data set is 1101.0 MeV ± 0.5 MeV, and 2143.0 MeV ± 1.5 MeV for the 2.2 GeV data set. These uncertainties are assumed to be Gaussian distributed, with the widths equal to 0.5 MeV and 1.5 MeV for the 1.1 and 2.2 GeV data sets, respectively. The effects due to these systematic uncertainties are determined by running multiple simulations with different beam energies. Ratios between the $e-p$ to $e-e$ ratios with different beam energies and those obtained with the nominal beam energy, are shown in Fig 4.53 for the 2.2 GeV beam energy setting. Note that as the z positions of the detectors were determined using Eq. 4.23 (see Section 4.3.2), which depend also on the beam energy. Thus, there is a strong correlation between the beam energy and detector z positions. That is, for every 1 MeV increase in the beam energy, it corresponds to a 2.3 mm shift in z for the 1.1 GeV energy setting, and a 1.2 mm shift in z for the 2.2 GeV energy setting, as shown in Fig. 4.54. Therefore, the systematic uncertainties for the beam energy will include the beam-energy-dependent part of the detector position systematic uncertainties. In fact, these two systematic effects will partially cancel out each other due to this correlation. The total systematic uncertainties on the cross sections due to the beam energy are about 0.1% for the 2.2 GeV data set

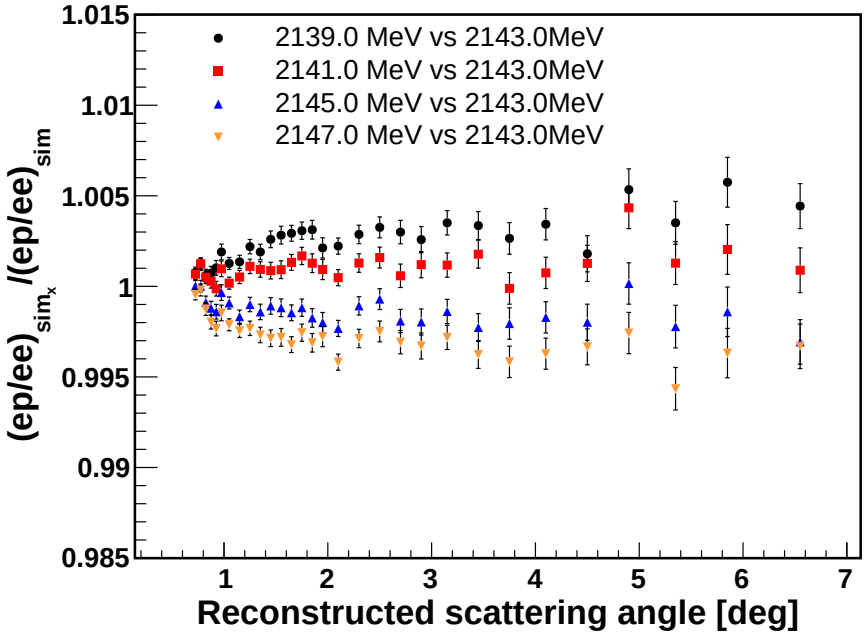

Figure 4.53: The $e-p$ to $e-e$ ratios from simulations with different beam energies (labeled as sim_x) over those obtained with the nominal beam energy (labeled as sim), in the case of the 2.2 GeV energy setting. For the scattering angles below 1.6°, data points are obtained using the bin-by-bin method, otherwise, the integrated Møller method is applied.

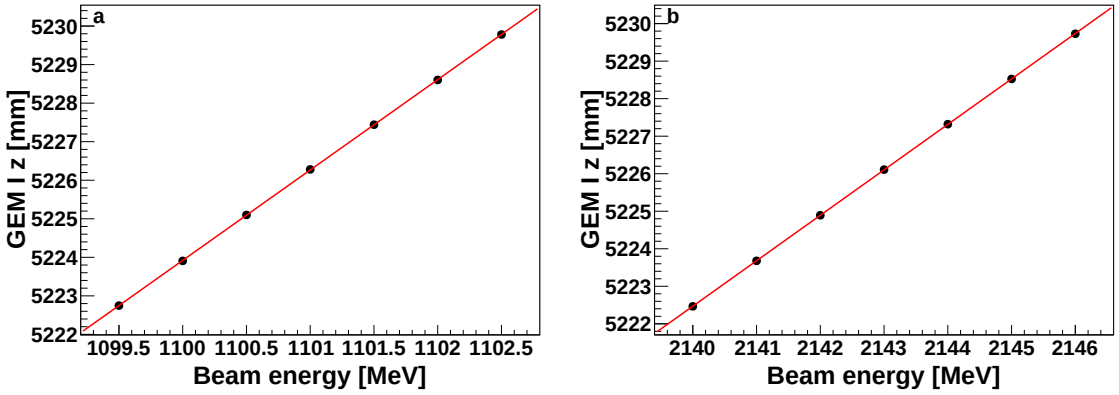

Figure 4.54: Correlation between the beam energies and the determined z position of GEM-I for the 1.1 GeV (**a**) and 2.2 GeV (**b**) energy settings. Similar relations can be obtained for GEM-II and the HyCal.

and 0.07% for the 1.1 GeV data set.

Geometric acceptance: this item includes the uncertainties in the detector positions, beam position, dead module removal cuts for certain HyCal modules (due to low trigger efficiency and no ADC readout), and microscopic gaps between the modules. For the detector positions of the GEMs, the beam-energy-dependent part is included in the systematic uncertainties due to the beam energy. The energy-independent part may come from the statistical uncertainties in the selected double-arm Møller events, the uncertainties in the beam position and so on. It is assumed to be around 1 mm, since the determined values for the detector positions using data from the production runs (see Table 4.2) and the surveyed results agree at this level. The effects on the cross section results are determined by running a number of simulations with slightly different GEM positions, varied around the measured positions based on a Gaussian distribution with 1 mm width. For data points obtained using the integrated Møller method, the shifts in the GEM positions mostly just affect the normalization of the data points, at around $\pm$ 0.05%. For data points obtained using the bin-by-bin method, it starts from nearly 0 at the most forward angle and then increases to about 0.05% at around 3.0° and 1.6° for the 1.1 and 2.2 GeV data set, respectively. The $e-p$ to $e-e$ ratios from a few versions of these simulations versus those obtained from the standard simulation are shown in Fig 4.55. The Q^2-dependent uncertainty mostly comes from the Møller through the bin-by-bin method. For the HyCal position, the effect is rather negligible since the HyCal reconstructed coordinates are eventually replaced by the GEM coordinates after matching. The tilting angles of the detectors were surveyed by the Jefferson Lab survey group before the experiment took place. The maximum tilting angle of all the detectors is about 0.016°. The effect will very likely get averaged out (at least partially) by combining the data from the full 2π azimuthal angle. The systematic uncertainties are studied using the simulation and found to be negligible. Similarly, for the systematic uncertainties due to the beam

position, the effect will get averaged out by using the data from the full 2π azimuthal angle, and it is also shown to be negligible. There were in total 3 $PbWO_4$ and 4 Pb-glass dead modules in the HyCal and they needed to be removed during the analysis. The cut to remove a dead module would remove all the hits reconstructed inside a circle around the center of a dead modules, with the radius as 1.5 times the size of the module (20.75mm for a $PbWO_4$ and 38.15mm for a Pb-glass module). These cuts are varied from 1 to 2 times the size of the module and the RMSs of the cross sections are assigned as the associated systematic uncertainties. There should be no need to use a larger cut size since the lateral shower width is very narrow in the HyCal. On average nearly 80% of the energy deposition is in the central module of a cluster. Apparently, only angular bins containing dead modules would be affected, and it is at maximum 0.14% for the 1.1 GeV cross sections and 0.11% for the 2.2 GeV cross sections, at around 3.9° where there were two low efficiency Pb-glass modules removed during the analysis. For the microscopic gaps between the modules, the systematic uncertainties are studied by randomly varying the sizes of the $PbWO_4$ modules by 20 μm and 100 μm for the Pb-glass modules in the simulation, and then comparing the results to those obtained with standard sizes. The observed variations are a few times smaller than the statistical uncertainties of the cross section results, and they are uncorrelated. Thus, this effect should be rather negligible.

Energy loss and multiple scattering due to external materials: radiative effects such as the bremsstrahlung radiation, ionization energy loss and also multiple scattering are simulated by Geant4 as particles propagate inside the experimental setup. They depend on the geometric and material information in the simulation about these external materials, and also the physics list used in the simulation for computing these effects. They may cause systematic uncertainties in the results as they may not reflect exactly the reality. These systematic uncertainties are studied by

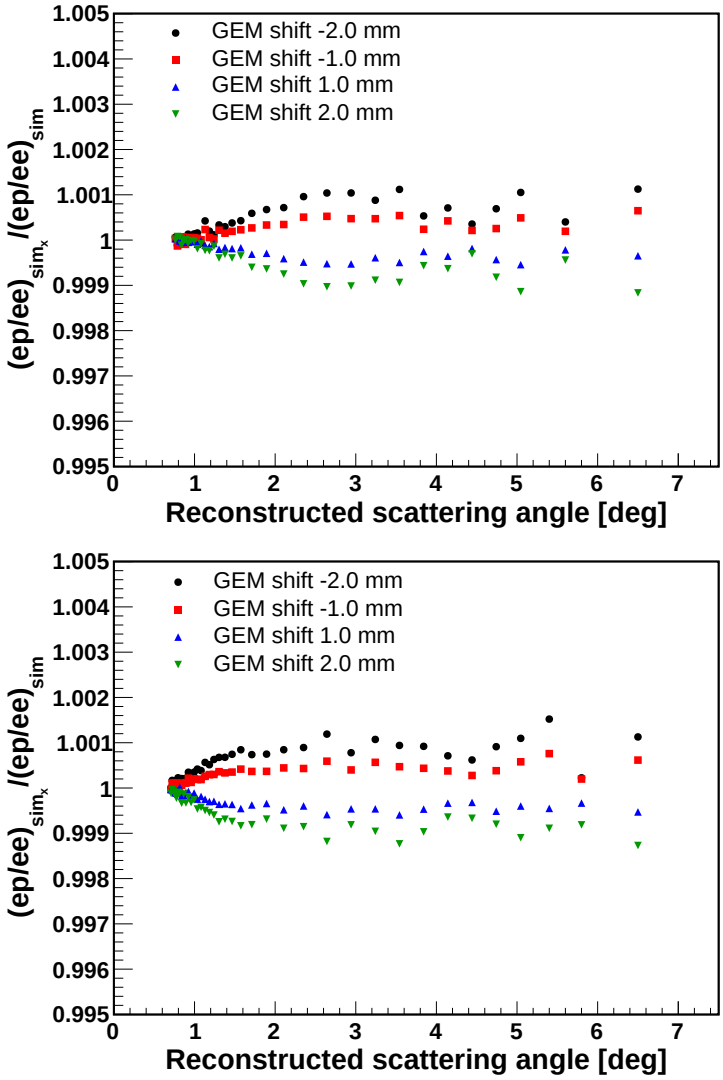

Figure 4.55: The $e-p$ to $e-e$ ratios from different simulations (labeled as sim_x) with shifted GEM positions (positive shift means shift to down stream) over those obtained from the standard simulation (labeled as sim), for the 1.1 GeV (top) and 2.2 GeV (bottom) energy settings.

changing the areal densities of the external materials between the target and HyCal by ±20%, shifting the positions for some of the dominant sources of radiative effects (the aluminum vacuum window for instance), and also changing the physics list used in the simulation. The observed deviation from the default simulation is mostly on the normalization of the data points. In order words, these radiative effects due to external materials mostly shift all data points in the same way and no clear angular dependency was observed. A systematic uncertainty of 0.2% is assigned for this source.

4.10.3 Systematic uncertainties from Models

Internal radiative corrections for the $e-p$ and $e-e$: The systematic uncertainties due to the radiative corrections arise mainly from higher order contributions to the cross sections for both elastic $e-p$ and $e-e$ scatterings. The next-to-leading order diagrams (see Fig. 4.32 and Fig. 4.33) are calculated exactly beyond the ultra-relativistic approximation [79] and included in the analysis. These corrections also include the multi-photon emission and multi-loop processes, which are approximated at the $Q^2 \to 0$ limit by the exponentiation procedure described in Ref. [79]. However, these higher order contributions are not calculated exactly, and the possible systematic uncertainties are estimated based on the approach by Arbuzov and Kopylova [85], for some of the higher order radiative corrections. The estimated systematic uncertainties for both the $e-p$ and Møller are correlated and Q^2-dependent [86]. The estimated systematic uncertainties on the cross sections are shown in Fig. 4.56 for the 1.1 GeV and 2.2 GeV data sets. The Q^2-dependence is larger for the Møller and it affects the cross section results through the use of the bin-by-bin method. This can be seen from the uncertainties below 1.6° for the 2.2 GeV and 3.0° for the 1.1 GeV where the bin-by-bin method is applied. On the other hand, the Q^2-

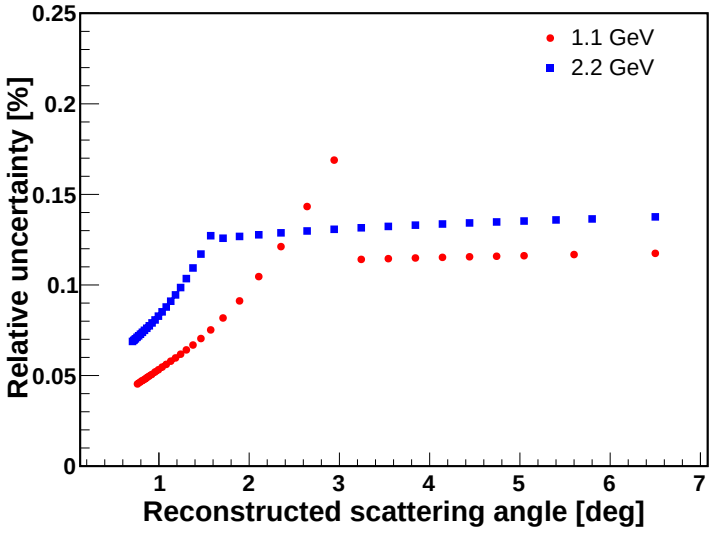

Figure 4.56: Relative systematic uncertainties for the cross sections due to internal radiative corrections for the $e-p$ and $e-e$. Blue squares are for the 2.2 GeV energy setting, red dots are for the 1.1 GeV energy setting.

dependence from the $e-p$ are estimated to be much smaller. The Q^2-dependent systematic uncertainties from the Møller can be suppressed by using the integrated Møller method for all angular bins, which will turn all systematic uncertainties from the Møller into normalization uncertainties for the cross sections. This requires high precision GEM efficiency measurements particularly for the forward angular region, which unfortunately cannot be achieved with the PRad setup (see Section 4.6), but can be achieved with an additional GEM plane. In addition, the collaboration has been working on calculating exactly the next-to-next-leading order diagrams for both the $e-p$ and $e-e$ elastic scatterings, beyond the ultra-relativistic approximation. These improvements will be discussed in Chapter. 6.

Consider that the Q^2-dependent systematic uncertainty is larger for the Møller scattering and the potential impact on r_p will be more significant, a second, independent estimate was provided by the Duke postdoc researcher Vladimir Khachatryan [87]. This estimation follows the method developed for the MOLLER experi-

ment at JLab [88], where the authors have calculated two-loop electroweak corrections to the parity-violating asymmetry for the Møller scattering, in the kinematic range of the MOLLER experiment. Based on their mathematical framework, we were able to estimate the contribution from the next-to-next-leading order diagrams on the Born cross section in the PRad kinematic range. The estimated Q^2-dependent systematic uncertainties are smaller than those estimated in the first approach, for any reasonable photon energy cut for the PRad experiment (20 MeV to 70 MeV). Thus, we still use the uncertainty from the first approach as a conservative estimate for the Møller radiative correction.

Inelastic $e-p$: The inelastic $e-p$ contribution to the cross section is simulated using the Christy 2018 empirical fit [75] to the existing inelastic $e-p$ scattering world data. It produces a good agreement between the data and simulation, with at most a 10% difference for the magnitude and a 0.5% difference for the position of the Δ-resonance peak, in the $PbWO_4$ detector region (see section 4.5.2). A similar conclusion can be drawn if one uses the MAID 2007 model [89]. The systematic uncertainties on the cross sections are determined by running multiple simulations. Each simulation has the inelastic model randomly scaled and shifted, based on two random numbers generated by two Gaussian distributions, with their widths as 10% and 0.5%, corresponding to the observed differences in the magnitude and position of the Δ-resonance peak, respectively. The systematic uncertainties are found to be negligible in the $PbWO_4$ detector region ($<<$ 0.02% for both energy settings), and then increase almost linearly with larger angles in the Pb-glass region, as shown in Fig. 4.57. In the case of the 2.2 GeV setting, the sudden increase for the last two angular bins is due to the slightly larger kinematic cuts used (see Table 4.3). The largest uncertainty is about 0.35% for the 2.2 GeV data set and 0.04% for the 1.1 GeV data set.

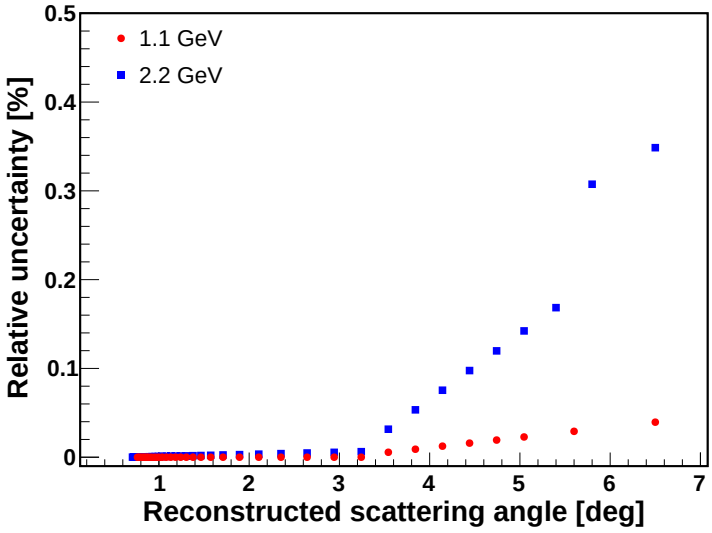

Figure 4.57: Relative systematic uncertainties for the cross sections due to the inelastic $e-p$ contribution. Blue squares are for the 2.2 GeV energy setting, red dots are for the 1.1 GeV energy setting.

4.11 Proton Electric Form Factor Extraction

In the very low Q^2 region, the $e-p$ elastic scattering cross section is dominated by the electric form factor. This is due to the fact that τ approaches zero, and also in the case of PRad, the very forward angular range ensures that ϵ is nearly at its maximum. For the PRad kinematic range, the contribution from the term $(\tau/\epsilon) \times (G_M^p)^2$ in the cross section (see Eq. 2.16) is around 10% in the largest Q^2 bin, and is less than 2% in the $Q^2 < 0.01(\mathrm{GeV}/c)^2$ range. One can assume the proton magnetic form factor with some parameterizations or models, and extract G_E^p alone with a proper systematic uncertainty associated with this assumption. This systematic uncertainty is only included in the electric form factor results. For the PRad G_E^p extraction, the Kelly proton magnetic form factor [84] was assumed. To study the systematic uncertainty associated with this assumption, multiple G_M^p parameterizations and models were

used [90, 91, 92, 93, 94], including the standard dipole form,

$$G^p_{M,\text{dipole}} = \mu_p \frac{1}{(1 + \frac{Q^2}{0.71(\text{GeV/c})^2})^2}, \tag{4.32}$$

where μ_p is the magnetic moment of a proton. These G^p_M parameterizations are shown in the top plot of Fig. 4.58. The difference between these parameterizations is around 2% in the largest Q^2 bin and less than 0.5% in the $Q^2 < 0.01(\text{GeV}/c)^2$ range. The relative differences between the extracted G^p_E using other G^p_M parameterizations or models, and the G^p_E extracted using the Kelly G^p_M parameterization are shown in the bottom plot of Fig. 4.58. The extracted G^p_E varies by no more than 0.3% at $Q^2 = 0.06$ (GeV/c)^2, which is the largest Q^2 accessible to the experiment, and $<$ 0.01% in the $Q^2 < 0.01$ (GeV/c)^2 region. The total relative systematic uncertainties of G^p_E, including the additional source related to the G^p_M assumption, are shown in Fig. 4.59. The extracted proton electric form factors G^p_E from both the 1.1 and 2.2 GeV data sets are shown in Fig. 4.60.

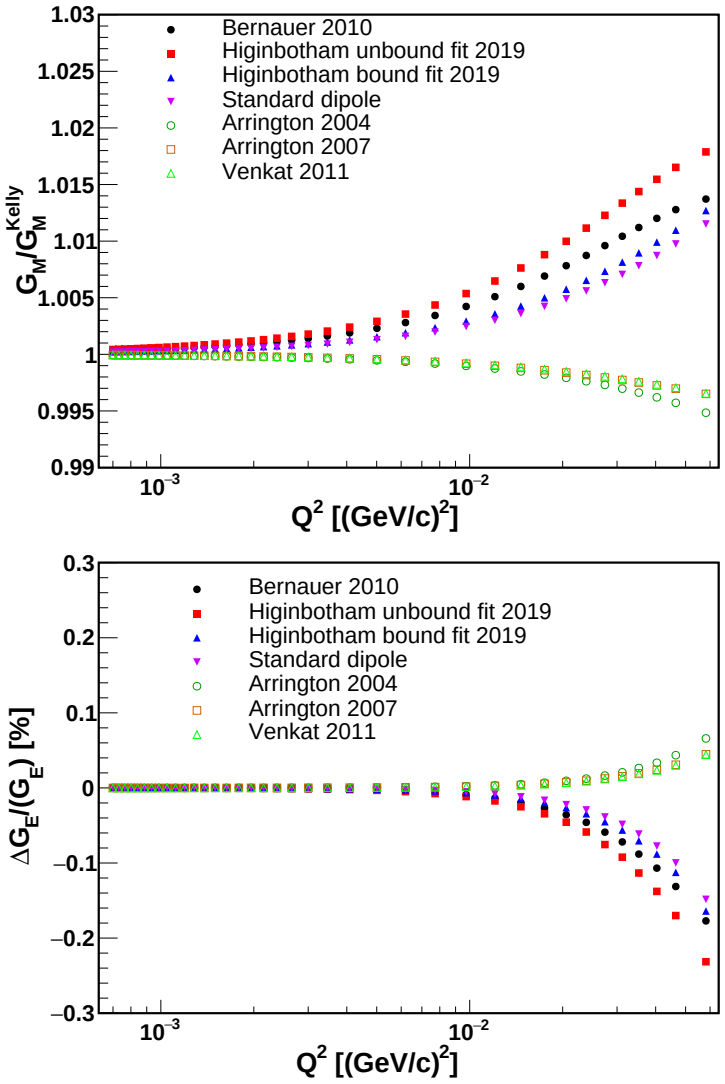

Figure 4.58: **Top plot**: Different G_M^p parameterizations [90, 91, 92, 93, 94], divided by the Kelly G_M^p parameterization [84]. **Bottom plot**: The relative difference between the extracted G_E^p using other G_M^p parameterizations or models [90, 91, 92, 93, 94] and the extracted G_E^p using the Kelly G_M^p parameterization [84].

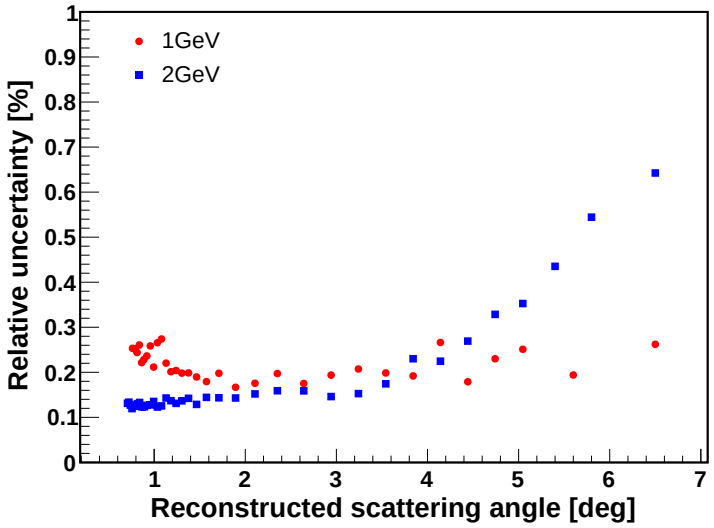

Figure 4.59: The total relative systematic uncertainties of the proton electric form factor G_E^p for the 1.1 and 2.2 GeV data sets.

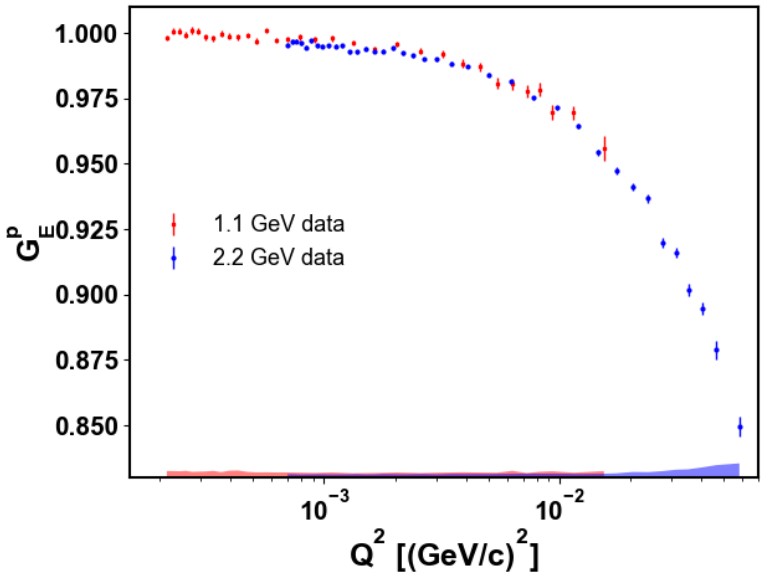

Figure 4.60: The extracted proton electric form factors G_E^p from both the 1.1 (red) and 2.2 GeV (blue) data sets. The proton magnetic form factor G_M^p is assumed to be the Kelly form factor [84] in the extraction. Statistical uncertainties are shown as the error bars, systematic uncertainties are shown as the shadow bands at the bottom.

Chapter 5

Radius Extraction

The slope of $G_E^p(Q^2)$ as $Q^2 \to 0$ is directly proportional to r_p^2 (see Eq. 1.1). A common practice is to fit $G_E^p(Q^2)$ to a functional form and then obtain r_p by extrapolating to $Q^2 = 0$. However, each functional form handles the higher order effects of $G_E^p(Q^2)$ differently and may introduce a model-dependent bias in the extrapolated r_p result. Thus, it is critical to choose a robust functional form that is most likely to yield an unbiased determination of r_p given the uncertainties in the data set, and test the chosen functional form over a broad range of parametizations of $G_E^p(Q^2)$. This study was discussed in the paper of X. Yan, et al. [12] and will be summarized in Section 5.1 of this chapter. To determine the systematic uncertainty in r_p, a Monte Carlo technique was used to randomly smear the cross section and $G_E(Q^2)$ data points for each known source of systematic uncertainties, which were described in Section 4.10 and Section 4.11. The r_p was extracted from the smeared data and the process was repeated 100,000 times. The RMS of the r_p distribution was recorded as the systematic uncertainty. The studies related to the systematic uncertainty of r_p will be discussed in Section 5.2 of this chapter. Due to the fact that different normalization uncertainties might exist between the 1.1 and 2.2 GeV data sets, the radius result was obtained by introducing two independent normalization constants n_1 and n_2 to the 1.1 and 2.2 GeV data sets, respectively, but the Q^2-dependence was kept identical during the fitting. The proton charge radius result will be discussed in Section 5.3 of this chapter.

5.1 Search for Robust Fitters

As described in [12], to search for the robust fitters for the PRad data set, first of all, a large number of pseudo-data sets were generated based on a number of well-known G_E^p parameterizations and models [84, 93, 94, 95, 96, 97, 98] with known input r_p values. The pseudo-data points were sampled based on the PRad Q^2 range, binning and statistical uncertainties. Second, a number of functional forms for G_E^p (fitters) were used to fit and extract r_p from these pseudo-data sets. These G_E^p parameterizations are summarized in the following list, with p_i as free parameters:

- Dipole:

$$G_E^p(Q^2) = \big(1 + \frac{Q^2}{p_1}\big)^{-2}, \tag{5.1}$$

  where r_p can be determined as $\sqrt{12/p_1}$.

- Monopole:

$$G_E^p(Q^2) = \big(1 + \frac{Q^2}{p_1}\big)^{-1}, \tag{5.2}$$

  where r_p can be determined as $\sqrt{6/p_1}$.

- Gaussian:

$$G_E^p(Q^2) = e^{-Q^2/p_1}, \tag{5.3}$$

  where r_p can be determined as $\sqrt{6/p_1}$.

- Multi-parameter polynomial expansion of Q^2:

$$G_E^p(Q^2) = 1 + \sum_{i=1}^{N} p_i Q^{2i}, \tag{5.4}$$

  where r_p can be determined as $\sqrt{-6p_1}$ and the maximum order N is defined by the user.

- Multi-parameter rational function of Q^2 (rational (N, M)):

$$G_E^p(Q^2) = \frac{1 + \sum_{i=1}^{N} p_i^a Q^{2i}}{1 + \sum_{j=1}^{M} p_j^b Q^{2j}}, \tag{5.5}$$

  where r_p can be determined as $\sqrt{6(p_1^b - p_1^a)}$ and the maximum order N and M are defined by the user.

- Continuous fraction expansion:

$$G_E^p(Q^2) = \frac{1}{1 + \frac{p_1 Q^2}{1 + \frac{p_2 Q^2}{1 + \ldots}}}, \tag{5.6}$$

  where r_p can be determined as $\sqrt{6p_1}$.

- Multi-parameter polynomial expansion of z:

$$G_E^p(Q^2) = 1 + \sum_{i=1}^{N} p_i z^i, \tag{5.7}$$

  after making a conformal mapping through [13]:

$$z = \frac{\sqrt{T_c + Q^2} - \sqrt{T_c - T_0}}{\sqrt{T_c + Q^2} + \sqrt{T_c - T_0}}, \tag{5.8}$$

  where $T_c = 4m_\pi^2$, m_π is the mass of a π^0 meson, and T_0 is a free parameter representing the point that is mapping onto $z = 0$ ($T_0 = 0$ for this study). The charge radius is given by $r_p = \sqrt{-3p_1/2T_c}$.

In addition, it is a common practice to include an additional normalization parameter (floating parameter) to handle systematic uncertainties associated with the normal-

ization of the data points, such that the final functional form of a fitter is

$$f(Q^2) = nG_E^p(Q^2), \tag{5.9}$$

where n is the floating parameter and $G_E^p(Q^2)$ can be any of the functions listed above.

Lastly, the mean value and RMS of the extracted r_p values were compared to the input r_p. In addition to minimizing the value of the Root-Mean-Square Error (RMSE $= \sqrt{\text{bias}^2 + \text{RMS}^2}$), it is also required that a robust fitter must have the mean value of the extracted r_p agree with the input r_p within the value of the RMS, for all the input form factor models used in the test. The results for some of the fitters are shown in Fig 5.1 to Fig 5.4, which apply to the entire PRad kinematic range (1.1 and 2.2 GeV data sets together). Single parameter fitters (excluding the floating parameter) such as the dipole, monopole, Gaussian and the first order polynomial expansion of Q^2 and z tend to give biased results with very small uncertainties. Fitters including more than two parameters (excluding the floating parameter) such as the third order polynomial expansions of Q^2 and z tend to give unnecessarily large uncertainties even though the results are well consistent with the input r_p within their RMS values. The robust fitters identified from this study include the two-parameter rational function (rational (1,1)):

$$f(Q^2) = nG_E(Q^2) = n\frac{1 + p_1^a Q^2}{1 + p_1^b Q^2}, \tag{5.10}$$

and the second order polynomial expansion of z (second order z transformation):

$$f(Q^2) = nG_E(Q^2) = n\big(1 + p_1 z + p_2 z^2\big). \tag{5.11}$$

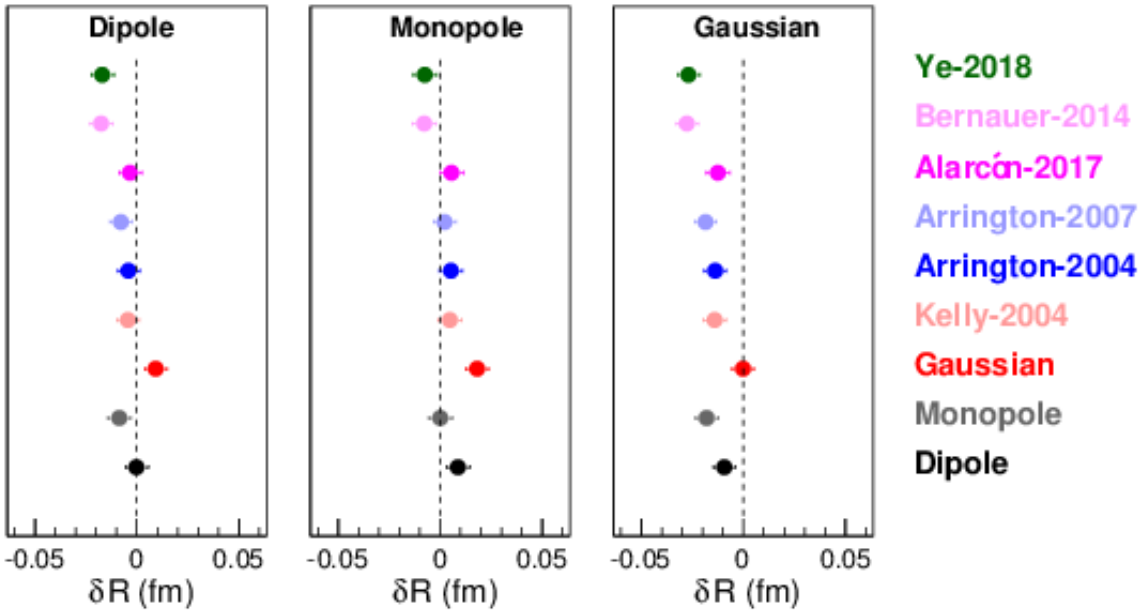

Figure 5.1: Robust fitter test results for the dipole, monopole and Gaussian fitters, based on the full PRad kinematic range, binning and statistical uncertainties. The figure is taken from Ref. [12]. Input form factor models can be found from Ref. [84, 93, 94, 95, 96, 97, 98].

The second order continuous fraction is also a robust fitter, but it is mathematically equivalent to the rational (1,1), so it will be excluded from further discussions. In addition, the second order polynomial expansion of Q^2 is slightly less robust compared to the rational (1,1) and the second order z transformation, as the deviations between the extracted r_p and the input r_p are close to the RMS values for some models.

5.2 Systematic Uncertainty on the Radius

The systematic uncertainties on the radius include all of those that can affect the cross section results, as discussed in Section 4.10, and also the uncertainty associated with the assumption about G_M^p during the extraction of G_E^p as discussed in the Sec-

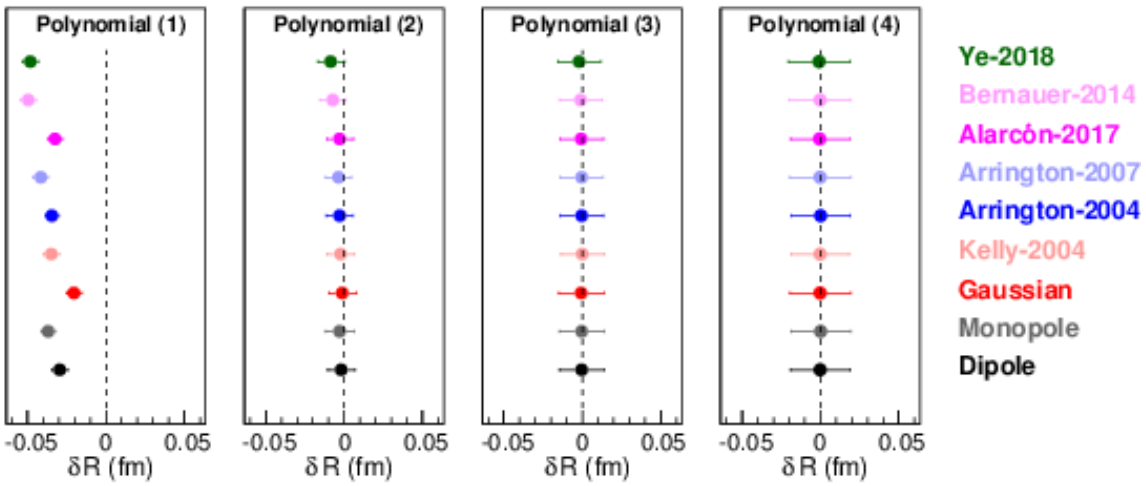

Figure 5.2: Robust fitter test results for the multi-parameter polynomial expansion of Q^2, based on the full PRad kinematic range, binning and statistical uncertainties. The figure is taken from Ref. [12]. Input form factor models can be found from Ref. [84, 93, 94, 95, 96, 97, 98].

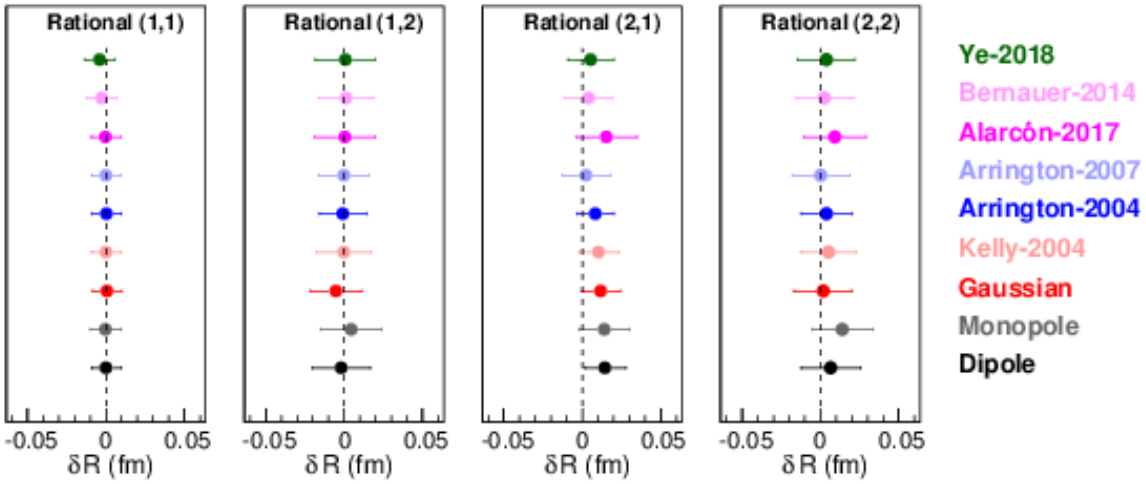

Figure 5.3: Robust fitter test results for the multi-parameter rational function of Q^2, based on the full PRad kinematic range, binning and statistical uncertainties. The figure is taken from Ref. [12]. Input form factor models can be found from Ref. [84, 93, 94, 95, 96, 97, 98].

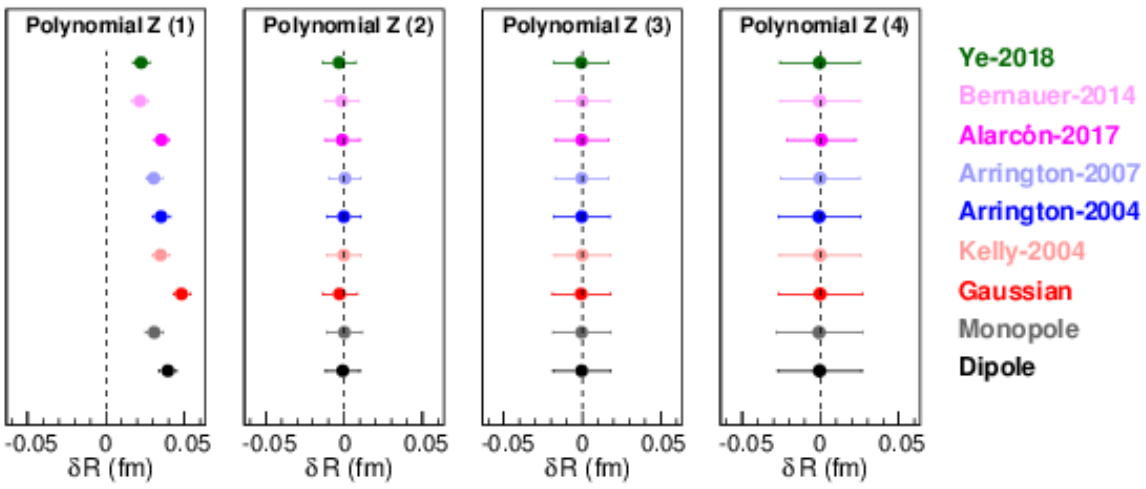

Figure 5.4: Robust fitter test results for the multi-parameter polynomial expansion of z, based on the full PRad kinematic range, binning and statistical uncertainties. The figure is taken from Ref. [12]. Input form factor models can be found from Ref. [84, 93, 94, 95, 96, 97, 98].

tion 4.11. A Monte-Carlo technique was used to evaluate the effect of these systematic uncertainties on the radius result. First of all, 100,000 data sets were generated based on the PRad cross section results. Then the data points were smeared by all the systematic uncertainty sources at once, and a set of G_E^p data points was extracted from each smeared cross section data set. For each systematic uncertainty source, if it was uncorrelated, then each cross section data point was smeared independently by a random number generated from a Gaussian distribution, with its width as the systematic uncertainty of this data point. If the systematic uncertainty source was correlated, then the correlation between different angular or Q^2 data points must be included in the smearing. Typically, the correlation could be described by low order polynomials or splines. Then the data points would be multiplied or divided by these correlation functions. For the mixed uncertainties (partially correlated and partially uncorrelated), such as those related to event selection cuts, the cross section tables were generated by randomly choosing the cuts within a given range ($\pm$ 50% of the

nominal kinematic cut for the 2.2 GeV $e-p$ in the $PbWO_4$ region for instance). For the uncertainty associated with the G_M^p assumption, a G_M^p model was randomly selected from Ref. [84, 90, 91, 92, 93, 94], and also the standard dipole model (see Eq. 4.32), when extracting G_E^p from the cross section data points.

Second, the extracted G_E^p data sets were fitted separately and a r_p value was extracted from each of these data sets. Only the statistical uncertainties were used during these extractions. Lastly, the RMS of these extracted r_p values was assigned as the systematic uncertainty. The distributions for these extracted r_p using the rational (1,1) and the second order z transformation are shown in Fig. 5.5. The contributions from individual systematic uncertainties are listed in Table 5.1, for the rational (1,1) fitter. In this case, the data points were smeared by the individual systematic uncertainty source only, while effects from other sources were turned off. The table also includes the systematic uncertainties for the normalization parameters n_1 and n_2 for the 1.1 and 2.2 GeV data sets respectively. The systematic uncertainties obtained with the second order z transformation are in general very similar to those from the rational (1,1), but slightly larger.

5.3 Proton Charge Radius Result

The $G_E^p(Q^2)$ extracted from the 1.1 GeV and 2.2 GeV data sets were fitted simultaneously using the rational (1,1) function. Independent normalization parameters n_1 and n_2 were assigned to the 1.1 and 2.2 GeV data sets, respectively, to allow for differences in the normalization uncertainties, but the Q^2-dependence was identical. The normalization parameters and r_p obtained from the fit to the rational (1,1) function are [99]:

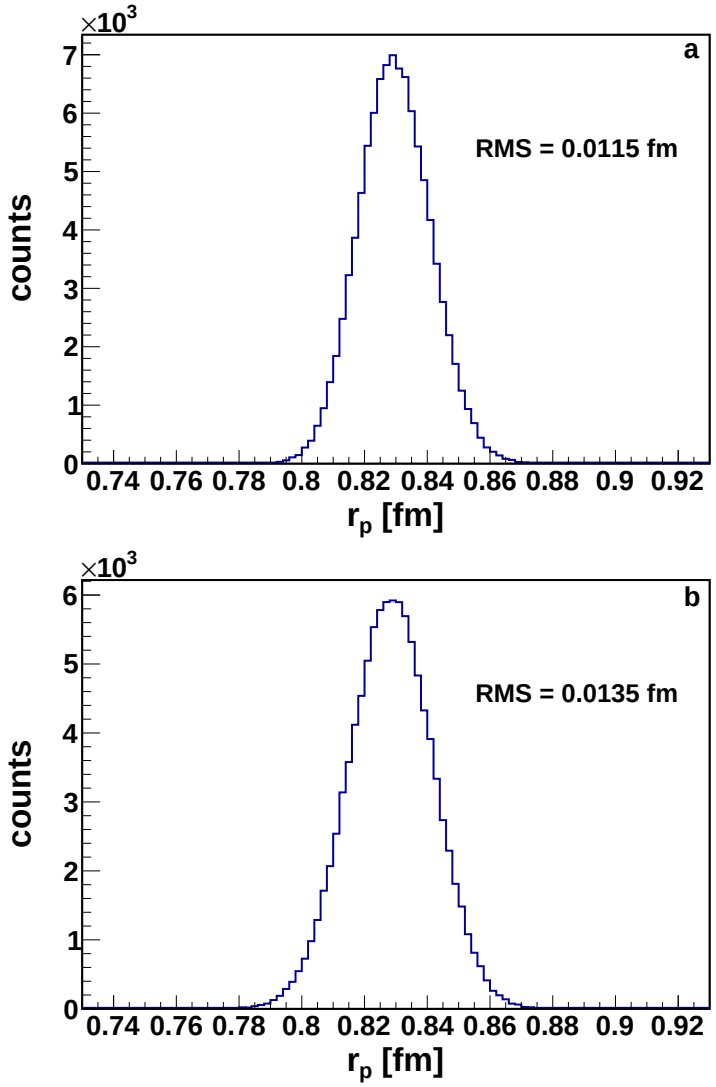

Figure 5.5: Distributions of r_p extracted using (**a**) the rational (1,1) and (**b**) the second order z transformation; from data sets that were smeared by all the PRad systematic uncertainties. The RMS of the distribution in (**a**) is 0.0115 fm and that for (**b**) is 0.0135 fm.

Item	r_p uncertainty [fm]	n_1 uncertainty	n_2 uncertainty
Event selection	0.0070	0.0002	0.0006
Radiative correction	0.0069	0.0010	0.0011
Detector efficiency	0.0042	0.0000	0.0001
Beam background	0.0039	0.0017	0.0003
HyCal response	0.0029	0.0000	0.0000
Acceptance	0.0026	0.0001	0.0001
Beam energy	0.0022	0.0001	0.0002
Inelastic ep	0.0009	0.0000	0.0000
G_M^p parameterization	0.0006	0.0000	0.0000
Total	0.0115	0.0020	0.0013

Table 5.1: The systematic uncertainty table for r_p and the normalization parameters. Items are arranged in decreasing order of the effect on r_p. The parameters n_1 and n_2 are the normalization parameters for the 1.1 GeV and 2.2 GeV data sets, respectively. Uncertainties are estimated using the rational (1,1) function.

$$\begin{aligned} r_p &= (0.831 \pm 0.007_{\text{stat.}} \pm 0.012_{\text{syst.}}) \text{ fm}, \\ n_1 &= 1.0002 \pm 0.0002_{\text{stat.}} \pm 0.0020_{\text{syst.}}, \\ n_2 &= 0.9983 \pm 0.0002_{\text{stat.}} \pm 0.0013_{\text{syst.}}. \end{aligned} \tag{5.12}$$

Only the statistical uncertainties were used when evaluating the central values. The rational (1,1) fit and the G_E^p data points from the experiment are shown in Fig. 5.6, compared to two recent G_E^p models [96, 97]. The 68% point-wise confidence level band for the total uncertainties of the result is shown in Fig. 5.7, compared to those from the same G_E^p models [96, 97]. The total uncertainties were taken as the quadratic sum of the total systematic uncertainties and the statistical uncertainties.

The rational (1,1) function describes the data reasonably well, with a reduced χ^2 of 1.3 when considering only the statistical uncertainties. The quality of the fit is shown in Fig. 5.8, where (**a**) shows the residuals (differences between data points

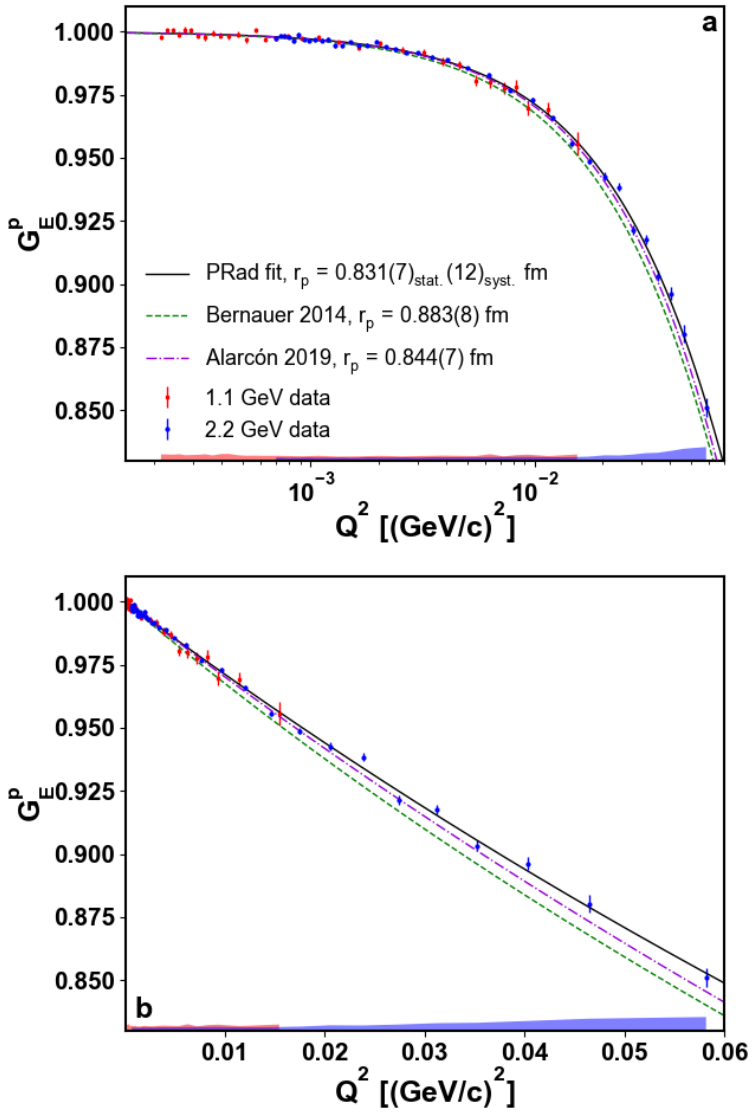

Figure 5.6: The proton electric form factor G_E^p as a function of Q^2. (**a**) uses a logarithmic x-axis while (**b**) uses a linear one. The data points are normalized by the n_1 and n_2 normalization parameters, for the 1.1 GeV (red) and 2.2 GeV (blue) data sets separately. Statistical uncertainties are shown as error bars. Systematic uncertainties are shown as colored bands. The solid black curve shows the $G_E(Q^2)$ from the fit to the function given by Eq. 5.10. Also shown are the parameterizations from the previous high-precision, magnetic spectrometer based $e-p$ experiment [96] (green dash line) and the calculation of Alarcon *et al.* [97] (purple dash line).

and the fit) of the fit, and (**b**) shows the pull distribution (residuals weighted by the statistical uncertainties of the data points). The largest deviation is about 2.5 standard deviations. For the pull distributions, if the uncertainties describe the fluctuation in the data points very well, one would expect that about 68% of the data points fall inside ± 1. This number is about 67% for the 1.1 GeV data set and about 58% for the 2.2 GeV data set.

The results obtained with the second order z transformation are very similar to those from the rational (1,1): $n_1 = 1.0002 \pm 0.0002_{\text{stat.}} \pm 0.0021_{\text{syst.}}$, $n_2 = 0.9983 \pm 0.0002_{\text{stat.}} \pm 0.0013_{\text{syst.}}$, and $r_p = (0.830 \pm 0.008_{\text{stat.}} \pm 0.013_{\text{syst.}})$ fm. Fig 5.9 shows the results obtained from the rational (1,1) and the second order z transformation, and also results obtained from other slightly less robust fitters. Based on our robustness tests [12], lower order functional forms such as the monopole, dipole, and the first order expansion of Q^2 (not shown here) tend to give smaller statistical uncertainties, but have larger uncertainties from the truncation of the Q^2 range and the extrapolation to $Q^2 = 0$, and also tend to produce larger biases depending on the input $G_E^p(Q^2)$ parametrization used. On the other hand, higher order functional forms such as the third order polynomial expansion of Q^2 (not shown here) and z transformation tend to give very large overall uncertainties. The results also confirm that rational (1,1) and the second order z transformation are the most robust fitting functions, giving the most consistent results with the least uncertainties for the Q^2 range of the PRad experiment.

The consistency of the radius extraction was further studied by extracting r_p from various sub-sets of the experimental data, such as the data collected with only the 1.1 GeV electron beam, only the 2.2 GeV electron beam, just the $PbWO_4$ modules, and the Q^2 range limited to < 0.016 (GeV/c)^2 and > 0.002 (GeV/c)^2. All the data sub-sets were fitted with the rational (1,1) functional form and the r_p values obtained are

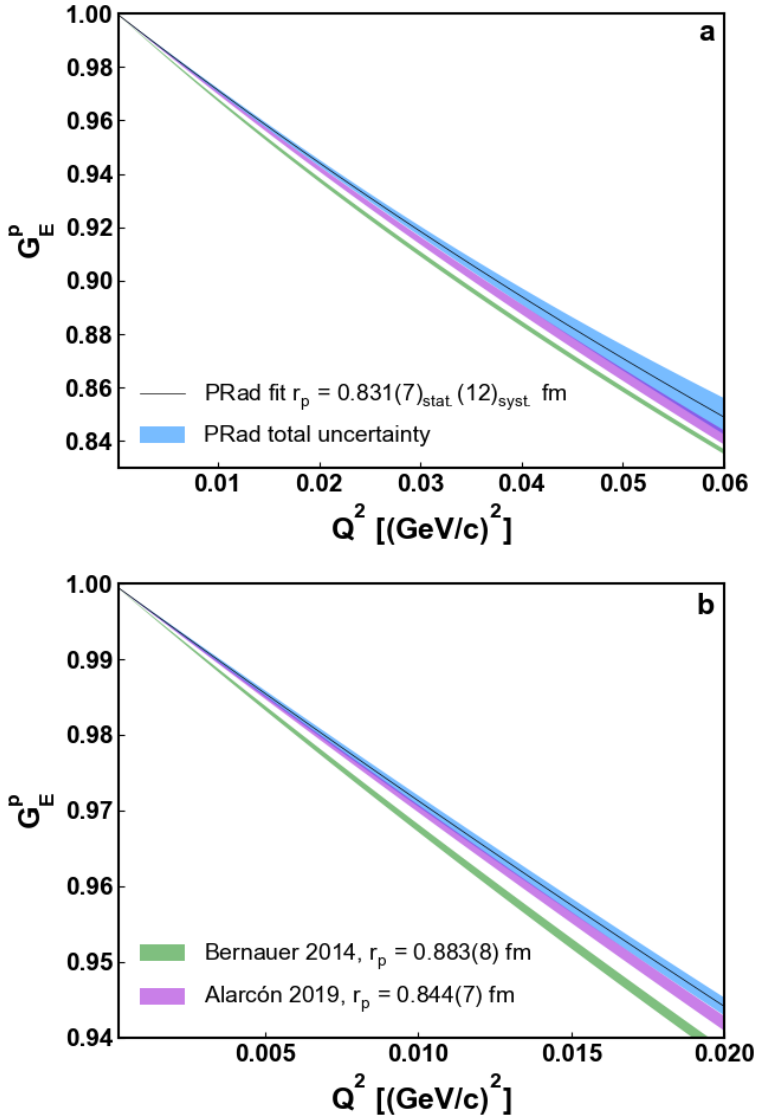

Figure 5.7: The 68% point-wise confidence level band of the rational (1,1) fit to the $G_E^p(Q^2)$ extracted from the PRad data (blue). Also shown are the bands from the previous high-precision, magnetic spectrometer based $e-p$ scattering experiment [96] (green) and the calculation of Alarcon *et al.* [97] (purple). **(a)** is for the entire PRad Q^2 coverage, **(b)** shows a zoom-in view for the $Q^2 < 0.02$ (GeV/c)^2 region.

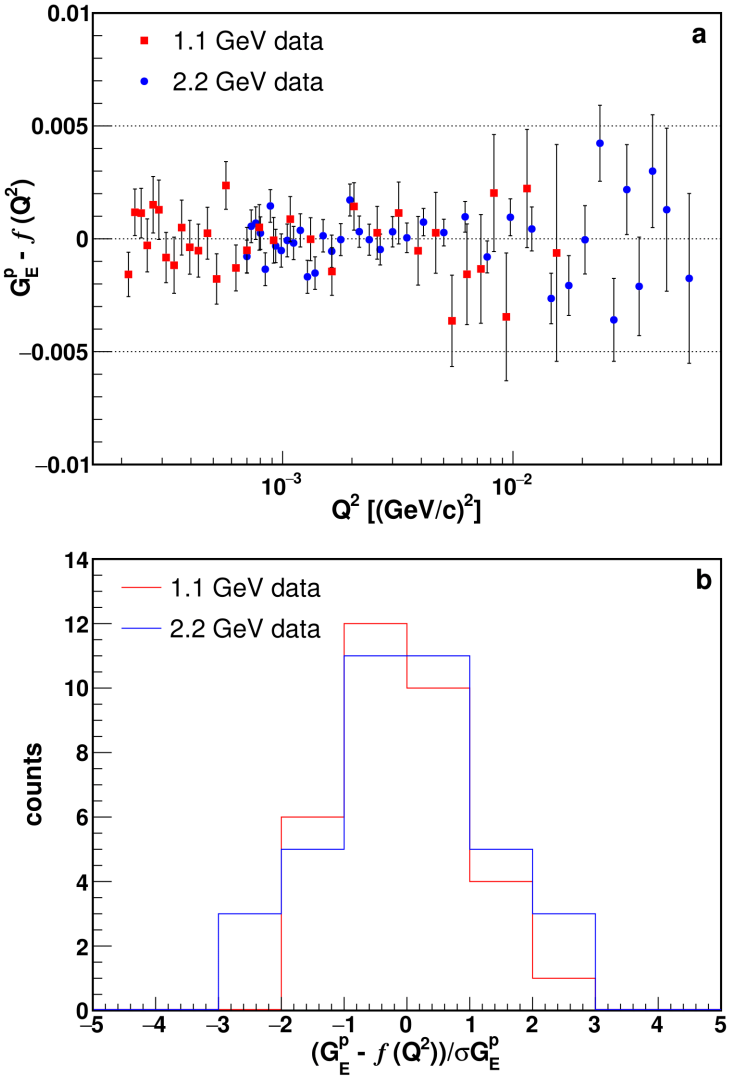

Figure 5.8: (**a**) shows the residuals between PRad G_E^p data points and the fit using the rational (1,1) fitter. Red squares are from the 1.1 GeV data set and blue dots are from the 2.2 GeV data set. Error bars contain only the statistical uncertainties. (**b**) shows the pull distributions (residuals weighted by the statistical uncertainties of the data points) for the 1.1 GeV (red) and 2.2 GeV (blue) data sets.

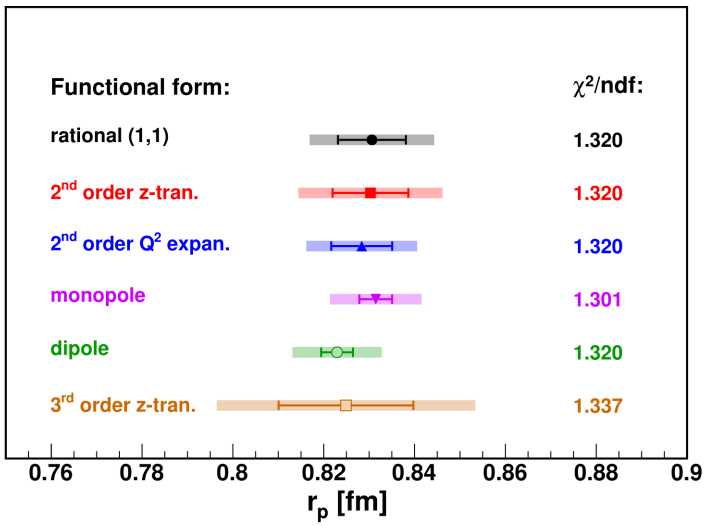

Figure 5.9: The r_p results obtained when using different fitters. Statistical uncertainties are shown as error bars, and the total uncertainties (quadratic sum of the total systematic and statistical uncertainties) are shown as colored bands. The rational (1,1) and the second order z transformation are identified as robust fit functions by Yan *et al.* [12].

consistent within statistical uncertainties as shown in Fig. 5.10 (**a**). However, the r_p values extracted from some data sub-sets, such as the ones with restricted Q^2 range, have larger uncertainties because the Q^2 coverage is reduced, and the rational (1,1) is not the most robust functional form for these data sub-sets. This is demonstrated in Fig. 5.10 (**b**), where the 1.1 GeV and 2.2 GeV data sets are separately fitted using the two best functional forms for these particular data sets, as determined from the robustness study [12].

The statistical fluctuation of the result was studied by separating the entire data set randomly into 20 subsets (10 for the 1.1 GeV and 10 for the 2.2 GeV settings). Each subset is then fitted with the same functional form, which is the monopole fitter for the 1.1 GeV subsets and the rational (1,1) for 2.2 GeV subsets[1]. The results

[1]The reason for choosing a lower order fitter for the 1.1 GeV subsets was that the uncertainty by using the rational (1,1) was too large (over 0.1 fm for each data point).

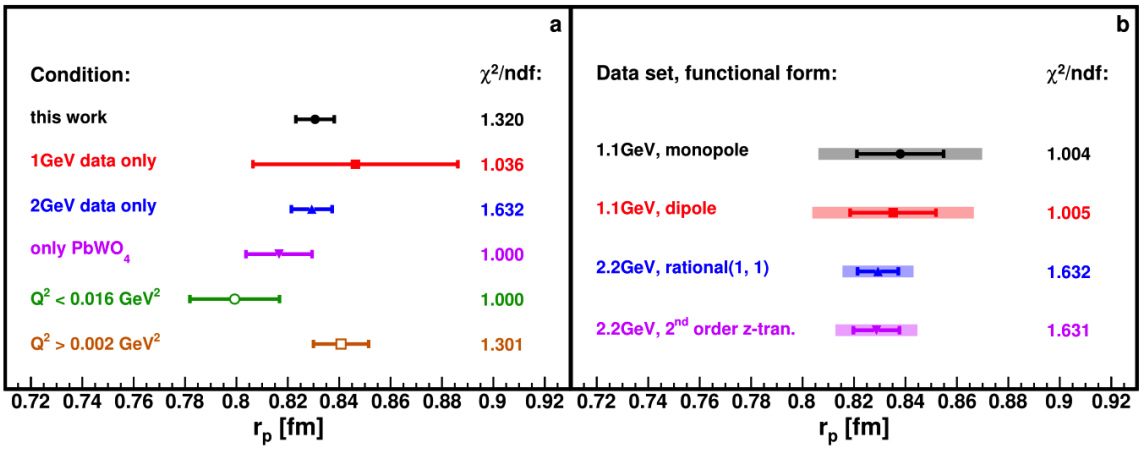

Figure 5.10: (**a**): the extracted r_p values under different conditions, as listed in the figure. All data points are obtained using the rational (1,1) fitter. Error bars show only the statistical uncertainties. (**b**): the monopole and dipole fits for the 1.1 GeV data points, and the rational (1,1) and the second order z transformation fits for the 2.2 GeV data points. Error bars show the statistical uncertainties. Colored bands show the total uncertainties.

from the subsets are well consistent statistically with the ones obtained by fitting the whole data sets, which are almost identical to the weighted averages from the subsets by their statistical uncertainties, as shown in Fig. 5.3.

Another important study is to extract the r_p result using only the integrated Møller method. As discussed in Section 4.10, a number of dominant systematic uncertainties are Q^2-dependent ones due to the Møller and they affect the result through the bin-by-bin method, as in this case, the $e-p$ to $e-e$ normalization is performed separately for each angular bin. On the other hand, for the integrated Møller method, all systematic uncertainties from the Møller can only affect the normalization of all data points and cannot introduce any Q^2-dependent systematic uncertainty. However, the integrated Møller method is more sensitive to systematic uncertainties such as the GEM efficiency, which cannot be determined well enough when the scattering angles are smaller than 1.3°. If one removes all data points below 1.3° for both en-

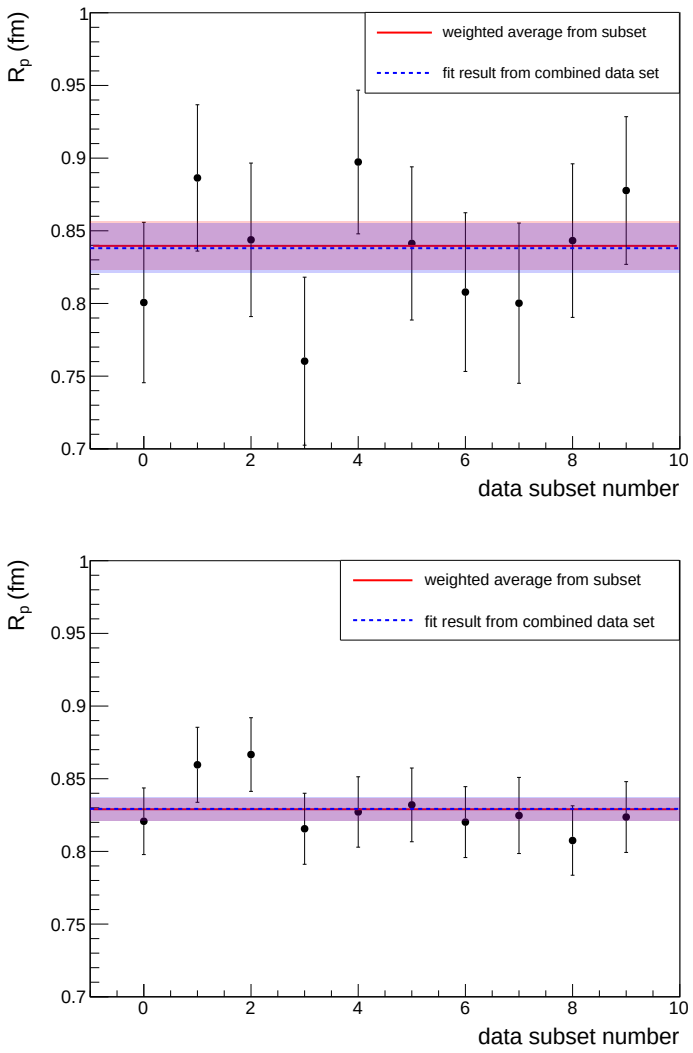

Figure 5.11: Radius results from the 10 different 1.1 GeV subsets (top plot), obtained using the monopole fitter, and 10 different 2.2 GeV subsets (bottom plot), obtained using the rational (1,1) fitter. Red solid lines and red shadow bands show the weighted average and statistical uncertainty from the subsets. Blue dash lines and blue shadow bands (almost underneath the rad bands) show the r_p and its statistical uncertainty by fitting the whole data set.

ergy settings and apply only the integrated Møller method, the extracted results will be: $n_1 = 1.0001 \pm 0.0003_{\text{stat.}} \pm 0.0018_{\text{syst.}}$, $n_2 = 0.9984 \pm 0.0004_{\text{stat.}} \pm 0.0014_{\text{syst.}}$, and $r_p = (0.834 \pm 0.010_{\text{stat.}} \pm 0.008_{\text{syst.}})$ fm, using the rational (1,1) fitter. They agree with the results shown in Eq. 5.12 within 1 standard deviation of the statistical uncertainties. In this case, the minimum Q^2 will be 6.3×10^{-4} (GeV/c)^2 for the 1.1 GeV and 2.4×10^{-3} (GeV/c)^2 for the 2.2 GeV data sets. In addition, removing data points below 1.3° also significantly reduces the effect due to the background generated from the upstream beam halo blocker, which is the dominating background source particularly in the forward angular region. The consistency of the r_p results demonstrates that the empty target run subtraction was rather effective.

Chapter 6

Possible Improvements on the Result

In this chapter, we discuss and present studies concerning a follow-up experiment to the PRad experiment, which we can PRad-II. The systematic uncertainty of the PRad r_p result is dominated by those uncertainties that primarily affect the low Q^2 data points. One of the reasons is that in the low Q^2 region, form factors with different r_p values all converge to unity, while at the highest Q^2 region, they can differ by a few percent. If one has a 0.1% Q^2-dependent systematic shift for the data points in the low Q^2 region, the impact on the extracted r_p is significantly larger than the case if the same systematic shift appears in the high Q^2 region. These systematic uncertainties include the beam-line background subtraction, radiative correction for the Møller, event selection, beam energy and acceptance. In particular, many of them are dominated by the Møller, which occupies mostly the forward angular region and its angular distribution is very sensitive to these systematic uncertainties. The Q^2-dependent systematic uncertainties from the Møller are introduced to the cross sections through the use of the bin-by-bin method. If the precision of the GEM efficiency measurement can be improved in this region, one should consider using the integrated Møller method for all the data points. In this case, both statistical and systematic uncertainties due to the Møller can only affect the normalizations of the data points and will not contribute to the systematic uncertainties of r_p. For example, in the cases of the beam energy and detector position systematic uncertainties, one finds that if the integrated Møller method is applied to all angular bins, these two systematic uncertainties mostly just shift all the results up or down at the same time,

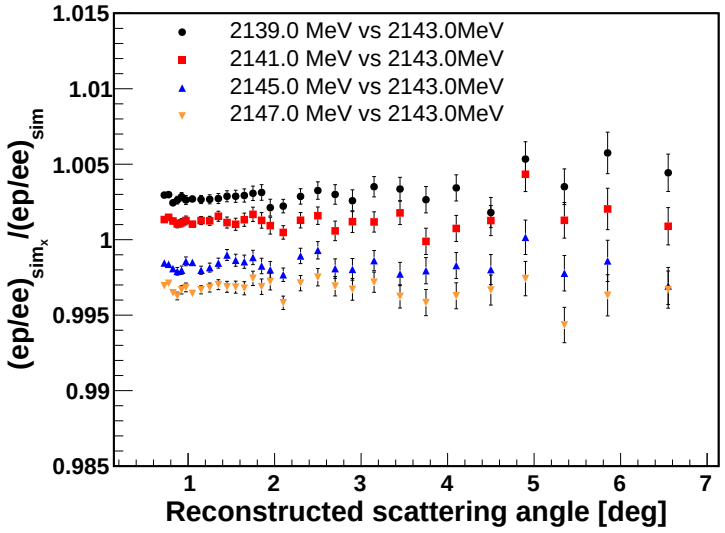

Figure 6.1: The $e-p$ to $e-e$ ratios from different simulations with different beam energies (labeled as sim_x) over the one with the nominal beam energy (labeled as sim), in the case of the 2.2 GeV energy setting. The integrated Møller method is applied to all angular bins.

as shown in Fig. 6.1 and Fig. 6.2.

These can be compared to Fig. 4.53 and Fig 4.55, for which the bin-by-bin method is applied to the angular bins with $\theta < 1.6°$, and the results show obvious Q^2 dependency in this region. Similarly, this method can be applied to turn the Q^2-dependent systematic uncertainties in the Møller event selection and radiative correction completely into normalization uncertainties. However, in the case of the PRad experiment, the GEM efficiency can not be determined well enough in the forward angular region because of two major reasons. First, the HyCal position reconstruction is not good enough to resolve the dead areas on the GEMs, such as the GEM spacers. This causes a significant bin migration effect and the uncertainty in the GEM efficiency correction is very dominant in the very forward angular region (see Fig. 4.29). This difficulty can be overcome by using another layer of GEM detectors. When calculating the GEM efficiency in this case, one would require a matching hit pair on one

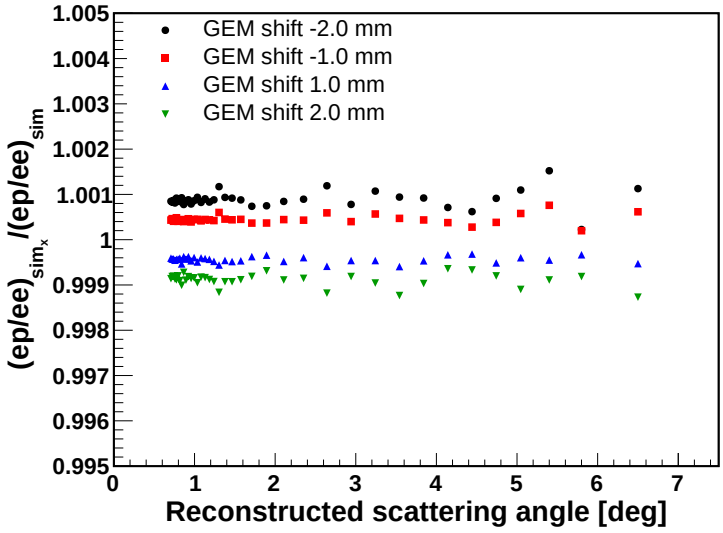

Figure 6.2: The $e-p$ to $e-e$ ratios from different simulations with shifted GEM positions (positive shift means shift to down stream, labeled as sim_x) over the one obtained from the standard simulation (labeled as sim), in the case of the 2.2 GeV energy setting. The integrated Møller method is applied to all angular bins.

GEM layer and the HyCal, and then look for whether there is a hit found on the other GEM layer. The incident angle would be determined by the matching GEM hit, which will eliminate the bin migration issue due to the HyCal resolution and non-uniformity in the position reconstruction. The expected systematic uncertainty in the GEM efficiency correction, due to the GEM dead areas, is shown to be better than 0.1% (see Fig. 6.3), and the corresponding systematic uncertainty on r_p will be much smaller than that from the PRad. The uncertainty is determined using a similar approach as discussed in Section 4.6, by comparing the $e-p$ to $e-e$ ratios obtained using perfect GEM detectors in the simulation and those with more realistic GEMs including the spacers and other dead areas. This systematic uncertainty can be further reduced if one assembles the second GEM using a new technique [123], which requires no spacers in between the GEM foils. Second, the very forward angular region suffers from the background that is generated from very-small-angle-scattering

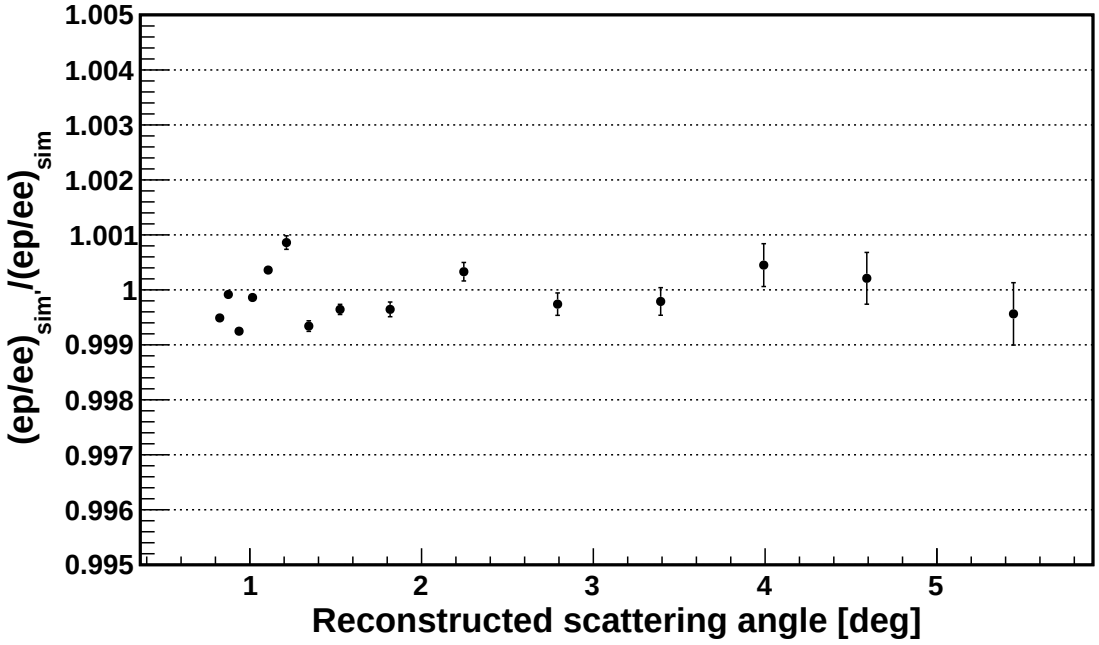

Figure 6.3: The expected GEM efficiency correction uncertainty on the cross section if a second GEM layer were used.

particles hitting the downstream beam pipe and other surrounding objects (see Section 4.5.4). This type of background cannot be rejected by the HyCal alone, but can be rejected when combining one GEM layer and the HyCal, since these tracks cannot be projected back to the target region. In addition, other backgrounds for the GEM efficiency measurement, such as the cosmic events and high energy photons, will be rejected easily by having a second GEM layer. The collaboration is currently working on more detailed simulations to study the improvement of the GEM efficiency. We will also consider using the overlapping region of the PRad GEM data (there was a 4.4 cm $\times$ 123 cm overlapping region for PRad GEMs, see Section 3.4) to demonstrate the improvement, as in this case there were two separated GEM planes in this region.

Another benefit of having two separated GEM detector layers is that, once the distance in between the two layers is large enough, one can reconstruct the vertex-z

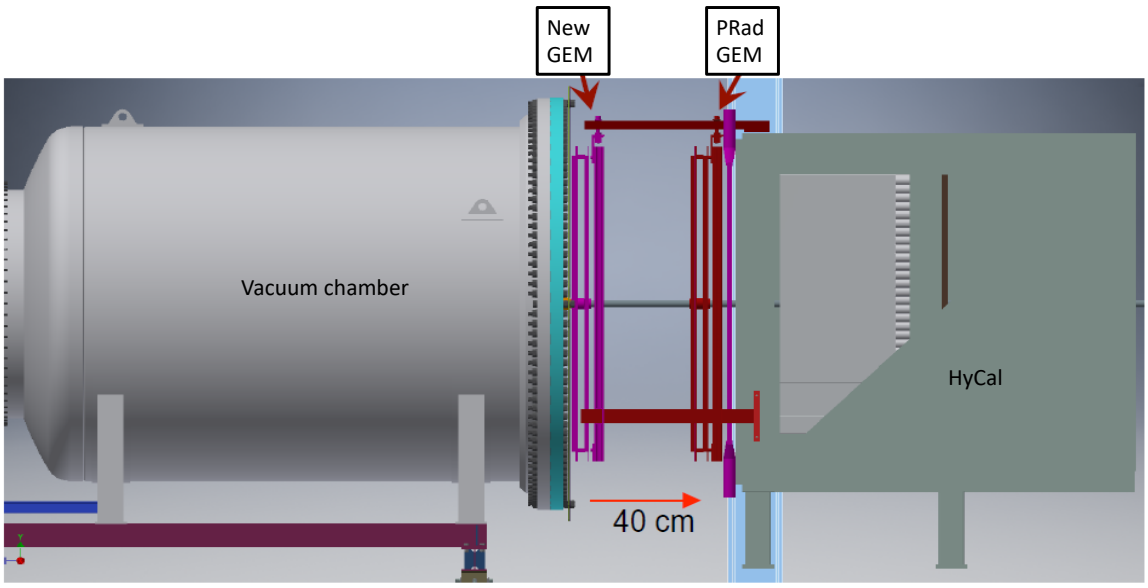

Figure 6.4: The proposed experimental setup for PRad-II.

for the $e-p$ events with a reasonable resolution in order to reject the background that is generated very far away from the target center. In particular, it can reject the background generated from the upstream beam halo blocker, which is about 2 m upstream from the target and its background is a few times larger than all the other beam-line backgrounds combined. This can significantly suppress the systematic uncertainties related to the beam-line background subtraction. The proposed setup will have the PRad HyCal and GEMs pushed slightly downstream and have the second GEM layer placed immediately after the vacuum chamber, as shown in Fig. 6.4. With a 40 cm distance between the two GEM layers, the vertex-z resolution can be better than 30 cm as shown in Fig. 6.5 for the 2.2 GeV beam setting, which is sufficient to reject the background generated from the upstream halo blocker. The resolution can be further improved by using a thiner aluminum vacuum window (0.8 mm instead of 1.6 mm as for the PRad experiment for example), or by pushing the PRad GEMs and the HyCal slightly downstream, at a cost of sacrificing slightly the maximum Q^2

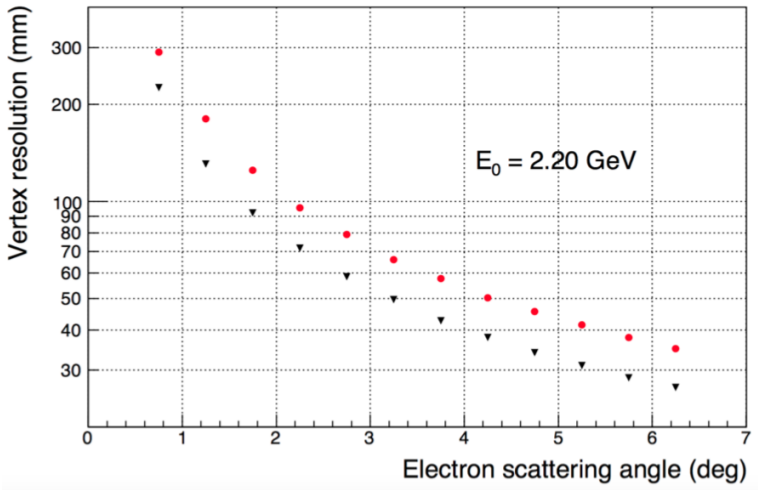

Figure 6.5: The vertex-z resolution for the $e-p$ events as a function of the scattering angle, reconstructed using two GEMs layers that are separated by 40 cm, for the 2.2 GeV beam energy setting. For the red dots, the simulation uses a 1.6 mm thick aluminum vacuum window, which is true in the case of the PRad experiment. The black triangles assume a 0.8 mm thick vacuum window. The plot is taken from [124].

coverage.

Other than the possible improvements mentioned above, there is a plan to include calculations for the next-to-next-leading order Feynman diagrams in the radiative correction (currently only the next-to-leading order diagrams included), which will further reduce this systematic uncertainty. The dominant part is the Møller radiative correction and it can already be reduced by using the integrated Møller method. The remaining part comes from the $e-p$ elastic scattering, and it should be reasonable to assume that even higher order contributions should be one order of magnitude smaller than that from the next-to-next-leading order. The future experiment should also consider to increase the statistics by a factor or 4 at least so that the statistical uncertainty of r_p can be suppressed to a 0.003 fm level. The increase of statistics can also help reducing the systematic uncertainties due to the event selection and HyCal response in the large angular region. For the PRad experiment, the energy

spectrum agreement between the data and simulation is significantly worse in the Pb-glass region. As shown in Fig. 4.47 and Fig. 4.48, the variation on the cross section is significantly larger if one changes the size of the event selection cuts, compared to the $PbWO_4$ region. This is partially due to the lack of statistics for the energy calibration of the HyCal. And also for the same reason, one has to combine multiple modules to extract certain properties, such as their light attenuation and non-uniformity properties in the energy reconstruction. With more statistics, these types of studies can be done module by module, and thus improving the agreement between the data and the simulation. It should be reasonable to assume a factor of 2 reduction for the systematic uncertainties associated with the event selection and HyCal response in the large angular region. With 4 times more statistics, a second GEM layer, the planned use of the integrated Møller method for all data points and the same beam energy settings as for the PRad experiment, the projected statistical and systematic uncertainty for PRad-II are shown in Table 6.1 (as PRad-II type A), and compared to those from the PRad experiment. The major improvement comes from the planned use of the integrated Møller method for all data points. This item alone can already reduce the total systematic uncertainty by about a factor of 2, as long as the GEM efficiency is known to better than 0.1% precision. As discussed earlier in this chapter, this method will turn all the systematic uncertainties from the Møller into normalization uncertainties, and thus will not introduce any systematic uncertainties in r_p. Such systematic uncertainties include the Møller event selection, Møller radiative correction, acceptance and beam energy. Further improvements may come from the rejection of some beam-line background using two GEM planes, fixing all the dead modules of the HyCal, better modeling for the HyCal response, better simulation for the target gas profile and so on.

The future experiment can also exploit possible benefits from enlarging the Q^2

Item	PRad δr_p [fm]	PRad-II type A δr_p [fm]	PRad-II type B δr_p [fm]
Stat. uncertainty	0.0075	0.0036	0.0034 (0.0036)
Event selection	0.0070	0.0034	0.0024 (0.0024)
Radiative correction	0.0069	0.0004	0.0004 (0.0004)
Detector efficiency	0.0042	0.0028	0.0028 (0.0030)
Beam background	0.0039	0.0016	0.0012 (0.0013)
HyCal response	0.0029	0.0014	0.0005 (negligible)
Acceptance	0.0026	negligible	negligible (negligible)
Beam energy	0.0022	0.0001	0.0001 (0.0001)
Inelastic ep	0.0009	0.0009	0.0002 (negligible)
G_M^p parameterization	0.0006	0.0006	0.0007 (0.0006)
Total syst. uncertainty	0.0115	0.0049	0.0040 (0.0042)
Total uncertainty	0.0137	0.0061	0.0052 (0.0055)

Table 6.1: The uncertainty table for r_p from the PRad experiment, and projected uncertainties for PRad-II. Uncertainties are estimated using the rational (1,1) function (Eq. 5.10). PRad-II type A assumes the same beam energy settings as PRad. PRad-II type B assumes an additional 3.3 GeV beam energy setting. For PRad-II type B, the numbers in the parenthesis are estimated assuming the Pb-glass detectors will not be used for all three beam energy settings. Otherwise, they will be used for the 1.1 GeV and 2.2 GeV settings.

coverage and overlapping region, such as using the 0.55 GeV, 1.65 GeV, 2.75 GeV, and 3.3 GeV beam energies. This will help constraining possible beam-energy-dependent systematic uncertainties. One possible configuration is to add an additional 3.3 GeV electron beam setting and use only the $PbWO_4$ part of the HyCal for this beam energy. The $PbWO_4$ detectors provides a scattering angle coverage from 0.7° to about 4.5° (including the corners of $PbWO_4$ detectors), and a maximum Q^2 coverage of 0.066 (GeV/c^2) with the 3.3 GeV beam, which is similar to the PRad experiment. The excellent energy resolution of the $PbWO_4$ detectors will still allow one to remove almost completely the inelastic $e-p$ contribution and reduce its systematic uncertainty. As shown in Fig. 6.6, the inelastic $e-p$ events can be safely rejected using a 3σ energy cut, even at 4.5° with the 3.3 GeV beam energy. The inelastic $e-p$ contribution is less than 0.1% in the $PbWO_4$ region at this beam energy setting. The $PbWO_4$ detectors also behaved more uniformly and were better modeled for the

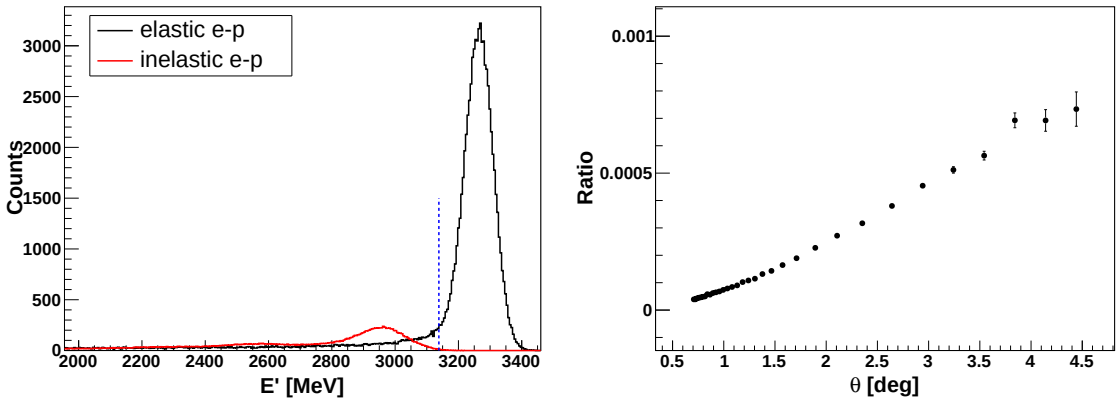

Figure 6.6: Left plot: the energy spectrums for the elastic (black histogram) and inelastic (red histogram) $e-p$ with the 3.3 GeV beam energy at around 4.5° scattering angle. Only the $PbWO_4$ part of the HyCal is used. The blue dash line indicates a 3σ kinematic cut. Right plot: the ratio between the inelastic $e-p$ and elastic $e-p$ counts with 3.3 GeV beam energy as a function of the scattering angle θ, using the 3σ kinematic cut.

PRad experiment. Thus the systematic uncertainties associated with HyCal response and event selection are also expected to be under better control.

A possible PRad-II type B run plan consists of both 1.1 and 2.2 GeV runs with 2 times more statistics compared to the PRad, and an additional 3.3 GeV setting using only the $PbWO_4$ part of the HyCal. The beam time for the 3.3 GeV setting is assumed to be roughly 260 hours with a 55 nA beam current (included 52 hours of beam time for the empty target runs). This plan can produce a similar statistical uncertainty for r_p as the PRad-II type A. The Q^2 coverage for each beam energy setting and the projected relative statistical uncertainties on the cross section are shown in Fig. 6.7. An advantage of this run plan is that, the $e-p$ elastic scattering cross section will be measured at least twice for most part of the total Q^2 coverage, which is very useful for cross-checking the beam-energy-dependent systematic uncertainties.

Since the beam energy setting is different, it is also important to study the robustness of the rational (1,1) fitter for this configuration. The results, obtained following

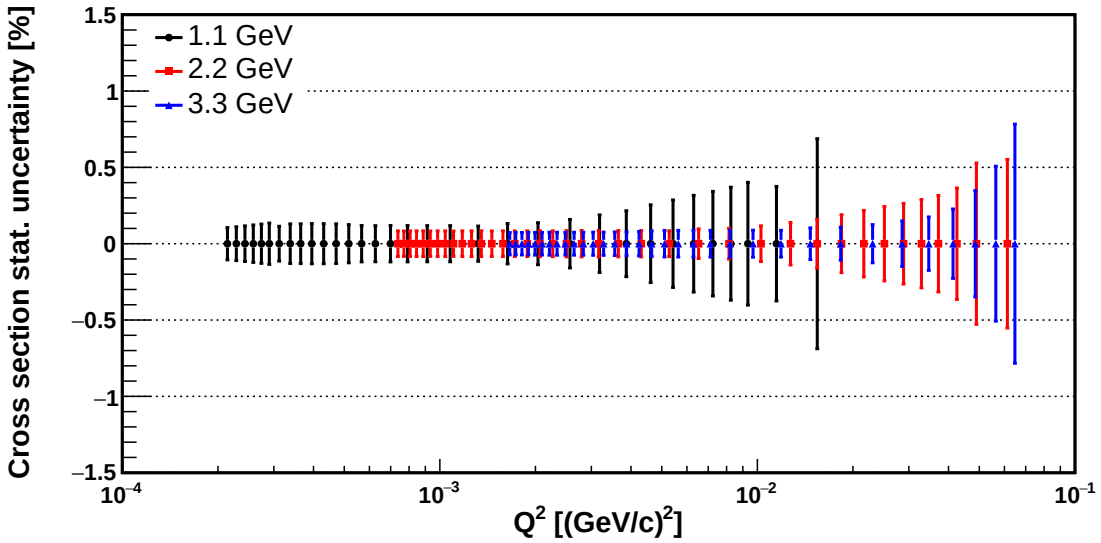

Figure 6.7: The Q^2 coverage and the relative statistical uncertainties for the cross sections for each beam energy setting in the PRad-II type B run plan.

the same approach in Ref. [12], are shown in Fig. 6.8[1]. The study indicates that the rational (1,1) fitter is still a robust fitter for this configuration. Assuming a second GEM layer will be available, the projected statistical and systematic uncertainties for the PRad-II type B are shown in Table 6.1, and compared to those from the PRad experiment. The improvement is also dominated by the use of the integrated Møller method for all data points. For both types of the PRad-II experiments, the expected total uncertainties on r_p are over two times smaller than that from the PRad experiment. The projected total uncertainties are shown in Fig. 6.9, along with the PRad result and other recent r_p measurements.

[1]The form factor model from Ref. [98] is removed from the test as the r_p parameter was fixed to the CODATA-2014 value during fitting. This approach is different from the fitting procedures used for other form factor models used in the robustness test.

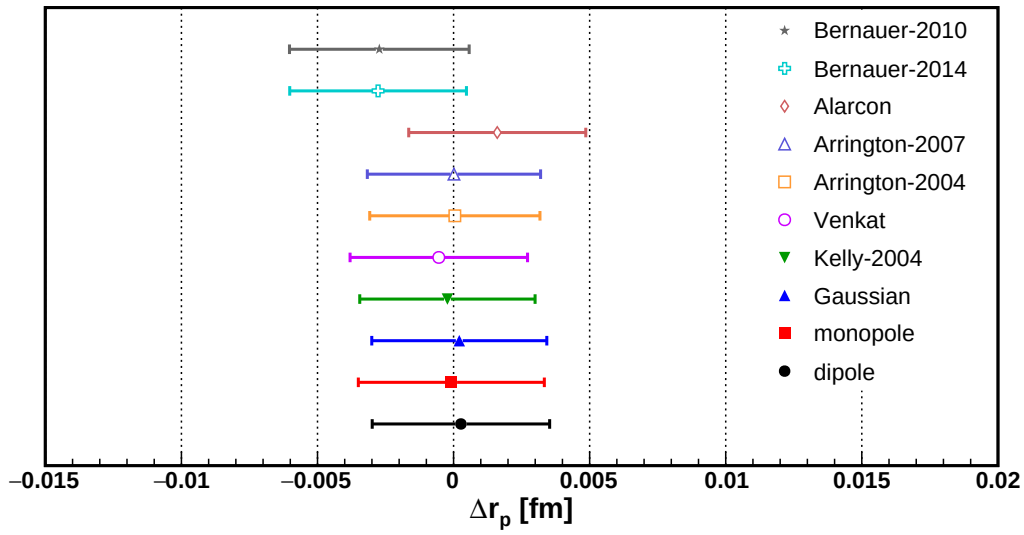

Figure 6.8: Robust fitter test results for the rational (1,1) fitter, based on the PRad-II type B kinematic range, binning and statistical uncertainties, as shown in Fig. 6.7. Input form factor models can be found from [84, 90, 93, 94, 95, 96, 97, 92].

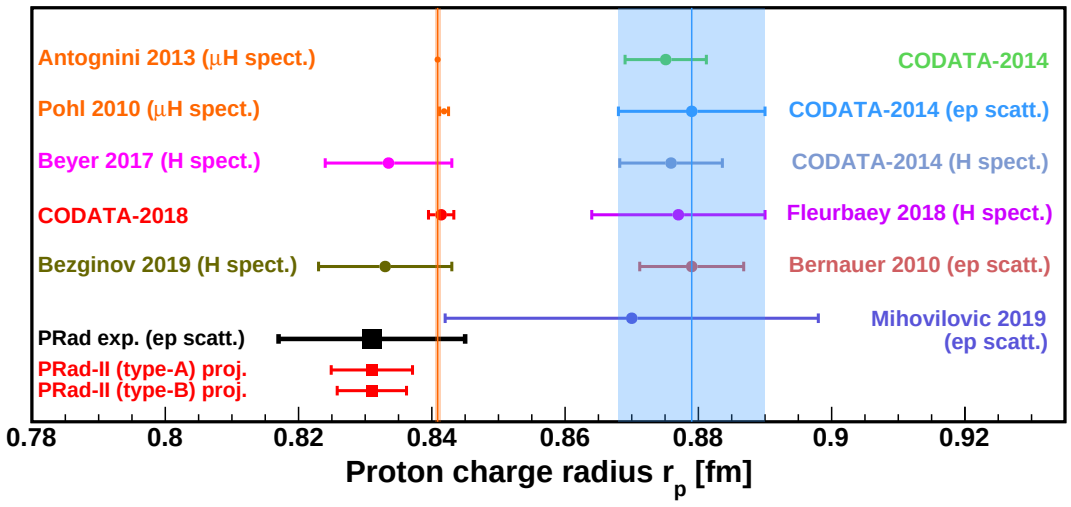

Figure 6.9: Projected total uncertainties on r_p for PRad-II type A and type B run plans are shown along with the PRad r_p result and other recent r_p measurements.

Chapter 7

Conclusion

In conclusion, this dissertation presents the analysis and results for the PRad experiment, which measured the proton electric form factor G_E^p in the Q^2 region $Q^2 = 2.1 \times 10^{-4} - 0.06$ $(\mathrm{GeV/c})^2$. The PRad r_p result, obtained by fitting G_E^p using the rational (1,1) function, is shown in Figure 7.1, with statistical and systematic uncertainties summed in quadrature. The result is also compared with a number of previous r_p measurements. It shows a significant discrepancy compared to results obtained from previous $e-p$ elastic scattering experiments. For instance, it is about 3-standard deviations smaller than the high-precision electron scattering measurement at MAMI [5], which was a spectrometer based experiment and the Q^2 was limited to higher values (> 0.0038 $(\mathrm{GeV/c})^2$), and it is about 2.7-standard deviations smaller than the CODATA-2014 recommended value for r_p based on the results from previous $e-p$ scattering experiments. However, the result of this experiment is in agreement with the muonic hydrogen spectroscopic measurements [1, 6], and also two recent ordinary hydrogen spectroscopic results including the 2S-4P transition frequency measurement [18] and the 2S-2P Lamb shift measurement [20]. This result is also consistent with the most recent announced r_p value from CODATA-2018 [100]. The result of this experiment does not support any fundamental difference between the $e-p$ and $\mu-p$ interactions.

The comparison between the PRad G_E^p and a number of previous measured G_E^p data sets [15, 36, 37] are shown in Fig. 7.2. The top plot shows the full PRad Q^2 range and the bottom plot shows only the $Q^2 < 0.02$ $(\mathrm{GeV}/c)^2$ range. The G_E^p data set for the Mainz 2010 experiment [5, 96] is obtained from Ref. [15]. Generally speak-

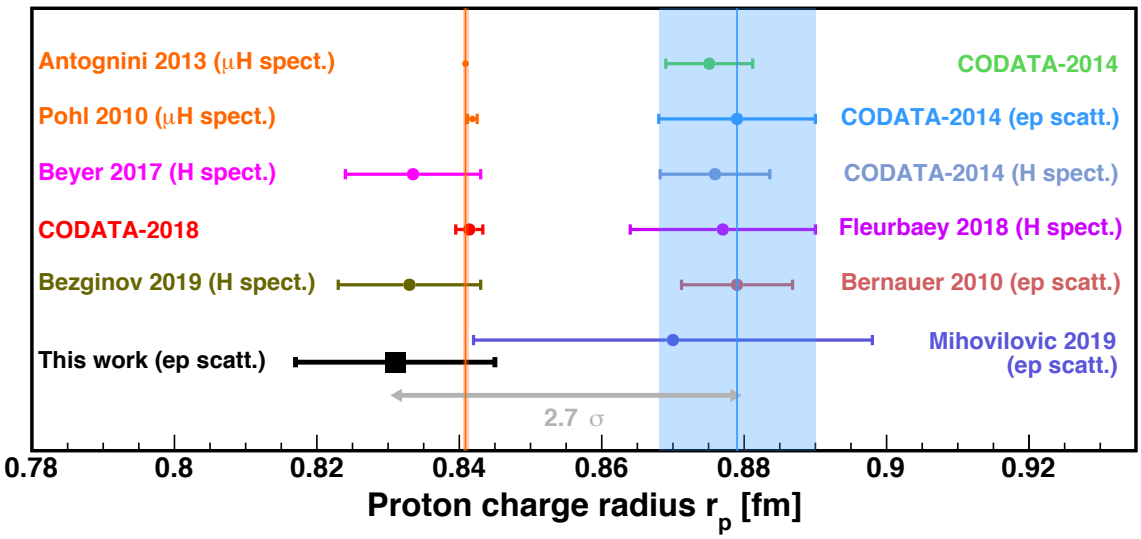

Figure 7.1: The r_p extracted from the PRad data, shown along with the other measurements of r_p since 2010 and the CODATA recommended values. The PRad result is 2.7-σ smaller than the CODATA recommended value for $e-p$ scattering experiments [7]. Other results can be found from [1, 5, 6, 18, 19, 20, 22, 100]

ing, the PRad G_E^p data points are consistent with the previous measurements in the $Q^2 < 0.02$ $(\mathrm{GeV}/c)^2$ range, while the PRad points are consistently larger in the higher Q^2 range. To understand this difference, one may consider various systematic uncertainties of these experiments. The PRad experiment is less sensitive to systematic uncertainties associated with the integrated luminosity of the measurement, as the Møller scattering was measured simultaneously and data points with difference Q^2 were collected at the same time. However, it is more sensitive to inelastic $e-p$ contribution due to a worse energy resolution compared to magnetic spectrometers, and also to the detector response of the Pb-glass shower detectors of the HyCal. Systematic uncertainties due to these two sources can be reduced significantly for PRad-II as discussed in Ch. 6. The difference may also arise from radiative corrections, which are quite different for the PRad experiment and other magnetic-spectrometer-based experiments. Lastly, the difference may be also related to the proton magnetic form

factor contribution in the cross section. Important inputs can be obtained in the future from high precision G_M^p measurements at very low Q^2. Such measurements may be provided by experiments such as (but not limited to) Ref. [25, 53].

The comparison between the r_p result obtained from this experiment, and other r_p results from previous $e-p$ elastic scattering experiments and analyses are shown in Fig. 7.3[1]. Compared to the previous measurements, the PRad experiment used a spectrometer-free approach and is the first $e-p$ elastic scattering experiment to cover two orders of magnitude of low Q^2 region in one detector setting. This means that for each beam energy setting, data points at different Q^2 were recorded simultaneously, with all the detectors fixed in location for the entire data taking process. This eliminates the need for having vast multitude of normalization parameters, which may introduce additional systematic uncertainties to the result. The lowest Q^2 measured by this experiment, $2.1\times10^{-4}(\mathrm{GeV/c})^2$, is currently the lowest measured value for all $e-p$ elastic scattering experiments. This reduces the uncertainties due to extrapolation in the r_p extraction. Further measurements for r_p are certainly needed particularly from lepton-proton elastic scattering experiments. A number of $e-p$ and $\mu-p$ elastic scattering experiments are currently under preparation [21, 23, 24, 25, 26, 27, 53], which will certainly provide useful inputs for the puzzle. The initial state radiation technique has been proven to be viable by the ISR experiment at MAMI [22], and a new experiment is planned using the same technique, but with a point-like jet target and an improved spectrometer entrance flange to further reduce the systematic uncertainties [21]. An important result is expected in the next few years from the MUSE collaboration [23], which will use e^+, e^-, μ^+ and μ^- beams to perform lepton-proton elastic scattering measurements, and has a sufficiently large Q^2 coverage (0.002 to 0.07 $(\mathrm{GeV/c})^2$). The expected precision on r_p is about 0.01 fm for each of the incident

[1]Thanks to Douglas Higinbotham for providing all the references for the plot.

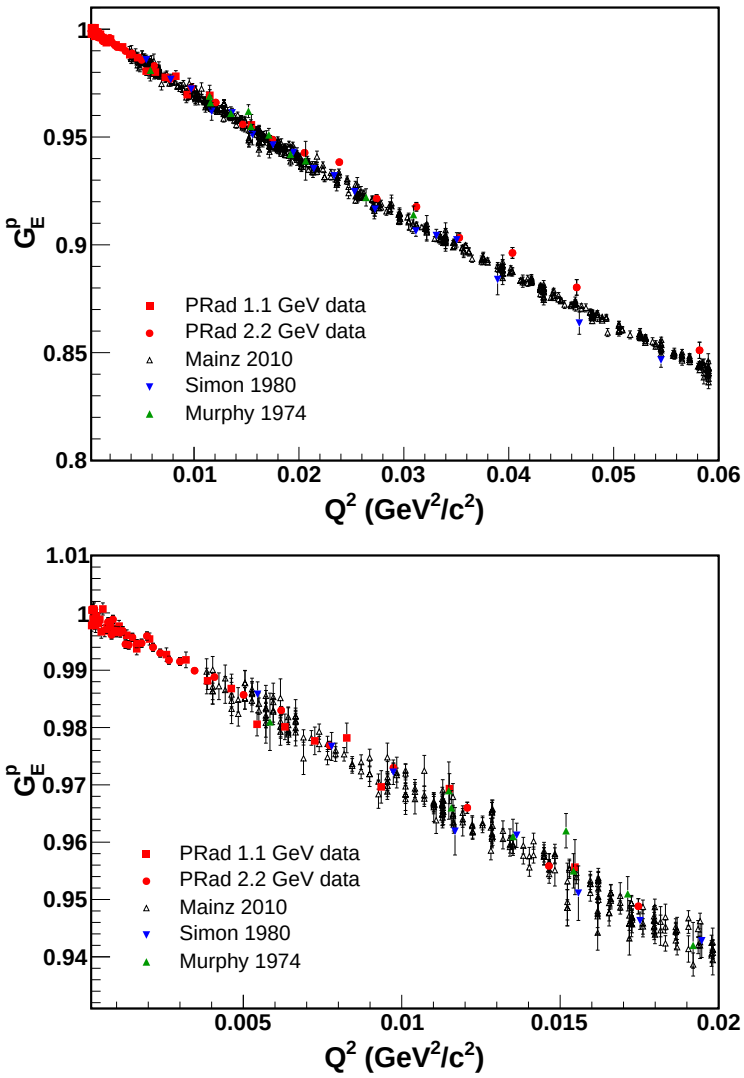

Figure 7.2: Comparison between PRad G_E^p and a number of previously measured G_E^p data sets [15, 36, 37]. The top plot is for the full PRad Q^2 range while the bottom plot is only for $Q^2 < 0.02$ (GeV/c)^2. The error bars for the PRad data contain only statistical uncertainties.

leptons. This experiment can directly test the lepton universality and will be very important for fully resolving the proton charge radius puzzle. In addition, the PRad collaboration has a plan to perform a follow-up experiment to the PRad experiment. As discussed in Chapter 6, this new experiment will include a second GEM plane to improve the tracking capacity and the precision of the GEM efficiency measurements, which allows the application of the integrated Møller method to all angular bins. It is quite possible that the new experiment can reduce the total uncertainty of r_p by a factor of 2 to 3, compared to the PRad result.

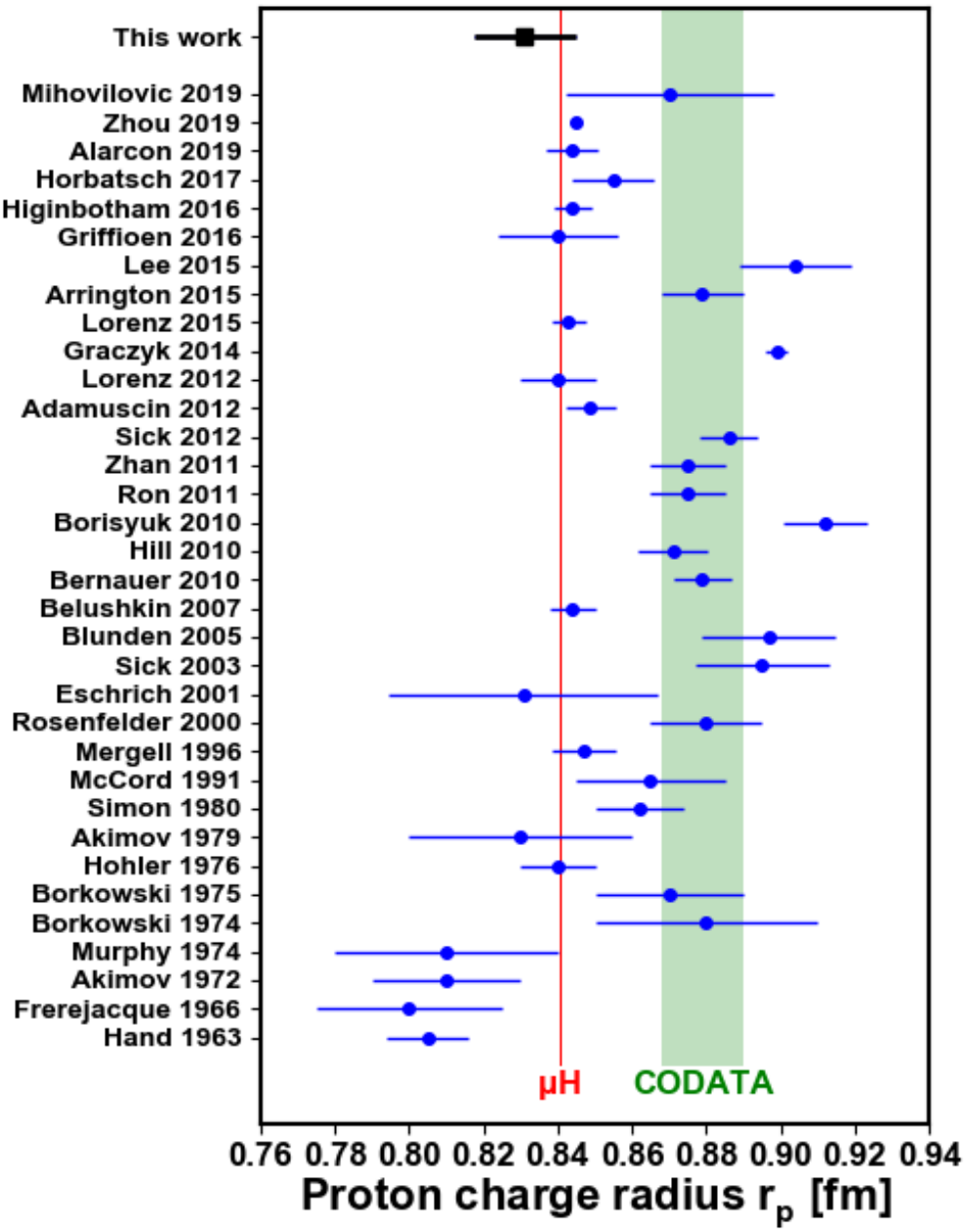

Figure 7.3: The r_p extracted from the PRad data (black squares), shown along with the other measurements or analyses of r_p from $e-p$ elastic scattering experiments (blue dots). Data points are obtained from references (bottom to top) [30, 101, 102, 37, 48, 95, 103, 104, 36, 105, 106, 107, 108, 109, 110, 111, 5, 112, 113, 114, 38, 115, 116, 117, 118, 119, 120, 13, 15, 16, 121, 97, 122, 22]

Appendix A

Cross Section and Form Factor Data

The fitting function (rational (1,1)) used to obtain the PRad final r_p result is,

$$f(Q^2) = nG_E^p(Q^2) = n\frac{1 + p_1^a Q^2}{1 + p_1^b Q^2}, \tag{A.1}$$

where n is 1.0002 for the 1.1 GeV data set and 0.9983 for the 2.2 GeV data, p_1^a is -0.07146 and p_1^b is 2.88141, both in $(\mathrm{GeV/c})^{-2}$. Please see Chapter 5 for more details Table A.1 and Table A.2 contain the cross sections and the $f(Q^2)$, that is, they include the floating parameters n. Our best estimates for the floating parameter n for the two beam energy settings are listed above. Table A.3 and Table A.4 contain the proton electric form factor $G_E^p(Q^2)$ without the floating parameter n, i.e. $f(Q^2)/n$.

The bin width for each θ angle bin is shown as "θ_{bw}" in Table A.1 and Table A.2. The polar angle coverage of a polar angle bin goes from $\theta - 0.5\theta_{bw}$ to $\theta + 0.5\theta_{bw}$.

E_ℓ [MeV]	θ [°]	θ_{bw} [°]	Q^2 [GeV/c]^2	σ [mb/sr]	$\delta\sigma_{\text{stat.}}$ [mb/sr]	$\delta\sigma_{\text{syst.}}$ [mb/sr]	$f(Q^2)$ [1]	$\delta f(Q^2)_{\text{stat.}}$ [1]	$\delta f(Q^2)_{\text{syst.}}$ [1]
1101	0.7625	0.025	0.000215	2173.30000	4.27660	11.14500	0.99801	0.00098	0.00253
1101	0.7875	0.025	0.000229	1920.60000	3.95980	9.79210	1.00070	0.00103	0.00252
1101	0.8125	0.025	0.000244	1694.70000	3.71820	8.38080	1.00060	0.00110	0.00244
1101	0.8375	0.025	0.000259	1496.80000	3.51490	7.89930	0.99916	0.00117	0.00261
1101	0.8625	0.025	0.000275	1335.40000	3.33650	6.01830	1.00090	0.00125	0.00222
1101	0.8875	0.025	0.000291	1190.50000	3.12730	5.51420	1.00060	0.00132	0.00229
1101	0.9200	0.040	0.000312	1026.60000	2.28790	4.92340	0.99847	0.00111	0.00236
1101	0.9575	0.035	0.000338	874.24000	2.17710	4.57160	0.99805	0.00124	0.00258
1101	0.9945	0.039	0.000365	753.64000	1.83400	3.24370	0.99964	0.00122	0.00211
1101	1.0355	0.043	0.000396	639.98000	1.52630	3.43360	0.99868	0.00119	0.00265
1101	1.0810	0.048	0.000431	538.60000	1.26520	2.97920	0.99842	0.00117	0.00274
1101	1.1310	0.052	0.000472	450.10000	1.03500	2.01120	0.99908	0.00115	0.00220
1101	1.1840	0.054	0.000517	373.16000	0.83371	1.52830	0.99692	0.00111	0.00201
1101	1.2405	0.059	0.000568	312.19000	0.65870	1.29390	1.00090	0.00106	0.00204
1101	1.3040	0.068	0.000628	253.75000	0.51715	1.02260	0.99708	0.00102	0.00198
1101	1.3775	0.079	0.000700	204.03000	0.41431	0.82302	0.99765	0.00101	0.00198
1101	1.4655	0.097	0.000793	159.52000	0.32207	0.61447	0.99839	0.00101	0.00189
1101	1.5740	0.120	0.000914	119.67000	0.24211	0.43621	0.99746	0.00101	0.00179
1101	1.7105	0.153	0.001080	85.90400	0.17184	0.34341	0.99791	0.00100	0.00197
1101	1.8935	0.213	0.001323	57.04200	0.10879	0.19283	0.99631	0.00095	0.00166
1101	2.1065	0.213	0.001637	37.08100	0.07857	0.13113	0.99396	0.00106	0.00175
1101	2.3525	0.279	0.002041	23.93300	0.05027	0.09441	0.99566	0.00105	0.00196
1101	2.6420	0.300	0.002574	14.97400	0.03506	0.05211	0.99294	0.00117	0.00174
1101	2.9420	0.300	0.003190	9.72850	0.02670	0.03721	0.99203	0.00137	0.00192
1101	3.2420	0.300	0.003873	6.55510	0.02000	0.02711	0.98838	0.00152	0.00205
1101	3.5420	0.300	0.004621	4.59280	0.01651	0.01826	0.98702	0.00179	0.00196
1101	3.8420	0.300	0.005434	3.27990	0.01337	0.01262	0.98078	0.00202	0.00188
1101	4.1420	0.300	0.006313	2.42860	0.01090	0.01275	0.98034	0.00223	0.00261
1101	4.4420	0.300	0.007257	1.82920	0.00887	0.00650	0.97789	0.00241	0.00175
1101	4.7420	0.300	0.008265	1.41160	0.00735	0.00638	0.97840	0.00259	0.00225
1101	5.0460	0.308	0.009353	1.08360	0.00619	0.00540	0.96986	0.00283	0.00243
1101	5.6000	0.800	0.011506	0.71577	0.00377	0.00273	0.96955	0.00262	0.00188
1101	6.5000	1.000	0.015468	0.38535	0.00374	0.00197	0.95586	0.00480	0.00251

Table A.1: Cross section table for the 1.1 GeV data set.

E_ℓ [MeV]	θ [°]	θ_{bw} [°]	Q^2 [GeV/c]^2	σ [mb/sr]	$\delta\sigma_{\text{stat.}}$ [mb/sr]	$\delta\sigma_{\text{syst.}}$ [mb/sr]	$f(Q^2)$ [1]	$\delta f(Q^2)_{\text{stat.}}$ [1]	$\delta f(Q^2)_{\text{syst.}}$ [1]
2143	0.7075	0.015	0.000700	770.68000	1.12020	2.17990	0.99548	0.00072	0.00131
2143	0.7230	0.016	0.000731	708.49000	1.02900	2.03670	0.99672	0.00072	0.00133
2143	0.7395	0.017	0.000765	647.43000	0.93569	1.78110	0.99676	0.00072	0.00127
2143	0.7570	0.018	0.000801	588.99000	0.85118	1.53890	0.99621	0.00072	0.00119
2143	0.7755	0.019	0.000841	532.97000	0.77834	1.44190	0.99450	0.00073	0.00124
2143	0.7955	0.021	0.000885	483.98000	0.70171	1.31900	0.99717	0.00072	0.00125
2143	0.8170	0.022	0.000934	433.38000	0.64203	1.21350	0.99526	0.00074	0.00129
2143	0.8400	0.024	0.000987	387.58000	0.57302	1.10740	0.99490	0.00074	0.00132
2143	0.8655	0.027	0.001048	344.10000	0.50158	0.92061	0.99516	0.00073	0.00123
2143	0.8935	0.029	0.001116	302.80000	0.44735	0.81152	0.99485	0.00074	0.00123
2143	0.9240	0.032	0.001194	264.97000	0.39036	0.72446	0.99518	0.00074	0.00126
2143	0.9575	0.035	0.001282	228.76000	0.33633	0.62901	0.99287	0.00073	0.00127
2143	0.9945	0.039	0.001383	196.55000	0.28454	0.56710	0.99274	0.00072	0.00134
2143	1.0355	0.043	0.001499	167.69000	0.24187	0.44462	0.99405	0.00072	0.00122
2143	1.0810	0.048	0.001634	140.92000	0.20253	0.37934	0.99297	0.00072	0.00125
2143	1.1310	0.052	0.001789	117.65000	0.16705	0.35418	0.99304	0.00071	0.00142
2143	1.1840	0.054	0.001960	98.22900	0.13930	0.28399	0.99429	0.00071	0.00136
2143	1.2405	0.059	0.002152	81.22500	0.11288	0.22507	0.99233	0.00069	0.00130
2143	1.3040	0.068	0.002377	66.41200	0.09185	0.19050	0.99132	0.00069	0.00135
2143	1.3775	0.079	0.002653	53.22400	0.07312	0.15754	0.99008	0.00068	0.00141
2143	1.4655	0.097	0.003002	41.55000	0.05614	0.11158	0.98986	0.00067	0.00127
2143	1.5740	0.120	0.003463	31.14800	0.04103	0.09216	0.98826	0.00066	0.00143
2143	1.7105	0.153	0.004089	22.30600	0.02713	0.06532	0.98714	0.00061	0.00142
2143	1.8935	0.213	0.005009	14.78300	0.01759	0.04313	0.98404	0.00059	0.00141
2143	2.1065	0.213	0.006197	9.61710	0.01315	0.02956	0.98134	0.00068	0.00149
2143	2.3525	0.279	0.007726	6.12150	0.00874	0.01979	0.97523	0.00071	0.00155
2143	2.6420	0.300	0.009739	3.82970	0.00631	0.01215	0.97134	0.00082	0.00154
2143	2.9420	0.300	0.012069	2.46440	0.00485	0.00725	0.96437	0.00097	0.00141
2143	3.2420	0.300	0.014646	1.64330	0.00373	0.00498	0.95424	0.00112	0.00146
2143	3.5420	0.300	0.017469	1.14160	0.00307	0.00384	0.94722	0.00133	0.00165
2143	3.8420	0.300	0.020537	0.81784	0.00252	0.00380	0.94111	0.00151	0.00217
2143	4.1420	0.300	0.023848	0.60265	0.00206	0.00256	0.93677	0.00168	0.00210
2143	4.4420	0.300	0.027401	0.44210	0.00166	0.00233	0.91986	0.00184	0.00248
2143	4.7420	0.300	0.031196	0.33932	0.00138	0.00201	0.91612	0.00199	0.00301
2143	5.0460	0.308	0.035285	0.25817	0.00116	0.00172	0.90179	0.00218	0.00318
2143	5.4000	0.400	0.040354	0.19505	0.00100	0.00150	0.89474	0.00250	0.00389
2143	5.8000	0.400	0.046477	0.14266	0.00106	0.00144	0.87877	0.00361	0.00478
2143	6.5000	1.000	0.058188	0.08600	0.00068	0.00099	0.84966	0.00376	0.00546

Table A.2: Cross section table for the 2.2 GeV data set.

E_ℓ [MeV]	θ [°]	Q^2 [GeV/c]^2	$G_E^p(Q^2)$ [1]	$\delta G_E^p(Q^2)_{\text{stat.}}$ [1]	$\delta G_E^p(Q^2)_{\text{syst.}}$ [1]
1101	0.7625	0.000215	0.99779	0.00098	0.00253
1101	0.7875	0.000229	1.00050	0.00103	0.00252
1101	0.8125	0.000244	1.00040	0.00110	0.00244
1101	0.8375	0.000259	0.99895	0.00117	0.00260
1101	0.8625	0.000275	1.00070	0.00125	0.00222
1101	0.8875	0.000291	1.00040	0.00131	0.00228
1101	0.9200	0.000312	0.99825	0.00111	0.00236
1101	0.9575	0.000338	0.99783	0.00124	0.00258
1101	0.9945	0.000365	0.99942	0.00122	0.00211
1101	1.0355	0.000396	0.99846	0.00119	0.00265
1101	1.0810	0.000431	0.99821	0.00117	0.00273
1101	1.1310	0.000472	0.99886	0.00115	0.00220
1101	1.1840	0.000517	0.99670	0.00111	0.00201
1101	1.2405	0.000568	1.00070	0.00106	0.00204
1101	1.3040	0.000628	0.99686	0.00102	0.00198
1101	1.3775	0.000700	0.99743	0.00101	0.00198
1101	1.4655	0.000793	0.99817	0.00101	0.00189
1101	1.5740	0.000914	0.99724	0.00101	0.00179
1101	1.7105	0.001080	0.99769	0.00100	0.00197
1101	1.8935	0.001323	0.99609	0.00095	0.00166
1101	2.1065	0.001637	0.99374	0.00106	0.00175
1101	2.3525	0.002041	0.99544	0.00105	0.00196
1101	2.6420	0.002574	0.99272	0.00117	0.00174
1101	2.9420	0.003190	0.99181	0.00137	0.00192
1101	3.2420	0.003873	0.98816	0.00152	0.00205
1101	3.5420	0.004621	0.98680	0.00179	0.00196
1101	3.8420	0.005434	0.98057	0.00202	0.00188
1101	4.1420	0.006313	0.98012	0.00223	0.00261
1101	4.4420	0.007257	0.97768	0.00241	0.00175
1101	4.7420	0.008265	0.97819	0.00259	0.00225
1101	5.0460	0.009353	0.96965	0.00283	0.00243
1101	5.6000	0.011506	0.96934	0.00262	0.00188
1101	6.5000	0.015468	0.95565	0.00480	0.00250

Table A.3: Electric form factor G_E^p table for the 1.1 GeV data set.

E_ℓ [MeV]	θ [°]	Q^2 [GeV/c]^2	$G_E^p(Q^2)$ [1]	$\delta G_E^p(Q^2)_{\text{stat.}}$ [1]	$\delta G_E^p(Q^2)_{\text{syst.}}$ [1]
2143	0.7075	0.000700	0.99715	0.00073	0.00131
2143	0.7230	0.000731	0.99840	0.00073	0.00133
2143	0.7395	0.000765	0.99844	0.00072	0.00127
2143	0.7570	0.000801	0.99789	0.00072	0.00119
2143	0.7755	0.000841	0.99617	0.00073	0.00124
2143	0.7955	0.000885	0.99885	0.00073	0.00126
2143	0.8170	0.000934	0.99693	0.00074	0.00129
2143	0.8400	0.000987	0.99657	0.00074	0.00133
2143	0.8655	0.001048	0.99684	0.00073	0.00123
2143	0.8935	0.001116	0.99653	0.00074	0.00123
2143	0.9240	0.001194	0.99686	0.00074	0.00126
2143	0.9575	0.001282	0.99454	0.00073	0.00127
2143	0.9945	0.001383	0.99441	0.00072	0.00135
2143	1.0355	0.001499	0.99573	0.00072	0.00122
2143	1.0810	0.001634	0.99464	0.00072	0.00125
2143	1.1310	0.001789	0.99471	0.00071	0.00142
2143	1.1840	0.001960	0.99597	0.00071	0.00136
2143	1.2405	0.002152	0.99400	0.00069	0.00130
2143	1.3040	0.002377	0.99299	0.00069	0.00136
2143	1.3775	0.002653	0.99175	0.00069	0.00141
2143	1.4655	0.003002	0.99152	0.00067	0.00128
2143	1.5740	0.003463	0.98992	0.00066	0.00143
2143	1.7105	0.004089	0.98881	0.00061	0.00142
2143	1.8935	0.005009	0.98570	0.00059	0.00141
2143	2.1065	0.006197	0.98300	0.00068	0.00149
2143	2.3525	0.007726	0.97688	0.00071	0.00155
2143	2.6420	0.009739	0.97298	0.00082	0.00155
2143	2.9420	0.012069	0.96599	0.00098	0.00141
2143	3.2420	0.014646	0.95585	0.00112	0.00146
2143	3.5420	0.017469	0.94881	0.00133	0.00165
2143	3.8420	0.020537	0.94270	0.00152	0.00217
2143	4.1420	0.023848	0.93835	0.00169	0.00211
2143	4.4420	0.027401	0.92141	0.00184	0.00248
2143	4.7420	0.031196	0.91766	0.00200	0.00302
2143	5.0460	0.035285	0.90331	0.00219	0.00319
2143	5.4000	0.040354	0.89625	0.00250	0.00390
2143	5.8000	0.046477	0.88026	0.00362	0.00479
2143	6.5000	0.058188	0.85109	0.00377	0.00547

Table A.4: Electric form factor G_E^p table for the 2.2 GeV data set.

Bibliography

[1] R. Pohl *et al.*, "The size of the proton," Nature **466**, 213 (2010). doi:10.1038/nature09250

[2] H. Gao, "Nucleon Electromagnetic Form Factors," Int. J. Mod. Phys. E **12**, 1 (2003) [Erratum-ibid. E **12**, 567 (2003)].

[3] M. I. Eides, H. Grotch and V. A. Shelyuto, "Theory of light hydrogen - like atoms," Phys. Rept. **342**, 63 (2001) doi:10.1016/S0370-1573(00)00077-6 [hep-ph/0002158].

[4] P. J. Mohr, B. N. Taylor and D. B. Newell, "CODATA Recommended Values of the Fundamental Physical Constants: 2010," Rev. Mod. Phys. **84**, 1527 (2012) doi:10.1103/RevModPhys.84.1527 [arXiv:1203.5425 [physics.atom-ph]].

[5] J. C. Bernauer *et al.* [A1 Collaboration], "High-precision determination of the electric and magnetic form factors of the proton," Phys. Rev. Lett. **105**, 242001 (2010) doi:10.1103/PhysRevLett.105.242001 [arXiv:1007.5076 [nucl-ex]].

[6] A. Antognini *et al.*, "Proton Structure from the Measurement of $2S - 2P$ Transition Frequencies of Muonic Hydrogen," Science **339**, 417 (2013). doi:10.1126/science.1230016

[7] P. J. Mohr, D. B. Newell and B. N. Taylor, Rev. Mod. Phys. **88**, no. 3, 035009 (2016) doi:10.1103/RevModPhys.88.035009 [arXiv:1507.07956 [physics.atom-ph]].

[8] A. Antognini, F. Kottmann, F. Biraben, P. Indelicato, F. Nez and R. Pohl, "Theory of the 2S-2P Lamb shift and 2S hyperfine splitting in muonic hydrogen," Annals Phys. **331**, 127 (2013) doi:10.1016/j.aop.2012.12.003 [arXiv:1208.2637 [physics.atom-ph]].

[9] C. E. Carlson, "The Proton Radius Puzzle," Prog. Part. Nucl. Phys. **82**, 59 (2015) doi:10.1016/j.ppnp.2015.01.002 [arXiv:1502.05314 [hep-ph]].

[10] G. A. Miller, Phys. Rev. C **99**, no. 3, 035202 (2019) doi:10.1103/PhysRevC.99.035202 [arXiv:1812.02714 [nucl-th]].

[11] E. Kraus, K. E. Mesick, A. White, R. Gilman and S. Strauch, "Polynomial fits and the proton radius puzzle," Phys. Rev. C **90**, no. 4, 045206 (2014) doi:10.1103/PhysRevC.90.045206 [arXiv:1405.4735 [nucl-ex]].

[12] X. Yan *et al.*, "Robust extraction of the proton charge radius from electron-proton scattering data," Phys. Rev. C **98**, no. 2, 025204 (2018) doi:10.1103/PhysRevC.98.025204 [arXiv:1803.01629 [nucl-ex]].

[13] G. Lee, J. R. Arrington and R. J. Hill, "Extraction of the proton radius from electron-proton scattering data," Phys. Rev. D **92**, no. 1, 013013 (2015) doi:10.1103/PhysRevD.92.013013 [arXiv:1505.01489 [hep-ph]].

[14] M. Horbatsch and E. A. Hessels, "Evaluation of the strength of electron-proton scattering data for determining the proton charge radius," Phys. Rev. C **93**, no. 1, 015204 (2016) doi:10.1103/PhysRevC.93.015204 [arXiv:1509.05644 [nucl-ex]].

[15] K. Griffioen, C. Carlson and S. Maddox, "Consistency of electron scattering data with a small proton radius," Phys. Rev. C **93**, no. 6, 065207 (2016) doi:10.1103/PhysRevC.93.065207 [arXiv:1509.06676 [nucl-ex]].

[16] D. W. Higinbotham, A. A. Kabir, V. Lin, D. Meekins, B. Norum and B. Sawatzky, "Proton radius from electron scattering data," Phys. Rev. C **93**, no. 5, 055207 (2016) doi:10.1103/PhysRevC.93.055207 [arXiv:1510.01293 [nucl-ex]].

[17] J. C. Bernauer and M. O. Distler, "Avoiding common pitfalls and misconceptions in extractions of the proton radius," arXiv:1606.02159 [nucl-th].

[18] A. Beyer *et al.*, "The Rydberg constant and proton size from atomic hydrogen," Science **358**, 79-86 (2017).

[19] H. Fleurbaey *et al.*, "New Measurement of the $1S - 3S$ Transition Frequency of Hydrogen: Contribution to the Proton Charge Radius Puzzle," Phys. Rev. Lett. **120**, no. 18, 183001 (2018) doi:10.1103/PhysRevLett.120.183001 [arXiv:1801.08816 [physics.atom-ph]].

[20] N. Bezginov, T. Valdez, M. Horbatsch, A. Marsman, A. C. Vutha and E. A. Hessels, "A measurement of the atomic hydrogen Lamb shift and the proton charge radius," Science **365**, no. 6457, 1007 (2019). doi:10.1126/science.aau7807

[21] M. Mihovilovic *et al.*, "First measurement of proton's charge form factor at very low Q^2 with initial state radiation," Phys. Lett. B **771**, 194 (2017) doi:10.1016/j.physletb.2017.05.031 [arXiv:1612.06707 [nucl-ex]].

[22] M. Mihovilovic *et al.*, "The proton charge radius extracted from the Initial State Radiation experiment at MAMI," arXiv:1905.11182 [nucl-ex].

[23] R. Gilman *et al.* [MUSE Collaboration], "Studying the Proton "Radius" Puzzle with μ p Elastic Scattering," arXiv:1303.2160 [nucl-ex].

[24] D. Marchand, "A new platform for research and applications with electrons: the PRAE project," EPJ Web Conf. **138**, 01012 (2017). doi:10.1051/epjconf/201713801012

[25] T. Suda *et al.* "Measurement of Proton Charge Radius by Low-Energy Electron Scattering," J. Particle Accelerator Society of Japan **15** (2018) 52-59.

[26] The COMPASS collaboration, "d-Quark Transversity and Proton Radius (Addendum to the COMPASS-II Proposal)".

[27] A. Vorobyev and N. Sagidova, "Method for precision measurement of the Range – Energy relation for protons in pure hydrogen gas," arXiv:1912.06065 [physics.ins-det].

[28] A. Gasparian, M. Khandaker, H. Gao, & D. Dutta, "A proposal for Jefferson Laboratory: High Precision Measurement of the Proton Charge Radius (2011)". JLab PAC40 proposal.

[29] F. Halzen and A. D. Martin, "Quarks And Leptons: An Introductory Course In Modern Particle Physics" (Wiley, New York, 1984).

[30] L. N. Hand, D. G. Miller and R. Wilson, "Electric and Magnetic Formfactor of the Nucleon," Rev. Mod. Phys. **35**, 335 (1963). doi:10.1103/RevModPhys.35.335

[31] A. V. Gramolin, V. S. Fadin, A. L. Feldman, R. E. Gerasimov, D. M. Nikolenko, I. A. Rachek and D. K. Toporkov, "A new event generator for the elastic scattering of charged leptons on protons," J. Phys. G **41**, no. 11, 115001 (2014) doi:10.1088/0954-3899/41/11/115001 [arXiv:1401.2959 [nucl-ex]].

[32] N. Hasan, J. Green, S. Meinel, M. Engelhardt, S. Krieg, J. Negele, A. Pochinsky and S. Syritsyn, "Computing the nucleon charge and axial radii directly at $Q^2 = 0$ in lattice QCD," Phys. Rev. D **97**, no. 3, 034504 (2018) doi:10.1103/PhysRevD.97.034504 [arXiv:1711.11385 [hep-lat]].

[33] R. G. Sachs, "High-Energy Behavior of Nucleon Electromagnetic Form Factors," Phys. Rev. **126**, 2256 (1962). doi:10.1103/PhysRev.126.2256

[34] C. F. Perdrisat, V. Punjabi and M. Vanderhaeghen, "Nucleon Electromagnetic Form Factors," Prog. Part. Nucl. Phys. **59**, 694 (2007) doi:10.1016/j.ppnp.2007.05.001 [hep-ph/0612014].

[35] J. Arrington, W. Melnitchouk and J. A. Tjon, "Global analysis of proton elastic form factor data with two-photon exchange corrections," Phys. Rev. C **76**, 035205 (2007) doi:10.1103/PhysRevC.76.035205 [arXiv:0707.1861 [nucl-ex]].

[36] G. G. Simon, C. Schmitt, F. Borkowski and V. H. Walther, "Absolute electron Proton Cross-Sections at Low Momentum Transfer Measured with a High Pressure Gas Target System," Nucl. Phys. A **333**, 381 (1980). doi:10.1016/0375-9474(80)90104-9

[37] J. J. Murphy, Y. M. Shin and D. M. Skopik, "Proton form factor from 0.15 to 0.79 fm-2," Phys. Rev. C **9**, 2125 (1974) Erratum: [Phys. Rev. C **10**, 2111 (1974)]. doi:10.1103/PhysRevC.9.2125, 10.1103/PhysRevC.10.2111

[38] X. Zhan *et al.*, "High-Precision Measurement of the Proton Elastic Form Factor Ratio $\mu_p G_E/G_M$ at low Q^2," Phys. Lett. B **705**, 59 (2011) doi:10.1016/j.physletb.2011.10.002 [arXiv:1102.0318 [nucl-ex]].

[39] J. Arrington, P. G. Blunden and W. Melnitchouk, "Review of two-photon exchange in electron scattering," Prog. Part. Nucl. Phys. **66**, 782 (2011) doi:10.1016/j.ppnp.2011.07.003 [arXiv:1105.0951 [nucl-th]].

[40] C. E. Carlson and M. Vanderhaeghen, "Two-Photon Physics in Hadronic Processes," Ann. Rev. Nucl. Part. Sci. **57**, 171 (2007) doi:10.1146/annurev.nucl.57.090506.123116 [hep-ph/0701272 [HEP-PH]].

[41] T. W. Donnelly and A. S. Raskin, "Considerations of Polarization in Inclusive electron Scattering from Nuclei," Annals Phys. **169**, 247 (1986). doi:10.1016/0003-4916(86)90173-9

[42] C. B. Crawford *et al.*, "Measurement of the proton electric to magnetic form factor ratio from vector H-1(vector e, e' p)," Phys. Rev. Lett. **98**, 052301 (2007) doi:10.1103/PhysRevLett.98.052301 [nucl-ex/0609007].

[43] D. Hasell *et al.*, "The BLAST experiment," Nucl. Instrum. Meth. A **603**, 247 (2009). doi:10.1016/j.nima.2009.01.131

[44] M. E. Christy *et al.* [E94110 Collaboration], "Measurements of electron proton elastic cross-sections for 0.4 ¡ Q**2 ¡ 5.5 (GeV/c)**2," Phys. Rev. C **70**, 015206 (2004) doi:10.1103/PhysRevC.70.015206 [nucl-ex/0401030].

[45] T. Janssens, R. Hofstadter, E. B. Hughes and M. R. Yearian, "Proton form factors from elastic electron-proton scattering," Phys. Rev. **142**, 922 (1966). doi:10.1103/PhysRev.142.922

[46] M. Goitein *et al.*, "Elastic electron-proton scattering cross-sections measured by a coincidence technique," Phys. Rev. D **1**, 2449 (1970). doi:10.1103/PhysRevD.1.2449

[47] C. Berger, V. Burkert, G. Knop, B. Langenbeck and K. Rith, "Electromagnetic form-factors of the proton at squared four momentum transfers between 10-fm**-2 and 50 fm**-2," Phys. Lett. **35B**, 87 (1971). doi:10.1016/0370-2693(71)90448-5

[48] F. Borkowski, P. Peuser, G. G. Simon, V. H. Walther and R. D. Wendling, "Electromagnetic Form-Factors of the Proton at Low Four-Momentum Transfer," Nucl. Phys. B **93**, 461 (1975). doi:10.1016/0550-3213(75)90514-3

[49] P. E. Bosted *et al.*, "Measurements of the Deuteron and Proton Magnetic Form-factors at Large Momentum Transfers," Phys. Rev. C **42**, 38 (1990). doi:10.1103/PhysRevC.42.38

[50] W. Bartel *et al.*, "Small-Angle Electron-Proton Elastic Scattering Cross Sections for Momentum Transfers between 10 and 105 f $^{-2}$," Phys. Rev. Lett. **17**, 608 (1966). doi:10.1103/PhysRevLett.17.608

[51] S. Stein *et al.*, "Electron Scattering at 4-Degrees with Energies of 4.5-GeV - 20-GeV," Phys. Rev. D **12**, 1884 (1975). doi:10.1103/PhysRevD.12.1884

[52] M.I. Niculescu, Ph.D. thesis, Hampton University

[53] A. Denig, "Recent results from the Mainz Microtron MAMI and an outlook for the future," AIP Conf. Proc. **1735**, no. 1, 020006 (2016). doi:10.1063/1.4949374

[54] A. Antognini, Ph.D. dissertation, Ludwig-Maximilians-University Munich, "The Lamb Shift Experiment in Muonic Hydrogen."

[55] J. R. Sapirstein and D. R. Yennie, "Theory Of Hydrogenic Bound States," Adv. Ser. Direct. High Energy Phys. **7**, 560 (1990). doi:10.1142/9789814503273_0012

[56] W. E. Lamb and R. C. Retherford, "Fine Structure of the Hydrogen Atom by a Microwave Method," Phys. Rev. **72**, 241 (1947). doi:10.1103/PhysRev.72.241

[57] H. A. Bethe, "The Electromagnetic shift of energy levels," Phys. Rev. **72**, 339 (1947). doi:10.1103/PhysRev.72.339

[58] R. D. McKeown, "The Jefferson Lab 12 GeV Upgrade," J. Phys. Conf. Ser. **312**, 032014 (2011) doi:10.1088/1742-6596/312/3/032014 [arXiv:1009.3503 [physics.ins-det]].

[59] J. Benesch, Private communication, Jefferson Lab.

[60] F. Sauli, "The gas electron multiplier (GEM): Operating principles and applications," Nucl. Instrum. Meth. A **805**, 2 (2016). doi:10.1016/j.nima.2015.07.060

[61] The SoLID collaboration, "SoLID (Solenoidal Large Intensity Device) Updated Preliminary Conceptual Design Report" https://hallaweb.jlab.org/12GeV/SoLID/download/doc/solid-precdr-2018.pdf

[62] A. Gasparian [PrimEx Collaboration], "A high performance hybrid electromagnetic calorimeter at Jefferson Lab,"

[63] The Primakoff Experiment at Jefferson Lab. https://www.jlab.org/primex/

[64] I. Larin *et al.* [PrimEx Collaboration], "A New Measurement of the π^0 Radiative Decay Width," Phys. Rev. Lett. **106**, 162303 (2011) doi:10.1103/PhysRevLett.106.162303 [arXiv:1009.1681 [nucl-ex]].

[65] Y. Zhang, Ph.D thesis, "A Precision Measurement of Neutral Pion Lifetime."

[66] C. W. Fabjan and F. Gianotti, "Calorimetry for Particle Physics" CERN-EP/2003-075

[67] S. Danagulian [PrimEx Collaboration], "LED based light monitoring system for the PrimEx experiment at Jefferson Lab,"

[68] D. I. Sober *et al.*, "The bremsstrahlung tagged photon beam in Hall B at JLab," Nucl. Instrum. Meth. A **440**, 263 (2000). doi:10.1016/S0168-9002(99)00784-6

[69] M. J. French *et al.*, "Design and results from the APV25, a deep sub-micron CMOS front-end chip for the CMS tracker," Nucl. Instrum. Meth. A **466**, 359 (2001). doi:10.1016/S0168-9002(01)00589-7

[70] S. Martoiu, H. Muller, A. Tarazona and J. Toledo, "Development of the scalable readout system for micro-pattern gas detectors and other applications," JINST **8**, C03015 (2013). doi:10.1088/1748-0221/8/03/C03015

[71] B. A. Mecking *et al.* [CLAS Collaboration], "The CEBAF Large Acceptance Spectrometer (CLAS)," Nucl. Instrum. Meth. A **503**, 513 (2003). doi:10.1016/S0168-9002(03)01001-5

[72] G. D. Lafferty and T. R. Wyatt, "Where to stick your data points: The treatment of measurements within wide bins," Nucl. Instrum. Meth. A **355**, 541 (1995). doi:10.1016/0168-9002(94)01112-5

[73] R. Wigmans and M. T. Zeyrek, "On the differences between calorimetric detection of electrons and photons," Nucl. Instrum. Meth. A **485**, 385 (2002). doi:10.1016/S0168-9002(01)02141-6

[74] D. Romanov, I. Larin, A. Gasparian, L. Gan, M. Khandaker, and M. Kubantsev, "HyCal Reconstruction Fine Tuning and Transition Region Performance Measured During Calibration Run," PrimEx Note #83. https://www.jlab.org/primex/

[75] M. E. Christy and P. E. Bosted, "Empirical fit to precision inclusive electron-proton cross- sections in the resonance region," Phys. Rev. C **81**, 055213 (2010) doi:10.1103/PhysRevC.81.055213 [arXiv:0712.3731 [hep-ph]].

[76] Kramer, Mark A, "Nonlinear principal component analysis using autoassociative neural networks," AIChE Journal. 37 (2): 233?243. doi:10.1002/aic.690370209

[77] K. O'Shea, R. Nash, "An Introduction to Convolutional Neural Networks," arXiv:1511.08458.

[78] S. Agostinelli *et al.* [GEANT4 Collaboration], "GEANT4: A Simulation toolkit," Nucl. Instrum. Meth. A **506**, 250 (2003). doi:10.1016/S0168-9002(03)01368-8

[79] I. Akushevich, H. Gao, A. Ilyichev and M. Meziane, "Radiative corrections beyond the ultra relativistic limit in unpolarized ep elastic and Mller scatterings for the PRad Experiment at Jefferson Laboratory," Eur. Phys. J. A **51**, no. 1, 1 (2015). doi:10.1140/epja/i2015-15001-8

[80] O. Tomalak, "Two-photon exchange correction in elastic lepton-proton scattering," Few Body Syst. **59**, no. 5, 87 (2018) doi:10.1007/s00601-018-1413-8 [arXiv:1806.01627 [hep-ph]].

[81] O. Tomalak and M. Vanderhaeghen, "Two-photon exchange correction in elastic unpolarized electron-proton scattering at small momentum transfer," Phys. Rev. D **93**, no. 1, 013023 (2016) doi:10.1103/PhysRevD.93.013023 [arXiv:1508.03759 [hep-ph]].

[82] O. Tomalak and M. Vanderhaeghen, ' 'Subtracted dispersion relation formalism for the two-photon exchange correction to elastic electron-proton scattering: comparison with data," Eur. Phys. J. A **51**, no. 2, 24 (2015) doi:10.1140/epja/i2015-15024-1 [arXiv:1408.5330 [hep-ph]].

[83] L. W. Mo and Y. S. Tsai, "Radiative Corrections to Elastic and Inelastic e p and mu p Scattering," Rev. Mod. Phys. **41**, 205 (1969). doi:10.1103/RevModPhys.41.205

[84] J. J. Kelly, "Simple parametrization of nucleon form factors," Phys. Rev. C **70**, 068202 (2004). doi:10.1103/PhysRevC.70.068202

[85] A. B. Arbuzov and T. V. Kopylova, "On higher order radiative corrections to elastic electron?proton scattering," Eur. Phys. J. C **75**, no. 12, 603 (2015) doi:10.1140/epjc/s10052-015-3833-7 [arXiv:1510.06497 [hep-ph]].

[86] Chao Gu, Private communication, Duke University.

[87] Vladimir Khachatryan, Private communication, Duke University.

[88] A. G. Aleksejevs, S. G. Barkanova, V. A. Zykunov and E. A. Kuraev, "Estimating two-loop radiative effects in the MOLLER experiment," Phys. Atom. Nucl. **76**, 888 (2013) [Yad. Fiz. **76**, 942 (2013)]. doi:10.1134/S1063778813070028

[89] D. Drechsel, S. S. Kamalov and L. Tiator, "Unitary Isobar Model - MAID2007," Eur. Phys. J. A **34**, 69 (2007) doi:10.1140/epja/i2007-10490-6 [arXiv:0710.0306 [nucl-th]].

[90] S. Venkat, J. Arrington, G. A. Miller and X. Zhan, "Realistic Transverse Images of the Proton Charge and Magnetic Densities," Phys. Rev. C **83**, 015203 (2011) doi:10.1103/PhysRevC.83.015203 [arXiv:1010.3629 [nucl-th]].

[91] D. W. Higinbotham and R. E. McClellan, "How Analytic Choices Can Affect the Extraction of Electromagnetic Form Factors from Elastic Electron Scattering Cross Section Data," arXiv:1902.08185 [physics.data-an].

[92] J. C. Bernauer, "Measurement of the elastic electron-proton cross section and separation of the electric and magnetic form factor in the Q^2 range from 0.004 to 1 $(GeV/c)^2$,"

[93] J. Arrington, "Implications of the discrepancy between proton form-factor measurements," Phys. Rev. C **69**, 022201 (2004) doi:10.1103/PhysRevC.69.022201 [nucl-ex/0309011].

[94] J. Arrington and I. Sick, "Precise determination of low-Q nucleon electromagnetic form factors and their impact on parity-violating e-p elastic scattering," Phys. Rev. C **76**, 035201 (2007) doi:10.1103/PhysRevC.76.035201 [nucl-th/0612079].

[95] F. Borkowski, G. G. Simon, V. H. Walther and R. D. Wendling, "On the determination of the proton RMS-radius from electron scattering data," Z. Phys. A **275**, no. 1, 29 (1975). doi:10.1007/BF01409496

[96] J. C. Bernauer *et al.* [A1 Collaboration], "Electric and magnetic form factors of the proton," Phys. Rev. C **90**, no. 1, 015206 (2014) doi:10.1103/PhysRevC.90.015206 [arXiv:1307.6227 [nucl-ex]].

[97] J. M. Alarcón, D. W. Higinbotham, C. Weiss and Z. Ye, "Proton charge radius extraction from electron scattering data using dispersively improved chiral effective field theory," Phys. Rev. C **99**, no. 4, 044303 (2019) doi:10.1103/PhysRevC.99.044303 [arXiv:1809.06373 [hep-ph]].

[98] Z. Ye, J. Arrington, R. J. Hill and G. Lee, "Proton and Neutron Electromagnetic Form Factors and Uncertainties," Phys. Lett. B **777**, 8 (2018) doi:10.1016/j.physletb.2017.11.023 [arXiv:1707.09063 [nucl-ex]].

[99] W. Xiong *et al.*, "A small proton charge radius from an electron proton scattering experiment," Nature **575**, 147-150 (2019). doi:10.1038/s41586-019-1721-2

[100] CODATA internationally recommended 2018 values of the fundamental physics constants. https://physics.nist.gov/cuu/Constants/

[101] D. Frerejacque, D. Benaksas and D. J. Drickey, "Proton Form-factors From Proton Observation," Phys. Rev. **141**, 1308 (1966). doi:10.1103/PhysRev.141.1308

[102] Y. K. Akimov *et al.*, "Small angle scattering of electrons by protons," Sov. Phys. JETP **35**, 651 (1972) [Zh. Eksp. Teor. Fiz. **62**, 1231 (1972)].

[103] G. Hohler, E. Pietarinen, I. Sabba Stefanescu, F. Borkowski, G. G. Simon, V. H. Walther and R. D. Wendling, "Analysis of Electromagnetic Nucleon Form-Factors," Nucl. Phys. B **114**, 505 (1976). doi:10.1016/0550-3213(76)90449-1

[104] Y. K. Akimov *et al.*, "Investigation Of Elastic Electron - Proton Scattering In The Region Of Squared Momentum Transfers 0.12-f**-2 <= Q**2 <= 0.5-f**-2," Sov. J. Nucl. Phys. **29**, 474 (1979) [Yad. Fiz. **29**, 922 (1979)].

[105] M. McCord, H. Crannell, L. W. Fagg, J. T. O'Brien, D. I. Sober, J. W. Lightbody, X. K. Maruyama and P. A. Treado, "Preliminary results of a new determination of the rms charge radius of the proton," Nucl. Instrum. Meth. B **56/57**, 496 (1991). doi:10.1016/0168-583X(91)96079-Z

[106] P. Mergell, U. G. Meissner and D. Drechsel, "Dispersion theoretical analysis of the nucleon electromagnetic form-factors," Nucl. Phys. A **596**, 367 (1996) doi:10.1016/0375-9474(95)00339-8 [hep-ph/9506375].

[107] R. Rosenfelder, "Coulomb corrections to elastic electron?proton scattering and the proton charge radius," Phys. Lett. B **479**, 4 (2000)

[108] I. Eschrich *et al.*, "Measurement of the Σ^- charge radius by Σ^--electron elastic scattering," Phys. Lett. B **522**, 3-4 (2001)

[109] I. Sick, "On the RMS radius of the proton," Phys. Lett. B **576**, 62 (2003) doi:10.1016/j.physletb.2003.09.092 [nucl-ex/0310008].

[110] P. G. Blunden and I. Sick, "Proton radii and two-photon exchange," Phys. Rev. C **72**, 057601 (2005) doi:10.1103/PhysRevC.72.057601 [nucl-th/0508037].

[111] M. A. Belushkin, H.-W. Hammer and U.-G. Meissner, "Dispersion analysis of the nucleon form-factors including meson continua," Phys. Rev. C **75**, 035202 (2007) doi:10.1103/PhysRevC.75.035202 [hep-ph/0608337].

[112] R. J. Hill and G. Paz, "Model independent extraction of the proton charge radius from electron scattering," Phys. Rev. D **82**, 113005 (2010) doi:10.1103/PhysRevD.82.113005 [arXiv:1008.4619 [hep-ph]].

[113] D. Borisyuk, "Proton charge and magnetic rms radii from the elastic *ep* scattering data," Nucl. Phys. A **843**, 59 (2010) doi:10.1016/j.nuclphysa.2010.05.054 [arXiv:0911.4091 [hep-ph]].

[114] G. Ron *et al.* [Jefferson Lab Hall A Collaboration], "Low Q^2 measurements of the proton form factor ratio mu_pG_E/G_M," Phys. Rev. C **84**, 055204 (2011) doi:10.1103/PhysRevC.84.055204 [arXiv:1103.5784 [nucl-ex]].

[115] I. Sick, "Problems with proton radii," Prog. Part. Nucl. Phys. **67**, 473 (2012). doi:10.1016/j.ppnp.2012.01.013

[116] C. Adamuscin, S. Dubnicka and A. Z. Dubnickova, "New value of the proton charge root mean square radius," Prog. Part. Nucl. Phys. **67**, 479 (2012). doi:10.1016/j.ppnp.2012.01.014

[117] I. T. Lorenz, H.-W. Hammer and U. G. Meissner, "The size of the proton - closing in on the radius puzzle," Eur. Phys. J. A **48**, 151 (2012) doi:10.1140/epja/i2012-12151-1 [arXiv:1205.6628 [hep-ph]].

[118] K. M. Graczyk and C. Juszczak, "Proton radius from Bayesian inference," Phys. Rev. C **90**, 054334 (2014) doi:10.1103/PhysRevC.90.054334 [arXiv:1408.0150 [hep-ph]].

[119] I. T. Lorenz, U. G. Meißner, H.-W. Hammer and Y.-B. Dong, "Theoretical Constraints and Systematic Effects in the Determination of the Proton Form Factors," Phys. Rev. D **91**, no. 1, 014023 (2015) doi:10.1103/PhysRevD.91.014023 [arXiv:1411.1704 [hep-ph]].

[120] J. Arrington and I. Sick, "Evaluation of the proton charge radius from e-p scattering," J. Phys. Chem. Ref. Data **44**, 031204 (2015) doi:10.1063/1.4921430 [arXiv:1505.02680 [nucl-ex]].

[121] M. Horbatsch, E. A. Hessels and A. Pineda, "Proton radius from electron-proton scattering and chiral perturbation theory," Phys. Rev. C **95**, no. 3, 035203 (2017) doi:10.1103/PhysRevC.95.035203 [arXiv:1610.09760 [nucl-th]].

[122] S. Zhou, P. Giulani, J. Piekarewicz, A. Bhattacharya and D. Pati, "Reexamining the proton-radius problem using constrained Gaussian processes," Phys. Rev. C **99**, no. 5, 055202 (2019) doi:10.1103/PhysRevC.99.055202 [arXiv:1808.05977 [nucl-th]].

[123] W. H. You, Y. Zhou, C. Li, H. F. Chen, M. Shao, Y. J. Sun, Z. B. Tang and J. B. Liu, "A large-area GEM detector using a novel self-stretching technique," Chin. Phys. C **39**, no. 4, 046001 (2015) doi:10.1088/1674-1137/39/4/046001 [arXiv:1405.1872 [physics.ins-det]].

[124] A. Gasparian, H. Gao, D. Dutta, N. Liyanage & E. Pasyuk "Precision Deuteron Charge Radius Measurement with Elastic Electron-Deuteron Scattering". JLab PR12-17-009.

Biography

Weizhi Xiong attended the No. 86 middle school and high school of Guangzhou from 2001 to 2007, and came to the United States of America for higher educations in 2007. Xiong received a bachelor degree in physics from University of South Carolina in 2012. In the fall of 2013, Xiong attended Duke University and joined the Medium Energy Physics Group in 2014.